Development of a Diverter Piloted Switched Vortex Valve for Secondary Flow Modulation

Patrick Boyle

Lincoln College

Oxford Thermofluids Institute

University of Oxford

A thesis submitted for the degree of

Doctor of Philosophy

Hilary Term 2022

Abstract

Active modulation of coolant flow rates would improve cycle efficiencies for jet engines. This thesis presents a proof of concept multistage fluidic device, the staged switched vortex valve (staged SVV), which modulates flow rates by switching between high and low flow impedance states. It is shown that the device can be actively switched between states using conventional mass flow injection and, with minimal modifications, 200Hz acoustic tones.

A grey-box model of the staged switched vortex valve is developed as part of the investigation. This model encapsulates the complex fluid interactions associated with the vortex chamber and the diverter switch sections within black-box objects tuned with steady-state and transient characteristics. The model convincingly reproduces pressures and mass flow rates associated with steady conditions, switching events and self-excited oscillatory instabilities. Furthermore, the model can predict the conditions that will trigger switching and oscillatory instabilities.

The model is used in conjunction with the physical device to investigate the effects inter-stage duct impedances and sub-switching control signals can have on the stability and performance of the staged SVV. It is discovered that an appropriately sized inter-stage impedance can be used to improve the steady-state performance, with a localised constriction area ratio of 0.25 in one of the ducts affecting a 3.8% increase in the device's turn-down ratio (TDR). However, the resulting increase in inter-stage pressure losses also makes the device more susceptible to self-excited oscillations. Sub-switching acoustic signals can also be used to improve steady-state

performance. A 5.6% increase in the TDR is achieved by applying a 640Hz acoustic tone to the unattached side of the pilot diverter section. Moreover, sub-acoustic tones can also be used to stabilise the staged SVV and suppress self-excited oscillations.

Table of contents

List of figures

Nomenclature

Roman Symbols

$\bar{u}$	mean jet velocity
$\mathbf{u}$	input vector
$\mathbf{u}$	output vector
$\mathbf{x}$	state vector
$\dot{m}$	mass flow rate
$\dot{m}_{\mathrm{e}}$	entrainment mass flow rate
$\dot{m}_{\mathrm{r}}$	recirculation mass flow rate
$\dot{m}_{\mathrm{tot}}$	staged SVV total mass flow rate
A	area
c	speed of sound
C_{D}	orifice meter discharge coefficient
d, D	diameter
d_{3D}	3D printing layer height
d_{psx}	laser cut perspex roughness height
D_{h}	hydraulic diameter
F	steady-state characterisation function
f	frequency
f_{D}	Darcy friction factor
f_{n}	natural shear-layer instability frequency
f_{p}	jet preffered mode frequency
$G(s)$	tranfer function
h	nozzle width
J	supply jet momentum
K_{L}	pressure loss coefficient
L	length
L_{leg}	pilot stage leg length
$L_{\mathrm{N\text{-}S}}$	nozzle-to-splitter distance
$L_{\mathrm{S\text{-}S}}$	speaker-to-speaker distance

p	static pressure
p_a	atmospheric pressure
Q	volumetric flow rate
q	dynamic pressure
q_oR	radial duct pitot-static measurement
q_oT	tangential duct pitot-static measurement
q_sol	solenoid pitot-static measurement
R	Radius
R_gas	air gas constant
R_I	pressure loss parameter of duct model
Re	Reynolds number
s	entropy
St	Strouhal Number
T	temperature
t_sw	switching time
u_0	jet centreline flow velocity
V	volume
V_crit	critical recirculation bubble volume
w	specific work
$\mathrm{V_{RMS}}$	RMS Voltage

Greek Symbols

α	attachment state variable
β	orifice meter diameter ratio
ϵ	orifice meter expansibility factor
ϵ_r	surface roughness height
η	thermodynamic efficiency
γ	heat capacity ratio
μ	dynamic viscosity
ρ	density
τ	sub-switching response time
θ	momentum thickness

Pressure Differences

Δp_c	$= p_\mathrm{c}^+ - p_\mathrm{c}^-$
Δp_c^+	$= p_\mathrm{nozz} - p_\mathrm{c}^+$
Δp_c^+	$= p_\mathrm{nozz} - p_\mathrm{out}^+$
Δp_c^-	$= p_\mathrm{nozz} - p_\mathrm{c}^-$

$\Delta p_{\text{out}} = p^{+}_{\text{out}} - p^{-}_{\text{out}}$

$\Delta p^{-}_{\text{out}} = p_{\text{nozz}} - p^{-}_{\text{out}}$

Superscripts

x^{+} attached side of a wall attachment device

x^{-} unattached side of a wall attachment device

Subscripts

$x_{\text{c,nozz}}$ control port nozzle

x_{c} control port

x_{nozz} supply nozzle

x_{out} outlet port

x_{p} pilot stage

x_{R} radial (non-vortex) state

x_{r} radial side of the SVV

x_{SVV} SVV stage

x_{s} supply port

x_{t0} value at previous iterative time step

x_{T} tangential (vortex) state

x_{t} tangential side of the SVV

x_{vx} vortex chamber

x_I mass flow node parameter of duct model

x_i pressure node parameter of duct model

Acronyms / Abbreviations

CFD Computational Fluid Dynamics

FSO Full Scale Output

LAFPA Localised Arc-Filament Plasma Actuator

LES Large Eddy Simulation

PIV Particle Image Velocimetry

PR Pressure Ratio

PSFVV Plasma Switched Fluidic Vortex Valve

RANS Reynolds Averaged Navier-Stokes

SDBD Single Dielectric Barrier Discharge

SFC Specific Fuel Consumption

SJ Synthetic Jet

SPL Sound Pressure Level

SVV Switched Vortex Valve

TDR Turndown Ratio

TET Turbine Entry Temperature

Circuit Symbols

Diverter

Loudspeaker

Orifice Meter

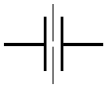

Pressure Regulator

Switched Vortex Valve

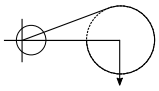

Variable Flow Restriction (screwed gate or ball valve)

Chapter 1
Introduction

1.1 Background

The gas turbine is a relatively recent invention, with much of its initial development occurring in the late 1930s. There is some debate about who should be credited as the inventor of the jet engine. The first patent of a simple jet engine with an axial compressor was submitted by Guillaume in 1922 [30]. However, Guillaume's design was never built. During the 1930s, both Sir Frank Whittle in Britain and Hans von Ohain in Germany started developing turbojet engines with centrifugal compressors. Whittle was the first to submit a patent for his design in 1931 [115], but Ohain was the first to develop a working prototype. The first jet engine-powered flight occurred on the 27th of August 1939. The aircraft was a Heinkel He 178 with a HeS 3 turbojet engine developed by Ohain. Just two years later, Whittle's engine, the Power Jets W.1 turbojet, was used to power the flight of a Gloster E.28/39. Though initially much less fuel-efficient, the jet engine could produce greater thrust and had a much higher power-to-weight ratio than conventional piston engines. Consequently, after their initial development, jet engines based on Wittle's design rapidly started to supplant piston engines in aircraft. Culminating in the flight of the first jet-powered civil aircraft in 1952, the de Havilland Comet.

Since the 1950s, the design of civil jet engines has changed dramatically. In the civil aviation industry, the emphasis has been on lowering running costs by improving engine efficiencies. To this end, turbojets were superseded by turboprop and turbofan engines for civil aircraft. Turboprops and turbofans can achieve much higher fuel

efficiencies, and they produce less noise pollution due to their improved propulsive efficiencies. However, it wasn't until the mid-1960s, with the introduction of high bypass ratio turbofan engines, that fuel efficiencies started to exceed that of the best piston engines. Later, with the introduction of the first three spool turbofan engines by Rolls Royce in 1972, greater fuel efficiencies could be achieved by allowing the fan to spin at lower speeds than the intermediate compressor stage. Since the 1970s, a major source of efficiency gains has been achieved by allowing turbine entry temperatures (TETs) to increase (more on this in section 1.2). Higher TETs have become possible through improved blade materials and the introduction of blade cooling.

Since the first jet-powered civil aircraft flight, the global market for commercial jet flight has grown dramatically. It has been estimated by ATAG [1] that as of 2020, civil aviation was responsible for 4.1% of global GDP. In 2016 there were 3.7 commercial flights in a single year [76]. Up until the emergence of the COVID-19 pandemic, there had been consistent growth of 5% every year for the last decade [76]. It was also predicted that this growth would continue until 2030 [76]. The pandemic has been responsible for a dramatic drop in passenger traffic of 94.4% between April 2019 and April 2020 [1]. However, there is no reason not to expect the pre-pandemic trend to reassert itself in a post-pandemic world. If the pre-pandemic trend does continue, there will be a $\sim$80% increase in global flights by 2030 versus 2018 levels. This growing air travel market will be happening against the backdrop of an ongoing climate crisis. The climate crisis is being driven by rising greenhouse emissions. Despite an 80% reduction in CO_2 emissions per passenger per kilometre since the 1950s, the growth in global air travel means that airlines are now responsible for over 2% of global CO_2 emissions [1].

Strong incentives already existed within the aviation industry to continue to improve engine efficiencies and reduce fuel consumption. However, there are now

additional pressures to improve fuel efficiencies by the impending climate crisis. In response to the crisis, various aerospace institutions and political bodies have started setting CO_2 emissions targets. A commonly cited target is a 50% reduction in CO_2 emissions relative to 2005 levels, published by the International Air Transport Association (IATA) and the Air Transport Action Group ATAG [76]. Whilst new propulsion and energy storage technologies remain in development, a parallel strategy is to continue improving efficiencies for conventional jet engines.

1.2 Joule Cycle

In the past, a reliable method for improving engine performance and lowering specific fuel consumption SFC was to increase TET. The Joule cycle can be used to explain why increasing TETs has been a viable path towards greater engine efficiencies. The idealised cycle for a jet engine is described by the Joule cycle. Pressure-volume and temperature-entropy diagrams for the Joule cycle are presented in figure 1.1 alongside a simplified schematic of a gas turbine.

The processes shown in figure 1.1 are as follows

- $1 \rightarrow 2s$**.** air is ingested by the engine and passes through the fan and the compressor, and there is an isentropic rise in temperature and pressure
- $2 \rightarrow 3$**.** air and fuel are mixed and ignited in the combustion temperature, and there is a reversible, isobaric temperature rise
- $3 \rightarrow 4s$**.** air exerts work w_{in} on the turbine driving the compressor and fan, the air expands as it passes through the turbine and there is an isentropic temperature and pressure drop
- $4s \rightarrow 1$**.** air leaves the turbine as exhaust at ambient pressure, this is represented in the cycle as reversible, isobaric cooling

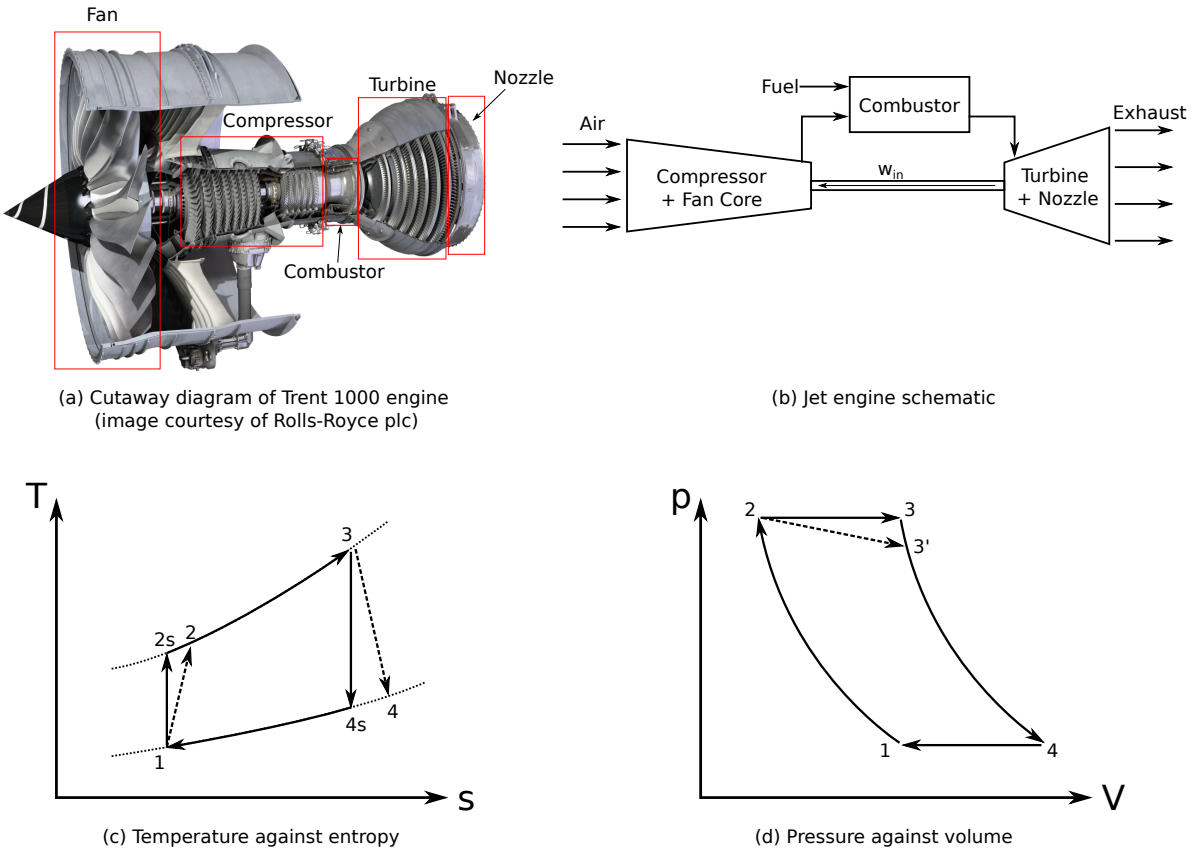

(a) Cutaway diagram of Trent 1000 engine (image courtesy of Rolls-Royce plc)

(b) Jet engine schematic

(c) Temperature against entropy

(d) Pressure against volume

Fig. 1.1 Idealized Joule cycle

It can be shown that the thermodynamic efficiency of this idealised process is given by

$$\eta = 1 - \frac{1}{\left(\frac{p_{2s}}{P_1}\right)^{\frac{\gamma-1}{\gamma}}} = 1 - \frac{T_1}{T_{2s}} \tag{1.1}$$

where γ is the heat capacity ratio. Whilst the specific work done on the gas is given by

$$w = \left[T_3\left(1 - \left(\frac{P_2}{P_1}\right)^{\frac{\gamma-1}{\gamma}}\right) - T_1\left(\left(\frac{P_2}{P_1}\right)^{\frac{\gamma-1}{\gamma}} - 1\right)\right] \tag{1.2}$$

Thus for an idealised Joule cycle, the thermodynamic efficiency and engine power are improved by increasing the compression ratio p_{2s}/p_1. Whilst the power, for a given size of engine, can also be increased by increasing the TET (T_3). Theoretically, the thermodynamic efficiency could be improved by increasing the p_{2s}/p_1 without increasing the TET by reducing $T_3 - T_2s$. However, for real gas turbines, some inefficiencies cause the engine cycle to deviate from the idealised Joule cycle. There

are losses in the compressors, turbines and nozzle that mean the associated processes are not isentropic. Furthermore, a pressure drop across the combustion chamber ensures that $p_3' < p_2$. The combination of all these effects is that real engine cycles have thermodynamic efficiencies that are not purely functions of p_2/p_1. TET emerges as a factor affecting thermodynamic efficiency and engine power/thrust. There is a strong incentive to increase both the compression ratio and TETs, as the increased thermodynamic efficiency results in an increase in fuel efficiency as measured using the specific fuel consumption SFC.

Up to the early 1960s, the maximum TET was limited by the material properties of turbine blades and the maximum thermal stresses they could withstand without risk of failure. Since the introduction of blade cooling, there has been a marked increase in the TETs (figure 1.2), and they continue to increase with improvements in cooling effectiveness.

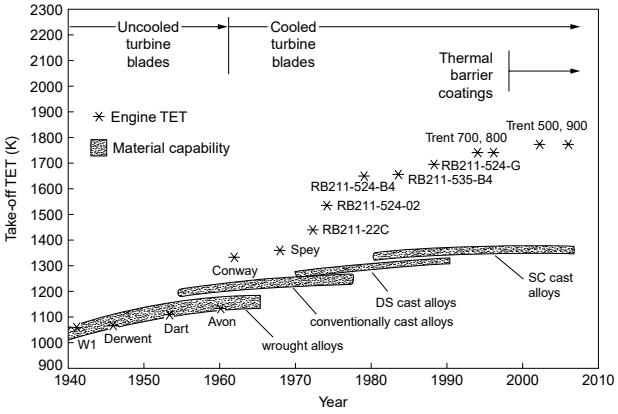

Fig. 1.2 Evolution of turbine entry temperatures for Rolls Royce engines [83]

However, the efficiency gains achievable by increasing cooling effectiveness are limited. The TETs could reach higher levels by simply raising coolant flow rates or developing blade materials that can withstand higher temperatures. However, Horlock et al. [32] show, through cycle efficiency calculations, that raising TETs only has a marginal impact on the engine efficiency if it is achieved by increasing coolant

flow rates. Whilst the exotic metals required to make high-temperature alloys are expensive, thus developing blades capable of withstanding ever higher temperatures may eventually become economically unviable. Furthermore, there is a direct link between engine temperature and NO_x emissions. Consequently, the choice of TET could ultimately be limited by NO_x emissions requirements. As an alternative to increasing TETs, engine efficiencies could be improved upon by active control of coolant flow rates.

1.3 Coolant Flow Modulation

Blade cooling involves extracting some of the compressor air and redirecting it to regions of the turbine that require air cooling. The fraction of compressor flow bled off as coolant is conventionally set by fixed restrictions in the coolant flow paths. Without active flow control, these constrictions have to be calibrated so as to provide sufficient coolant for maximum engine power conditions. Consequently, during cruise when the engine is operating well below maximum power, more coolant is being bled away from the compressor than is strictly required.

The efficiency gains associated with the higher TETs achievable with blade cooling are partially offset by an efficiency penalty associated with bleeding coolant air away from the compressor. The compressor does work on the air w_{in} to raise the pressure. This energy is recovered with excess as w_{net} in the turbine section, but this is only possible because of the enthalpy rise across the combustion chamber. The coolant air does not pass through the combustion chamber, so there is no w_{net} returned by this fraction of the compressor core flow. Furthermore, there are additional losses where the coolant flow is reintroduced to the core flow in the turbine. These additional losses are because of the flow velocity mismatch leading to flow mixing losses and the dilution of the hot mainstream by the coolant (reducing the energy density of the

mainstream). Culley [17] states that for every 1% reduction in the coolant flow rate, the SFC reduces by 0.5-0.7% for commercial jet engines. Therefore, over-cooling the engine during cruise is detrimental to engine efficiency. This assertion is supported by numerical simulations presented in Kim et al. [44]. Kim's simulations indicate that for constant engine power levels, active coolant flow modulation (where coolant flow rates are tied to TET) will lower the TET, lower SFC, and increase compressor and turbine efficiencies.

The coolant flow rates could be regulated using conventional mechanical valves. However, mechanical valves robust enough to reliably operate at high temperatures and pressures are generally quite heavy. Furthermore, an improperly maintained valve could get stuck in a restrictive state leading to the turbine section being starved of coolant. Consequently, redundancies would need to be incorporated into the system, adding further weight and expense.

This thesis presents a fluidic device (a staged switched vortex valve) as a viable alternative to mechanical valves. Fluidic devices are flow cavities that utilise various fluid dynamic phenomena, such as Coandă effect, to manipulate flows. These devices do not have any moving parts and are thus considerably lighter and less susceptible to wear and tear than conventional mechanical valves.

1.4 Fluidics

The field of fluidics began at the Harry Diamond Laboratories in 1959 [41], with the development of flow cavities that were designed to perform analogue and digital operations. These devices were developed in parallel to electronic digital logic devices. There exist fluidic versions of the logic gates, diodes, amplifiers and oscillators. The idea was that fluidic components could be used to construct logic circuits for carrying

out computational tasks. There was a flurry of development with fluidic devices during the 1960s and into the early 1970s with the development of fluidic based devices for a wide range of computational tasks. Figure 1.3 presents some fluidic devices commercially available in the 1960s, and figure 1.4 presents an exploded schematic of a fluidic integrated circuit developed as part of a pneumatic actuator control system for nuclear rockets [19]. There was even a fluidic based programmable computer built as a proof of concept in 1964 called FLODAC [24]. However, research into this field dropped off dramatically in the 1970s as electronic digital logic became the widely accepted method for computation.

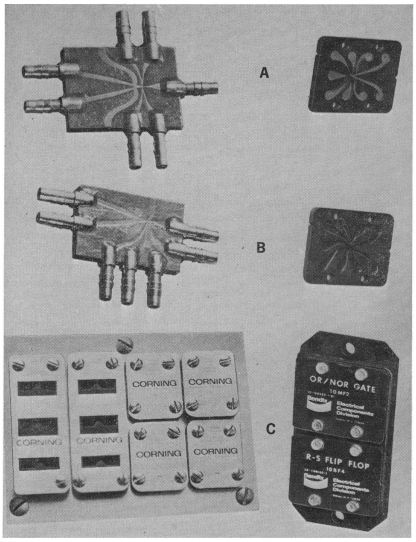

Fig. 1.3 Examples of commercially manufactured fluidic A. flip-flops, B. AND/OR Gates and C. integrated systems by the Bendix Corporation (right-side elements) and Corning Glass Works (left-side elements) [112]

Though they were originally developed to carry out computational tasks, they have since been adapted for other uses. Without any moving parts, they can operate reliably in harsh environmental conditions [47], require little maintenance, and can be constructed as sealed units to avoid leaks where the working fluid is potentially hazardous [97, 98].

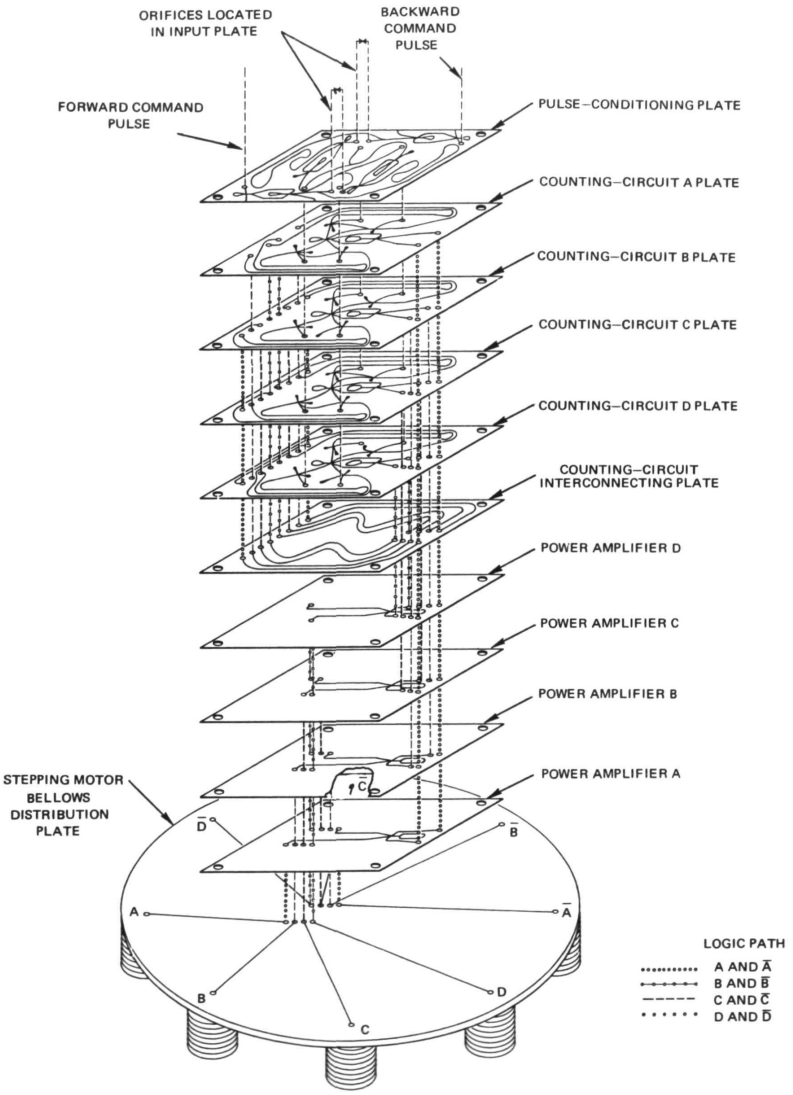

Fig. 1.4 Example of a fluidic integrated circuit [19]

From the perspective of jet engine design, research into fluidic devices has primarily concentrated upon their utilisation as either flow measurement [102, 79, 113] or flow control devices. Flow control devices could solve or mitigate a range of issues, such as tip leakage flows [4, 106, 96], cooling inefficiencies [25], noise production [80] and flow transition/separation [15, 34].

1.4.1 Coandă Effect

Many fluidic devices have the Coandă effect as the basic working principle. This phenomenon is named after Henri Coandă and can be described as the tendency for a jet to attach itself to an adjacent wall. A schematic of the flow field associated with the Coandă effect is presented in figure 1.5. The jet leaving the nozzle entrains fluid at both free shear layers. However, for the shear layer closest to the adjacent wall, the mass flow rate required to supply entrainment is restricted. Consequently, there is a reduction in pressure in the wall side entrainment region. The resulting pressure difference across the jet pushes the jet towards the wall where it attaches itself. In the steady attached state (figure 1.5), entrainment on the attached side of the jet results in the formation of a recirculating recirculation bubble with a permanent region of low pressure p_B that maintains attachment.

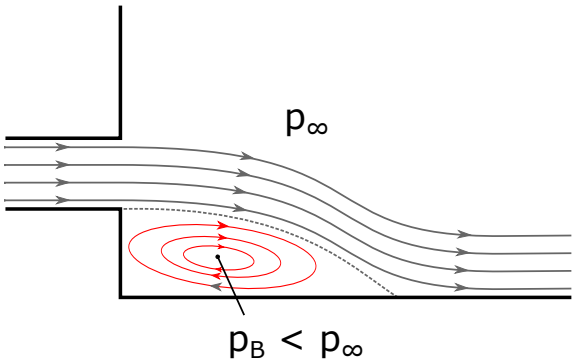

Fig. 1.5 Schematic for jet reattachment to a parallel adjacent wall

1.4.2 Diverter Switch

A category of fluidic devices that utilise the Coandă effect are wall attachment devices. These devices typically have a diverter switch section, examples of which are presented in figure 1.6. At its most basic (figure 1.6 (a)), a diverter switch consists of just a supply nozzle and a diverging duct. Most of the mass flow rate enters the cavity via the supply nozzle, a jet is formed in the diverging duct, and the Coandă

effect ensures that it attaches to one of the two angled sidewalls of the duct.

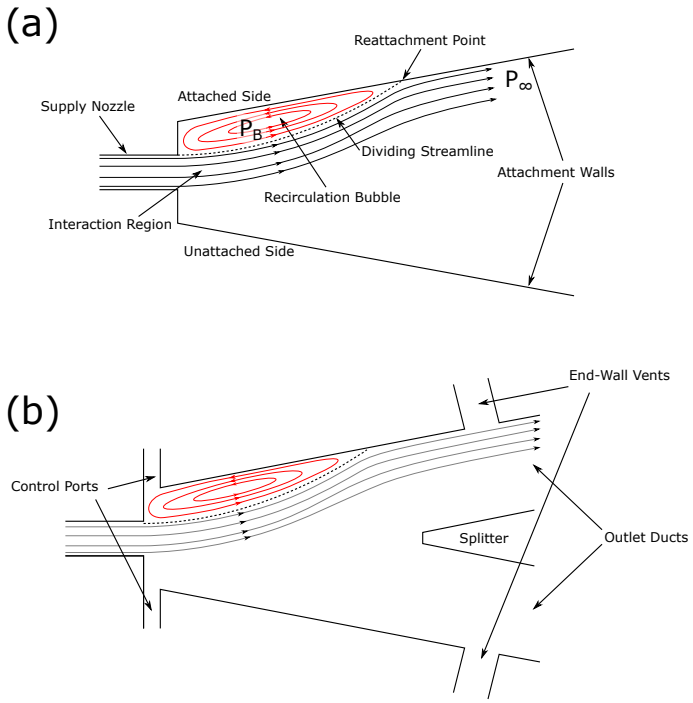

Fig. 1.6 Examples of diverter switch sections

If device is bistable then the jet can form a stable and distinct attachment state with either of the two sidewalls. To switch between these attachment states requires some form flow disturbance that will destabilise the attachment state and push the jet towards the opposite wall so that it can reattach there. A common method involves mass flow injection via a control port on what is initially the attached side of the device.

A useful feature of diverter switches is that the size of the flow disturbance required to switch a diverter stage is generally considerably less than the flow disturbance that occurs at the outlet ports due to the diverter switching. For instance, if a diverter is switched using a control jet, the mass flow rate of the control jet is typically 10-12% that of the supply jet. Therefore, a switching control jet will cause a swing in mass flow rates at the outlet ports roughly ten times that of the

control jet. Consequently, a diverter section can be thought of as a flow perturbation amplifier.

1.4.3 Switched Vortex Valve

Figure 1.7 presents a schematic of a switched vortex valve (SVV). An SVV is a wall attachment device that consists of a diverter switch section and a cylindrical vortex chamber. In one of the attachment states, most of the SVV supply flow is directed by the diverter section towards the tangential port of the vortex chamber. Flow entering the vortex chamber via the tangential port will follow a path that is tangential to the vortex chamber wall. The curved wall of the vortex chamber encourages the formation of a strong vortex centred on the outlet duct. In this state, the large radial static pressure drop across the vortex increases the overall flow impedance of the SVV.

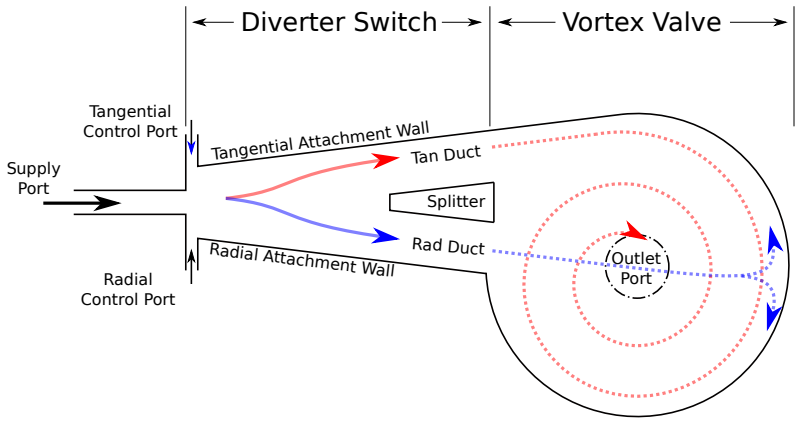

Fig. 1.7 Switched Vortex Valve

When the diverter section is in the opposite attachment state, most of the SVV flow enters the vortex chamber via the radial port . The radial inlet port encourages the jet to bisects the vortex chamber radially. The jet then splashes against the vortex chamber wall, forming two weaker counter-rotating vortices. Neither of these vortices is centred on the outlet port. Therefore, the pressure difference between the inlet and outlet ports of the vortex chamber is considerably less than that for

the other attachment state, and the overall flow impedance of the SVV is lower. Therefore a significantly higher mass flow rate can be passed for a set pressure ratio across the device than in the case of tangential state.

These attachment states of the SVV are labelled as tangential and radial, referring to the primary flow paths into the vortex chamber. If the SVV can be switched at will between attachment states, it can be used to modulate coolant flow rates. The SVV could restrict coolant flow rates during cruise by being in the tangential state whilst maximising coolant flow rates during take-off and landing by switching to the radial state.

A coolant flow modulation system based on an SVV presents some distinct advantages when compared with a conventional mechanical valve. Fluidic valves do not have any moving parts; this means that they can reliably operate under adverse environmental whilst generally being lighter and more resistant to wear and tear. The latter property means that fluidic valves can operate a lot longer than mechanical valves without maintenance. Furthermore, although the SVV presented here is bistable, they can be intentionally designed to be monostable. This means that without a continuous application of a control signal, the SVV will revert to one of the two attachment states. If the stable attachment state is the radial state, then the monostable device will fail-safe to the high flow state.

However, a coolant modulation system based on an SVV requires a reliable mechanism for switching the SVV between the radial and tangential states. Actively switching a wall-attachment device requires the introduction of a flow actuator. The actuator produces the flow disturbance needed to change the attachment state (section 2.1). This flow disturbance can take the form of mass flow injection via the control ports. Typically, mass flow injection control requires mechanical actuators that open and close flow paths connecting the control ports to a pressure source. An

example of this is the solenoid switched diverter [18, 21]. Although these control flow actuators would be considerably smaller than those required to modulate the coolant flow directly, they still have moving parts and still have some of the same drawbacks as the larger mechanical actuators that could be used modulate the coolant flow rates directly.

Alternatively, the SVV could be switched by one of a wide range of zero net mass flow actuators, for example there are thermal plasma actuators [105, 87, 13], SDBD actuators [15], SJ actuators [10, 63], piezoelectric benders [27, 28] and ultrasonic buzzers [59, 57]. However, this thesis will focus just on switching triggered by mass flow injection and acoustic actuators. It has already been shown that acoustic tones can actuate and switch wall-attachment devices [63, 62, 59, 61, 57, 70, 69]. Acoustic tones can be produced using piezoelectric buzzers. Piezoelectric buzzers are robust, lightweight actuators, but their control authority is limited. What this means, is that there is an upper limit to a diverter section's mass flow rate that can be switched by directly by piezoelectric buzzers.

The limited control authority of acoustic actuators can be overcome with the addition of a diverter pilot stage, forming a staged SVV (figure 1.8). The diverter section of the pilot stage acts as a control signal amplifier because the control authority of a diverter switch is greater than the actuation signal required to switch it. When the pilot stage's diverter section is switched, most of the pilot's supply flow is redirected from one of the SVV control ports to the other. Provided that the pilot stage flow rate is high enough, when the pilot diverter section is switched, the change in SVV control flow rates switches the SVV stage.

The staged architecture of the staged SVV allows a relatively weak control signal, such as that produced by an acoustic generator, to control the state of the SVV stage. However, multi-stage fluidic devices are susceptible to undesirable oscillatory insta-

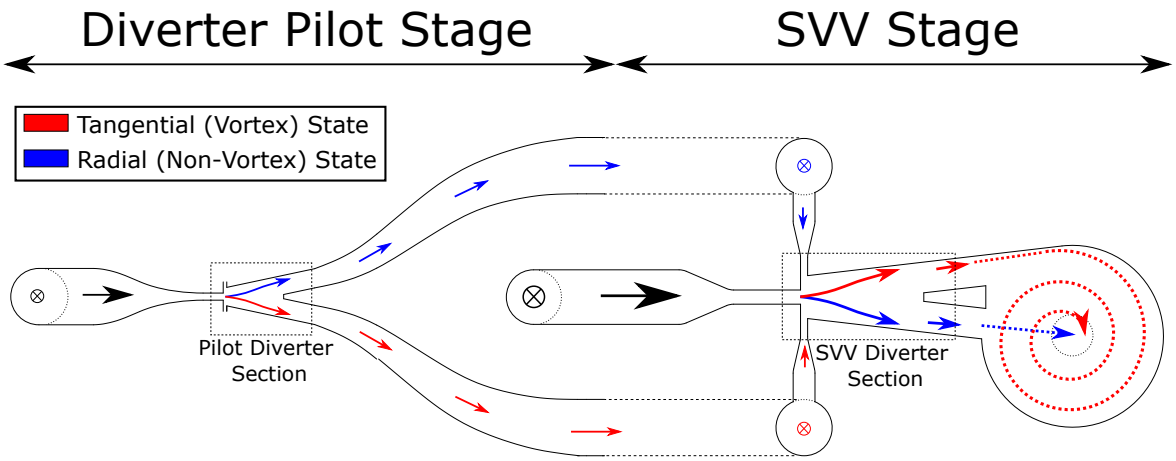

Fig. 1.8 2-Stage device with main flow paths marked for the tangential (vortex) and radial (non-vortex) states.

bilities. These oscillatory instabilities are thought to occur as the result of adverse back-pressures imposed by downstream stages on upstream stages that destabilise wall attachment [103]. Attaining a better understanding of the mechanisms behind these instabilities and how to avoid them is an important step in bringing multi-stage fluidic devices into practical usage.

1.5 Thesis Outline

The thesis will start with an overview of the relevant literature in chapter 2. Chapter 2 focuses upon wall-attachment devices, the switching mechanisms of wall attachment devices and the modelling of staged devices. Chapter 3 will present both the staged SVV and the structure of the numerical model that has been built to simulate it. The model in its original iteration is designed to model a staged SVV controlled by mass flow injection. The proceeding chapter will present the experimental characterisation of the staged SVV with mass flow injection control. The characterisation data is used to tune the model. Chapter 5 covers the experimental validation of the mass flow injection version of the model. The chapter also explores oscillatory instabilities and the effects of inter-stage duct impedances and outlet impedances on steady-state

performance and dynamic stability. Chapter 6 covers the acoustic actuation of the staged SVV. Both the model and the physical device it is based on were controlled using mass flow injection until this point. Consequently, the model and the physical device have to be modified to accommodate this alternative actuation method for the staged SVV. Chapter 6 covers these modifications as well as an exploration of the effects of acoustic control upon steady-state performance and dynamic stability. Finally, the conclusions and some concepts for further research ideas are presented in chapter 7.

Chapter 2
Literature Review

2.1 Wall Attachment Devices

Wall attachment devices are a sub-category of fluidic devices that utilise the Coandă effect. Both the pilot and SVV stages of the staged SVV are examples of wall attachment devices. For bistable wall attachment devices, the device can be switched between two stable and distinct states. Wall attachment devices typically have a diverter switch section. At its most basic, a diverter switch constitutes just a supply nozzle and a diverging duct. Two examples of diverter switches are presented in figure 2.1.

In a wall attachment device, a supply jet is driven by a pressure source located upstream of the supply nozzle. When flows are first established, the jet will bisect the duct region. However, this symmetrical state is dynamically unstable. Flow is entrained on both sides of the jet, leading to jet spreading. The entrainment mass flow can be supplied either by the outlet or by the jet itself. However, the jet is constrained by the cavity, reducing the availability of fluid that can supply the entrainment. Consequently, there is a corresponding pressure drop that arises at both jet shear layers. If there is a slight perturbation from the symmetrical state due to manufacturing asymmetries or flow turbulence, the shear layer pressures will change. In general, the shear layer that is pushed closer to a cavity wall by the perturbation from symmetry will be more constrained. Therefore, the pressure at this shear layer will be slightly lower than that at the other shear layer. The subsequent pressure difference between the jet shear layers will push the jet closer to

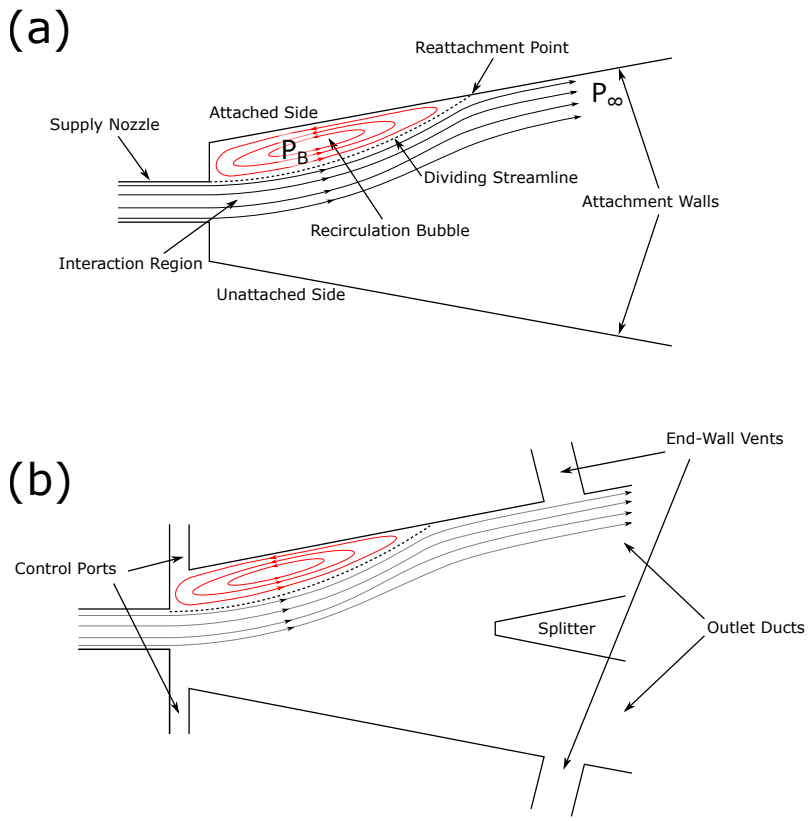

Fig. 2.1 Examples of a basic switch section (a) and a diverter (b)

the duct wall, which will further constrain one of the shear layers, increasing this pressure difference. This self-reinforcing phenomenon means that the jet will quickly move towards and impinge itself upon one of the side walls, i.e. the jet attaches to the wall.

The flow field presented in figure 2.1 is that of a stable attachment state. In the attached state, the entrainment region on the attached side of the jet is cut off from the outlet boundary. Therefore, fluid entrained on the attached side of the jet has to be supplied by the jet itself. In other words, the mass flow entrained on the attached side of the jet has to be returned to the entrainment region at the reattachment point (figure 2.1(a)) to maintain continuity. Consequently, a stable recirculation bubble is formed in the attached side entrainment region.

Most attempts to understand the steady-state configuration of an attached jet are rooted in the models for jet reattachment developed by Bourque & Newman [5]. It appears that many of the general concepts, terminologies and assumptions used to describe the behaviour of attached jets can be traced back to Bourque & Newman [5]. Bourque & Newman [5] first developed their model as part of a general exploration of the Coandă effect. Bourque & Newman [5] considered two scenarios for jet reattachment, one was for reattachment to an inclined plate (figure 2.2) and the other was for jet reattachment to an offset parallel plate (figure 2.3).

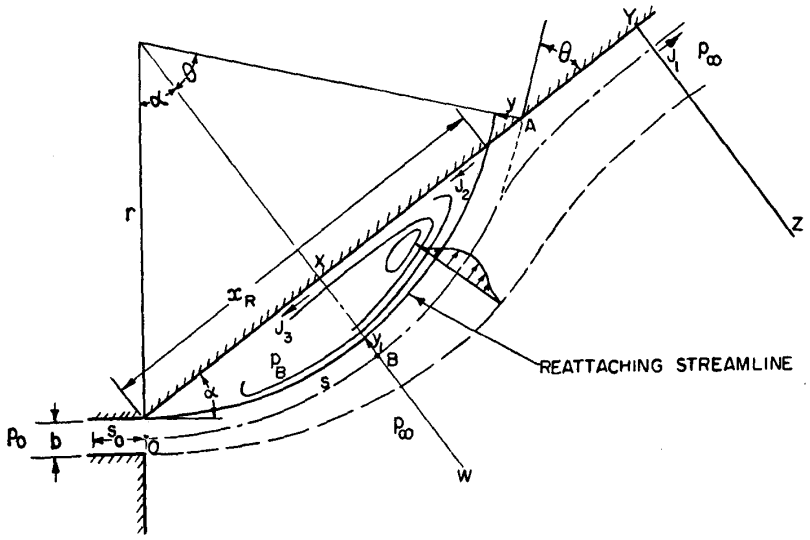

Fig. 2.2 Visual schematic of jet reattachment model for an angled plate from Bourque & Newman [5]

In Bourque & Newman's [5] description of jet reattachment, it is assumed that the pressure inside the entrainment region p_{B} is approximately constant and that the jet has a symmetrical Görtler velocity profile. The pressure difference across the jet $(p_{\mathrm{B}} - p_{\infty})$ provides the centripetal force that acts on the jet, forcing it to curve towards the attachment wall. If it is assumed that $(p_{\mathrm{B}} - p_{\infty})$ can be treated as a constant, then the jet centreline will follow a circular curve of radius R until it impinges upon the wall. When the jet impinges upon the wall, a portion of the jet momentum J_2 is returned to the entrainment region, whilst the rest J_1 is

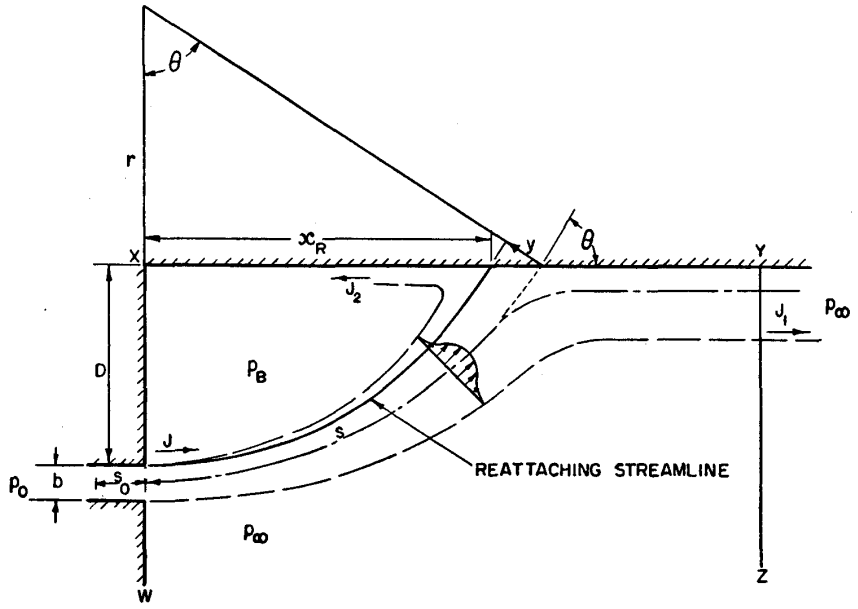

Fig. 2.3 Visual schematic of jet reattachment model for an offset parallel plate from Bourque & Newman [5]

convected downstream. The reattaching (dividing) streamline marks the division between these two portions of the jet flow. The wall location where the dividing streamline impinges upon the attachment wall x_R is known as the reattachment point.

Bourque & Newman [5] developed two different models intended to predict x_R, the attachment point and the control volume models. The attachment point model uses conservation of momentum flux at the reattachment point combined with continuity arguments and geometric relations to get x_R. The control volume model also uses a conservation of momentum flux argument but applies it to the control volume WXYZ (figure 2.2 and 2.3) instead of at a point to get x_R.

There has been a succession of studies that built upon the jet reattachment models developed by Bourque & Newman [90, 91, 53–55, 20, 84, 69]. The latest of these models was developed by Nicholls [69]. Nicholls [69] argues against the quasi-steady assumptions presented by Lush [54] and Chang [12] and develops a dynamic model for jet attachment in a diverter built upon an unsteady jet curvature

equation

$$\gamma\ddot{R} + \zeta\dot{R} - \frac{\bar{J}}{\rho R} = \frac{1}{\rho}\Delta p \tag{2.1}$$

where $\bar{J}$ is the momentum of the jet integrated across the supply nozzle exit, Δp is the pressure difference across the jet, and the coefficients γ and ζ are complex functions of the jet-diverter geometry and the jet spreading rate. This equation improves upon an earlier unsteady jet curvature equation derived by Ries [84], correcting for some errors in Ries's derivation. This equation was derived by Nicholls [69] from the radial incompressible Navier-Stokes momentum equation in polar coordinates, applying the following assumptions to the jet flow

- that the influence of viscous terms is small and that they can be discarded
- that the radial component of flow velocities does not vary in the tangential direction
- that R is only a function of time and does not vary spatially

Nicholls [69] showed that this model of jet attachment can be used to develop an active control system for a diverter. Nicholls [69] used acoustic actuators to provide the input signals and incorporates acoustic control into the model as a modification to the jet spreading rates (more on this in section 2.1.2).

Wall attachment devices are typically bistable, with two stable and distinct attachment states. Once the flow is established, switching between these states generally requires a pressure/flow disturbance that destabilises jet attachment. Wall attachment devices are typically more responsive to flow disturbances at or close to the attached side recirculation bubble. Consequently, wall attachment devices are often switched by suitably large flow/pressure disturbance close to the recirculation bubble.

Wall attachment devices can be switched passively. Passive switching can be triggered by changing operating conditions. For instance, Tesar [99] presents a flow

control valve that is designed to switch when the attached side back-pressure exceeds a certain threshold. Alternatively, wall attachment devices can be switched by some form of passive feedback mechanism. Feedback switching is common for fluidic oscillators. [95, 109, 82]. Consider, for example, the fluidic oscillator presented in figure 2.4. The static pressure difference between the attached side vent and the attached side control port drives flow down the feedback path. Consequently, there is alternating mass flow injection at the control ports that periodically switches the device between attachment states.

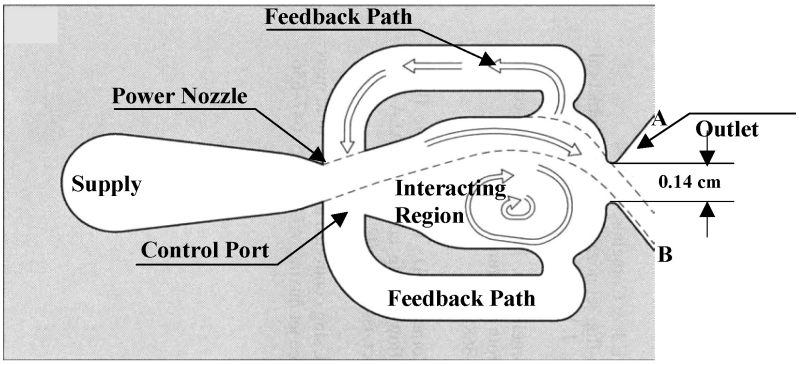

Fig. 2.4 Schematic of a fluidic oscillator from Raman & Raghu [81]

The focus of this thesis is an actively controlled fluidic valve. Wall attachment devices can be actively controlled with actuators providing control signals that either alter the jet position or switch the device. Actively controlled wall attachment devices can be subdivided into two categories. There are those devices that are controlled by the injection or expulsion of mass flow via the control ports and those that are controlled using zero net mass flow actuators.

To actively control a wall-attachment device by the mass flow injection/expulsion typically requires the use of a flow actuator that can apply a variable restriction to the control flow path. For example, Culley [18] and Feikema & Culley [18] present diverters switched by mass flow injection via solenoid valves. Unfortunately, mechanical valves have moving parts that make them heavy and more susceptible to wear

and tear. An alternative is to use flow actuators that do not have any moving parts, such as piezo-electric or plasma actuators.

Examples of fluidic devices actuated by piezo-electric and plasma actuators are listed below

i Gregory et al. [27, 28] presents a fluidic oscillator actuated by piezo-electric benders.

ii Gregory et al. [29] presents a fluidic oscillator actuated using a thin-film plasma actuator

iii Gokoglu et al. [25] presents a numerical simulation of a fluidic oscillator that has a natural oscillation frequency that is modified by plasma actuation.

iv Chen et al. [13] presents a switched vortex valve (SVV) switched using a spark-plasma actuator. This will be discussed in greater detail in section 2.3.

v Martin et al. [63] presents a diverter switched using a synthetic jet actuator driven by a piezo-electric buzzer.

vi Mair et al. [62, 59, 61, 57, 58] presents a range of acoustically actuated diverter designs, with piezo-electric buzzers providing the acoustic control signals.

vii Nichols [70, 69] also presents a diverter that is acoustically actuated with piezo-electric buzzers, but focusses more upon sub-switching jet deflection than acoustically triggered switching.

The actuators in these examples do not add or remove mass flow, but they do create a large enough flow disturbance to destabilise wall attachment and trigger switching. This study is particularly interested in wall-attachment devices switched using actuators that generate acoustic signals.

2.1.1 Mass Flow Injection

The traditional method for switching wall attachment devices is by injecting mass into the recirculation bubble. This control method has been used for both passively [109, 82] and actively [18, 21] controlled fluidic diverters. Passively controlled diverters generally have feedback mechanisms that drive mass flow injection at the control ports. Actively controlled diverters in Culley [18] and Feikema & Culley [21] have control flows that are introduced by opening and closing solenoid valves.

An early attempt to model the switching process for mass flow injection is presented by Muller [67, 68]. The model presented by Muller [67, 68] builds upon earlier work by Bourque & Newman [5], which developed models for the reattachment of a jet to an angled and a parallel wall. According to Muller [67, 68], the switching process starts with the quasi-steady growth of the recirculation bubble, when a control flow $\dot{m}_c$ is introduced at the attached control port.

The recirculation bubble grows in size through a combination of jet deflection and an increase in the recirculation bubble pressure. The control jet deflects the main jet by imparting transverse $(-\hat{y})$ momentum to the main jet (figure 2.5). As a result, the main jet is deflected away from the attachment wall at the nozzle outlet. The pressure difference across the main jet will still force it to curve back towards the attachment wall. However, the change to the main jet inlet angle will increase the size of the recirculation region.

In addition to deflecting the jet, the control flow partially feeds attached side entrainment. Consequently, there is a transient mismatch between the mass flows entering and leaving the recirculation bubble. Consider the schematic of the attached flow field of a diverter in figure 2.6. Shear layer mixing at the attached jet boundary

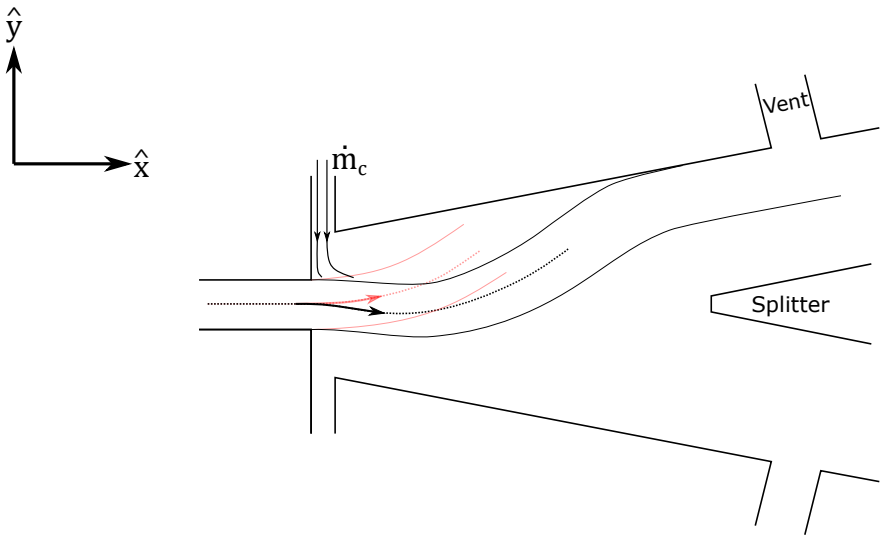

Fig. 2.5 Deflection of a diverter supply jet by a control flows at the attached side of the diverter.

entrains mass flow $\dot{m}_\mathrm{e}$ from inside the separation region. As the jet impinges upon the wall at the attachment point, a portion of the jet mass flow $\dot{m}_\mathrm{r}$ is returned to the entrainment region. This mass flow is referred to as either the returned flow or recirculated flow, depending on the author. Under steady-state conditions, the total mass of air inside the entrainment region is constant. Thus, without control flows, the entrained and recirculating mass flow rates are the same, see figure 2.1. When a control jet $\dot{m}_\mathrm{c}$ is introduced, there is a transient increase in the mass flow rate entering the bubble, i.e.

$$\dot{m}_\mathrm{net} = \dot{m}_\mathrm{c} + \dot{m}_\mathrm{r} - \dot{m}_\mathrm{e} > 0 \tag{2.2}$$

With a net positive mass flow rate entering the entrainment region, the recirculation bubble pressure p_B will increase. The centripetal force acting on the jet is the result of the pressure difference across the jet. Hence, as p_B increases, the jet curvature decreases, and the bubble volume increases in size. As the bubble increases in size, the angle at which the jet impinges upon the wall $(\theta - \alpha)$ decreases and the attached side shear boundary length increases. As $(\theta - \alpha)$ decreases, less of the jet flow is redirected towards the entrainment region, i.e. $\dot{m}_\mathrm{r}$ decreases. Assuming the flow entrainment rate is approximately constant, it is expected that $\dot{m}_e$ will increase

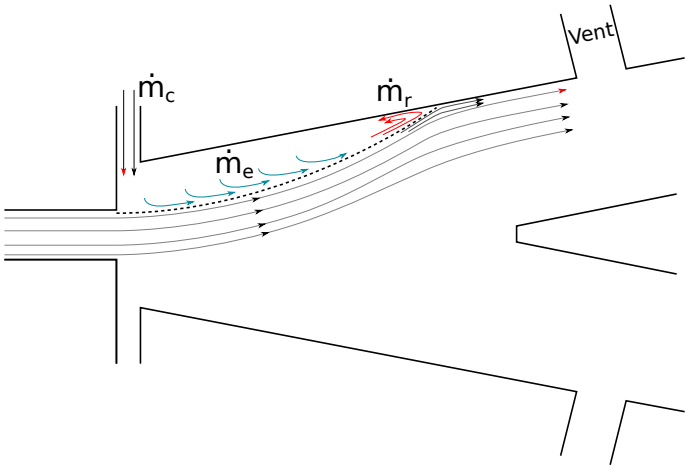

Fig. 2.6 Diverter recirculation bubble mass flow sources and sinks

as the shear layer boundary length increases. Thus as the bubble grows in size, $\dot{m}_{\text{net}}$ will decrease. Provided that $\dot{m}_c$ is sufficiently small, the bubble growth rate will decelerate as the bubble size increases until a new steady-state is achieved where $\dot{m}_{\text{net}} = 0$.

Muller [67, 68] introduces the concept of a critical bubble volume V_{crit}. If the bubble volume remains less than V_{crit}, the switch's response to control flows is quasi-steady. However, the unsteady switching process will begin if the control flow pushes the bubble volume beyond V_{crit}. Muller's [67] switching model was made in reference to a vented diverter (figure 2.7). Muller [67, 68] postulated that when $V = V_{\text{crit}}$, the dividing streamline of the jet intercepts with the edge of the vent (bleed line). If $V > V_{\text{crit}}$, then the entrainment region is exposed to the open vent. Consequently, the entrainment region is no longer confined, and the attachment state is destabilised.

Muller [67, 68] applies a quadratic function to experimental observations to link the $\dot{m}_{\text{net}}$ to the transient bubble volume. Muller [67, 68] found that for larger control flow rates, the switching behaviour changes from 'slow' switching to fast 'dynamic' switching, which corresponds to the end-wall and opposite wall switching mechanisms

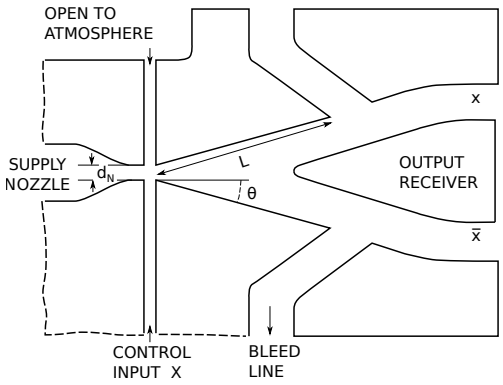

Fig. 2.7 Vented diverter from Muller [67]

described later by Lush [54, 55] and Epstein [20].

Lush [54] subdivides the switching process into three phases. First is the quasi-steady growth phase, where the bubble grows in response to the mass flow injection at the control port. The second is the detachment of the jet and the subsequent flipping of the jet as it moves towards the other attachment wall. Finally, the third stage is the re-establishment of an attached flow field and the shrinking of the new bubble down to its steady-state size. Lush [54] used this model of diverter switching to get reasonable estimates of the switching times based on entrainment models of bubble growth and shrinkage in the first and third stages of the switching process. In general, it was found that switching times decreased as control flow rates increased since higher control flow rates will accelerate the bubble growth portion of the switching process.

Epstein [20] continued to use the phased description of the switching process laid out by Lush [54]. However, Epstein [20] expands on this by introducing three different diverter switching mechanisms with mass flow injection:

1. **End-Wall Switching.** This switching mechanism is associated with vented diverters with short attachment walls (figure 2.8). As the recirculation bubble grows in response to control mass flows, the attachment point migrates towards the edge of the wall. Once the attachment point crosses the end of the wall,

the "attached" side entrainment is no longer constrained. Consequently, the jet detaches from the wall and is pushed by the transverse momentum of the control jet towards the opposite wall, where the jet reattaches itself.

2. **Splitter Switching.** As the jet curvature decreases, eventually, it will start to interact with the splitter. The splitter interactions will differ depending on the splitter geometry. Unfortunately, the exact mechanism for splitter-jet interactions is unknown. However, it would appear that these interactions lead to instabilities that will destabilise the attachment state, at which point the jet starts to reattach to the opposite wall.

3. **Opposite Wall Switching.** This occurs if the set-back distance is small or the control jet momentum is high. The momentum of the control signal is sufficient to create a large enough supply jet deflection that the jet attaches to the opposite wall whilst remaining attached to the original. As the "attached" side recirculation bubble grows in response to the transient mass flow mismatch for the bubble, both reattachment points travel downstream until the jet is pushed into the second outlet.

In this thesis, the wall attachment devices are all unvented, and the set-back distance is large enough to make opposite wall switching unlikely. Hence, it is generally assumed that, for mass flow injection control, the switching mechanism is splitter switching.

Feikema & Culley [21] presents a RANS model for a solenoid valve controlled diverter switch first presented two years earlier by Culley [18]. The model was in part designed to find the optimum location and magnitude of a switching control signal. With reference to simulations, Feikema & Culley [21] argues that a control jet switches a diverter by partially blocking the supply jet and deflecting it towards the unattached side of the diverter. Consequently, the degree to which the control

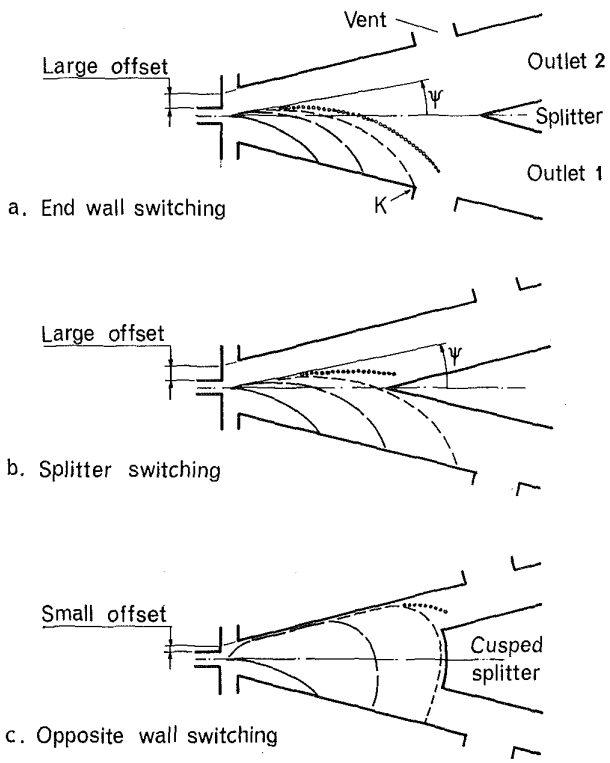

Fig. 2.8 "Jet path during the switching transient" [20].

jet penetrates the supply jet determines the reliability of the switching signal, which is parameterised by the momentum flux ratio

$$\sqrt{J} = \sqrt{\frac{\rho_c v_c^2}{\rho_s v_s^2}} \tag{2.3}$$

where v_c is the control jet flow velocity and v_s is the supply jet flow velocity. Feikema & Culley [21] finds that the optimum switching control signal has $\sqrt{J} = 2.5$. This description of mass flow injection triggered switching resembles Epstein's [20] 'fast' opposite wall switching mechanism. According to Epstein [20], this switching mechanism can arises when the set-back distance is small. As it happens, the diverter geometry used by Feikema & Culley [21] has zero set-back distance.

2.1.2 Acoustic Actuation

Only a handful of studies [63, 62, 59, 57, 61, 58, 70] have investigated acoustically actuated wall attachment devices.

The first example of an acoustically controlled fluidic device was presented by Martin et al. [63] in 2014. Martin et al.'s device is a diverter switched using synthetic jet (SJ) actuators (figure 2.9). The acoustic actuators used by Matin et al. [63] were not intended to interact directly with the diverter jet but indirectly as SJ actuators.

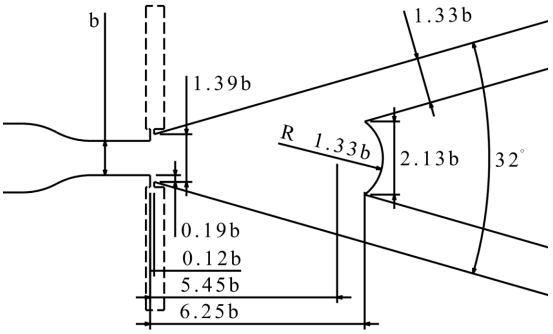

Fig. 2.9 Diagram of the switch used by Martin et al. [63], dashed lines represent the synthetic jet cavities ($b = 12$ mm). Diagram is copied from Martin et al. [63].

An SJ actuator is an acoustically driven Helmholtz oscillator. A schematic of an SJ actuator is presented in figure 2.10. SJs typically consists of a flow cavity with a nozzle at one end and an acoustic actuator diaphragm at the other. The acoustic actuator drives periodic ingestion and expulsion of fluid through the nozzle. An SJ actuator injects a net positive momentum flux into the free stream, even though there is zero net mass flow rate. Typically, such devices have two maximum response frequencies, f_1 and f_2, that are related to the natural resonance frequency of the acoustic actuator diaphragm f_D and the Helmholtz resonator frequency of the cavity and nozzle f_H [23].

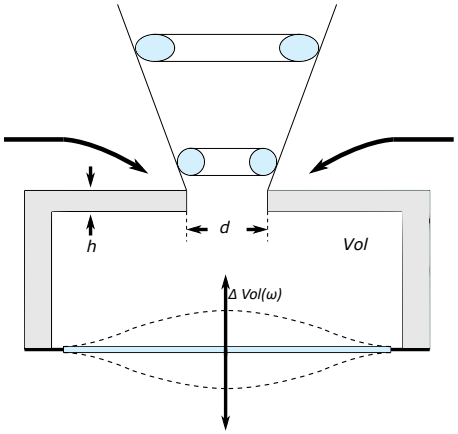

Fig. 2.10 Schematic of a synthetic jet actuator, adapted from a similar diagram in [10]

In a similar fashion to the mass flow injection case, SJs attached to the control ports can be used to impart transverse momentum to the supply jet. Martin et al. [63] initially hypothesise that an SJ can switch a diverter by injecting transverse momentum at the attached side of the diverter and thus switch the diverter by creating a large enough supply jet deflection that jet attachment is destabilised. At SJ frequencies $f_1 = 630\,\text{Hz}$ and $f_2 = 1000\,\text{Hz}$, it was found using hot-wire anemometry that the peak SJ velocities were the same. However, despite these similar jet velocities, the diverter would only switch when a 630 Hz signal was applied. Therefore, Martin et al. [63] concludes that there must be more to acoustic-jet interactions in this case than just SJ momentum injection.

Mair et al. [62, 59, 61, 57, 58] developed laminar flow diverters switched with sonic piezo-electric actuators and turbulent flow diverters switched with ultrasonic buzzers. These devices do bear some resemblance to Martin et al.'s SJ switched diverter [63]. However, Mair et al.'s devices were designed for direct acoustic-jet interactions.

In the process of developing acoustically actuated diverters Mair et al. [62, 59, 61, 57, 58] also developed theories about acoustic jet interactions to explain the

observed behaviour of diverters when directly actuated with acoustics. Mair et al. [62, 59, 61, 57, 58] builds upon previous studies of acoustic-jet interactions from outwith the fluidics field.

Acoustic-Jet Interactions

Before discussing the acoustic-jet interactions in detail, it is useful first to consider the evolution of an unexcited free jet. Figure 2.11 presents a schematic of the free-jet development process. Upon entering the unbounded volume, shear stresses at the jet boundaries lead to the formation of axisymmetric instability waves at the free shear-layer boundaries [16]. These waves grow in amplitude as they are convected downstream. Eventually, the boundary layer 'rolls up', forming shear-layer roll-up vortices that continue to increase in size as they are convected downstream. These roll-up vortices enhance turbulent mixing at the shear-layer. The turbulent mixing at the shear-layer boundaries drives jet spreading. This mixing diffuses the jet momentum out into the broader volume, resulting in additional mass flow being entrained by the jet, increasing the jet's width. Meanwhile, the jet inviscid core shrinks as the boundary layers broaden. The inviscid core terminates at the point where these broadening boundary layers meet, after which the centreline velocity of the jet will start decreasing. Immediately downstream of the inviscid core, there is the interaction region where vortices start to interact with each other. Towards the end of the interaction region, the vortices start to break down into smaller vortices that exist over a range of frequencies. Ultimately, the jet evolves into an isotropic self-similar region of turbulence [118].

In 1971, Crow & Champagne [16] identified two modes of instability in a free jet. There are the shear-layers' small scale instability waves and a larger scale global jet instability (jet preferred mode).

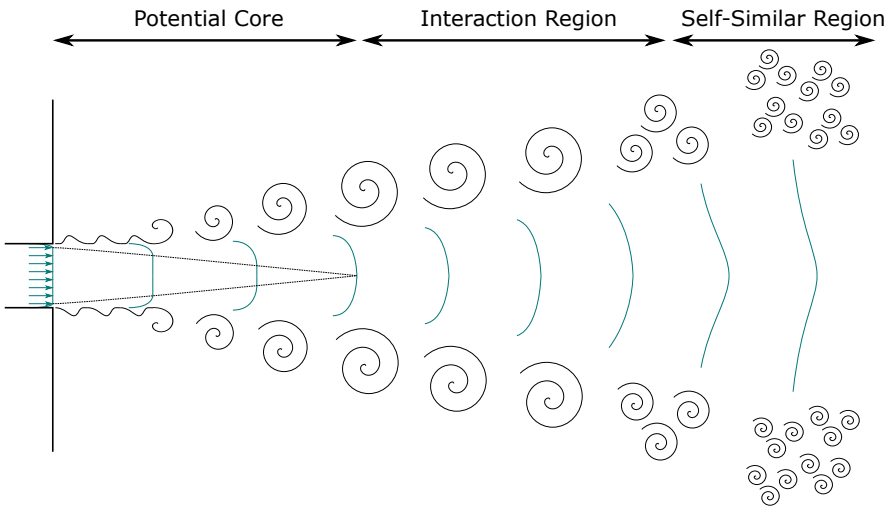

Fig. 2.11 Free jet development

The boundary layer instability waves form because free shear-layer boundaries are typically unstable when subjected to small disturbances over a range of frequencies [65, 66, 52]. This instability is known as the Kevin-Helmholtz instability [89]. All the disturbances in the unstable frequency range grow in amplitude as they are convected downstream, but one frequency grows to dominate the others. This frequency is the natural shear-layer roll-up frequency f_{n}, and its increasing amplitude ultimately results in the formation of the shear-layer roll-up vortices. In multiple studies [37, 120, 119, 35, 38], it has been found that f_{n} corresponds to a particular momentum thickness Strouhal number

$$St_{\theta} = \frac{f_{\mathrm{n}}\theta}{\bar{u}} = 0.012 \tag{2.4}$$

where θ is the momentum thickness and $\bar{u}$ is the mean jet velocity.

Crow & Champagne [16] identified the jet preferred mode by acoustically exciting a circular jet. It was found that acoustic excitation would result in the formation of large axisymmetric coherent structures in the jet with periodic variations in the jet centreline velocity. The preferred mode is the excitation frequency f_{p} which leads to the highest fluctuating jet oscillation amplitude before saturation [16].

$$St_{\mathrm{D}} = \frac{f_{\mathrm{p}} D}{u_0} = 0.3 \tag{2.5}$$

where D is the nozzle width and u_0 is the centreline flow velocity of the jet. Many studies with circular jet profiles have identified the jet preferred mode St_{D} to be at or close to 0.3 [16, 11, 87, 88, 43, 36, 94], but there are exceptions. For instance, according to O'Neill et al. [71], $St_{\mathrm{D}} = 0.78$, whilst for Ko & Davies [48] $St_{\mathrm{D}} = 0.43$. Mair et al. [57, 56] argue that in these cases, the frequencies attributed to the jet preferred mode are actually related to the shear-layer instabilities. The jet preferred mode St_{D} has generally been found to be different when the jet cross-section is not circular. Mair [57] with a rectangular cross-section nozzle and aspect ratio of 3 found the hydraulic diameter Strouhal number $St_{\mathrm{D_h}}$ to be 0.45 for the jet preferred mode. Jiang et al. [40], on the other hand, found that for rectangular nozzles with aspect ratios between 3 and 6, the nozzle width Strouhal number St_{h} was 0.22 for the jet preferred mode.

It has been shown that acoustic tones can excite shear-layer instabilities at the applied excitation frequency [16, 120]. Artificially amplified instabilities will have a noticeable impact on the jet development, provided that the amplitude of the amplified instability exceeds the natural f_{n} instability amplitude. By increasing the amplitude of shear-layer instabilities, acoustic actuation will trip the shear-layer resulting in an early transition to shear-layer roll-up [16, 120]. From the perspective of a fixed location downstream of the transition point, acoustic actuation will increase the size of the roll-up vortices as they will be allowed more time to grow. These larger vortices will increase turbulent mixing and will thus increase the mass flow entrainment rate.

It has also been shown that acoustic tones will also excite global jet instabilities, increasing the turbulent mixing rate downstream of the transition point [16]. The

mechanism that underlies this interaction is still uncertain. However, it has been theorised by Mair et al. [57, 56] that the jet preferred mode and the shear-layer instabilities are related. This theory speculates that the jet preferred mode arises because exciting the jet at sub-harmonics of f_{n} encourages the roll-up vortices to pair up and merge, forming larger coherent structures. As these large structures convect downstream, they would perturb the jet, resulting in the enhanced jet fluctuations associated with the jet preferred mode. Irrespective of the underlying mechanism, introducing an excitation frequency that matches the jet preferred mode f_{p} will dramatically increase turbulent mixing and is often associated with maximising jet spreading and entrainment rates [16, 57, 56].

In general, acoustically exciting a jet will increase turbulent mixing and, by extension, the shear-layer entrainment rates. It is this feature of jet-acoustic interactions that Mair et al. [61, 57, 58] use to interpret the response of diverters to direct acoustic actuation.

Mair et al. [62] present an acoustically actuated diverter (see figure 2.12). The device was operated at low flow rates to ensure that the supply jet was initially laminar. Piezo-electric actuators that operate in the audible range were used to apply acoustic tones to both the attached and unattached sides of the jet. Although it was possible to switch the device from both sides of the device, the frequency ranges over which the device could be switched were different, with the diverter being switchable for a wider range of frequencies when excited from the unattached side. Furthermore, the minimum SPL required to switch the diverter was an order of magnitude lower when switching from the unattached side. Mair et al. [62] reproduced the unattached side switching process with LES simulations. The LES simulations showed that unattached side excitation of the diverter triggers the formation of large roll-up vortices at the unattached shear-layer of the jet. Mair et al. [62] argue that the

pressure difference across these vortices effectively lowered the pressure difference across the attached jet, weakening jet attachment. Although it was difficult to identify the reattachment point in the simulation, the LES simulation could be used to find the transient static pressure at the unattached side of the jet. In response to acoustic actuation, this pressure would increase until it exceeded the pressure at the attached side of the jet. When the pressure difference across the device changed sign in the simulation, the acoustic excitation could be turned off, and the flow would enter into the opposite attachment state.

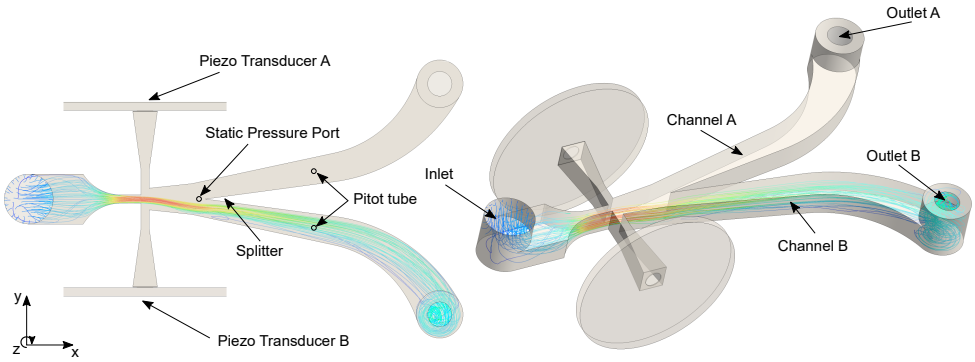

Fig. 2.12 An acoustically actuated diverter from Mair et al. [62]

A later paper by Mair et al. [61] presents a more thorough exploration of the same device. In this paper, the focus entirely on unattached side actuation, which has been identified as a far easier method for switching the diverter. Both studies identify the optimum excitation frequency as being the one that minimises the switching time. However, whereas the earlier paper ties the optimum frequency to the jet preferred mode $St_{\mathrm{D_h}} = 0.3$, the latter paper states that the optimum frequencies actually match the natural shear-layer instability $St_\theta = 0.012$. It is shown that there is good agreement between the prediction of f_n for a laminar jet velocity profile and the observed optimum excitation frequencies over a range of supply-exhaust pressure ratios ($PR = 1.0005 - 1.003$). With reference to LES simulations, Mair et al. [61] show that exciting at f_n moves the transition to shear-layer roll-up vortices further

upstream. In this paper, Mair et al. [61] first describe the switching mechanism in terms of jet entrainment rates using the description of jet entrainment presented by Wygnanski & Fiedler [117] and by Crow & Champagne [16]. Mair et al.'s [61] LES simulations show that exciting from the unattached side predominantly leads to the formation of roll-up vortices at the unattached shear layer. This feature of acoustic excitation is backed up by PIV experiments with an attached jet, the results of which are presented in Mair [57]. These unattached side shear layer vortices dramatically increase turbulent mixing and flow entrainment rates at the unattached side shear layer. This increase in the entrainment rates within the confines of the diverter cavity leads to a localised pressure drop at the unattached side shear layer. Consequently, the pressure drop across the attached jet decreases, and jet attachment strength weakens. If the excitation SPL is high enough, the increased unattached side entrainment rate will destabilise wall attachment and trigger switching.

Another paper published by Mair et al. [59] presents a different acoustically actuated diverter (figure 2.13). This device was designed to operate at higher flow rates and is actuated by ultrasonic buzzers rather than sonic actuators. At the higher flow rates, the supply jet is initially turbulent. Therefore, the roll-up vortices form close to the nozzle outlet. Consequently, the roll-up point cannot be pushed much further upstream by acoustic actuation. Furthermore, the natural shear-layer instability frequencies predicted by LES for the flow rates tested 40-60 kHz were considerably higher than the 24 kHz produced using the ultrasonic buzzers. However, in spite of these observations, Mair et al. [59] were able to switch this diverter with unattached side actuation. With reference to work by Ho & Huang [31] and Oster & Wygnanski [72], it is argued in this paper that exciting at lower frequencies ($f < f_{\mathrm{p}}$) will enhance the pairing and merging of roll-up vortices. Consequently, acoustic actuation will lead to larger vortical structures that will reduce the pressure difference across the jet.

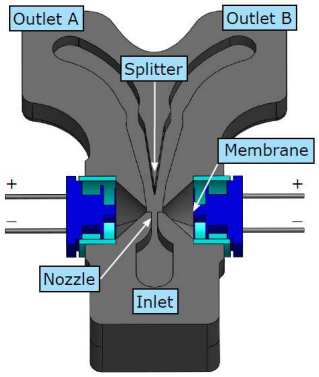

Fig. 2.13 Schematic of fluidic device with ultrasonic piezo transducers at control ports. Figure taken from Mair et al. [59].

As part of the design process for the ultrasonic device, Mair et al. [59] developed an acoustic model for the diverter cavity. This model was used to find resonance frequencies of the cavity and what effects different buzzer waveguide geometries would have on these frequencies. It was found that by matching the actuator frequency to the device resonance frequency, the SPL within the diverter cavity rose by a factor of 10, making it considerably easier to switch the diverter acoustically.

Mair explores the topic of acoustic actuation of higher Reynolds number diverters in greater depth in [57]. Here Mair shows that the optimum excitation frequency for higher flow rate devices corresponds to the jet preferred mode ($St_{\mathrm{D_h}} = 0.45$). It is possible that vortex merging is part of the underlying mechanism for the jet preferred mode. However, what this shows is that at higher flow rates, the optimum frequency for switching is the one that maximises jet spreading and entrainment.
f

The overarching argument made by Mair [57] is that the optimum frequency for acoustic actuation of a diverter is the one that maximises entrainment mass flow rates of the jet. At lower Reynolds numbers with laminar jets, the optimal frequency is f_{n}. Exciting the natural shear-layer instability ensures that roll-up vortices form as close as possible to the supply nozzle exit. However, at higher Reynolds numbers, the roll-up vortices already form very close to the nozzle exit. Consequently, the

optimal frequency is the one that maximises jet spreading after the transition point, which by definition corresponds to the jet preferred mode f_{p}.

Nicholls [69] built upon the work done by Mair et al. [62, 59, 61, 57, 58]. Acoustic actuation was incorporated into the analytical model of wall attachment developed by Nicholls [69]. However, rather than modelling the acoustic-shear layer interactions directly, Nicholls [69] modelled the effect of acoustic excitation as a time-varying modification to the jet spreading parameter at the attached and unattached sides of the jet. As part of the model's validation process, Nicholls' [69] compared the model's predictions of the dynamic responses of an acoustically actuated diverter with experimental observations. The acoustically controlled diverter was actuated with an amplitude modulated signal over a range of modulation frequencies from 20 to 880 Hz. At low flow rates, the model convincingly replicated both the magnitude and relative phases of the jet response to acoustic excitation.

In addition to this, Nicholls [69, 70] also developed a closed-loop control system for the acoustically actuated diverter. By modifying the jet attachment strength, acoustic excitation can modify the diverter jet position without necessarily switching the device. Nicholls [69, 70] shows that it is possible to use the amplitude modulation of the signal driving the acoustic actuators to continuously modulate the jet position, thereby improving the device's robustness in the presence of flow disturbances. The control system developed by Nicholls [69, 70] was able to maintain the devices insensitivity to outlet disturbances with a jet flow velocity of 90 m/s.

2.2 Vortex Valve

In fluidics, vortex devices commonly fall into one of two categories, vortex diodes and vortex triodes [46]. Examples of both diodes and triodes are presented in figures

2.14 and 2.15.

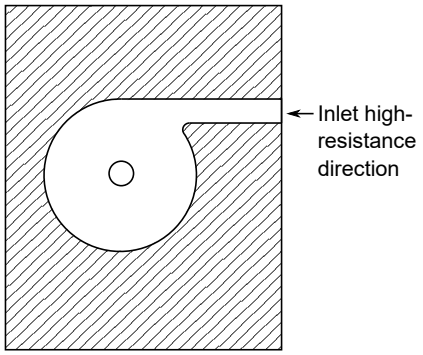

Vortex Dioide

Fig. 2.14 Schematic of a vortex diode adapted from a figure in Kirshner [46]

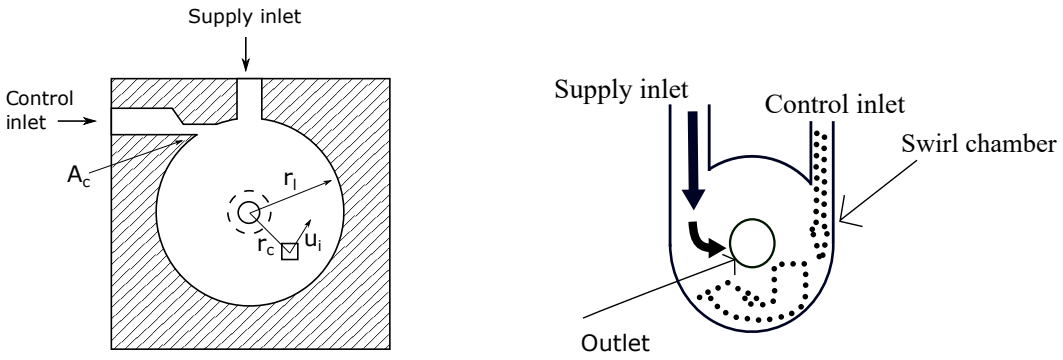

Turn-Down Amplifier Turn-Up Amplifier

Fig. 2.15 Examples of vortex amplifiers(triodes). Turn-down amplifier is adapted from a figure in Kirshner [46]. Turn-up amplifier is adapted from a figure in Woolhouse et al. [116]

The vortex diode is the older device, a design of which was first proposed by Thoma in 1929 [100]. The device consists of a cylindrical vortex cavity with two inlet/outlet ports. A diode has a port that connects tangentially to the vortex chamber and an inlet/outlet port at the centre of the vortex chamber. Vortex diodes were designed to effectively act as fluidic one-way valves. The diode restricts flow rates in one direction whilst providing minimal resistance for flows in the opposite direction. The flow direction for the high resistance state is marked on figure 2.14. In the high resistance state, the curved walls of the vortex chamber encourage the

formation of a strong vortex centred on the outlet port at the centre of the chamber. The vortex lengthens the flow path lengths and accelerates stream flow rates close to the outlet. The combination of both of these flow features ensures that the pressure loss coefficient ($K_{\mathrm{L}} = \Delta p/q$) is significantly higher in the high resistance state. Consequently, given a constant supply flow rate, there will be a larger pressure drop across the diode in the high resistance state. Conversely, if the pressure drop is fixed, the flow rate will be lower in the high resistance state.

Vortex triodes, also known as vortex valves or vortex amplifiers, were a later development. The design for the first vortex amplifier was proposed by Bowles & Horton [6] in 1960. Conceptually, these devices introduce additional inlet ports that modify the circulation within the vortex chamber. In both of the examples presented in figure 2.15, introducing the control flows will either increase (turn-down amplifier) or decrease (turn-up amplifier) the amount of circulation in the vortex chamber, which modifies the valve K_{L}.

The switched vortex valve (SVV) that will be discussed in section 2.3 is a key component of the staged SVV that is the focus of this thesis. The SVV has a turn-down vortex amplifier section, and it is the variable K_{L} value that allows the staged SVV to modulate flow rates. The K_{L} of the device varies depending on the relative flow rates at the tangential and radial inlet ports. A schematic of the vortex valve flow fields is presented in figure 2.16. The minimum K_{L} (radial) state corresponds to all the supply flow entering via the radial inlet port. In this state, the supply flows follow a direct path from the radial port to the outlet port with minimal pressure losses. Conversely, the maximum K_{L} (tangential) state occurs when all the flow enters the vortex chamber via the tangential inlet port. In the tangential state, the vortex chamber flow field resembles that of a diode in the high resistance state,

with a strong circulating flows filling the vortex chamber.

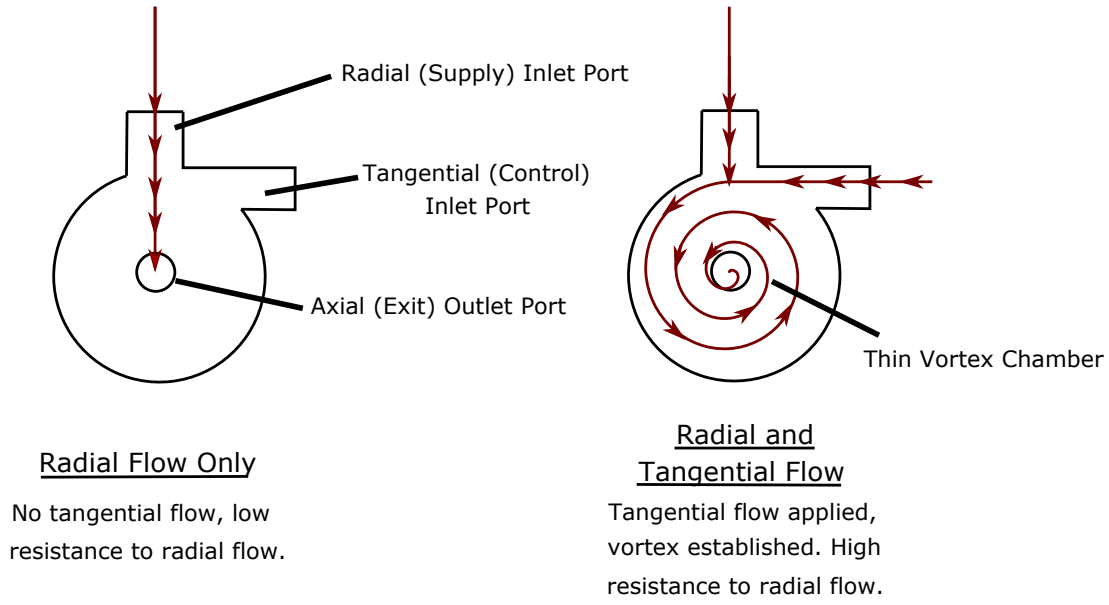

Fig. 2.16 Schematic of a turn-down vortex valve flow field, adapted from a figure in Parker et al. [73].

2.2.1 Characterisation of Vortex Valves

This thesis is based on a staged fluidic device with a turn-down vortex amplifier component. However, this section covers investigations that are based on vortex diodes [51], turn-down vortex amplifiers [45], turn-up vortex amplifiers [101] and vortex combustors [108, 107]. Despite the variations in design and intended applications, the vortex chamber flow fields are similar when these devices operate in purely vortex states. Therefore, some valuable insight into the steady-state behaviour of the vortex amplifier component can still be acquired from these disparate sources.

In Tippetts [101], it is argued that fluidic devices can be treated as Eulerian machines provided that flows are incompressible and there is no cavitation. According to Tippetts [101], this means that the steady-state behaviour of a device can be fully characterised by pressure differences and flow rates at the inlet/outlet boundaries.

Consider a vortex triode valve which has three inlet/outlet boundaries (figure 2.17). Tippetts [101] argued that three terminal devices can be characterised by four dimensional parameters, two dependent and two independent. Alternatively, three terminal devices can also be characterised by three non-dimensionalised parameters, two dependent and one independent. Tippetts [101] showed that there are many possible combinations of flow rates and pressure differences that could be used to characterise a three terminal device in this way. An example of a valid set of parameters that could be used to characterise a vortex triode is presented below

Dependent	**Independent**
$(p_\mathrm{r} - p_\mathrm{out}) \,/\, (kQ_\mathrm{out}^2)$	$Q_\mathrm{r}/Q_\mathrm{out}$
$(p_\mathrm{t} - p_\mathrm{out}) \,/\, (kQ_\mathrm{out}^2)$	

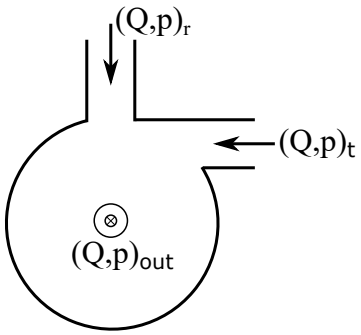

Fig. 2.17 Key parameters of a vortex valve

If Tippetts' [101] analysis is correct, then for flow rates low enough to avoid compressible flows but high enough to avoid laminar-turbulent transitions the non-dimensionalised characterisations should be Reynolds number independent. Consider the case where there is no radial inlet flow, i.e. $Q_\mathrm{r} = 0$. With one of the inlet flow parameters fixed, the system becomes a two terminal problem, and according to Tippetts' [101] analysis, this can be characterised by a single non-dimensional parameter

$$Eu = \frac{\Delta p_\mathrm{t}}{0.5\rho v^2} \tag{2.6}$$

where v is the average flow velocity at the inlet nozzle. Note that this is just the K_L parameter, but it is also referred to as the Euler number for a vortex device in some

sources [45, 51]. In cases where $Q_r = 0$, it might be expected that this parameter would remain constant over a wide range of Reynolds numbers. This assertion appears to hold true for Vatistas et al.'s investigation of vortex combustors [108, 107] but is contradicted by a later investigation of pressure drops across a vortex diode by Kulkarni et al. [51].

A schematic of the vortex chamber investigated by Vatistas et al. [108] is presented in figure 2.18. There are four tangential inlet ports, but the system is rotationally symmetrical, with all four inlets supplied by the same pressure. Therefore, the device can still be treated as a two terminal problem. Vatistas et al. [108] developed an analytical model for the pressure drop across the vortex chamber based on the assumption that the confined vortex can be treated as a Rankine vortex. For a Rankine vortex there is a clearly defined vortex core of radius R_C; at radii $> R_C$, the flows are irrotational (free-vortex), whilst for radii $< R_C$, flows are rotational (forced-vortex). Based on this description of the vortex chamber flow field, Vatistas et al. [108] derived an expression for the dimensionless pressure drop (Euler number) for the vortex chamber. According to this expression, the dimensionless pressure drop is only a function of the vortex chamber geometry and does not vary with the supply flow rate. This conclusion is corroborated by experimental measurements of the dimensionless pressure drop by Vatistas et al. [108].

Kulkarni et al. [51] presented the results of the experimental exploration of the pressure drops across a diode. In the reverse flow (high impedance) state, the diode flow field resembles that of a vortex amplifier in the tangential state. Unlike Vatistas et al., Kulkarni et al. [51] observed a strong Reynolds number dependence for the Euler number, see figure 2.19. This Reynolds number dependence is particularly stark at low-moderate flow rates, breaking with the Eulerian assumption made by

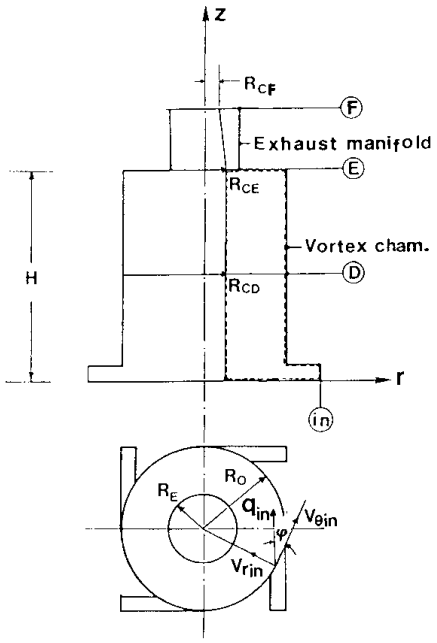

Fig. 2.18 Schematic of vortex chamber that is the basis of Vatistas et al.'s [108] investigation, figure copied from Vatistas et al. [108]

Tippetts [101] and appearing to contradict the results of Vatistas et al.'s [108] study.

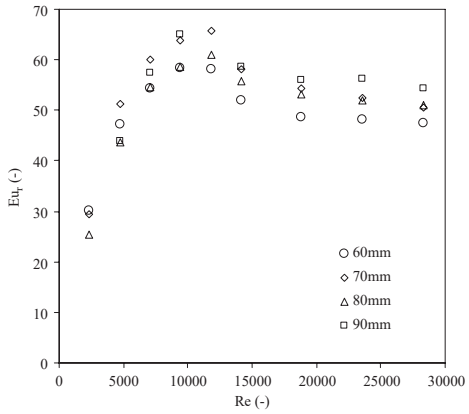

Fig. 2.19 Effect of Reynolds number on dimensionless pressure drop across a diode in the high impedance state, figure copied from Kulkarni et al. [51]

According to King [45], the performance of a vortex amplifier can be reduced to two non-dimensional parameters. Specifically, the control pressure ratio (CPR) and the flow turn-down ratio (TDR). In some sources, the radial inlet port is considered to be the main supply port of the vortex amplifier, and the tangential port is a

secondary control port. The CPR is defined as the pressure ratio

$$\frac{p_{\mathrm{t}} - p_{\mathrm{out}}}{p_{\mathrm{r}} - p_{\mathrm{out}}} = \frac{\Delta p_{\mathrm{t}}}{\Delta p_{\mathrm{r}}} \qquad \text{for } Q_{\mathrm{r}} = 0 \tag{2.7}$$

In other words, CPR is the ratio of Δp_{t} to Δp_{r} that restricts the supply flow rate Q_{r} down to zero. Therefore, CPR is effectively a measure of the control authority of the control signal Q_{t}. The TDR, on the other hand, is defined by King as

$$\frac{Q_{\mathrm{r},(Q_{\mathrm{t}}=0)}}{Q_{\mathrm{t},(Q_{\mathrm{r}}=0)}} \qquad \text{for } \Delta p_{\mathrm{r}} = \text{constant} \tag{2.8}$$

Since, $Q_{\mathrm{t}} = 0$ represents the high flow state and $Q_{\mathrm{r}} = 0$ the low flow state for a turn-down vortex amplifier, the TDR is a measure of the amplifier gain. In general, designers of vortex amplifiers aim to either minimise the CPT, maximise the TDR, or both.

2.3 Switched Vortex Valve

An SVV (figure 2.20) is the union of a diverter switch and a turn-down vortex amplifier, where the outlet ports of the diverter coincide with the vortex valve inlet ports. SVVs are typically bistable devices with two stable and distinct flow states that correspond to the attachment states of the diverter section. Wall attachment in the diverter section ensures that most of the supply flow is directed towards either the vortex valve's radial or tangential inlet ports. If the supply flow is directed by the diverter section towards the tangential port of the vortex valve, then the SVV is in the tangential state. Conversely, if the supply flows are directed towards the radial port of the vortex valve, then the SVV is in the radial state. In the tangential state, a strong vortex forms in the vortex chamber, and the vortex valve enters into a high K_{L} state. In the radial state, the amount of circulation in the vortex chamber

is considerably lower, and the vortex valve enters into a low K_{L} state. Consequently, given a constant supply pressure, the total flow rate of the SVV can be throttled by switching between the radial and tangential states.

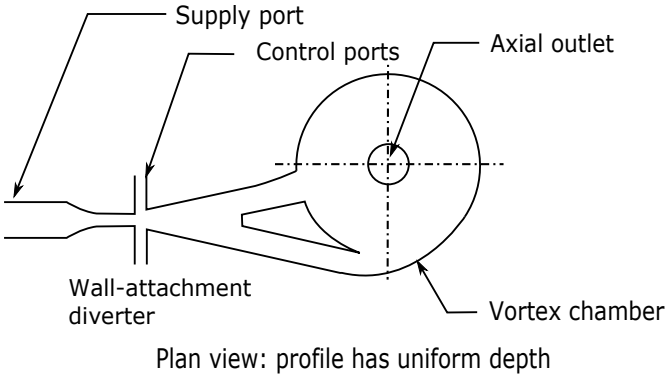

Fig. 2.20 Schematic of a switched vortex valve from Scanlon et al. [92]

An SVV has some distinct advantages over just a vortex amplifier in isolation. Either an SVV or a vortex amplifier could be used to modulate flow rates. However, the diverter section increases the control authority of any control signal. Typically, the control mass flow rate $\dot{m}_c$ required to switch a diverter is about 1/10th that of the supply flow rate $\dot{m}_s$. Therefore, the change in mass flow rates at the diverter outlets is typically a factor of 10 greater than the magnitude of a switching control flow rate. Consequently, the diverter section reduces how much control flow is required to effect a comparable change in the flow state of the vortex chamber. Furthermore, if the diverter section is bistable, the device can be switched with a transient control signal: remaining in the switched state until another switching control signal is introduced. This property could be potentially quite useful if the device is to be controlled by plasma or piezoelectric actuators rather than with mass flow injection.

The design concept for a switched vortex valve (SVV) was first proposed by Adams & Moore in 1963 [2]. There have been suggestions that an SVV could be used as a fuel injector air flow regulator [7] and as a pulse transmitting flow meter [113].

It was first presented as a secondary flow regulation device in Scanlon et al. [92, 78]. Scanlon et al. [92] proposed that an SVV could be used as a passive flow control device that would limit secondary flow rates in the event of a burst duct. The SVV was set up in such a fashion that when the pressure drop across the device exceeded a given threshold, the device would switch to the high K_L state.

Romero [86] and Koli et al. [49, 50] built upon this idea, both arguing that SVV valves could be used to actively modulate flow rates in a jet engine's secondary air system. Romero proposed using an array of smaller SVV devices operating in parallel to modulate sealant flow rates at the interface between the turbine's high pressure and intermediate pressure sections. Figure 2.21 shows both the array of SVVs constructed as part of a demonstrator experiment, and where these SVVs would be positioned in the turbine section of an engine.

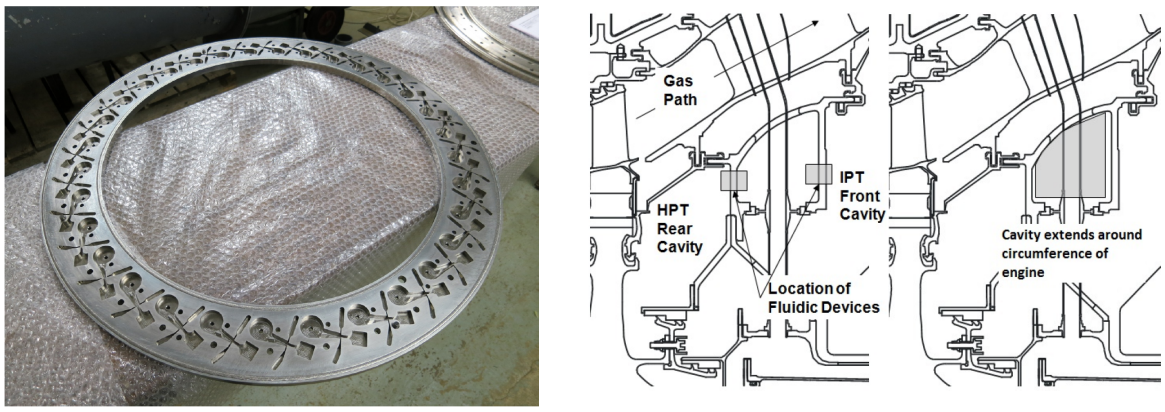

Fig. 2.21 SVV rim constructed as part of preparations for a demonstrator experiment based on optimised SVV geometry proposed by Romero [86]. Figures copied from Romero [86]

by Romero over a range of supply-to-outlet PRs are presented in figure 2.22. The theoretical flow rates marked on figure 2.22 represent the mass flow rates predicted by modelling the SVV as a pair of nozzles in series with isentropic compressible flow. These nozzles represent the SVV supply nozzle and the vortex chamber outlet port.

At low PRs, increasing the PR will increase the flow rate in both the radial and tangential states. However, as the PR increases, the rate at which mass flow rates increase decreases. Eventually, the mass flow rates stop increasing altogether. The SVV reaches this limiting mass flow rate at a lower PR in the radial state than in the tangential state. In both states, it is theorised that the mass flow rate stops increasing when flow chokes either in the supply nozzle or at the vortex chamber outlet.

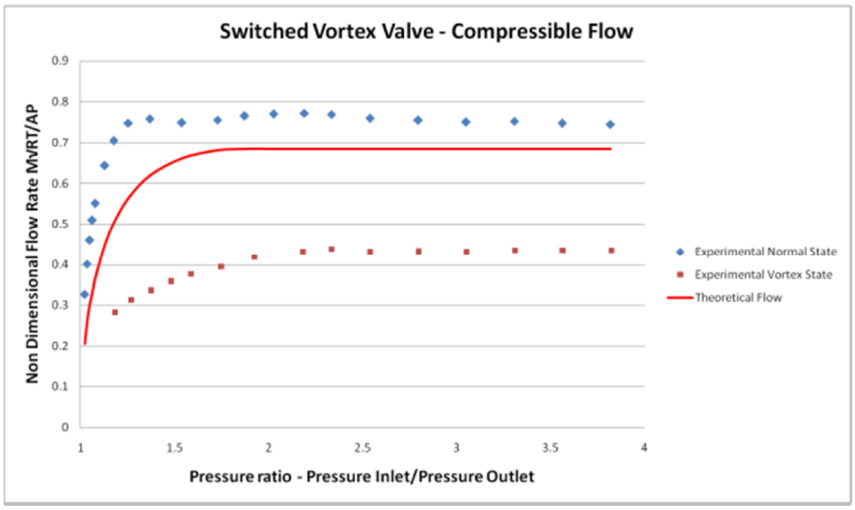

Fig. 2.22 Effect of supply pressure ratio on mass flow rates in the tangential (vortex) and radial (non-vortex) states, figure copied from Romero [86]

A common method to parameterise the performance of a vortex devices is to examine the flow turn-down ratio (TDR). The TDR is the ratio of flow rates in the high vs low flow states, so for an SVV

$$\text{TDR} = \frac{\dot{m}_{\text{out,rad}}}{\dot{m}_{\text{out,tan}}} \tag{2.9}$$

Romero [86] has shown that, at low PRs, as PR increases, the mass flow rates will increase faster in the radial state than the tangential state. Consequently, increasing the PR will have an initially positive effect on performance as the TDR increases. However, for $PR > 1.2$, the SVV is choked in the radial state and continuing

to increase the PR will detrimentally affect the performance with the TDR decreasing.

Koli et al. [49, 50] constructed a uRANS model based on the SVV geometry developed by Romero [86]. Koli et al. primarily focused upon the feasibility of using uRANS simulations to qualitatively and quantitatively predict the behaviour of the SVV device. The accuracy of these simulations was in part judged by Koli et al. [50] through direct comparison with experimental data from Romero's thesis [86]. Koli et al. [49, 50] concluded that uRANS simulations with the appropriate choice of turbulence model, specifically RSM, could reliably simulate some of the steady and dynamic behaviours of an SVV. In particular, Koli et al. [50] states that the simulations correctly predicted the following

- mass flow rates in the radial and tangential state
- settling times in the radial state
- bistable nature of the device
- switching between attachment states with control pressure reductions

Koli et al. [50] showed using the uRANS model that switching depends only on the pressure at the control ports, not the rate of change of that pressure. Koli et al. [50] also used the uRANS model to simulate the effect of vibrations generated by the turbine blade passing frequency and found the simulated SVV to be largely insensitive to these vibrations.

The sealant flow modulation system, described by Romero [86] and Koli et al. [49, 50], uses SVV cavities that are switched between high and low flow states by the injection or expulsion of air at SVV control ports. This switching mechanism necessitates the addition of mechanical valves to open and close flow paths to the control ports. However, as previously mentioned, it has been shown that it is possible to actuate wall-attachment devices with piezo-electric [27, 28, 63, 62, 59, 61, 57, 58, 69, 70]

or plasma [29, 13] actuators. Piezo-electric and plasma actuators are typically smaller and lighter than mechanical valves, and because they don't have any moving parts, they generally require less maintenance. This thesis focuses on the acoustic actuation of a staged SVV, where the acoustic signal could be created using high-temperature piezoelectric buzzers. However, Chen et al. [13] has shown that an SVV can also be switched using localised arc-filament plasma actuators (LAFPA).

A LAFPA is a thermal plasma actuator consisting of two wire-electrodes often constructed from steel or tungsten [87, 105]. These actuators are typically driven by an oscillating electrical potential. With a large enough signal amplitude, a single arc-filament forms periodically between the electrodes. The filament causes rapid local heating which is accompanied by a localised drop in density and the formation of an expanding circular pressure wave. LAFPA are efficient, large amplitude, broad-band devices and there have been studies [87, 105] investigating their applicability for mixing enhancement and noise mitigation in supersonic ($\sim$ Mach 1.3) jet nozzles.

Figure 2.23 presents a schematic of the plasma switched fluidic vortex valve (PSFVV) from Chen et al. [13]. The control ports have been replaced with LAFPAs, with plasma sparks formed between tungsten electrodes and aluminium plates. The electrodes were positioned such that there will be an electrode located within the entrainment region for either attachment state. A square wave voltage signal was applied to the attached side electrode to trigger switching. The plasma sparks would create low-density spots within the entrainment region. The thermal blockage effects of these low-density spots would lead to the recirculation bubble increasing in size until jet splitter-interactions destabilised the attachment state. With this switching mechanism, Chen et al. [13] found that provided the applied frequency was 3.7 kHz, it was possible to switch the PSFVV over a range of PRs up to PR = 1.1. It was theorised by Chen et al. [13] that the 3.7 kHz preferred frequency corresponded to a

resonance frequency of the PSFVV cavity.

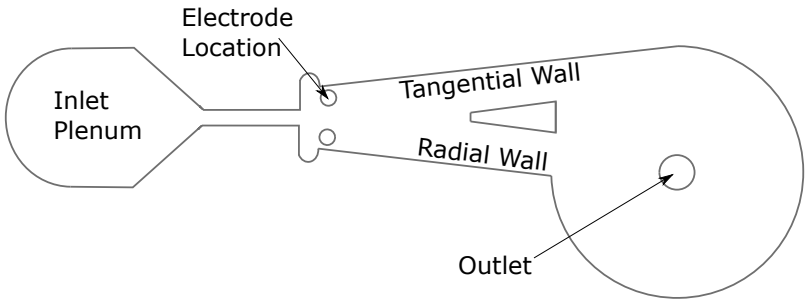

Fig. 2.23 Schematic of PSFVV device, adapted from a figure in [13].

2.4 Fluidic Staging

Tippetts & Royle [103], is the only example of steady-state characteristics being used to predict the behaviour of a multi-stage fluidic device with unvented diverter components. Specifically, Tippetts & Royle uses a paired set of unvented diverters (figure 2.24) as the illustrative example. This thesis focuses upon a staged SVV, which has two unvented diverter sections connected in series. Consequently, the intersection of characteristics method discussed by Tippetts & Royle [103] is very relevant to this thesis and provided inspiration for the structure of the grey-box model of the staged SVV (chapter 3).

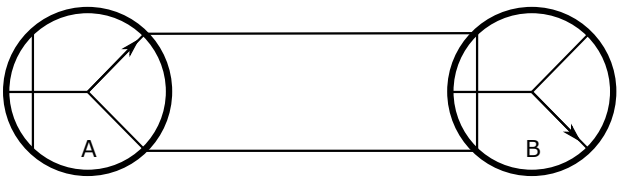

Fig. 2.24 2-stage diverter circuit adapted from a figure in Tippetts 1971 [103]

The intersection of characteristics method involves using the steady-state characteristics of individual components of the fluidic circuit to find the operating points of the circuit as a whole. To characterise a diverter, Tippetts & Royle [103] uses

volumetric flow rates Q and static pressures p at the diverter boundaries, see figure 2.25. The '+' and '-' superscripts are used to label flow parameters at the attached and unattached sides of the diverter, whilst subscripts 's', 'c' and 'o' label flow parameters at the supply, control and outlet ports.

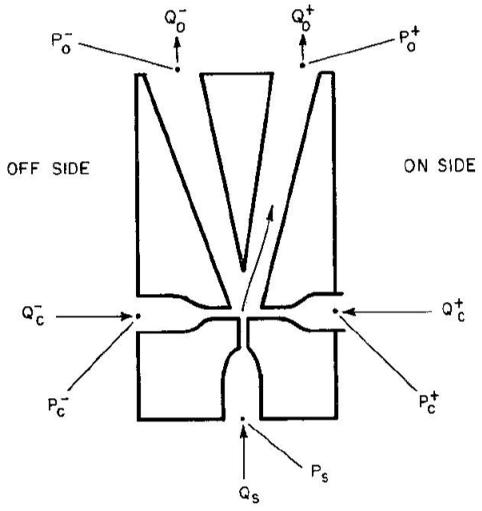

Fig. 2.25 Dimensional parameters of an unvented diverter, figure copied from Tippetts & Royle [103]

According to Tippetts & Royle [103], the quasi steady-state behaviour of a diverter can be characterised using eight dimensional flow parameters, four dependent and four independent. The following pressure differences were chosen to be the four dependent flow parameters

$$E_\mathrm{s} = p_\mathrm{s} - p_\mathrm{o}^-$$

$$E_\mathrm{c}^+ = p_\mathrm{c}^+ - p_\mathrm{s}$$

$$E_\mathrm{c}^- = p_\mathrm{c}^- - p_\mathrm{s}$$

$$E_\mathrm{o}^+ = p_\mathrm{o}^+ - p_\mathrm{o}^-$$

whilst the flow rates Q_s, Q_c^+, Q_c^-, Q_o^+ were chosen to be the four independent flow parameters. Figure 2.26 shows examples of dimensional characteristics for a diverter. Note that to have 1-dimensional curves like those presented in figure 2.26, three of the four independent parameters have to be fixed ($Q_c^+ = Q_c^- = 0$ and $Q_s = Q_o^+$). To fully characterise a diverter with dimensional parameters would require the construction of 4-dimensional surfaces for each of the four dependent flow parameters.

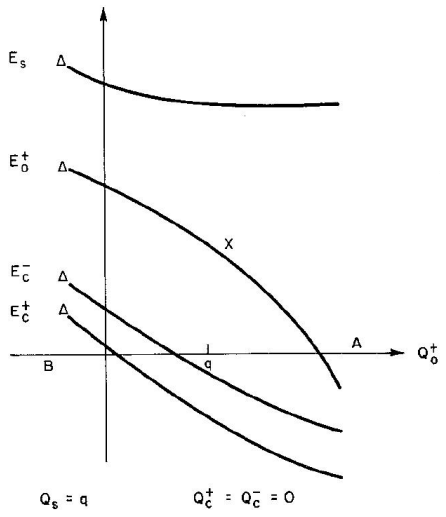

Fig. 2.26 Example of dimensional characteristics for a diverter ($Q_c^+ = Q_c^- = 0$ and $Q_s = Q_o^+$), figure copied from Tippetts & Royle [103]

To reduce the number of dimensions involved Tippetts & Royle [103] argue that the supply pressure is purely a function of Q_s at sufficiently high Reynolds numbers. Consequently, the characteristics can be non-dimensionalised with Q_s and E_{sx}. E_{sx} is the value of E_s for the diverter in the no-spill state ($Q_o^- = 0$) and is stated to be proportional to the supply nozzle dynamic head. The non-dimensionalised flow rate parameters become

$$\overline{Q_c^+} = Q_c^+ / Q_s$$

$$\overline{Q_c^-} = Q_c^- / Q_s$$

$$\overline{Q_o^+} = Q_o^+ / Q_s$$

whilst the non-dimensionalised pressure parameters become

$$\overline{E_{\mathrm{s}}} = E_{\mathrm{s}}/E_{\mathrm{sx}}$$

$$\overline{E_{\mathrm{c}}^{+}} = E_{\mathrm{c}}^{+}/E_{\mathrm{sx}}$$

$$\overline{E_{\mathrm{c}}^{-}} = E_{\mathrm{c}}^{-}/E_{\mathrm{sx}}$$

$$\overline{E_{\mathrm{o}}^{+}} = E_{\mathrm{o}}^{+}/E_{\mathrm{sx}}$$

Given two fully characterised diverter sections the valid operating points of the combined system is found by locating where the output characteristics of the upstream stage intersect with the input characteristics of the downstream characterics. In Tippetts & Royle [103] this is done graphically, an example of what this process looks like is presented in figure 2.27. The relevant parameters of this plot are defined follows

- E_{o}^{+} is the pressure difference between the outlet ports of the upstream stage2
- $n^{-} = Q_{\mathrm{o}}^{+}/Q_{\mathrm{o}}^{-}$ is the ratio of outlet flow rates for the upstream stage
- $-E_{\mathrm{c}} = -\left(E_{\mathrm{c}}^{+} - E_{\mathrm{c}}^{-}\right)$ is the pressure difference between the control ports of the downstream stage
- $m = Q_{\mathrm{c}}^{-}/Q_{\mathrm{c}}^{+}$ is the ratio of control flow rates for the downstream stage

When the two stages are connected as shown in figure 2.24, the attached outlet port of the upstream stage connects directly to the unattached control port of the downstream stage. Consequently, the operating point of the 2-stage circuit is found by identifying the intersection point marked by an 'X', where $E_{\mathrm{o}}^{+} = -E_{\mathrm{c}}$ and $n^{-} = m$. Having identified the operating point, it is then possible to work backwards from here to get the pressures and mass flow rates for both stages of the circuit.

In addition to predicting the steady-state behaviour, Tippetts & Royle [103] also discuss two scenario's that trigger oscillatory instabilities for the 2-stage circuit. In

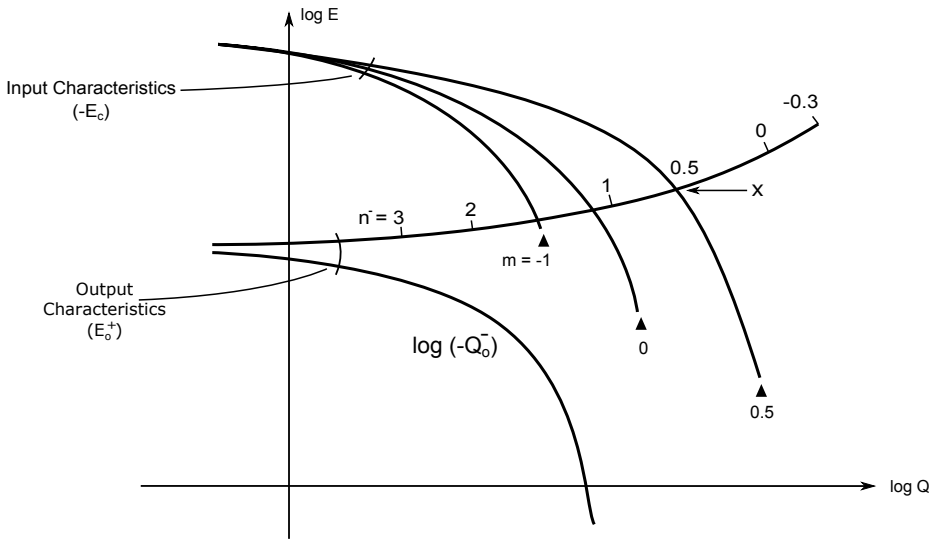

Fig. 2.27 Representation of 2-stage operating point, adapted from a figure in Tippetts & Royle [103]

both scenarios, the downstream stage (diverter B) oscillates between attachment states.

The first scenario occurs when the supply flow rate for diverter A (figure 2.24) is zero. In this case, despite there being no supply mass flow for diverter A, there is a non-zero mass flow that passes through diverter A following the flow path that connects the control ports of diverter B to each other. This flow is driven by the pressure difference between diverter A's control ports p_c^+ and p_c^-.

As discussed in section 2.1, wall attachment is maintained by a low pressure region p_B on the attached side of the jet. Consequently, p_c^+ will be at a higher pressure than p_c^-, and with zero supply flow for diverter A, this pressure difference will drive mass flow from the unattached side control port to the attached side control port. The resulting mass flow injection at the attached side control port will switch diverter B. After switching, the locations of diverter B's high pressure and low pressure control ports flip and mass flow between control ports reverses direction. Mass flow injection at what is now the attached side control port switches diverter B

back to its original attachment state, and the cycle begins again. This instability mode resembles the staged SVV oscillations discussed in section 6.4.2, where the upper stage is acoustically stabilised.

The second instability mode mentioned by Tippetts & Royle [103] is triggered as diverter A's supply pressure is lowered but without its supply mass flow rate reaching zero. Under steady-state conditions, the attached outlet port of diverter A connects to the unattached control port of diverter B. Consequently, the back pressure imposed on the attached outlet port of diverter A is greater than the back pressure imposed on the unattached outlet port. This pressure differential between the outlet ports acts in opposition to the primary flow path of diverter A, weakening jet attachment. Provided that diverter A supply flow rates are sufficiently high, Coandă based attachment will remain stable. However, at reduced supply flow rates, the adverse back-pressure differential destabilises attachment; switching diverter A. Switching a diverter by imposing adverse back-pressures is commonly referred to in the literature as load-switching. When diverter A switches, the resulting mass flow injection at the attached control port of diverter B will switch diverter B, which then load switches diverter A again. This instability mode resembles the staged SVV oscillations discussed in section 5.3.

Chapter 3
Grey-Box Model Design

3.1 Introduction

As outlined in section 2.3, the diverter section of an SVV amplifies the switching control signal. Typically, the control flow rate required to switch a diverter is approximately 1/10th that of the main flow. Consequently, the diverter section of an SVV reduces the amount of control flow needed to switch the device. However, switching flow rates would still have to be a substantial fraction of the coolant flow rate. Additional diverter stages can be used to reduce the amount of switching flow required. Figure 3.1 presents a general schematic of the 2-stage SVV that is the focus of this thesis. It consists of an SVV power stage and a diverter pilot stage. The SVV main stage geometry is based on the SVV geometry used by Turner et al. [104]. The pilot stage's diverter section geometry is a half-scale version of the SVV diverter switch section. The exact geometry of these stages is laid out in sections 4.2.1 and 4.3.1. Rather than switching the SVV directly, the actuation signals are applied at the control ports of the pilot stage. When the pilot diverter section switches in response to the actuation, the pilot flows are redirected from the unattached control port of the SVV to the attached control port. The resulting mass flow injection at the attached control port switches the SVV.

The magnitude of the control signal required to switch this staged SVV is considerably less than that needed to switch the SVV directly. In theory, the magnitude of the control signal needed to switch the device could be reduced further by adding even more diverter stages. However, with each additional fluidic stage, the device's

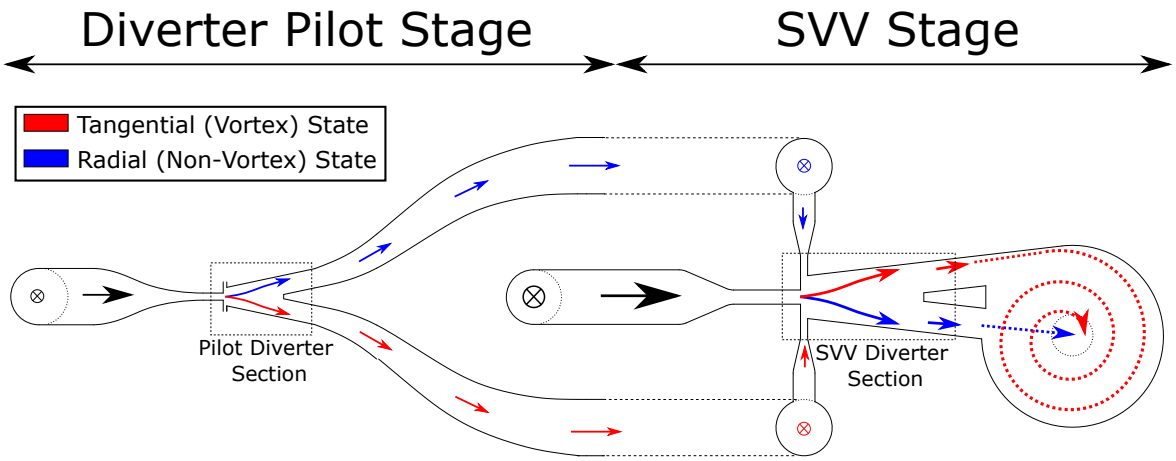

Fig. 3.1 2-Stage device with main flow paths marked for the tangential (vortex) and radial (non-vortex) states.

behaviour becomes more complex and difficult to predict. Furthermore, transient interactions between stages can lead to dynamic instabilities. A particular concern is the self-excited oscillations.

Self-excited oscillations of multi-stage fluidic devices are discussed in greater depth in section 2.4. However, to summarise, for two diverter sections connected in series, the downstream diverter will impose an adverse pressure difference across the outlet ports of the upstream diverter, weakening jet attachment for the upstream device. If the upstream stage supply flow rate is too low, the adverse back pressure difference will destabilise attachment and switch the upstream diverter. This load-switching of the upstream diverter will trigger a continuous cycle of switching in both stages.

In civil aviation, both the space and weight allocated to individual components in a jet engine are usually at a premium. If a staged SVV is to be used to modulate coolant flow rates, then its design will need to balance size and weight against steady-state performance. A measure of the steady-state performance is the radial state flow throughput, which should ideally be maximised. Most of the total flow is directed through the SVV stage. Consequently, the radial state mass flow rates (for a given overall device size) can be increased by maximising the size of the SVV stage

and minimising SVV feed losses. However, if the weight and size are constrained, this inevitably will result in prioritising the SVV stage to the detriment of the pilot stage. Hence, design incentives promote undersized pilots that may have lossy supply feeds, reducing the pilot supply flow rate. As previously mentioned, if the pilot supply flow rate is degraded too far, then the staged device could become unstable, entering a cycle of self-excited oscillations. Therefore, it would be useful to have a model to explore the root cause of this instability and predict the extent to which the pilot stage can be pushed in the pursuit of performance gains without triggering oscillations.

A model could also be used to make informed decisions about the physical design. These could include decisions such as the number of additional diverter stages; the relative scale of fluidic stages; and the geometry of supply manifolds and inter-stage ducting. All of these design choices could potentially affect both the dynamic stability and the steady-state performance. Furthermore, once a detailed staged SVV design has been settled upon, the model could then be used to conduct preliminary tests of the device.

Finally, it will be shown in chapters 5 and 6 that wall attachment devices will respond to control signals both large and small. Larger actuation signals can trigger switching by destabilising wall attachment. However, weaker, sub-switching actuation signals can also alter the steady-state behaviour of the staged SVV. If the pressure ratio across the device is fixed, the total mass flow rate will respond in a continuous analogue fashion to sub-switching control signals. This property can be useful, as it can be used to compensate for performance penalties associated with the device operating under off-design conditions. Under these circumstances, a sub-switching control signal could be used to push the device back towards its optimal performance state, maximising the radial state flow rate. A model could be used to find the control signal magnitude required to maximise performance for any given set of

operating conditions.

This chapter presents a model of the staged SVV constructed Matlab/Simulink.

3.2 Model Structure

To construct a model of the staged SVV, the device was conceptually subdivided into smaller components, namely the diverter switch sections, ducting, and the vortex chamber. A visualisation of this sub-division is presented in figure 3.2.

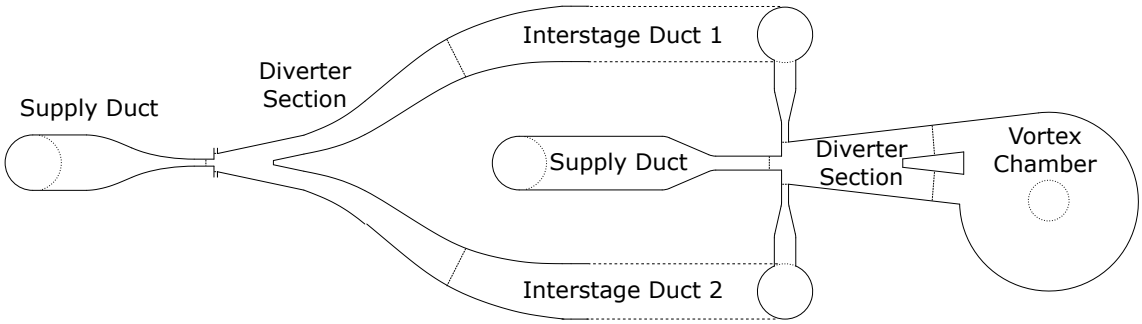

Fig. 3.2 Sub-division of pilot and SVV stages for modelling purposes.

The choice of where the divisions are positioned is dictated mainly by flow complexity. In the duct sections, the flow dynamics are comparatively simple and are modelled using the 1D discretisations of the Navier-Stokes momentum equation and the continuity equation (section 3.3). However, a more sophisticated CFD model would be necessary to recreate internal flow dynamics for the diverter switch sections and the vortex chamber. So instead, the model treats these components as black-box objects characterised by experimental data (section 3.4 and 3.5).

The advantages of using an empirical rather than a numerical approach towards modelling the switch sections and vortex chamber are speed and robustness. The simulation run times are short when compared with typical run times for CFD

simulations. Furthermore, since the model is driven by experimental data, it will implicitly model the cumulative effect of all the internal flow dynamics; this includes subtler flow dynamics that might be missed by a CFD simulation if, for instance, the spatial or temporal resolutions are not sufficiently high. However, this requires that each fluidic stage be individually characterised to produce the inputs for the model. Any geometric changes to the fluidic components would then need this characterisation to be repeated to update the model.

The modular structure used here also presents some distinct advantages. The pilot and SVV stages of the model can be tested individually as part of the debugging process. Only once both stages of the model are reliably reproducing experimental observations are they then combined to form a model of the staged SVV. Furthermore, as components can be easily modified or replaced, the model can be used to test potential design changes to an existing device. Examples of such changes include changing the scale or geometry of pilot/SVV stages, adding more diverter stages, or modifying duct geometries.

3.3 Duct Modelling

Each duct is modelled using a lumped parameter model similar to the one used by Potter [77] to model pipe flow dynamics. Each length of ducting is discretised into an alternating series of pressure and mass flow lumps. This staggered discretisation is similar to the staggered grid commonly used by CFD solvers [74]. An example of this subdivision process is presented in figure 3.3. The mass flow lump $\dot{m}_I$ is the fluid element bounded by pressure nodes p_i and p_{i+1}. Whilst the pressure lump p_i is the fluid element encapsulated by mass flow nodes $\dot{m}_{I-1}$ and $\dot{m}_I$. Capitalised indices 'I' are used to identify flow parameters associated with

the mass flow nodes. Conversely, pressure node parameters have lower case 'i' indices.

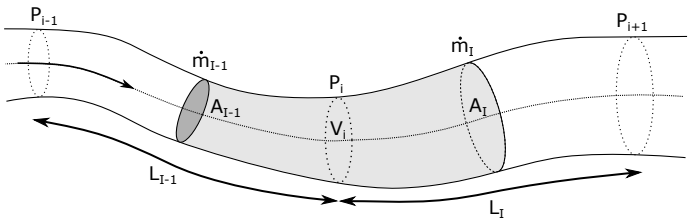

Fig. 3.3 Location of key parameters for a lumped parameter model.

The 2-stage model has eight duct sections: the pilot supply duct, pilot leg 1, pilot leg 2, SVV control duct 1, SVV control duct 2, SVV supply duct and two mass flow lumps connecting the SVV diverter section to the vortex chamber (figure 3.4). The subdivision of these ducts into mass flow and pressure lumps is presented in figure 3.4.

The evolution of mass flow and pressure lump values within the model is prescribed by discretised versions of the Navier-Stokes momentum and the continuity equations

$$\frac{d\dot{m}_I}{dt} = \frac{A_I}{L_I}\left[(p+q)_i - (p+q)_{i+1}\right] - R_I\,\dot{m}_I^2 \tag{3.1}$$

$$\frac{dp_i}{dt} = \frac{c^2}{V_i}\left[\dot{m}_{I-1} - \dot{m}_I\right] \tag{3.2}$$

where

- A_I is the cross-sectional area at the $\dot{m}_I$ node
- L_I is the length of the $\dot{m}_I$ lump
- q_i is the dynamic head at the p_i node
- R_I is the pressure loss parameter
- $c = \sqrt{\gamma R_{\text{gas}} T}$ is the speed of sound
- V_i is the volume of the p_i lump

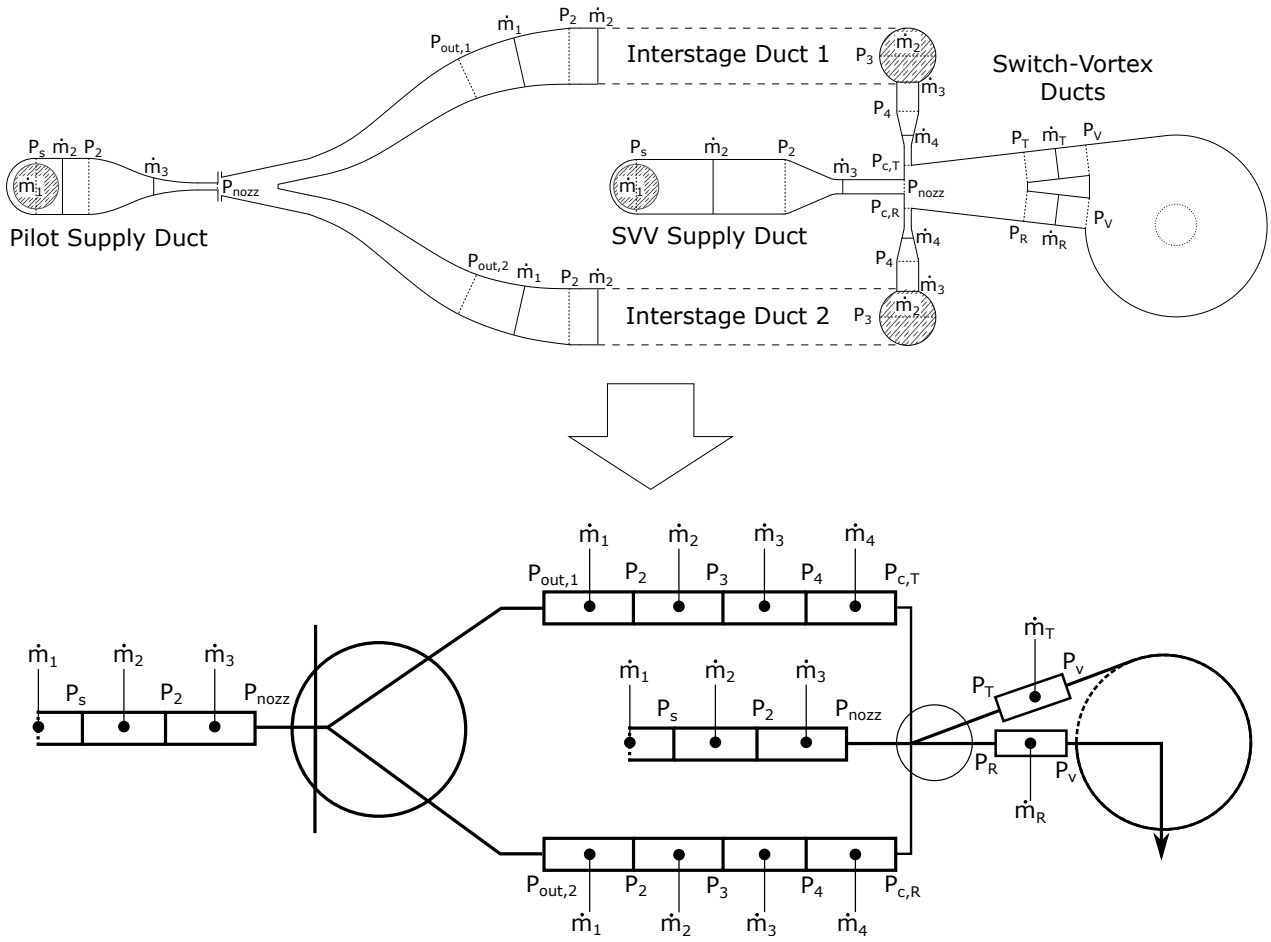

Fig. 3.4 Sub-division of ducts into mass flow and pressure lumps.

Full derivations of these relations are presented in appendix A. As part of the derivation of the discretised momentum relation, it is assumed that flows are incompressible and that A_I is constant for the mass flow lump. Neither of these assumptions are applied to the discretised continuity equation. Instead this discretisation uses the adiabatic version of the continuity equation and it is assumed that c is constant.

The dynamic head terms q_i and q_{i+1} are defined at the p_i nodes, but mass flow rates and, by extension, flow velocities are modelled at the $\dot{m}_I$ nodes. q_i is calculated using a linear interpolation

$$\dot{m}_i = \frac{1}{2}\left[\dot{m}_{I-1} + \dot{m}_I\right] \tag{3.3}$$

and

$$q_i = \frac{\dot{m}_i^2}{2\rho_i A_i^2} \tag{3.4}$$

The ordinary differential equations (A.8 and 3.2) are solved iteratively using Simulink at each mass flow and pressure node for each time step using an ODE solver (Matlab's **ode23t**). A major difference between this model and a typical CFD model is that it does not model viscous terms or the redirection of flow momentum by the duct directly. Instead, all the pressure losses are encapsulated by a pressure loss coefficient R_I.

$$R_I = \left[\frac{1}{2.\rho.A.D_\mathrm{h}} f_\mathrm{D} + \frac{1}{2.\rho.A.L} K_\mathrm{L}\right]_I \tag{3.5}$$

where f_D is the Darcy friction factor, and $K_\mathrm{L,fwd}$ is a pressure loss coefficient.

The f_D term is the skin friction contribution to pressure loss and is derived from the Darcy-Weisbach equation

$$\begin{aligned} \frac{\Delta p}{L} &= f_\mathrm{D}.\frac{\rho}{2}.\frac{\langle v\rangle^2}{D_\mathrm{h}} \\ &= f_\mathrm{D}.\frac{\dot{m}^2}{2.\rho.A^2.D_\mathrm{h}} \end{aligned} \tag{3.6}$$

The Colebrook–White equation [14] is used to get an estimate of f_D

$$\frac{1}{\sqrt{f_\mathrm{D}}} = -2\log_{10}\left[\frac{\epsilon_\mathrm{r}}{3.7D_\mathrm{h}} + \frac{2.51}{Re\sqrt{f_\mathrm{D}}}\right] \tag{3.7}$$

This is a phenomenological equation fitted to experimental data, where ϵ_r is the roughness height.

The K_L term in equation 3.5 was used to add pressure losses associated with sharp turns and sudden expansions/contractions. At most $\dot{m}_I$ nodes, the redirection of flows by the ducts was gentle enough to be treated as lossless ($K_\mathrm{L} = 0$); the

exceptions were at the p_s and p_3 nodes[1], where there are sharp right angle bends, which were assigned K_L values of 0.9. The loss coefficient for a typical 90° degree elbow fitting is 0.9, according to Howatson et al. [33].

3.3.1 Sensitivity of the Model to Surface Roughness

At each mass flow node, the effects of surface roughness are modelled by the f_D component of R_I (equation 3.5). f_D is calculated using surface roughness heights (equation 3.7). Theoretically, to accurately model the effect of surface roughness requires data on surface roughness heights ϵ_r.

However, over the range of pressure ratios modelled (1.01 - 1.22), frictional contributions to duct pressure losses are relatively small. Figures 3.5, 3.6 and 3.7 present the effect of varying ϵ_r on the pressure loss coefficients of the pilot supply duct, one of the interstage ducts and the SVV supply duct. The pressure loss coefficients were calculated by simulating the duct sections in isolation. The mass flow rates for these simulations match or exceed the maximum supply mass flow rates used to characterise the pilot stage (5 g/s) and the SVV stage (28 g/s). Note that the interstage ducts were constructed from a mixture of 3D-printed and acrylic components. Therefore, the effects of independently varying ϵ_r values for the 3D-printed and acrylic components are represented by two curves in figure 3.6.

The physical device that the model is based on consists of a 3D-printed pilot stage and an SVV stage assembled from a stack of laser-cut acrylic plates (see chapter 4). As an initial estimate, surface roughness heights of 25 µm (d_{3D}) and 1 µm (d_a) were assigned to mass flow nodes associated with the device's 3D-printed and acrylic plate sections, respectively. These values were based on the print resolution of the

[1]See figure 3.4 for node locations.

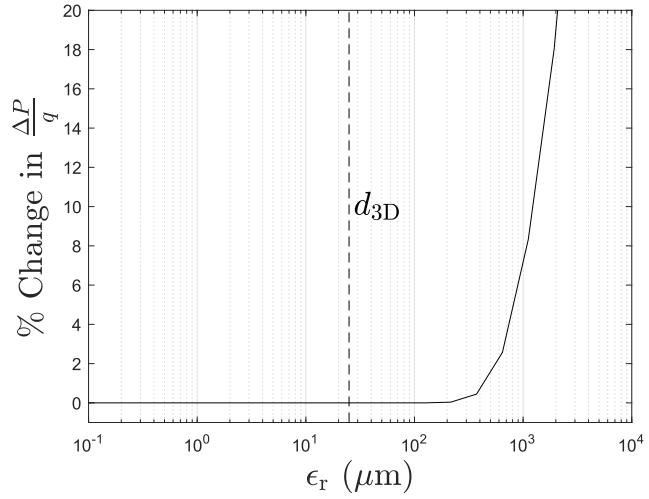

Fig. 3.5 Simulated effect of surface roughness on the total-to-total pressure loss coefficient of the pilot supply duct (p_s to p_{nozz} nodes as marked in figure 3.4). The duct flow rate is fixed at 5 g/s. The percentage change in the pressure loss coefficient is relative to the smooth ($\epsilon_r = 0$) case. The dynamic head q used to calculate $\Delta p/q$ is the supply nozzle dynamic head localised to pilot pressure node p_{nozz}.

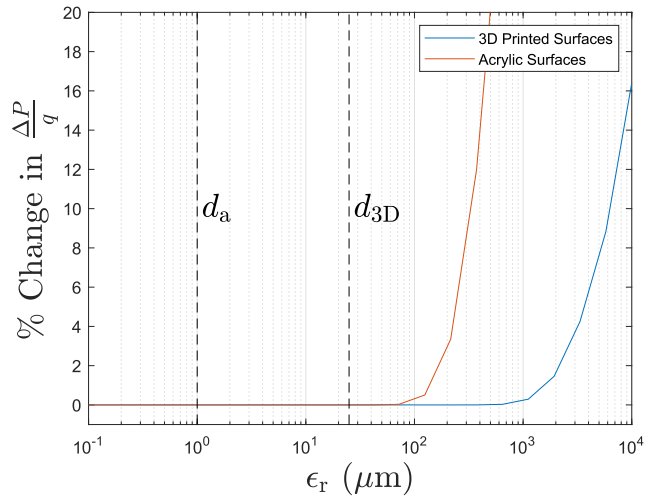

Fig. 3.6 Simulated effect of surface roughness on the total-to-total pressure loss coefficient of one of two identical interstage ducts (p_{out} to p_c nodes as marked in figure 3.4). The duct flow rate is fixed at 5 g/s. The percentage change in the pressure loss coefficient is relative to the smooth ($\epsilon_r = 0$) case. The dynamic head q used to calculate $\Delta p/q$ is the SVV control port dynamic head localised to pressure node p_c.

SLA printer (25 µm)[2] and the typical roughness heights of laser-cut acrylic 0.3-1.2 µm.

[2]The actual roughness heights of 3D-printed components are believed to be significantly less than the print resolution. A liquid resin printer was used to construct 3D-printed components, and the surface tension and viscosity of the resin smooths out discontinuities between print layers. Furthermore, since the 3D printer prints in layers, the surface roughnesses of 3D-printed surfaces are expected to vary with the print orientation.

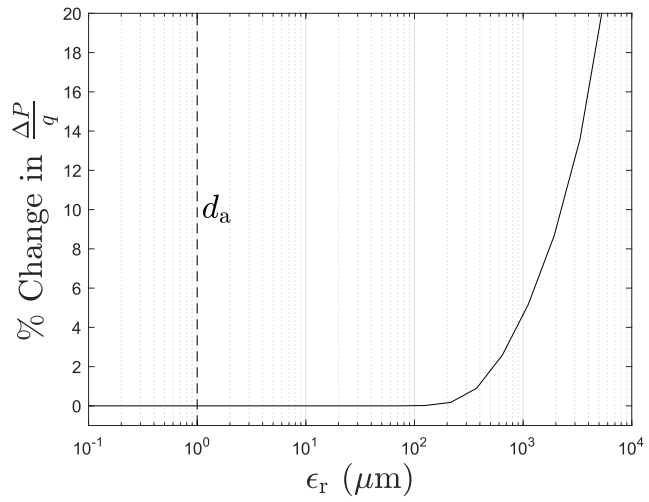

Fig. 3.7 Simulated effect of surface roughness on the total-to-total pressure loss coefficient of the SVV supply duct (p_{s} to p_{nozz} nodes as marked in figure 3.4). The duct flow rate is fixed at 24 g/s. The percentage change in the pressure loss coefficient is relative to the smooth ($\epsilon_r = 0$) case. The dynamic head q used to calculate $\Delta p/q$ is the supply nozzle dynamic head localised to SVV pressure node p_{nozz}.

As can be seen from figures 3.5, 3.6 and 3.7 ϵ_{r} values that have a substantial impact on duct pressure losses are much greater than the d_{3D} and d_{a} estimates.

3.4 Diverter Switch Modelling

A simplified view of the flow field within a diverter switch section is presented in figure 3.8. The supply jet issues from the supply nozzle and attaches to one of two attachment walls in the diverging duct. The device's behaviour as observed at the supply, outlet and control boundaries is dictated by jet position/curvature and the jet spreading rates at the shear layers. These jet properties are determined by the switch geometry, supply flow rate, control mass flow rates, surface roughness and applied back-pressures at the outlet boundaries. As discussed in section 2.1, a succession of analytical models have been developed that describe steady-state [5, 90, 91, 53] and dynamic [67, 68, 54, 55, 20, 84, 26, 69] jet attachment. A jet attachment model similar to the one presented by Nicholls [69] could have formed the basis of an analytical model of the switch sections. Alternatively, the switch sections of the

model could have been recreated using CFD. Examples of CFD simulations of diverter switches are presented by various authors [85, 21, 62, 59, 61, 57]. However, here non-dimensional analysis is used with the switch sections treated as black-box objects. Pressures and mass flow rates at the flow boundaries are measured over a range of flow conditions and are used to construct steady-state characteristics.

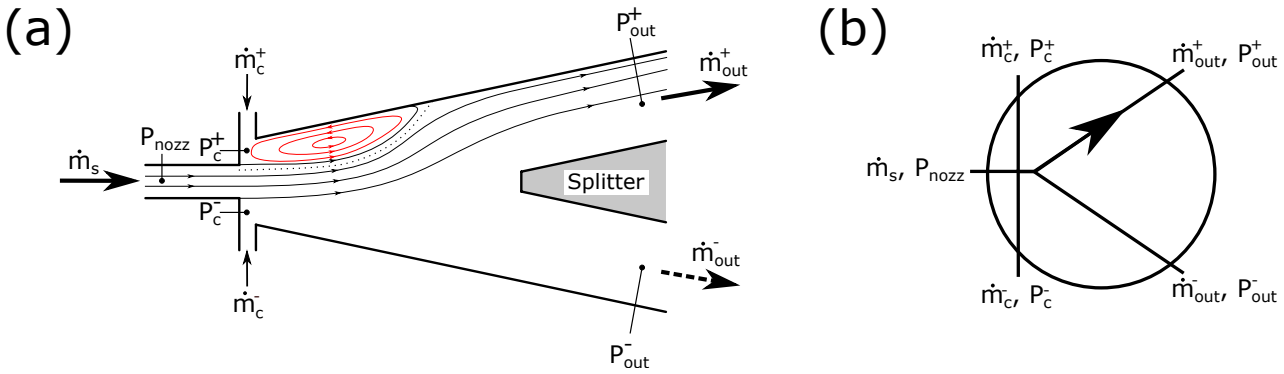

Fig. 3.8 Map of locations of key mass flows and pressures used to characterise a diverter switch section.

The form of these characteristics is derived using dimensional analysis. If boundary pressure differences

$$\Delta p_c^+ = p_{nozz} - p_c^+ \tag{3.8}$$

$$\Delta p_c^- = p_{nozz} - p_c^- \tag{3.9}$$

$$\Delta p_{out}^+ = p_{nozz} - p_{out}^+ \tag{3.10}$$

$$\Delta p_{out}^- = p_{nozz} - p_{out}^- \tag{3.11}$$

are treated as the dependent parameters, then it is assumed that the independent parameters will be

$$\dot{m}_s, \dot{m}_c^+, \dot{m}_c^-, \dot{m}_{out}^+, \rho, \mu, L$$

The mass flow rates provide boundary conditions for 4 of the 5 flow boundaries ($\dot{m}_{out}^-$ can be inferred from the conservation of mass). The density ρ and viscosity

μ describe the properties of the fluid (temperature is treated as a fixed variable). Finally, L is some key length scale for the switch. Thus for each boundary pressure difference $\Delta p \in \left[\Delta p_{\mathrm{c}}^{+}, \Delta p_{\mathrm{c}}^{-}, \Delta p_{\mathrm{out}}^{+}, \Delta p_{\mathrm{out}}^{-}\right]$ there exists an 8 dimensional characteristic of the form

$$f\left(\dot{m}_{\mathrm{s}}, \dot{m}_{\mathrm{c}}^{+}, \dot{m}_{\mathrm{c}}^{-}, \dot{m}_{\mathrm{out}}^{+}, \rho, \mu, L, \Delta p\right) = 0 \tag{3.12}$$

There are 3 physical dimensions mass, length and time. The Buckingham Π theorem [9] states that there should be 5 dimensionless Π groups. Choosing $[\dot{m}_s, \rho, L]$ as the repeating variables produces the following set of Π groups

$$\vec{\Pi} = \left[\frac{\dot{m}_{\mathrm{out}}^{+}}{\dot{m}_{\mathrm{s}}}, \frac{\dot{m}_{\mathrm{c}}^{+}}{\dot{m}_{\mathrm{s}}}, \frac{\dot{m}_{\mathrm{c}}^{-}}{\dot{m}_{\mathrm{s}}}, \frac{\mu L}{\dot{m}_{\mathrm{s}}}, \frac{\Delta p}{\dot{m}_{\mathrm{s}}/\left(\rho L^4\right)}\right] \tag{3.13}$$

If L^2 is chosen to be the supply nozzle cross-sectional area A_{nozz}, then $\Pi_5 = \Delta p/q_{\mathrm{nozz}}$ and $\Pi_4 \propto 1/Re$. Assuming that the flow is fully turbulent and incompressible, and is therefore Reynolds number independent, then the dimensionless characteristics are of the form

$$\frac{\Delta p}{q_{\mathrm{nozz}}} = F\left(\frac{\dot{m}_{\mathrm{out}}^{+}}{\dot{m}_{\mathrm{s}}}, \frac{\dot{m}_{\mathrm{c}}^{+}}{\dot{m}_{\mathrm{s}}}, \frac{\dot{m}_{\mathrm{c}}^{-}}{\dot{m}_{\mathrm{s}}}\right) \tag{3.14}$$

Within the model, these characteristics take the form of 3D lookup tables. For both pilot and SVV diverter sections, there are lookup tables for the control and outlet boundaries. These lookup tables are constructed by applying interpolations to experimental data (section 4.2.2 and 4.3.2).

For the SVV, the switch section and vortex chamber form a single unbroken cavity. Consequently, it is experimentally difficult to accurately measure $\dot{m}_{\mathrm{out}}^{+}$ for the SVV diverter section without disrupting the flow. To overcome this problem, the model uses the approximation $\dot{m}_{\mathrm{out}}^{-} = 0$. It is assumed that all of the flow exits the mixing region through the attached side channel. The SVV geometry is designed such that the diverter section directs most of the supply flow towards one

of the vortex chamber inlets. Minimising $\dot{m}^{-}_{\text{out}}$ ensures that the radial pressure drop across the vortex chamber is maximised in the tangential state and minimised in the radial state. With the $\dot{m}^{-}_{\text{out}} = 0$ approximation, the number of dimensions for the switch section characteristic is reduced by 1. The reduced order SVV switch section characteristics are of the form

$$\frac{\Delta p}{q_{\text{nozz}}} = F\left(\frac{\dot{m}^{+}_{\text{c}}}{\dot{m}_{\text{s}}}, \frac{\dot{m}^{-}_{\text{c}}}{\dot{m}_{\text{s}}}\right) \tag{3.15}$$

The characteristics predict the time-averaged steady-state behaviour, but this model is intended to be used to predict dynamic behaviour as well. The model groups the switch section dynamics into switching (3.4.2) and sub-switching (3.4.1) behaviour. Switching refers to the process by which a wall-attachment device transitions between attachment states, typically in response to some large perturbation at one of the flow boundaries. During a switching event: the jet detaches from the wall, migrates towards the opposite wall, and then re-establishes an attachment flow field. Sub-switching dynamics refers to the response of the attached jet to any boundary condition perturbations that do not trigger switching.

3.4.1 Sub-Switching Dynamics

It is assumed that the sub-switching dynamic behaviour of a diverter switch can be modelled by linear first-order differential equations. The system as a whole is likely non-linear. However, it is assumed that transient deviations from steady-state conditions are small and thus may be linearised. This assumption cannot be applied to switching dynamics (3.4.2). In the language of control theory, a generic non-linear

system can be described by the relations of the form

$$\dot{\mathbf{x}} = \mathbf{f}(\mathbf{x}, \mathbf{u}, \mathbf{t}) \tag{3.16}$$

$$\mathbf{y} = \mathbf{h}(\mathbf{x}, \mathbf{u}, \mathbf{t}) \tag{3.17}$$

where $\mathbf{x}$ is the state vector, $\mathbf{u}$ is the input vector, and $\mathbf{y}$ is the output vector. If the system is assumed to be approximately stationary, i.e. $\mathbf{f}$ and $\mathbf{h}$ do not vary significantly from their initial values at t_0, then

$$\dot{\mathbf{x}} = \mathbf{f}(\mathbf{x}, \mathbf{u}, \mathbf{t_0}) \text{ or } \mathbf{f}(\mathbf{x}, \mathbf{u}) \tag{3.18}$$

$$\mathbf{y} = \mathbf{h}(\mathbf{x}, \mathbf{u}, \mathbf{t_0}) \text{ or } \mathbf{h}(\mathbf{x}, \mathbf{u}) \tag{3.19}$$

If $\mathbf{x_0}, \mathbf{u_0}$ reference steady-state conditions

$$\mathbf{f}(\mathbf{x_0}, \mathbf{u_0}) = \mathbf{0} \tag{3.20}$$

then transient deviations from steady-state conditions are defined as

$$\delta\mathbf{x} = \mathbf{x} - \mathbf{x_0} \tag{3.21}$$

$$\delta\mathbf{u} = \mathbf{u} - \mathbf{u_0} \tag{3.22}$$

$$\delta\mathbf{y} = \mathbf{y} - \mathbf{y_0} \tag{3.23}$$

It can be shown that for sufficiently small deviations [22] that the transients are approximately linear systems and can be expressed in the state-variable form

$$\dot{\delta\mathbf{x}} = \mathbf{A}\delta\mathbf{x} + \mathbf{B}\delta\mathbf{u} \tag{3.24}$$

$$\delta\mathbf{y} = \mathbf{C}\delta\mathbf{x} + \mathbf{D}\delta\mathbf{u} \tag{3.25}$$

If the output δy of the system is 1D, then the system's response to input perturbations is governed by a set of transfer functions $G_i(s)$ where

$$G_i(s) \coloneqq \frac{\mathcal{L}\left[\delta y(t)\right]}{\mathcal{L}\left[\delta \mathbf{u_i}(\mathbf{t})\right]} = \frac{Y(s)}{U(s)} \tag{3.26}$$

Ignoring higher-order effects, it is assumed that a single-pole transfer functions can be used to approximate transient response. A single-pole transfer function can be expressed as

$$G_i(s) = \frac{1}{s\tau + 1} K_i \tag{3.27}$$

where τ is a time constant and elements of the vector $\mathbf{K}$ are system gains that correspond to elements of the input vector $\mathbf{u}$, i.e.

$$K_i = \left.\frac{\partial h}{\partial u_i}\right|_{\mathbf{x_0},\mathbf{u_0}} \tag{3.28}$$

The system response $\delta y(t)$ is given by

$$\begin{aligned} Y(s) &= \sum_i G_i(s) U_i(s) \\ &= \frac{1}{s\tau + 1} \sum_i K_i U_i(s) \end{aligned} \tag{3.29}$$

Expanding the vector product and rearranging produces

$$s \times Y(s) = \frac{1}{\tau}\left[-Y(s) + \sum_i \frac{\partial h}{\partial u_i} U(s)\right] \tag{3.30}$$

Applying an inverse Laplace transform to equation 3.30 returns a first-order differential relation for $y(t)$

$$\frac{d}{dt}\delta y(t) = \frac{dy(t)}{dt} = \frac{1}{\tau}\left[-\delta y(t) + \sum_i \frac{\partial h}{\partial u_i} \delta u_i(t)\right] \tag{3.31}$$

For non-dimensional diverter switch characteristics, where the steady-state mappings are of the form

$$\frac{\Delta p}{q_{\text{nozz}}} = F\left(\frac{\dot{m}_1}{\dot{m}_{\text{s}}}, \frac{\dot{m}_2}{\dot{m}_{\text{s}}}, \dots\right) \tag{3.32}$$

- $h(\mathbf{x}_0, \mathbf{u}_0) \rightarrow F$
- $y \rightarrow \Delta p / q_{\text{nozz}}$
- $\delta y \rightarrow \Delta p / q_{\text{nozz}} - F$
- $u_i \rightarrow \dot{m}_i / \dot{m}_{\text{s}}$

and equation 3.31 becomes

$$\frac{d}{dt}\left(\frac{\Delta p}{q_{\text{nozz}}}\right) = \frac{1}{\tau}\left[-\left(\frac{\Delta p}{q_{\text{nozz}}} - F\bigg|_{t_0}\right) + \sum_i \frac{\partial F}{\partial(\dot{m}_i/\dot{m}_{\text{s}})}\left(\frac{\dot{m}_i}{\dot{m}_{\text{s}}} - \frac{\dot{m}_i}{\dot{m}_{\text{s}}}\bigg|_{t_0}\right)\right] \tag{3.33}$$

where the t_0 subscript indicates the previous numerical time-step value. The values of F and τ come from lookup tables populated by experimental data (see section 4.2.4).

3.4.2 Switching Dynamics

Unlike the sub-switching dynamics, switching events result in dramatic non-linear changes in flow properties. The exact physical mechanisms that drive a switching event is still an active research area [57, 69]. Once again, the internal fluid dynamics of the switches are not modelled directly here. Instead, in the model, once a switching event has been triggered, the state of the diverter switch evolves smoothly from one state to the other in a finite time t_{sw}.

The model switching process is initiated when the dimensionless mass flow rate $\dot{m}_{\text{c}}^{+}/\dot{m}_{\text{s}}$ exceeds a threshold determined by experimental observation (see section

4.2.3). The switching times t_{sw} are functions of $\dot{m}_{\mathrm{s}}$ and $\dot{m}_{\mathrm{c}}^{+}$ and are likewise supplied to the numerical model in the form of a lookup table populated by experimental data, see sections 4.2.4 and 4.3.3.

In the model, each diverter section has a state variable α representing the attachment state of the diverter. The attachment walls of the diverter are arbitrarily labelled 0 and 1. If the jet is fully attached to wall 0, $\alpha = 0$ and when it is fully attached to wall 1, $\alpha = 1$. When the model's switching threshold is crossed, the state variable follows a normalised sigmoid function from its current state to the opposite state i.e.

$$\alpha = \frac{1}{1 + e^{\mp a(t-c)}} \tag{3.34}$$

The sigmoid function is chosen in the absence of an exact physical model for how a jet migrates from one attachment wall to the other. The sigmoid parameters a and c are chosen such that α goes from 0.001 to 0.999 or vice versa in t_{sw} seconds. The switching time t_{sw}, as with the sub-switching response time τ, is determined by experimental observations (see sections 4.2.4 and 4.3.3). When in an indeterminate state ($0 < \alpha < 1$), the steady-state characteristic maps used by relations of the form equation 3.33 are weighted mixtures. Given a pressure difference characteristic of the form

$$\frac{\Delta p}{q_{\mathrm{nozz}}} = F\left(\frac{\dot{m}_{\mathrm{out}}^{+}}{\dot{m}_{\mathrm{s}}}, \frac{\dot{m}_{\mathrm{c}}^{+}}{\dot{m}_{\mathrm{s}}}, \frac{\dot{m}_{\mathrm{c}}^{-}}{\dot{m}_{\mathrm{s}}}\right) \tag{3.35}$$

the value of F passed to equation 3.33 is given by

$$F_{\mathrm{mix}} = (1-\alpha) \times F\left(\frac{\dot{m}_{\mathrm{out},1}}{\dot{m}_{\mathrm{s}}}, \frac{\dot{m}_{\mathrm{c},1}}{\dot{m}_{\mathrm{s}}}, \frac{\dot{m}_{\mathrm{c},2}}{\dot{m}_{\mathrm{s}}})\right) + \alpha \times F\left(\frac{\dot{m}_{\mathrm{out},2}}{\dot{m}_{\mathrm{s}}}, \frac{\dot{m}_{\mathrm{c},2}}{\dot{m}_{\mathrm{s}}}, \frac{\dot{m}_{\mathrm{c},1}}{\dot{m}_{\mathrm{s}}})\right) \tag{3.36}$$

3.5 Vortex Chamber Modelling

The vortex chamber is treated similarly to the switch section (section 3.4), with the steady-state non-dimensionalised pressure drop being characterised by non-dimensionalised mass flow rates. In this case, there are 3 flow boundaries, which reduces to 2 when using the $\dot{m}^{-}_{\text{out}} = 0$ approximation.

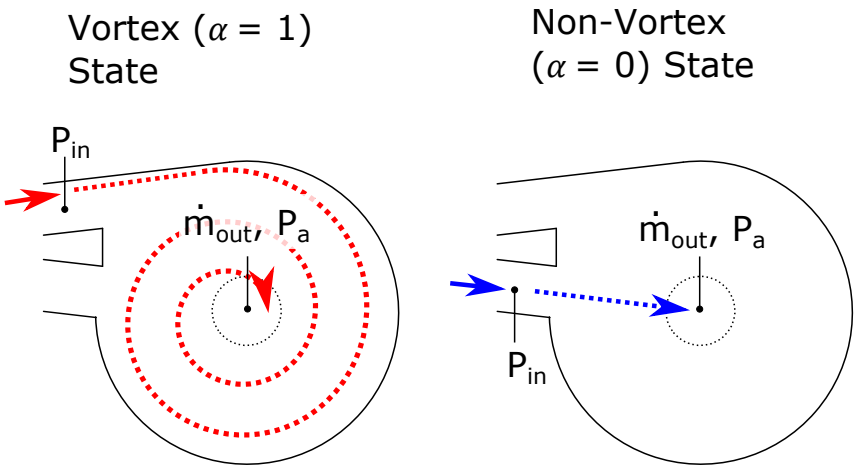

Fig. 3.9 Map of locations of key mass flows and pressures used to characterise a vortex chamber.

Using the same dimensional arguments as laid out in section 3.4 it might be expected that vortex chamber characteristics would be of the form

$$\frac{\Delta p}{q_{\text{vx}}} = F\left(Re, \alpha\right) \tag{3.37}$$

where q_{vx} is the dynamic head of the vortex outlet port and α is the state parameter for the vortex chamber. This parameter determines the vortex state of the vortex chamber. When the SVV is not switching, $\alpha = 1$ and $\alpha = 0$ correspond to the tangential and radial states, respectively. Attachment wall 1 for the switch section corresponds to the tangential inlet port for the vortex chamber. Consequently, the vortex chamber value of α and the SVV diverter section value of α are the same under steady-state conditions. However, the switching process

for the SVV diverter section and vortex chamber can be non-synchronous, with the vortex chamber having a different switching time from that of the diverter section.

Unlike the diverter sections, Reynolds number independence cannot be assumed because viscous forces are very influential for the vortex chamber. Large scale vortices are formed in both the radial and tangential states. The vortices will exhibit approximately inviscid flows at larger radii, with circumfrential flow velocities increasing when traversing radially towards the vortex centre. However, within a core region ($r < R_c$) of each vortex, viscous shear forces dominate. It has been argued by Vatistas [108, 107] that for a vortex chamber in a vortex state similar to that of the tangential state, the vortex core size and the dimensionless pressure drop across the vortex chamber are both entirely functions of the vortex chamber geometry. However, a more recent study by Kulkarni et al. [51] presents experimental data that contradicts Vatistas' conclusions. Kulkarni et al. [51] show that the non-dimensional pressure drop across a vortex diode in the vortex state does have a strong Reynolds number dependence. These studies are discussed in more detail in section 2.2.1.

It has been observed experimentally (section 4.3.4) that the vortex chamber studied here does exhibit some Reynolds number dependence in both the radial and tangential states. Furthermore, it is shown in section 4.3.4 that the vortex chamber is sensitive to the flow profile at its inlet boundary. The flow velocity profile at the vortex chamber inlets is linked directly to the switch section jet position, which is influenced by the SVV control mass flow rates $\dot{m}_c^{\pm}$. Consequently, the non-dimensionalised vortex chamber characteristics are expanded to include the switch section's non-dimensionalised control mass flow rates, i.e.

$$\frac{\Delta p}{q_{vx}} = F\left(\frac{\dot{m}_c^+}{\dot{m}_s}, \frac{\dot{m}_c^-}{\dot{m}_s}, Re, \alpha\right) \tag{3.38}$$

To model sub-switching behaviour, the switch section and the vortex chamber are treated as a single unit with one response time τ. However, asynchronous behaviour has been observed for switching events (section 4.3.3), where the pressure difference across the vortex chamber responds more slowly to a switching signal than the SVV diverter section does. Therefore, the SVV diverter and vortex chamber sections are treated as separate entities for switching dynamics, with their own switching times and flow state variables.

The method used to model the vortex chamber switching process is nearly identical to that used for the diverter sections. The state variable α is driven by a sigmoid function with a time constant equal to the vortex chamber switching time from 0.001 to 0.999 or vice versa. The vortex pressure difference coefficient of the intermediate state is given by

$$\frac{\Delta p_{\mathrm{vx}}}{q_{\mathrm{vx}}} = \alpha \times F\left(\ldots, \alpha = 0\right) + (1 - \alpha) \times F\left(\ldots, \alpha = 1, \right) \tag{3.39}$$

3.6 Summary

This chapter has presented the structure for a numerical model of a staged SVV. The model is designed to simulate the steady-state and dynamic behaviours of the staged SVV. It conceptually subdivides the model into ducts, diverter sections and a vortex chamber. The ducts are modelled using discretised versions of the Navier-Stokes momentum and the continuity equation, whilst the switch sections and vortex chamber are treated as black-box objects. The steady-state behaviour of the switch sections and vortex chamber are described by steady-state characteristics that map the boundary pressures to mass flow rates. The dynamics of these black-box objects are parametrised by characteristic response and switching times. The steady-state characteristics, response times, switching times and switching boundaries are all

tuning parameters determined by experimental data.

Chapter 4
Characterisation of the Staged Switched Vortex Valve

4.1 Introduction

The model presented in chapter 3 requires tuning data, namely steady-state characteristics, switching boundaries, response times, and switching times. These were acquired by direct measurement with physical devices, specifically a diverter pilot and an SVV. The physical devices have been built separately but were designed to be assembled into a staged SVV for later validation of the completed model (chapter 5).

4.2 Diverter Pilot Stage

4.2.1 Device Construction

The diverter pilot stage (figure 4.1) was designed around a 1:2 scaled version of the SVV diverter section geometry (section 4.3). The physical device was constructed from 3D-printed components. Each component was printed out of clear SLA resin using a Formlab Form 2 printer with a layer resolution of 25 µm. The components were bolted together with o-ring seals at the interfaces.

Static pressures were acquired using First Sensor HCX series pressure transducers. A list of the pressure transducers used for all pressure measurements in this thesis

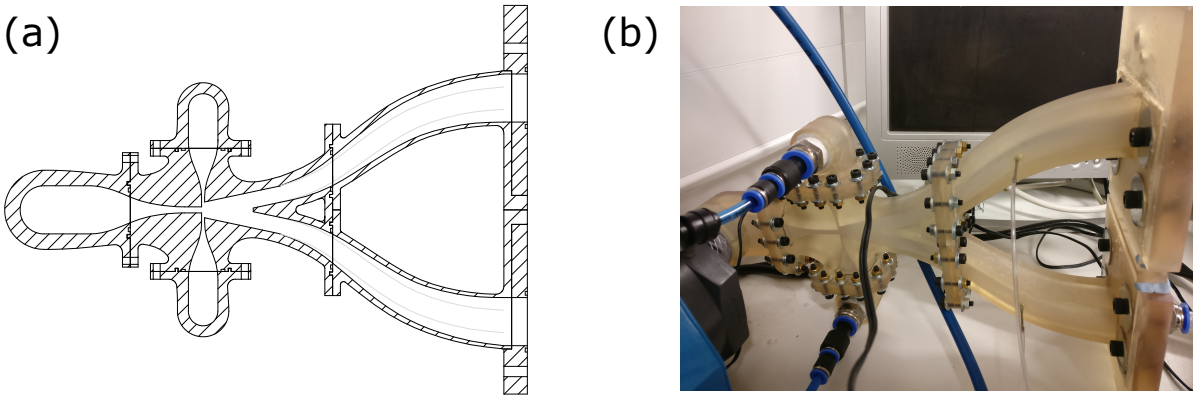

Fig. 4.1 Diverter pilot stage, a 2D slice (a) and a photo (b) of the constructed device

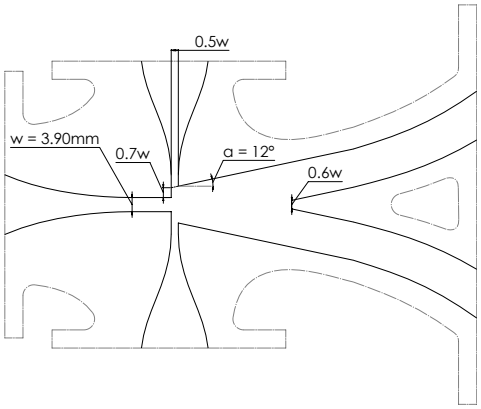

Fig. 4.2 Planar schematic of the pilot's diverter switch section (cavity depth = 20 mm)

is presented in table 4.1. The pressure transducers used for any given pressure measurement were chosen on a case by case basis. Typically, the pressure transducer chosen would have the smallest range possible without allowing the measured pressure to exceed the pressure transducer's range in order to minimise measurement uncertainties.

The pressure transducers were connected to 1.65 mm static pressure tappings drilled into the end walls of the pilot stage. The locations of the static pressure tappings are marked in figure 4.3.

Sensor Name	Range (mbar)	Accuracy (% FSO)
HCXPM005D6	-5 − 5	0.5
HCXPM010D6	-10 − 10	0.5
HCXM050D6	0 − 50	0.5
HCXM100D6	0 − 100	0.5
HCXM350D6	0 − 350	0.5
HCX001D6V	0 − 1000	0.5
HCX002D6V	0 − 2000	0.5

Table 4.1 List of First Sensor HCX series pressure transducers used for pressure measurements [93]

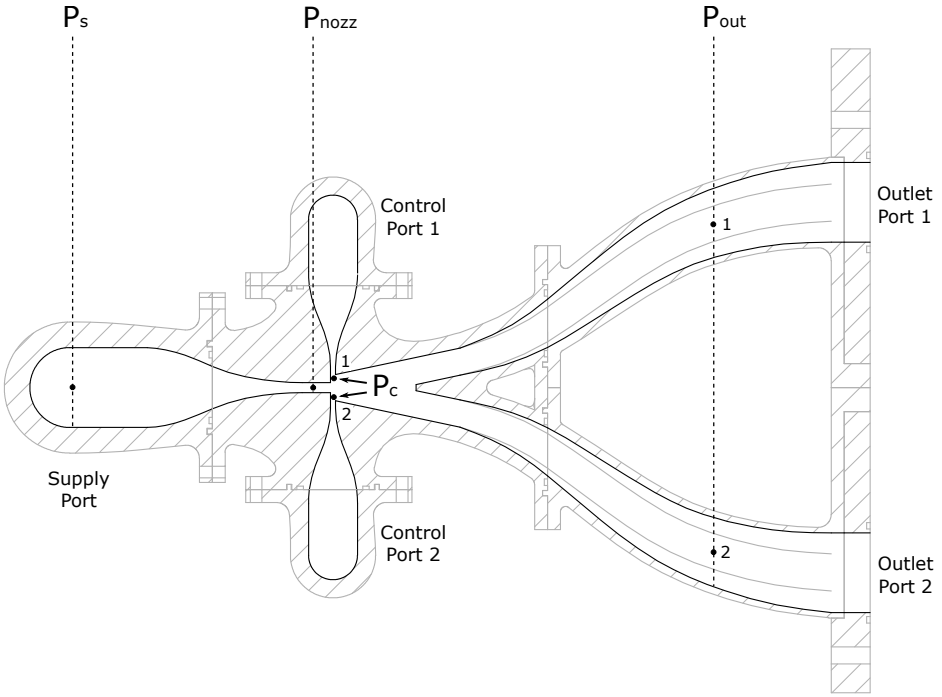

Fig. 4.3 Static pressure tapping locations

4.2.2 Switch Section Steady-State Characteristics

The experimental setup used to measure the steady-state characteristics of the pilot diverter section is presented as a circuit diagram in figure 4.4.

The orifice meters used to measure the supply and attached outlet flow rates ($\dot{m}_\mathrm{s}$, $\dot{m}^+_\mathrm{out}$) conform to ISO 5167-2 [3]. The orifice diameters are $12.81 \pm 0.05\,\mathrm{mm}$, and the pipe diameters are $28.6 \pm 0.02\,\mathrm{mm}$, so the diameter ratio $\beta = d/D = 0.4479$.

The mass flow rates are given by the equation

$$\dot{m} = \frac{C_{\mathrm{D}}}{\sqrt{1-\beta^4}} \epsilon \frac{\pi}{4} d^2 \sqrt{2\Delta p \rho_1} \tag{4.1}$$

and the associated measurement uncertainties are given by the practical working formula presented [39] as

$$\frac{\delta \dot{m}}{\dot{m}} = \sqrt{\left(\frac{\delta C_{\mathrm{D}}}{C_{\mathrm{D}}}\right)^2 + \left(\frac{\delta \epsilon}{\epsilon}\right)^2 + \left(\frac{2\beta^4}{1-\beta^4}\right)^2 \left(\frac{\delta D}{D}\right)^2 + \left(\frac{2}{1-\beta^4}\right)^2 \left(\frac{\delta d}{d}\right)^2 + \frac{1}{4}\left(\frac{\delta \Delta p}{\Delta p}\right)^2 + \frac{1}{4}\left(\frac{\delta \rho_1}{\rho_1}\right)^2} \tag{4.2}$$

where

- C_{D} is the orifice discharge coefficient and the relative uncertainty is

$$0.5 + 0.9\,(0.75 - \beta)\left(2.8 - \frac{D}{25.4}\right)\% \approx 1\% \tag{4.3}$$

- ϵ is the expansibility factor and the relative uncertainty is

$$3.5\frac{\Delta p}{\gamma p_1}\% \tag{4.4}$$

- $\Delta p = p_1 - p_2$ is the measured pressure difference across the plate measured with HCX series pressure transducers with an associated measurement uncertainty of 0.5%FSO [93]

- ρ_1 is the flow density upstream of the plate. ρ_1 is calculated using a combination of temprature, measured using a K-type thermocouple, and the upstream pressure p_1, measured using a second HCX series pressure transducer

For both orifice meters, the length of pipe upstream of the orifice plate exceeds $30D$, and the downstream pipe length exceeds $6D$. Therefore, according to table 3 in [3], there is not an additional 0.5% uncertainty for mass flow measurements associated with shorter orifice meter setups.

Omega FMA-A2323 mass flow meters were used to measure the control flow rates ($\dot{m}_c^+$, $\dot{m}_c^-$). Mass flow parameters were altered using variable impedances and regulator pressures. Pressures labelled p_s, p_c and p_{out} correspond to pressure tappings marked in figure 4.3. The '+' and '−' superscripts correspond to the attached and unattached sides of the device, respectively.

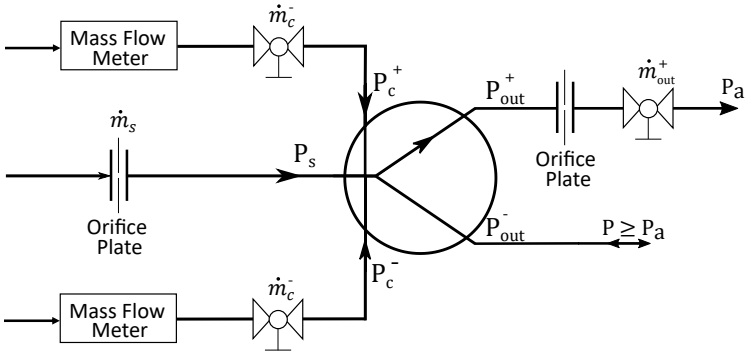

Fig. 4.4 Setup for measurement of pilot diverter section characteristics

To construct 3D characteristics of the form

$$\frac{\Delta p}{q_{nozz}} = F\left(\frac{\dot{m}_{out}^+}{\dot{m}_s}, \frac{\dot{m}_c^+}{\dot{m}_s}, \frac{\dot{m}_c^-}{\dot{m}_s}\right) \tag{4.5}$$

pressure differences $\Delta p_c^{\pm}$ and $\Delta p_{out}^{\pm}$ were recorded at approximately regular intervals within a 3D domain of dimensionless mass flow rates

$$0 \lesssim \frac{\dot{m}_{out}^+}{\dot{m}_s} \lesssim 1.5 \tag{4.6}$$

$$-0.15 \lesssim \frac{\dot{m}_c^+}{\dot{m}_s} \lesssim 0.15 \tag{4.7}$$

$$-0.15 \lesssim \frac{\dot{m}_c^+}{\dot{m}_s} \lesssim 0.15 \tag{4.8}$$

The Matlab function **griddatan** was then used to apply a 3D linear interpolation to the 3D dataset to produce regular grids of $\Delta p/q$ values used to populate the model's characteristic lookup tables.

In section 3.4, it was assumed that if diverter section flows are incompressible and fully turbulent, then the Reynolds number parameter could be discarded. This assumption was checked for the case of the pilot diverter section using three sets of characteristics constructed from measurements recorded for three different supply flow rates 0.99 g/s, 1.98 g/s, and 3.97 g/s. These flow rates span the range of pilot flow rates tested as part of the staged SVV setup (chapter 5). At these flow rates, the Reynolds numbers (calculated using the pilot nozzle hydraulic diameter) are 4600, 9200 and 18000. Conventionally, for fully developed flow in a duct, the flows are considered to be transitional for $Re = 2000 - 5000$ and fully turbulent for $Re > 5000$. Thus, diverter pilot flows are either in or close to the fully turbulent flow regime. Furthermore, since the maximum pilot nozzle Mach number is 0.13 ($\dot{m}_\mathrm{s} = 3.97\,\mathrm{g/s}$), flows are also in the incompressible flow regime.

The model has four characteristic lookup tables for the pilot diverter switch section, and these represent the 3D characteristics $\Delta p^+_\mathrm{out}/q_\mathrm{nozz}$, $\Delta p^-_\mathrm{out}/q_\mathrm{nozz}$, $\Delta p^+_\mathrm{c}/q_\mathrm{nozz}$ and $\Delta p^-_\mathrm{c}/q_\mathrm{nozz}$. In the model, it is simpler to use a single reference pressure p_nozz, as only p_nozz and q_nozz are then needed to convert all four characteristics to dimensional boundary pressures. It is difficult to apply physical interpretations to these parameters. However, they can be converted into $\Delta p_\mathrm{out}/q_\mathrm{nozz}$ and $\Delta p_\mathrm{c}/q_\mathrm{nozz}$ characteristics trivially

$$\frac{\Delta p_\mathrm{out}}{q_\mathrm{nozz}} = \frac{p^+_\mathrm{out} - p^-_\mathrm{out}}{q_\mathrm{nozz}} = \frac{\Delta p^-_\mathrm{out}}{q_\mathrm{nozz}} - \frac{\Delta p^+_\mathrm{out}}{q_\mathrm{nozz}} \tag{4.9}$$

$$\frac{\Delta p_\mathrm{c}}{q_\mathrm{nozz}} = \frac{p^+_\mathrm{c} - p^-_\mathrm{c}}{q_\mathrm{nozz}} = \frac{\Delta p^-_\mathrm{c}}{q_\mathrm{nozz}} - \frac{\Delta p^+_\mathrm{c}}{q_\mathrm{nozz}} \tag{4.10}$$

$$\tag{4.11}$$

Δp_out is the pressure difference across the outlets. For the pilot stage in isolation, Δp_out is created by pressure losses at the outlets. When incorporated into the 2-stage device, Δp_out is imposed by the control pressures of the SVV. When Δp_out is positive,

an adverse pressure gradient is being applied across the outlets that opposes wall attachment. Conversely, a negative Δp_{out} indicates a sympathetic outlet pressure gradient that strengthens the attachment state.

Δp_{c} is the pressure difference across the jet, with the p_{c}^{+} tapping sitting inside the recirculation bubble. Δp_{c} is an indirect measure of the jet curvature. As discussed in section 2.1, analytical models of steady-state attachment [5, 90, 91, 53, 12] use the Euler particle equation to link the pressure difference across the jet to the radius of curvature R, with

$$|\Delta p_{\text{c}}| = \frac{J}{R} \tag{4.12}$$

where J is the supply jet momentum. The pressure difference across the jet provides the centripetal force required for the attached jet to maintain a circular shape. Generally, a large negative Δp_{c} indicates a jet that is strongly attached.

2D slices of the Δp_{out} and the Δp_{c} characteristics are presented in figure 4.5 and 4.6. The plotted surfaces are slices of the 3D interpolation used to populate the characteristic lookup tables. The scatter data points of figures 4.5(a) and figure 4.6(a) are $\dot{m}_{\text{c}}^{-}/\dot{m}_{\text{s}}$ subsets of the experimental data used to construct the 3D interpolations. Note that the shapes of these characteristics are primarily functions of the conditions at the attached outlet port ($\dot{m}_{\text{out}}^{+}/\dot{m}_{\text{s}}$) and the attached control port ($\dot{m}_{\text{c}}^{+}/\dot{m}_{\text{s}}$). The shapes of these curves do not vary much when altering either $\dot{m}_{\text{s}}$ (figures 4.5(c) and 4.6(c)) or $\dot{m}_{\text{out}}^{-}$ (figures 4.5(b) and 4.6(b)), although, as will be discussed in section 4.2.3, conditions at the unattached control port do have a significant impact upon the switch stability. $\dot{m}_{\text{s}}$ does not have any significant effect, which shows that the influence of Reynolds number is small.

It is possible to acquire some insight into the diverter section's behaviour for various boundary conditions by focusing upon the exact shape of the Δp_{out} and the

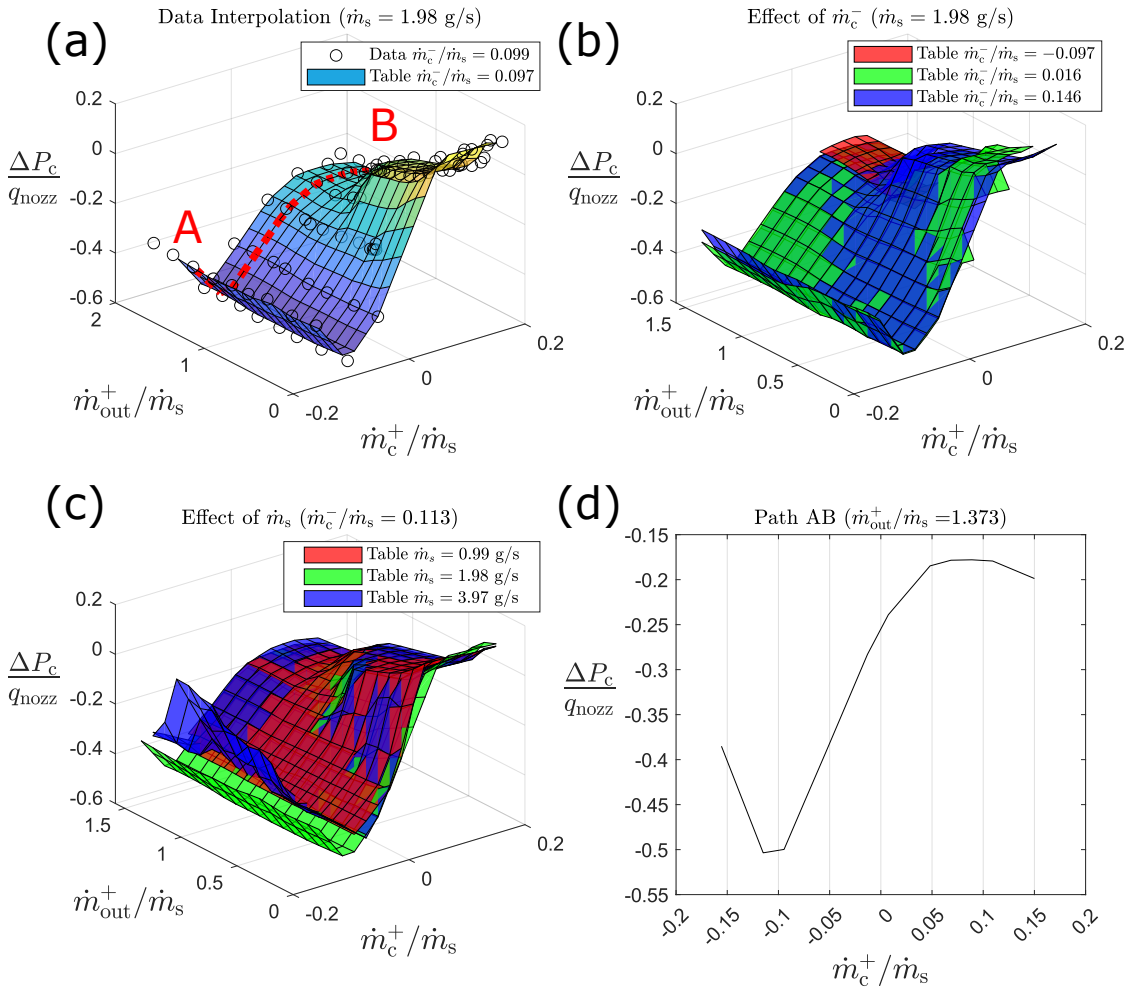

Fig. 4.5 $\dot{m}_c^-/\dot{m}_s$ = constant slices of $\Delta p_c/q_{nozz}$ lookup table.

Δp_c characteristics.

Starting with Δp_c, the dominant parameter affecting the jet pressure difference across the jet is $\dot{m}_c^+$. It might be expected that both $\dot{m}_c^+$ and $\dot{m}_c^-$ could influence the supply jet curvature and position. However, since $\dot{m}_c^-$ has little effect on the shape of either set of characteristics, it is clear that jet position and curvature are dominated by interactions between the jet, the attached side recirculation bubble and $\dot{m}_c^+$.

Consider the curve AB on figures 4.5(a) and (d). This $\dot{m}_{out}^+/\dot{m}_s = 1.373$ slice of the characteristic is positioned close to the upper limit of $\dot{m}_{out}^+/\dot{m}_s$. At high

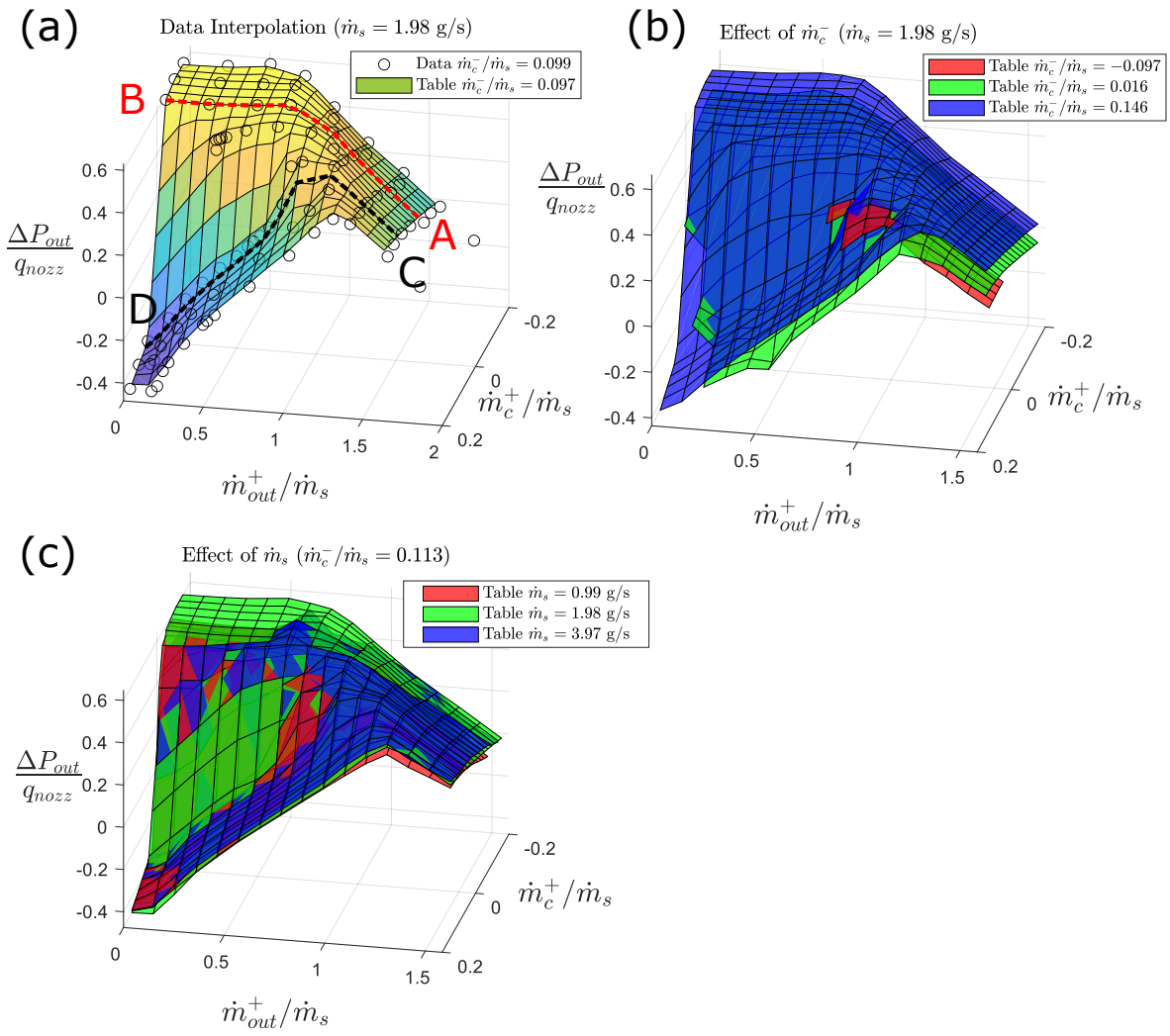

Fig. 4.6 $\dot{m}_c^-/\dot{m}_s$ = constant slices of $\Delta p_{out}/q_{nozz}$ lookup table.

$\dot{m}_{out}^+/\dot{m}_s$ values, the pilot stage's outlets are comparatively unrestricted, and the characteristic shapes are almost entirely dominated by $\dot{m}_c^+$. Generally, it is expected that negative $\dot{m}_c^+$ will shrink the recirculation bubble and increase jet curvature, whilst positive $\dot{m}_c^+$ will enlarge the recirculation bubble and reduce jet curvature. Assuming that jet curvature is driven by the pressure difference Δp_c, it might be expected that Δp_c would increase monotonically with $\dot{m}_c^+$. However, this is only the case for $-0.1 \lesssim \dot{m}_c^+/\dot{m}_s \lesssim 0.05$. It is theorised that for $\dot{m}_c^+/\dot{m}_s < -0.1$, the recirculation bubble has shrunk to the point where it vanishes (figure 4.7), and the p_c^+ tapping is measuring the jet pressure rather than an recirculation bubble pressure. The jet pressure is significantly larger than the bubble pressure, which would explain

the sharp rise in Δp_c observed at this lower boundary.

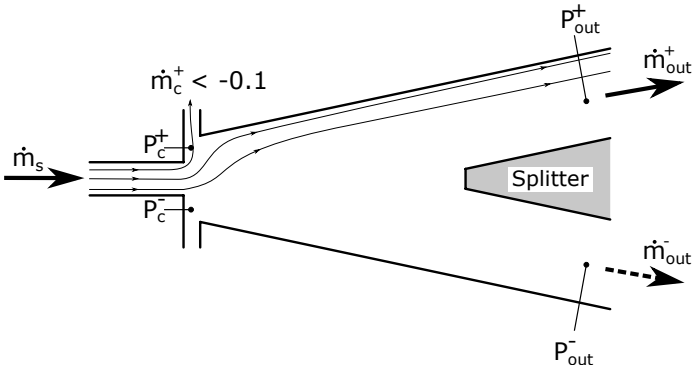

Fig. 4.7 Schematic of diverter section flow field for $\dot{m}_c^+/\dot{m}_s$ < -0.1.

It is also theorised that for $\dot{m}_c^+/\dot{m}_s > 0.05$ (figure 4.5(d)), the assumption that pressure is uniform over the entire recirculation bubble cannot be applied at the p_c^+ tapping. The p_c^+ tapping is located directly in the flow path of the $\dot{m}_c^+$ jet (figure 4.8). The control jet impinges upon the supply jet, imparting most of its momentum to the supply jet. However, upstream of the impingement point, the control jet flow velocities will ensure a local region of low static pressure around the p_c^+ tapping. At higher $\dot{m}_c^+$ values, this local pressure drop could counteract the more general rise in recirculation bubble pressure as the bubble size increases.

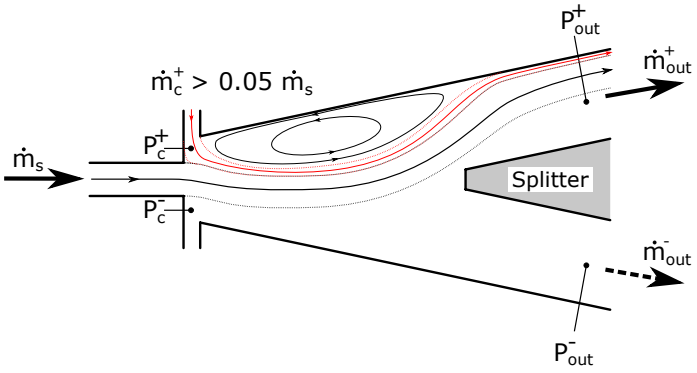

Fig. 4.8 Schematic of diverter section flow field for $\dot{m}_c^+/\dot{m}_s > 0.5$

Experimentally $\dot{m}_{out}^+/\dot{m}_s$ was changed by modifying the outlet impedance of the pilot stage by introducing a restriction at the attached outlet port. Data were

recorded at fixed $\dot{m}_c^+$ values while increasing the attached side outlet impedance until the diverter section switched or the outlet port was blocked entirely. Looking again at the figure 4.5(a), it is clear that the surface only deviates from the curve AB for $\dot{m}_c^+ > 0$ and $\dot{m}_{out}^+/\dot{m}_s < 1.25$. In other words, outlet constrictions only affect jet curvature when control flows have weakened wall attachment strength. This is consistent with the effect of outlet constrictions described by Kirshner [46]. Kirshner states that higher pressures in the reattachment region insulate the recirculation bubble from pressure rises associated with outlet port constrictions. Kirshner also states that introducing positive $\dot{m}_c^+$ will enlarge the recirculation bubble and lower the reattachment region pressures, thereby allowing the recirculation bubble to be influenced by downstream pressures.

The shape of the Δp_{out} characteristics figure 4.6 also requires some interpretation. The most notable feature is a sharp transition between positive and negative $\dot{m}_c^+$ operating points for $\dot{m}_{out}^+/\dot{m}_s < 1.25$. To understand the Δp_{out} curves better requires some understanding of how the outlet mass flow split is modified and how this affects the outlet pressures p_{out}^+ and p_{out}^-. Generally, for unrestricted outlet ports exhausting to atmosphere, the pilot diverter section naturally operates in the reverse flow state ($\dot{m}_{out}^- < 0$). The negative $\dot{m}_{out}^-$ is driven by entrainment at the unattached side shear layer of the jet. Given fixed supply $\dot{m}_s$ and control $\dot{m}_c^+$ flow rates, the outlet mass flow split is reduced by imposing a restriction at the attached side outlet, partially blocking $\dot{m}_{out}^+$ flows. The pressure drop across the restriction increases p_{out}^+, and by extension, increases Δp_{out}. However, as $\dot{m}_{out}^+$ is reduced by further tightening the outlet restriction, the fraction of the supply flow dynamic head recovered as static pressure in the attached duct decreases. Furthermore, for $\dot{m}_{out}^+/\dot{m}_s < 1$, a portion of the supply flow spills over into the unattached duct, and the resulting pressure recovery raises the pressure at p_{out}^-. Consequently, changes in the fraction of the supply dynamic head recovered as static pressure at both p_{out}^+ and p_{out}^- counteracts

the Δp_{out} increase due to the attached side restriction.

For $\dot{m}_{\text{c}}^{+} < 0$, (see path AB in figure 4.6(a)) the control flows have a stabilising effect on jet attachment, tighter attached side restrictions are therefore required to achieve a given $\dot{m}_{\text{out}}/\dot{m}_{\text{s}}$. However, changes in the pressure recovery contributions to Δp_{out} does flatten out the Δp_{out} curve at low $\dot{m}_{\text{out}}/\dot{m}_{\text{s}}$ values.

For $\dot{m}_{\text{c}}^{+} > 0$, (see path CD in figure 4.6(a)) the control flows have a destabilising effect on jet attachment. Therefore, $\dot{m}_{\text{out}}/\dot{m}_{\text{s}}$ is more sensitive to the attached outlet boundary conditions. A relatively small reduction in the outlet restriction size results in a much larger $\dot{m}_{\text{out}}/\dot{m}_{\text{s}}$ reduction. Thus for $\dot{m}_{\text{out}}^{+}/\dot{m}_{\text{s}} < 1.25$, the effect of pressure recovery contributions to Δp_{out} outweigh pressure losses associated with the outlet restriction. Consequently, tightening the outlet restriction reduces Δp_{out}.

4.2.3 Switching Boundaries

Generally speaking, it is possible to push the pilot diverter section from one attachment state to the other through a combination of outlet back pressures/restrictions and control flow rates $\dot{m}_{\text{c}}^{\pm}$. However, the evolution between attachment states can look very different depending on the choice of control flow rates, see figures 4.9 and 4.10. In the examples presented, the control flow rates are fixed whilst outlet constrictions are adjusted. If $\dot{m}_{\text{c}}^{-} < 0$, the device switches in what is considered to be a typical manner, with a sharp non-linear transition between attachment states. Note that there is hysteresis around the switching point with this sharp switching. However, if $\dot{m}_{\text{c}}^{-} > 0$, the switching process transforms into a quasi-steady reversible process.

This transformation to a quasi-steady switching process happens because $\dot{m}_{\text{c}}^{-} > 0$ control signals stabilise the diverter section by disrupting the unsteady switching

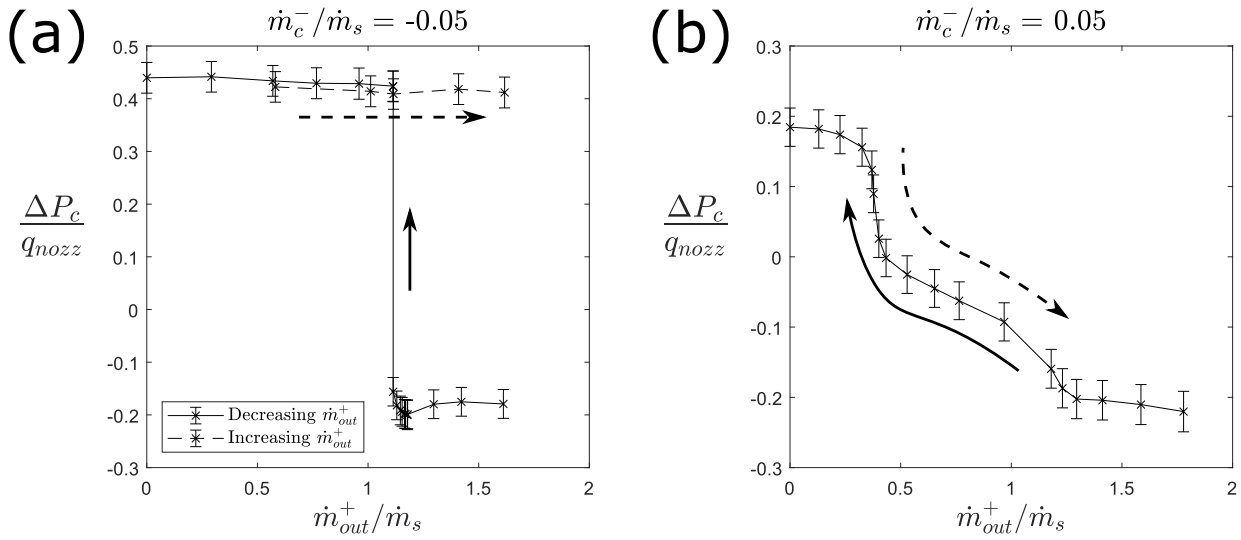

Fig. 4.9 Examples of observed switching behaviour for $\dot{m}_\mathrm{s} = 1.98\,\mathrm{g/s}$ ($\dot{m}_\mathrm{c}^+/\dot{m}_\mathrm{s} = 0.16$)

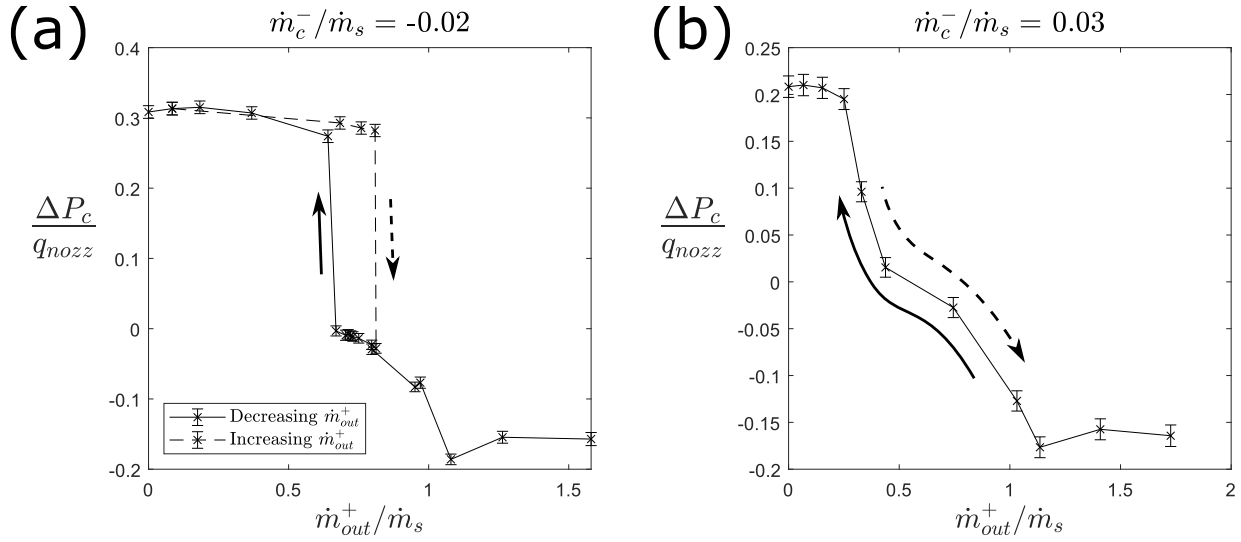

Fig. 4.10 Examples of observed switching behaviour for $\dot{m}_\mathrm{s} = 3.97\,\mathrm{g/s}$ ($\dot{m}_\mathrm{c}^+/\dot{m}_\mathrm{s} = 0.11$)

process. The unsteady switching process for a diverter can take on a few different forms (see section 2.1.1), but for the diverter geometry presented here, the switching process triggered by jet-splitter interactions is expected. This particular switching process follows the following steps. Control flows introduced at the attached side of the diverter ($\dot{m}_\mathrm{c}^+ > 0$) will force the recirculation bubble to grow in size until the jet starts to impinge upon the splitter. Jet-splitter interactions destabilise attachment, and the transverse momentum of the $\dot{m}_\mathrm{c}^+$ control jet pushes the supply

jet towards the opposite side of the diverter. As the supply jet approaches the opposite wall, p_c^- drops due to flow entrainment, a new recirculation bubble starts to form and the jet will attach itself to what was once the unattached side of the diverter.

If $\dot{m}_c^- > 0$, then unattached side control flows disrupt the unsteady switching process in a couple of ways. Firstly, the transverse momentum of the $\dot{m}_c^-$ jet will directly oppose that of the $\dot{m}_c^+$ jet. Consequently, under circumstances where jet-splitter interactions would ordinarily destabilise attachment allowing it to be pushed by the $\dot{m}_c^+$ jet towards the opposite attachment wall, the supply jet position may be fixed by the momentum of opposing control jets. Secondly, $\dot{m}_c^- > 0$ flows will supply entrainment on the unattached side of the supply jet. So even as the jet is pushed closer to the unattached wall by the $\dot{m}_c^+$ jet, p_c^- will not drop as quickly as it would if $\dot{m}_c^- \leq 0$, inhibiting the formation of a new recirculation bubble.

Over the range of operating points that were tested, the existence of a sharp switching threshold depended less upon the magnitude of control flow rates than the sign. Figure 4.11 presents a map of the $\dot{m}_c^{\pm}/\dot{m}_s$ states tested, with the marker symbol indicating whether or not a sharp switching threshold with hysteresis was observed[1]. The unsteady switching process was only observed for $\dot{m}_c^+ \approx 0$ or for operating points in the lower right quadrant ($\dot{m}_c^+ \geq 0, \dot{m}_c^- \leq 0$).

Regarding the model, if the device is in the lower right quadrant or $\dot{m}_c^+ = 0$ and it crosses a switching threshold, then the pilot diverter section will start switching in accordance to the mechanism laid out in section 3.4.2. The switching thresholds are constructed by following curves similar to those plotted in figures 4.9(a) and 4.10(a) from right to left and selecting the last stable value of $\dot{m}_{out}^+/\dot{m}_s$ before the device

[1]If a version of the staged SVV is to be used in a real engine, then the mass flow control ports are either going to be connected to an additional diverter stage or a pressure source greater than that within the pilot stage cavity. In either scenario it seems unlikely that both control flow rates would be negative. Consequently, the $\dot{m}_c^+ < 0, \dot{m}_c^- < 0$ quadrant was not explored.

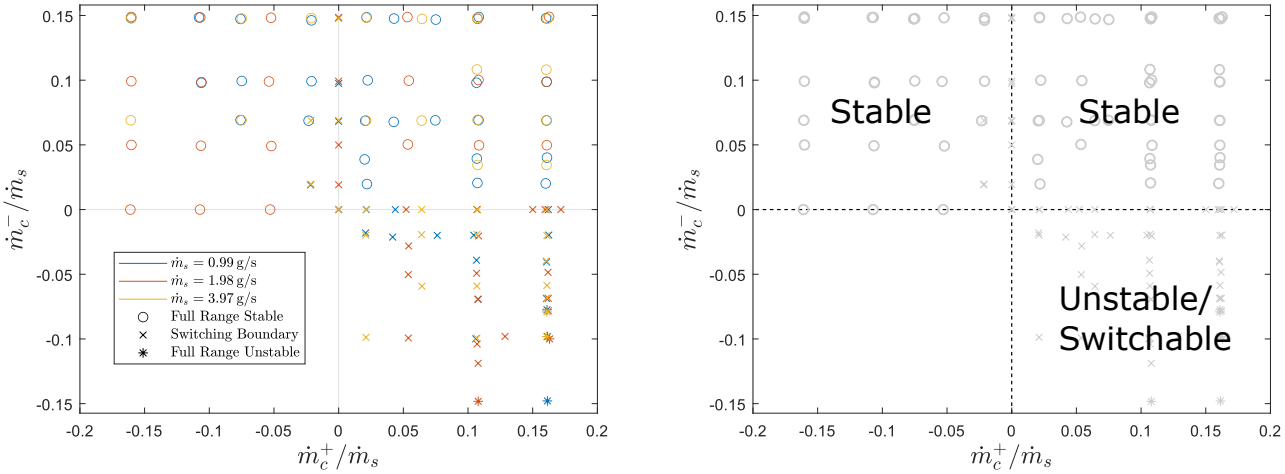

Fig. 4.11 Observed switching behaviour for range of $\dot{m}_c^{\pm}/\dot{m}_s$ values tested.

switches. Figures 4.12 and 4.13 present the switching boundary points observed alongside the linear interpolated points used to populate the switching boundary lookup tables in the model. The diverter switches when $\dot{m}_{out}^{+}/\dot{m}_s$ drops below the switching threshold value. The switching boundaries are largely unaffected by the dimensional $\dot{m}_s$ and are functions of the dimensionless $\dot{m}_c^{\pm}/\dot{m}_s$. In general, the stability boundary trends seem to agree with what might be expected. In the lower right quadrant, the device is destabilised, i.e. the $\dot{m}_{out}^{+}/\dot{m}_s$ threshold rises, if suction from the unattached side $\dot{m}_c^- < 0$ increases and or the recirculation bubble is further weakened by increasing $\dot{m}_c^+ > 0$. Increasing unattached side control flows for the $\dot{m}_c^+ = 0$ boundary ($\dot{m}_c^- > 0$) stabilises the device by both supplying unattached side entrainment and by imparting transverse momentum to the supply jet, deflecting it towards the attached side of the diverter section.

However, if the device is outside these two domains, then the model treats the transition between states as a sub-switching process. Under these circumstances, the state of the pilot diverter section α_p is tied directly to the outlet mass flow split, i.e.

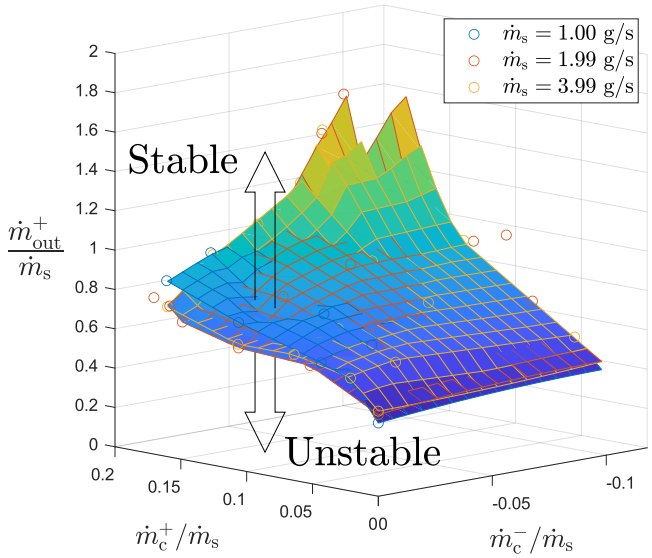

Fig. 4.12 Pilot diverter section switching boundary for $\dot{m}_c^- < 0$. Diverter section switches when it crosses the boundary from the stable domain into the unstable domain.

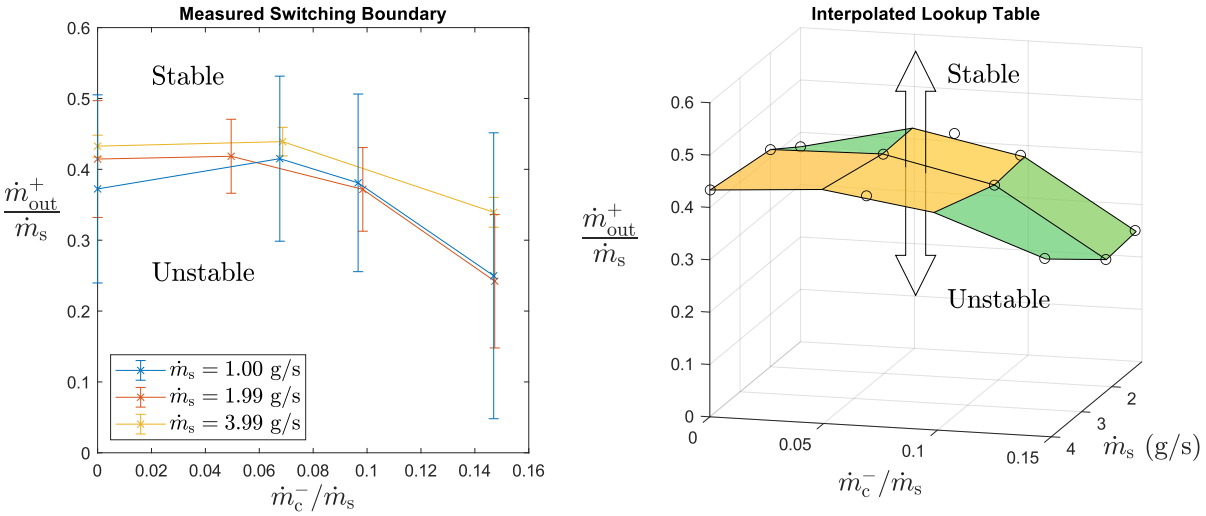

Fig. 4.13 Pilot diverter section switching boundary for $\dot{m}_c^+ = 0$. Diverter section switches when it crosses the boundary from the stable domain into the unstable domain.

$$\alpha_p = \begin{cases} \dot{m}^+_{out}/\dot{m}_s & \text{if initially } \alpha_p = 1 \text{ and } \dot{m}^+_{out}/\dot{m}_s < 1 \\ 1 & \text{if initially } \alpha_p = 1 \text{ and } \dot{m}^+_{out}/\dot{m}_s > 1 \\ 1 - \dot{m}^+_{out}/\dot{m}_s & \text{if initially } \alpha_p = 0 \text{ and } \dot{m}^+_{out}/\dot{m}_s < 1 \\ 0 & \text{if initially } \alpha_p = 0 \text{ and } \dot{m}^+_{out}/\dot{m}_s > 1 \end{cases} \tag{4.13}$$

4.2.4 Diverter Section Transients

The diverter switch model has two time parameters: response and switching times. The response time is the characteristic timescale of sub-switching dynamics τ, see equation 3.33. The switching-time t_{sw} is the time taken by the diverter to evolve from one state to the other in response to a switching trigger.

The experimental methodology used to acquire these times is very similar. A Norgren V05 series solenoid valve (V05A486M-Q116A) is connected to the attached side control port of the switch. The valve provides a step mass flow injection signal $\delta\dot{m}_{\text{c}}^{+}$, whilst HCX-series pressure transducers (table 4.1) record transient pressure variations at key locations (figure 4.14). The pressure transducer output voltages are recorded using a National Instruments (NI) cDAQ-9185 with the NI 9205 analogue input card. The input card has a maximum sampling rate of 250 kS/s, which over the 16 channels used allowed for 15.6 kS/s per channel. The actual sampling rate selected for pressure measurements was 15 kS/s. Consequently, the transient pressure measurements presented in this section have a time resolution of 66.7 µs.

Larger $\delta\dot{m}_{\text{c}}^{+}$ steps are used to trigger switching events and record switching times, whilst sub-switching response times are acquired with $\delta\dot{m}_{\text{c}}^{+}$ steps that are too small to trigger switching. Response times were, in general, difficult to acquire due to low signal-to-noise ratios. Consequently, $\delta\dot{m}_{\text{c}}^{+}$ were made as large as possible without triggering switching.

Response Times

Figure 4.15 presents an example of transient pressures measured for a sub-switching event. The transient pressure traces have been normalised such that the time-averaged signals evolve from 0 to 1 during the sub-switching event. At time $t = 0$ the

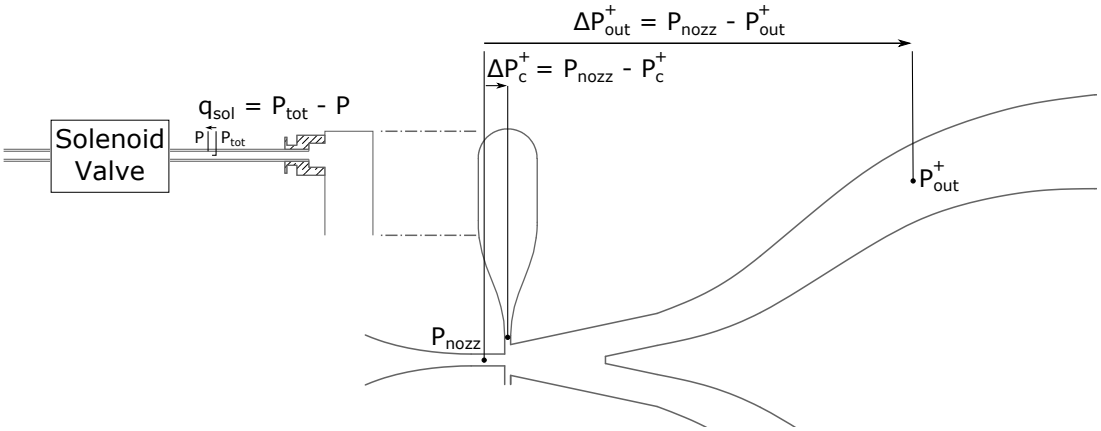

Fig. 4.14 Pilot diverter section transient pressure measurement locations.

solenoid valve opens, and there is a sudden rise in the control flow rate from $\delta\dot{m}_c^+ = 0$ to 2.1 g/s. The control flows fill the recirculation bubble of the pilot diverter section, and there is a subsequent rise in the bubble pressure p_c^+. In response to the growing bubble pressure, the recirculation bubble increases in size, the jet attachment point moves downstream, and the outlet mass flow split $\dot{m}_{out}^+/\dot{m}_s$ decreases. When $\dot{m}_{out}^+/\dot{m}_s$ decreases, the proportion of the supply jet dynamic head that is recovered as static pressure at p_{out}^+ decreases.

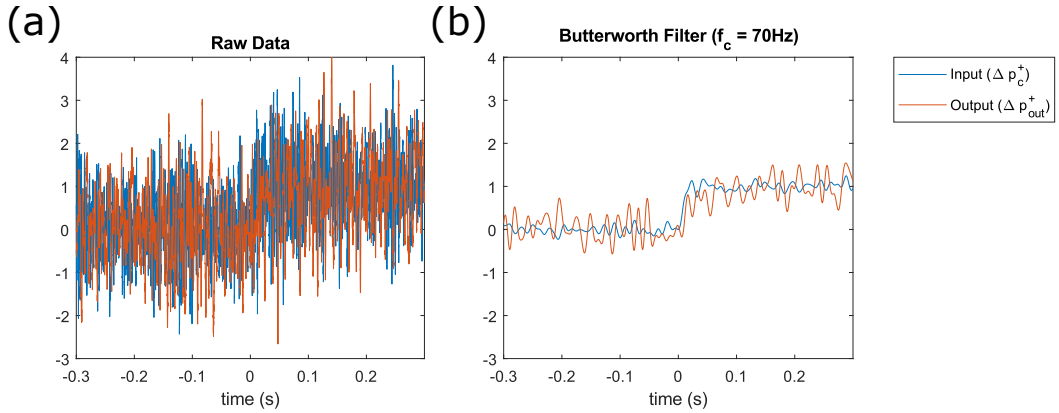

Fig. 4.15 Example of normalised transient pressure signals measured for sub-switching signal ($\dot{m}_s = 2.1$ g/s, $\delta\dot{m}_c^+ = 0.074$ g/s)

The recirculation bubble volume is small, so the bubble fill times are expected to be short enough that the p_c^+ signal can be treated as being concurrent with the $\delta\dot{m}_c^+$ signal. In contrast, the outlet pressure p_{out}^+ is linked to $\dot{m}_{out}^+/\dot{m}_s$ and the transient

operating point of the diverter section. To acquire a response time, transient pressure measurements Δp_c^+ and Δp_{out}^+ are treated as input and output signals of the diverter switch system.

The model simulates sub-switching dynamics by assuming that the response of a diverter section to a small input signal can be described by single pole transfer functions with time constant (response time) τ (see section 3.4.1). To get τ for a single measurement run, the Matlab function **tfest** can be used to get an estimate of the transfer function based on the input and output signals for the pilot diverter section.

However, as can be seen in figure 4.15(a) the signal-to-noise ratio is low, increasing the uncertainties associated with τ values extracted from any single transient response recording. To reduce measurement uncertainties, low-pass Butterworth filters were applied to both the input and output signals, and these filtered signals were then passed to the **tfest** function. Examples of filtered signals are presented in figures 4.15(b) and 4.16. In figure, the τ value extracted from the transient data is marked on the plot.

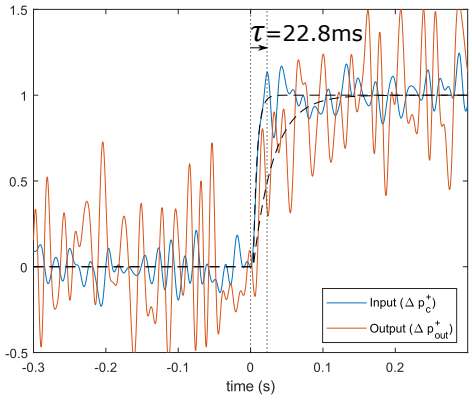

Fig. 4.16 Example of response time τ being extracted from filtered ($f_c = 70Hz$) transient data ($\dot{m}_s = 2.1\,\mathrm{g/s}$, $\delta\dot{m}_c^+ = 0.074\,\mathrm{g/s}$)

Note that despite the application of a strict ($f_c = 70Hz$) low-pass filter the pressure traces in figure 4.16 are still noisy. The primary noise source is turbulent pressure fluctuations at the free jet boundaries of the diverter supply jet. Figure 4.17 presents the frequency spectrum of this jet noise. The noise is broad spectrum and overlaps with frequency components of the step response. Consequently, the lower frequency components of this noise cannot be eliminated by filtering without negatively affecting the veracity of the input and output signals passed to **tfest**. However, a low-pass filter can still be used to minimise the contributions of higher frequency components, thereby making it easier to discern input and output signals, for an example of this compare figure 4.15(a) with 4.15(b).

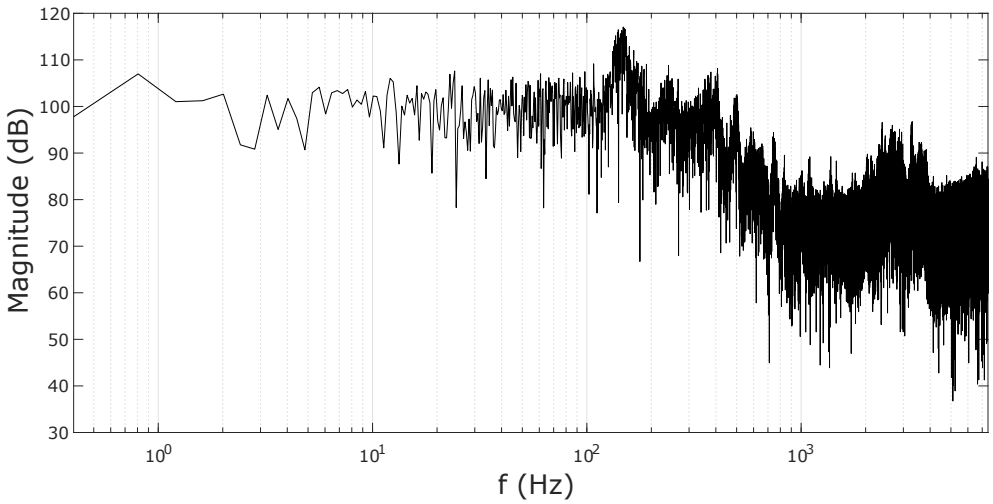

Fig. 4.17 Jet noise spectrum, acquired by applying Matlab's **FFT** function to a Δp^+_{out} recording where $\dot{m}_s = 5.9\,\text{g/s}$ and there is no control signal i.e. $\delta\dot{m}^+_c = 0\,\text{g/s}$.

To improve the accuracy of τ values used to tune the model, the transient measurement process was repeated 50 times per data point. Figure 4.18 presents a typical distribution of measured response times. Response times τ and their uncertainties quoted in this study (figures 4.19 and 4.18) are based on the mean and standard

deviation values of fitted normal distributions.

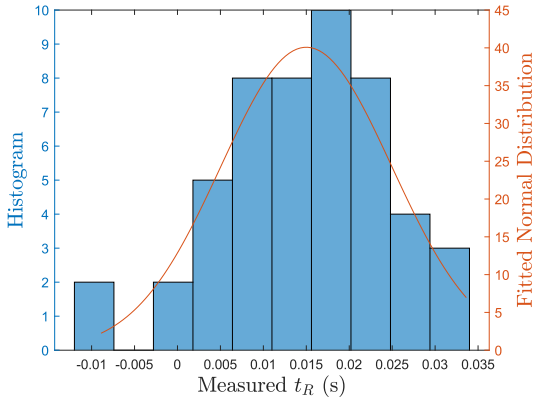

Fig. 4.18 Example of measured response times distribution ($\dot{m}_s = 2.1\,g/s$, $\delta\dot{m}_c^+ = 0.074\,g/s$).

Ideally, the choice of f_c for filtering should be sufficiently low that the signal-to-noise is maximised, but not so low that it negatively affects the accuracy of the measured τ values by removing high frequency components from the input and output signals. To make an informed decision, diverter response transients recorded at flow rates of 2.0 g/s, 5.9 g/s and 9.1 g/s were reanalysed multiple times using the process outlined above over a range of filter f_c values, see figure 4.19. At the lower supply flow rates (2.1 g/s), where the response times are longer, it is possible to get away with stricter filtering ($f_c = 70Hz$). However, at higher flow rates, there is a noticeable increase in the response time estimates for $f_c < 150\,Hz$.

To get the response times shown in figure 4.20 an $f_c = 300$ Hz filter was applied to input and output signals. This trend-line is imported directly into the model and used to ascertain the response times for both the pilot and SVV diverter sections.

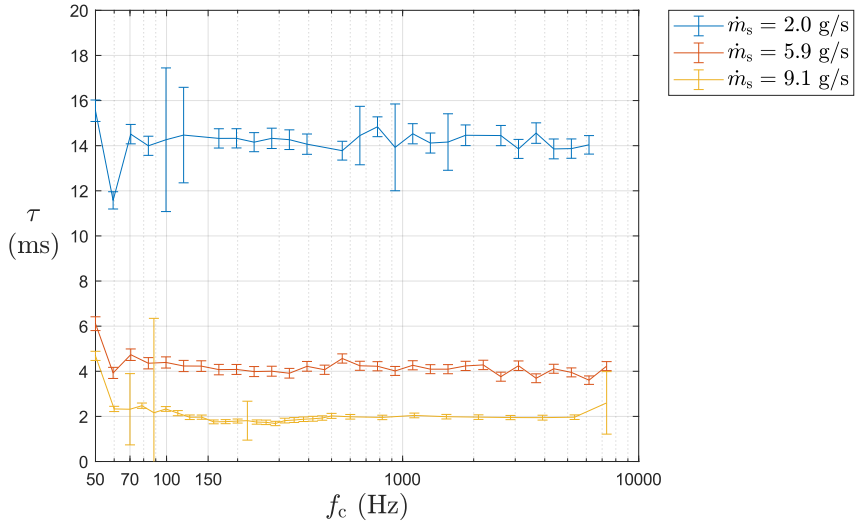

Fig. 4.19 Effect of Butterworth low-pass filter f_c on estimates of response times and their associated uncertainties.

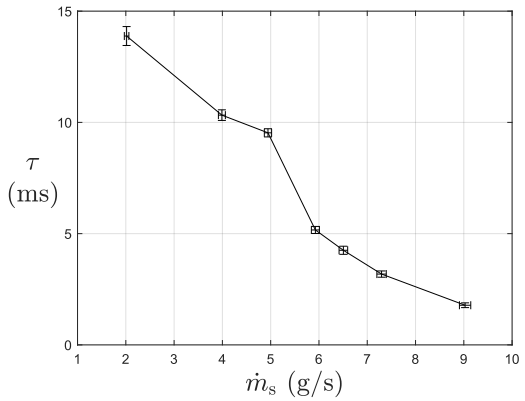

Fig. 4.20 Effect of supply mass flow rate upon the pilot diverter section's jet response time (2σ errorbars).

Switching Times

Figure 4.21 is a typical example of transient pressures measured for pilot switching events. Like the sub-switching case, all signals have been normalised such that the time-averaged values of signals evolve from 0 to 1. Unlike the sub-switching case, the signals are considerably stronger relative to the background noise. Δp_c^+ is still used as the input signal and Δp_{out}^+ is used as the output signal. However, a pitot-static measurement close to the solenoid valve outlet q_{sol} is used to check the assumption of section 4.2.4 that the recirculation bubble pressure rise and the control mass flow signal are concurrent. With the pitot probe occupying a substantial portion of the

control tubing cross-section (figure 4.14), it was not expected that the pitot-static measurement q_{sol} would return an accurate dynamic head value. However, positioned close to the solenoid outlet, q_{sol} is used to provide a transient signal indicative of the solenoid valve state. As can be seen from the normalised and filtered pressure traces in figure 4.21(b), the $\Delta p_{\mathrm{c}}^{+}$ transient adheres closely to the q_{sol} signal.

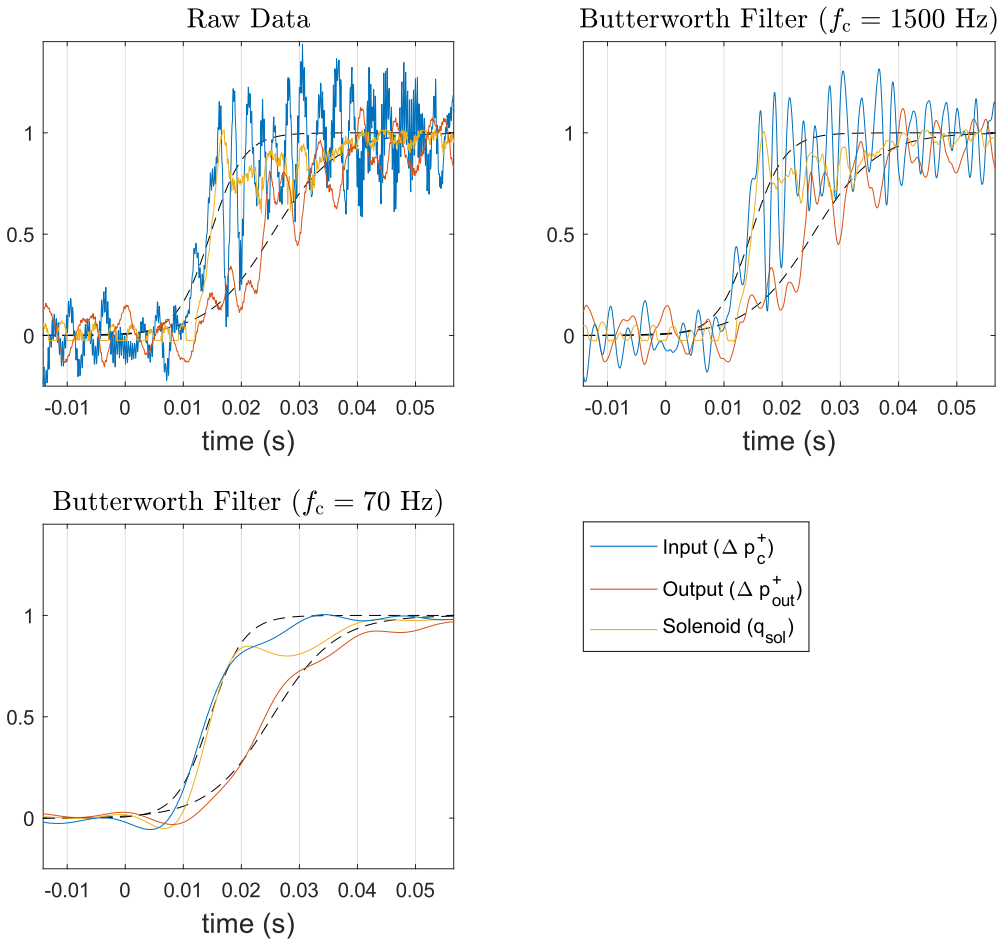

Fig. 4.21 Example of transient pressure signals measured for the pilot stage diverter section during a switching event ($\dot{m}_{\mathrm{s}} = 2.1\,\mathrm{g/s}$, $\delta\dot{m}_{\mathrm{c}}^{+} = 0.53\,\mathrm{g/s}$).

The switching time t_{sw} of the pilot stage diverter section is determined by fitting a sigmoid curve to the filtered output signal $\Delta p_{\mathrm{out}}^{+}$. Clearly, the shape of the output signal is not a perfect sigmoid, but a sigmoid function drives the switching process in the numerical model. The switching time is taken to be the time required for the

sigmoid fit to go from 0.001 to 0.999.

As with the sub-switching response times, the switching transient is re-recoded 50 times for each data point. The switching times and their uncertainties are then based on the mean and standard deviation of a normal distribution of t_{sw} values derived from the switching transients.

Of the conditions tested, switching times were shortest for $\dot{m}_{\mathrm{s}} = 9.1g/s$ and $\dot{m}_{\mathrm{c}}^{+}/\dot{m}_{\mathrm{s}} = 0.15$. Transients recorded for these flow conditions were used to determine a suitable value for f_{c}, since transients with the shortest switching times would be the most sensitive to over-filtering. Figure 4.22 shows the effect f_{c} has on the estimated value of t_{sw} for these flow conditions. The effects of over-filtering are evident for $f_{\mathrm{c}} < 500$ Hz.

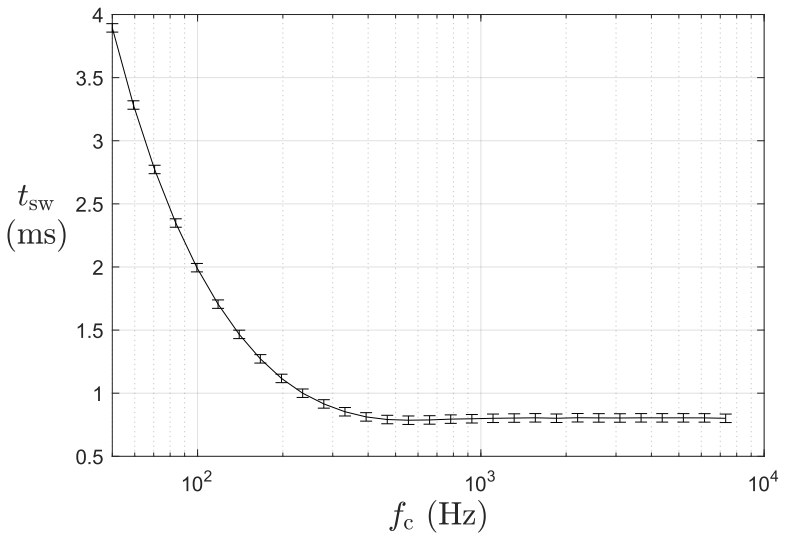

Fig. 4.22 Effect of f_{c} on the estimated value of t_{sw} acquired from switching transients recorded for $\dot{m}_{\mathrm{s}} = 9.1\,\mathrm{g/s}$ and $\dot{m}_{\mathrm{c}}^{+}/\dot{m}_{\mathrm{s}} = 0.15$.

Switching times for the pilot diverter section are presented in figure 4.23. These switching times are derived from transient switching data that has been filtered using an $f_{\mathrm{c}} = 1500$ Hz low-pass Butterworth filter. Switching times are functions of the sup-

ply flow rate $\dot{m}_s$ and, to a lesser extent, the relative switching signal strength $\delta\dot{m}_c^+/\dot{m}_s$.

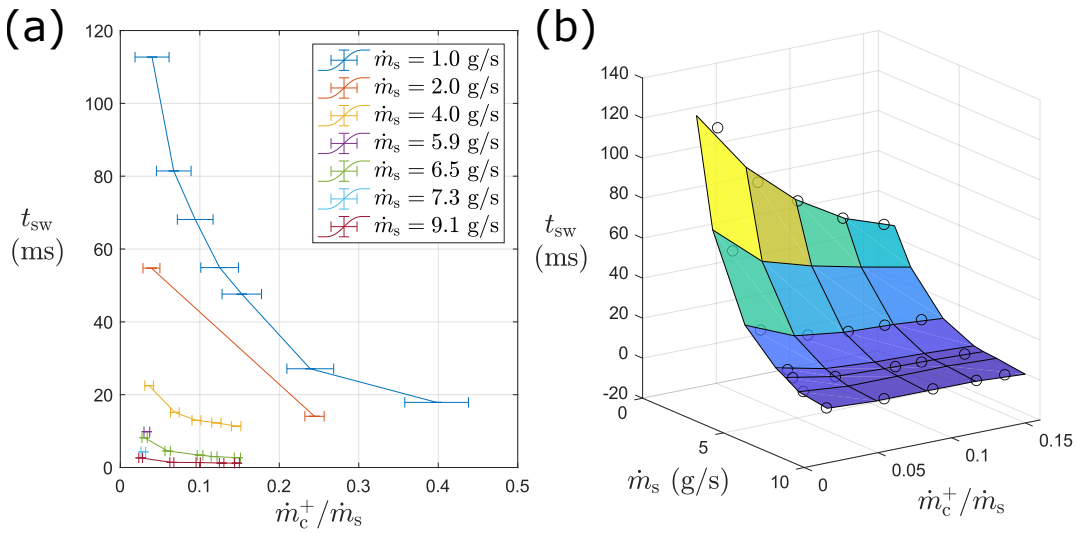

Fig. 4.23 (a) Measured pilot diverter section switching times (2σ errorbars) and (b) lookup table data constructed from a thin-plate smoothing spline interpolation.

4.3 Switched Vortex Valve

4.3.1 Device Construction

The SVV geometry used here is a 3.9:1 scaled-up version of the geometry used by Turner et al [104]. The 2D dimensions of the SVV cavity are presented in 4.24.

The SVV stage is larger than the pilot stage, with the diverter section of the SVV being double the size of the pilot's diverter switch section. The SVV was constructed from cut sheets of acrylic. The same SVV profile figure 4.24 was cut out of five 5 mm and two 10 mm sheets of acrylic, which were stacked to form a cavity 45 mm deep. The stack is sandwiched between two aluminium plates that form the cavity end-walls, and the whole assembly is bolted together to create an airtight seal (figure 4.25).

Like the pilot stage, pressure tappings are drilled into the end wall. The locations of the pressure tappings are marked in figure 4.26. Note that in addition to static

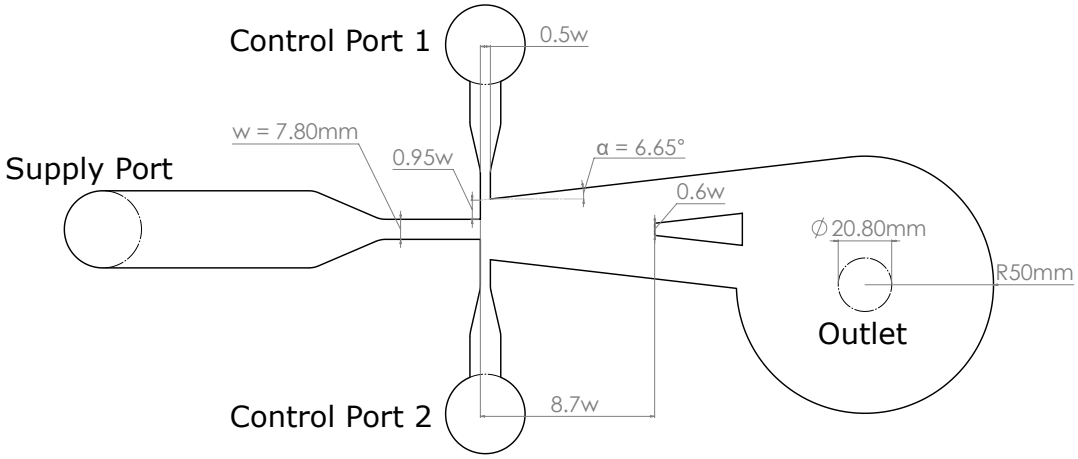

Fig. 4.24 SVV Cavity Schematic

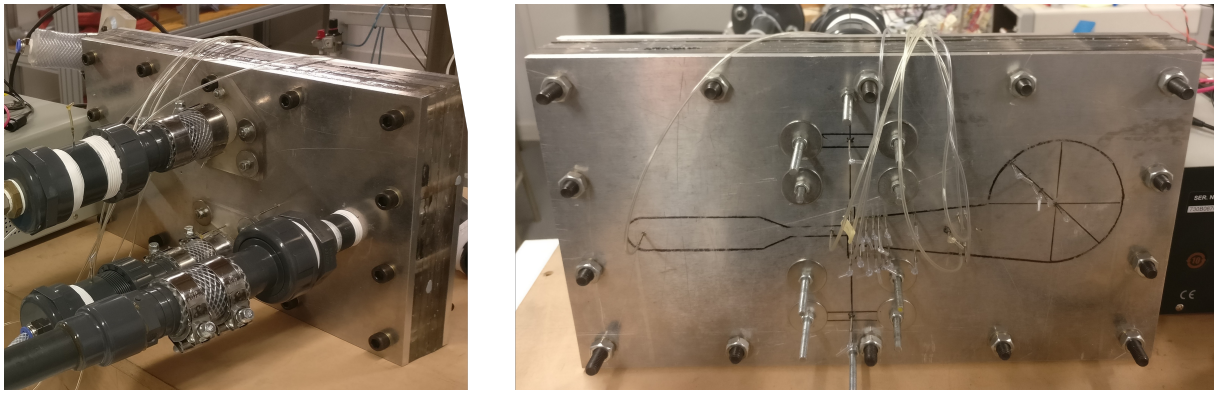

Fig. 4.25 Photos of the assembled SVV

tappings, there are also additional pitot probes on both sides of the splitter ($p_{\text{out},0}$).

4.3.2 Diverter Section Steady-State Characteristics

The SVV steady-state characteristics are measured using a similar experimental setup (figure 4.27) to that used to measure the pilot's diverter section characteristics.

Here the 12.81 mm orifice meters measure the supply mass flow rates and the attached side control flow rates ($\dot{m}_{\text{s}}$ and $\dot{m}_{\text{c}}^{+}$). The unattached side control mass flow rate ($\dot{m}_{\text{c}}^{-}$) was measured using two devices. When acquiring the subset of characteristic data where $\dot{m}_{\text{c}}^{-} < 2.1\,\text{g/s}$, the FMA A2323 mass flow meter was used. When at higher $\dot{m}_{\text{c}}^{-}$ values, the meter was replaced with a mass flow controller

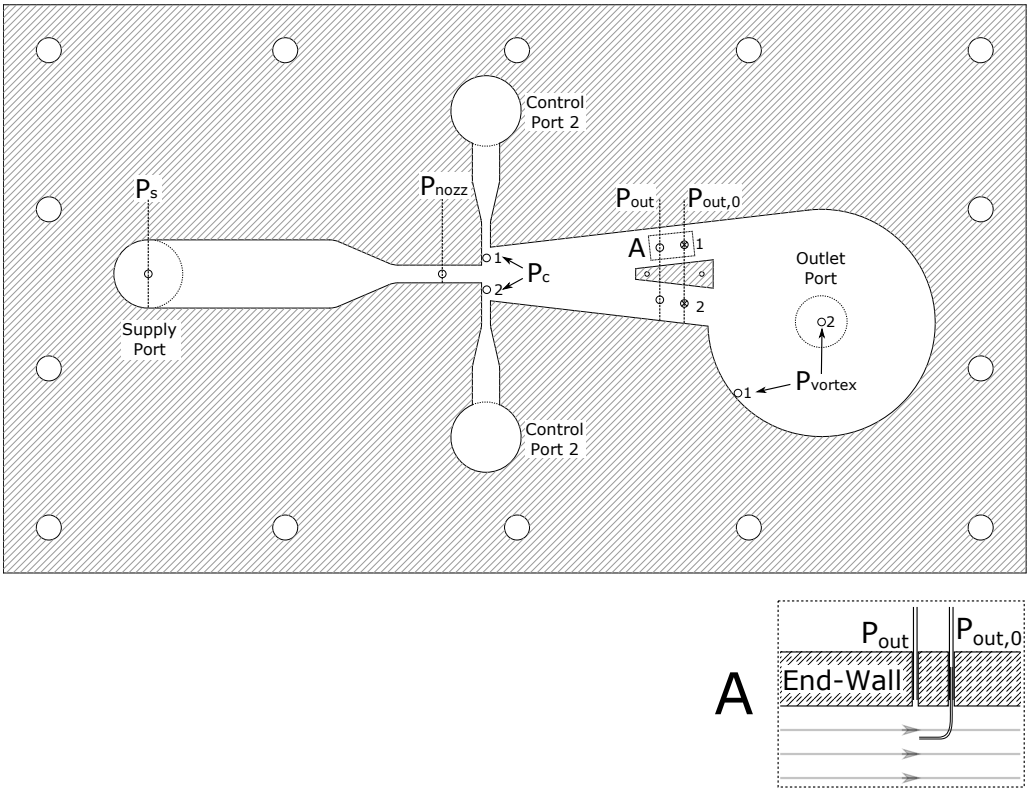

Fig. 4.26 Schematic of SVV with pressure tapping locations marked.

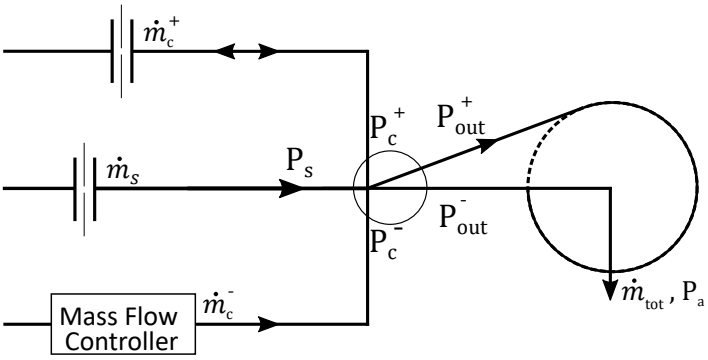

Fig. 4.27 Setup for measurement of SVV characteristics in tangential (vortex) state

FMA-2612A. The mass flow controller has a larger operating range ($0 - 11\,\mathrm{g/s}$) but lower absolute accuracy.

Steady-state characteristics of the SVV stage were gathered at different supply flow rates for both the radial (non-vortex) state and the tangential (vortex state). The choice of supply flow rates in each state span the range of supply flow rates observed when operating the SVV, specifically the flow rates observed when operat-

ing the SVV at pressure ratios of 1.01-1.07 in the radial state and 1.03-1.22 in the tangential state. In the radial state, tuning data is gathered at flow rates between 10.4 g/s and 27.6 g/s. In the tangential state, tuning data is gathered at flow rates between 5.3 g/s and 20.1 g/s. Thus minimum and maximum supply flow rates that tuning data was acquired at were 5.3 g/s and 27.6 g/s. These supply flow rates correspond to SVV supply nozzle hydraulic diameter Reynolds numbers of 11000 and 57000 and nozzle Mach numbers of 0.038 and 0.20. Consequently, flows in the SVV diverter section are expected to be fully turbulent and incompressible. It is anticipated that any coolant flow modulation device would have to be suitably sized to avoid accelerating flows into the compressible flow regime to minimise pressure losses in the high flow state.

The SVV diverter section Δp_{out} and Δp_{c} characteristics are presented in figures 4.28 and 4.29. Unlike the pilot stage, the outlet mass flow split $\dot{m}_{\text{out}}^{+}/\dot{m}_{\text{s}}$ could not be accurately measured without significant disruption to the diverter section flow field. Thus the $\dot{m}_{\text{out}}^{+}/\dot{m}_{\text{s}}$ dimension is missing from these characteristic surfaces. Despite this limitation, it is possible to identify where these characteristics are similar to the pilot diverter section characteristics and where they differ.

Like the pilot stage, the shape of these characteristics varies a lot more in the $\dot{m}_{\text{c}}^{+}$ direction than in the $\dot{m}_{\text{c}}^{-}$ direction. This is because diverter sections are more responsive to control flows at the attached control port. In both the radial and the tangential states, the shapes of the Δp_{c} characteristics are similar. As with the pilot stage, the attached side control flows can shrink or grow the recirculation bubble depending on whether $\dot{m}_{\text{c}}^{+}$ is negative or positive. As $\dot{m}_{\text{c}}^{+}$ increases, the jet curvature decreases and Δp_{c} increases, approaching 0 close to the switching boundary

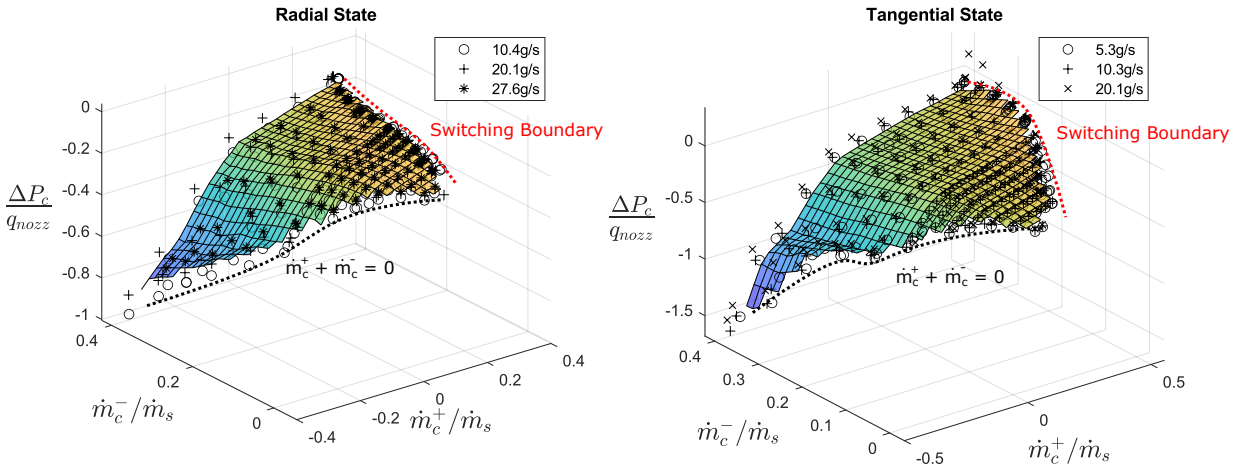

Fig. 4.28 SVV Δp_c characteristics

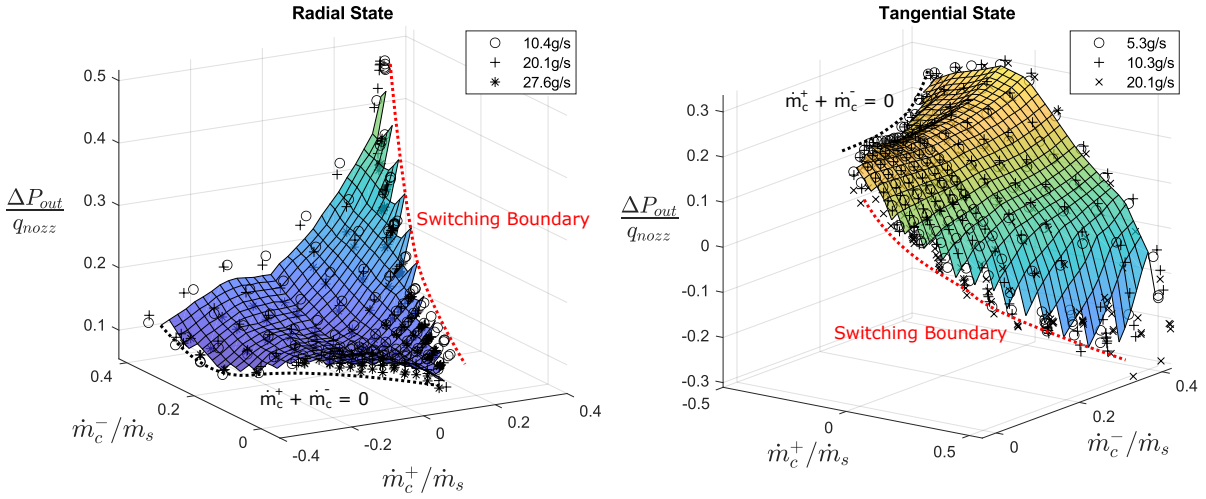

Fig. 4.29 SVV Δp_{out} characteristics

Missing from the Δp_{c} characteristics is a sharp Δp_{c} rise at low $\dot{m}_{\mathrm{c}}^+$ values, and a gradual Δp_{c} reduction at high $\dot{m}_{\mathrm{c}}^+$ values; both of these features were observed for the pilot diverter section Δp_{c} characteristics. Both sets of characteristics are bounded by the switching and the $\dot{m}_{\mathrm{c}}^+ + \dot{m}_{\mathrm{c}}^- = 0$ boundaries. The later boundary is imposed because as part of the staged SVV, for $\dot{m}_{\mathrm{c}}^+ + \dot{m}_{\mathrm{c}}^- < 0$, the pilot stage would have to have a negative supply flow rate. These boundaries limit the range of $\dot{m}_{\mathrm{c}}^+/\dot{m}_{\mathrm{s}}$ values that can be tested. The Δp_{c} characteristic features observed for the pilot diverter section at high and low $\dot{m}_{\mathrm{c}}^+$ values could simply lie outside of the range of $\dot{m}_{\mathrm{c}}^+$ values tested. However, it is more likely that these differences in steady-state behaviour arise due to subtle differences in the switch geometry and interactions

with the vortex chamber flow field.

The geometry of the pilot diverter section and the SVV diverter section are quite similar, but there are some differences

- the SVV diverter supply nozzle has an aspect ratio of 45:7.8, whilst the pilot diverter nozzle has an aspect ratio of 40:7.8
- the SVV diverter wall angle is 6.65°, whilst the pilot diverter wall angle is 12°
- the SVV $p_{\text{out}}^{\pm}$ tappings are located on either side of the splitter, whilst the pilot $p_{\text{out}}^{\pm}$ tappings are located further downstream in a diffusive duct

The vortex chamber flow field dictates conditions at the SVV's diverter-vortex chamber interface. The $p_{\text{out}}^{\pm}$ tappings are positioned close to this interface. As previously discussed, the flow field in the vortex chamber is dramatically different in the radial and tangential states. This difference in the vortex chamber flow field explains why the tangential and radial state versions of the Δp_{out} characteristics are so different from each other.

Switching Boundary

Even though the transient switch state of both the diverter and vortex chamber sections of the SVV may differ (section 4.3.3), the states are the same under steady-state conditions. Consequently, the switching boundary discussed in this section applies to the SVV as a whole.

The switching interfaces are found by extending the characteristic measurement process of section 4.3.2 in the $\dot{m}_{\text{c}}^{+}/\dot{m}_{\text{s}}$ direction until the SVV switches, figure 4.30 shows an example of this. At the switching point, there is a clear and dramatic change in characteristic pressures. For a given supply flow rate, a clear line delineates the edge of stability.

Note that unlike the pilot diverter section, if $\dot{m}_c^- > 0$ there is still an unsteady switching process for the SVV. This difference in behaviour is attributed to differences in the diverter wall angle (6.65° for the pilot stage versus 12° for the SVV stage). The shallower wall angle means that the jet does not need to be deflected as far by the $\dot{m}_c^+$ jet momentum before it is close enough to the unattached wall for a new recirculation bubble to start to form.

All of the measured switching points for both the radial and tangential states of the SVV are plotted in figure 4.31. The measured switching points form a 2-D surface; control flows $\dot{m}_c^+/\dot{m}_s$ that lie above the surface will trigger switching. Like the steady-state characteristics, the stability interfaces are affected slightly by variations in the supply flow rate, but it is not the dominant parameter. Higher $\dot{m}_c^+/\dot{m}_s$ values at the switching interface indicate greater stability for the SVV. Therefore, figure 4.31 shows that the stability of the SVV increases when introducing positive unattached side control flows ($\dot{m}_c^-/\dot{m}_s$). For $\dot{m}_c^- > 0$, the unattached side reinforces attachment by supply unattached side entrainment, thereby increasing p_c^+, and by imparting transverse momentum to the supply jet, deflecting it towards the attached side of the diverter section. There is also greater stability in the tangential state; this is consistent with other studies conducted with SVVs [50, 104]. It was observed in Turner et al. [104] that a precessing vortex can form in the radial state, producing upstream pressure fluctuations which destabilise the diverter section of the SVV.

4.3.3 SVV Transients

The setup used to record the transient response of the SVV is very similar to that used for the pilot stage diverter section (figure 4.32). However, unlike the pilot stage, there is also the dynamic response of the vortex chamber to consider. Furthermore,

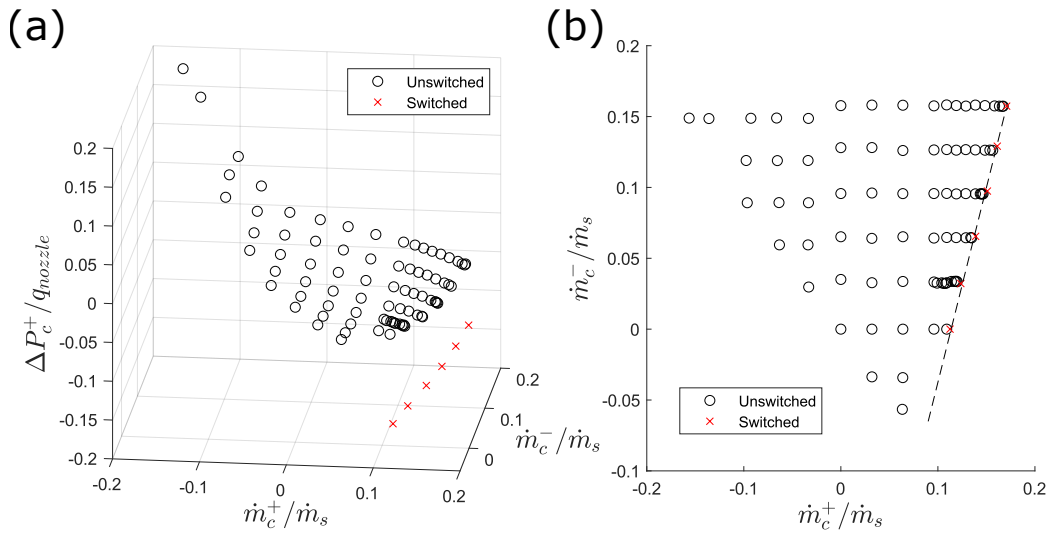

Fig. 4.30 Sample of the SVV $\Delta p_c^+/q$nozz characteristic data (non-vortex state, $\dot{m}_s = 21$ g/s) highlighting the sharp change in pressures associated with switching and showing that there is a distinct switching boundary that can be mapped out.

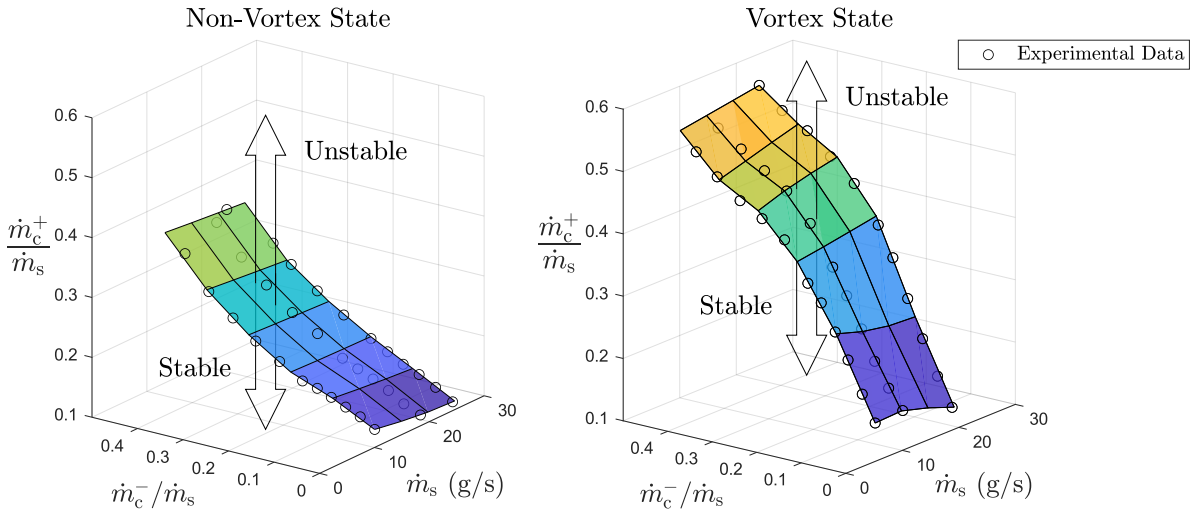

Fig. 4.31 SVV switching boundaries (experimental data and the interpolated lookup table as surfaces) for the radial (non-vortex) and tangential (vortex) states. SVV switches when it crosses the boundary from the stable domain into the unstable domain.

the greater size of the SVV allows for the introduction of pitot probes in the diverter section outlet legs. The larger cross-sectional areas of the outlet ducts ensure minimal flow disturbances due to the pitot probes. The pitot probes provide an indirect measure of the local flow velocities and are therefore useful indicators of the jet position.

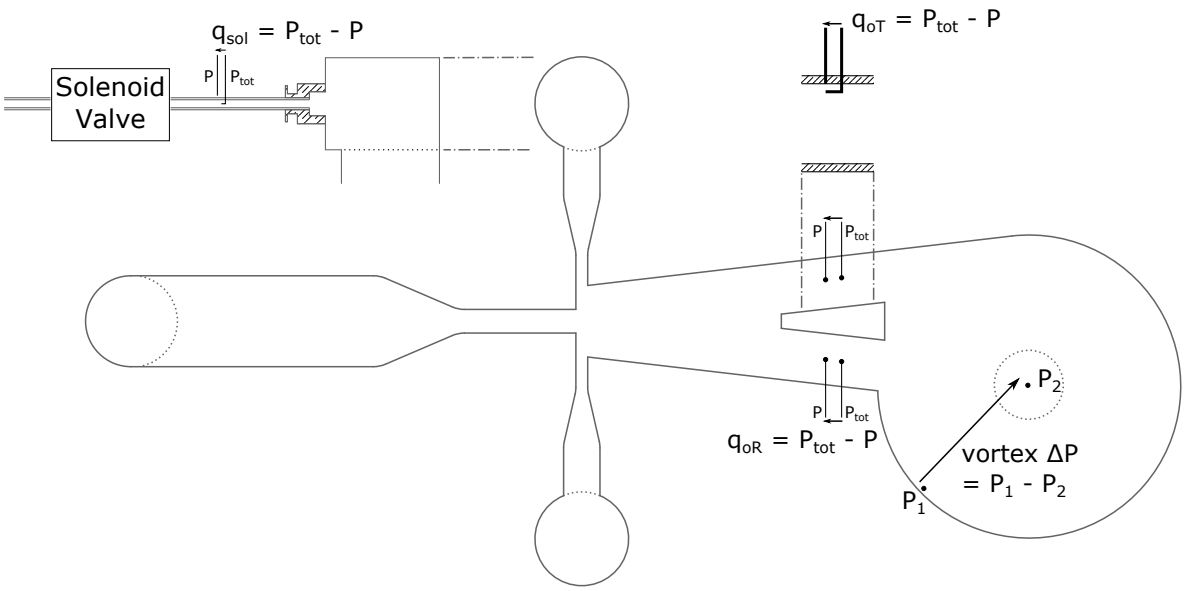

Fig. 4.32 SVV transient pressure measurement locations.

Switching Times

Figures 4.33 and 4.34 are typical examples of transient pressures measured for SVV switching events. Signals have been normalised such that the time-averaged values evolve between 0 and 1 in response to the solenoid signal. However, similar to the pilot stage, there is a lot of noise from turbulent fluctuations. Note that a strict ($f_c = 70\,\text{Hz}$) low-pass filter has been applied to the data in figures 4.33, 4.34, 4.35 and 4.35 to minimise noise and make it easier to assess what is happening inside the SVV during a switching event. However, as will be discussed towards the end of this sub-section, higher f_c values are used when evaluating the transient data to get switching times t_{sw}.

The pitot-static measurement close to the solenoid valve q_{sol} is treated as the input signal and sets the start time of the switching process. However, the choice of output signal is less clear. A selection of measurements can be used to determine the state of the SVV. Pitot-static measurements in both the tangential q_{oT} and radial q_{oR} legs of the diverter section determine the attachment state of the diverter section. Static pressure tappings located at the rim and the centre of the vortex chamber are

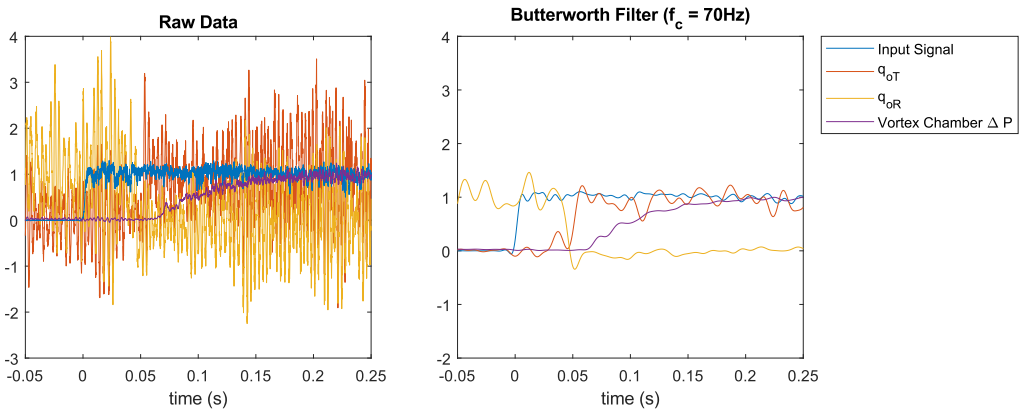

Fig. 4.33 Example of normalised transient pressures recorded for an SVV radial (non-vortex) to tangential (vortex) state switching event ($\dot{m}_s = 10\,\mathrm{g/s}$, $\delta\dot{m}_c^+ = 1.8\,\mathrm{g/s}$)

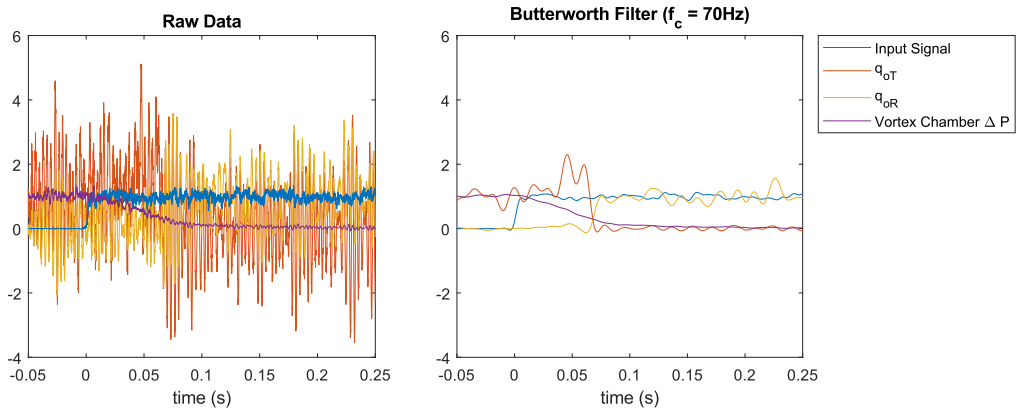

Fig. 4.34 Example of normalised transient pressures recorded for an SVV tangential (vortex) to radial (non-vortex) state switching event ($\dot{m}_s = 10\,\mathrm{g/s}$, $\delta\dot{m}_c^+ = 2.3\,\mathrm{g/s}$).

used to measure the static pressure drop across the vortex chamber, which is used as an indicator for the vortex state.

There is not a single switching time that can be applied to the SVV as a whole, primarily because flow interactions between the diverter section and the vortex chamber complicates the situation. When a switching signal is introduced in the radial state (figure 4.35), the diverter section attachment state switches first. There is no appreciable change to Δp_{vx} until the diverter section is fully switched. However, the process is a little different when switching from the tangential to the radial state. The initial perturbation of the supply jet by the $\delta\dot{m}_c^+$ signal is immediately detrimental to the strong vortex flow field. Consequently, Δp_{vx} has almost entirely

dropped to radial state values before the diverter section has completed the switching process.

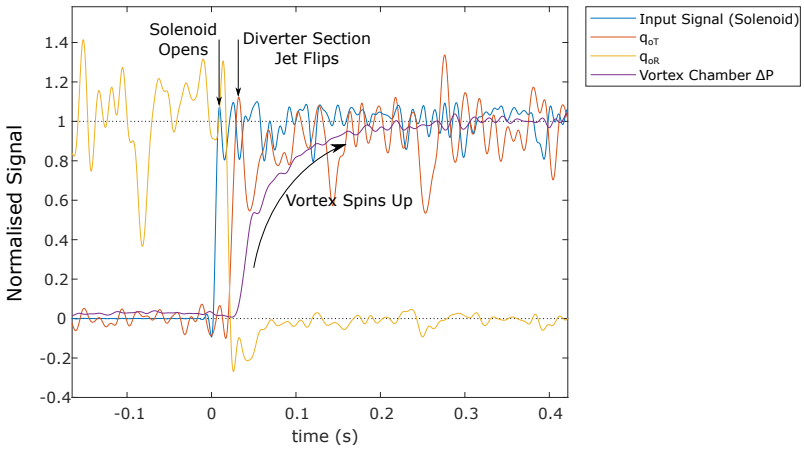

Fig. 4.35 Example of transient pressures measured for an SVV radial (non-vortex) to tangential (vortex) state switching event ($\dot{m}_s = 21\,\mathrm{g/s}$, $\delta\dot{m}_c^+ = 3.6\,\mathrm{g/s}$).

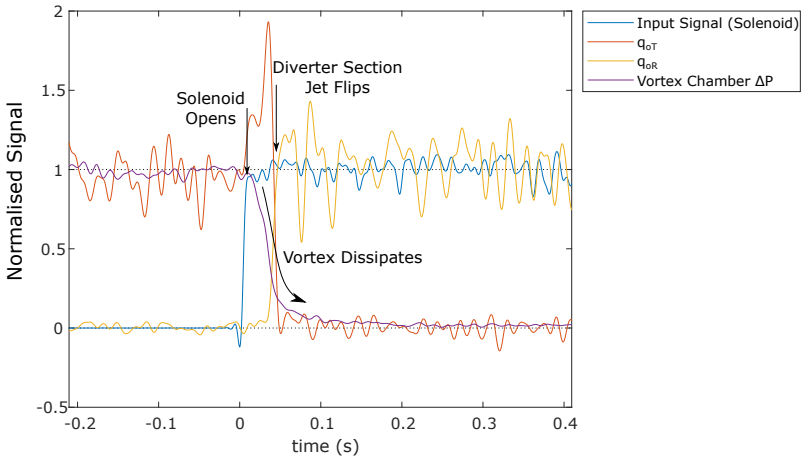

Fig. 4.36 Example of transient pressures measured for an SVV tangential (vortex) to radial (non-vortex) state switching event ($\dot{m}_s = 21\,\mathrm{g/s}$, $\delta\dot{m}_c^+ = 3.6\,\mathrm{g/s}$).

The vortex chamber characteristics (section 4.3.4) provide some insight into why this difference in switching behaviour has been observed. The vortex chamber characteristics $\Delta p_{vx}/q_{vx}$ are influenced by SVV control flow rates in both the radial and tangential states. However, the characteristic is relatively flat in the radial state for $\dot{m}_c^+ > 0$. This is not the case in the tangential state, where any increase in $\dot{m}_c^+$

has a detrimental effect upon the vortex chamber performance.

When the $\delta\dot{m}_c^+$ switching signal is introduced in the tangential state, the q_{oT} trace spikes (figure 4.36), with a 90% rise before the diverter section switches. The pitot probes used to measure q_{oT} are positioned along the centreline of the tangential duct. It is theorised that the jet is strongly attached to the tangential wall before the control signal is introduced. Then when the control signal is introduced, the jet lifts off the wall enough that the jet centreline moves closer to the duct centreline, hence the pitot pressure spike. Such a large change in the jet position will significantly impact the vortex chamber performance, as shown by the sensitivity of the characteristic to $\dot{m}_c^+$ values. As a result, there is a subsequent drop in the pressure across the vortex chamber. This means that what starts off as a sub-switching response of the vortex chamber blurs into a full switching event once the switch section switches.

The numerical model had to be modified to account for these interactions. The diverter section and the vortex chamber are modelled as separate components during a switching event, with their own state variables (α_{switch}, α_{vortex}) and switching times ($t_{sw,switch}$,$t_{sw,vortex}$). The diverter section switching is triggered when $\dot{m}_c^+$ crosses the SVV switching threshold (section 4.3.2). In the radial state, vortex chamber switching is triggered when the diverter section switching process is complete. In the tangential state, the vortex chamber switching is triggered at the same time that diverter section switching is triggered.

The diverter section's switching times are acquired by fitting a sigmoid function to the filtered q_{oT} transient for radial-to-tangential switching and the filtered q_{oR} transient for radial-to-tangential switching. The diverter switching time is then set by the time difference between the solenoid opening and the sigmoid fit reaching 0.001. The vortex chamber switching times are acquired by fitting a sigmoid function to a filtered vortex chamber pressure difference transient. The vortex chamber switching

time is taken as the time required for the sigmoid function to evolve from 0.001 to 0.999 or vice versa. The measurement process for each operating point is repeated 50 times to get reliable average values for the switching times.

In a similar fashion to the process outlined in section 4.2.4, the choice of f_c values used to filter the switching transients before applying sigmoid fits is determined by the effect f_c has on the estimated t_{sw} values for flow conditions that result in the smallest t_{sw} values. In this case the shortest switching times were observed when $\dot{m}_s = 29.8$ g/s and $\dot{m}_c^+/\dot{m}_s = 0.17$ g/s for radial-to-tangential state switching, and $\dot{m}_s = 21.3$ g/s and $\dot{m}_c^+/\dot{m}_s = 0.29$ g/s for tangential-to-radial state switching. Figure 4.37 shows the effect f_c has for these switching conditions. Switching time estimates are consistent for $f_c > 150$ Hz with radial-to-tangential state switching and for $f_c > 500$ Hz with tangential-to-radial state switching. Consequently, to avoid the effects of over-filtering f_c values of 300 Hz and 1000 Hz were applied with radial-to-tangential and tangential-to-radial state switching transients before applying sigmoid fits.

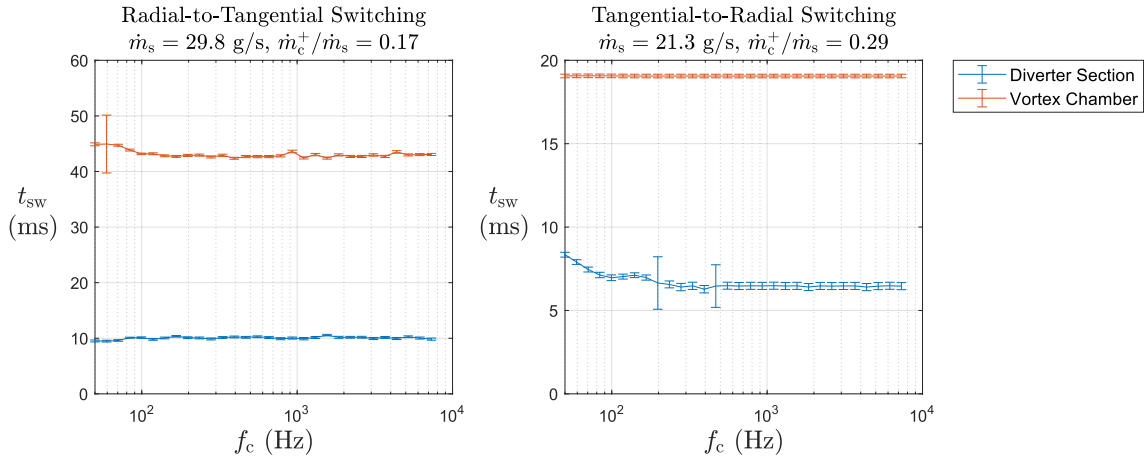

Fig. 4.37 Effect of low-pass filter corner frequency f_c on estimated values of switching times t_{sw}.

Switching times for the SVV diverter section are presented in figures 4.38 and 4.39, whilst the vortex chamber switching times are presented in figs.4.40 and 4.41. The switching times for the diverter section of the SVV are typically shorter than those for the vortex chamber. However, the shapes of all the switching time surfaces presented so far (including those for the pilot diverter section) are very similar. Switching times are functions of the supply flow rate $\dot{m}_\mathrm{s}$ and, to a lesser extent, the relative switching signal strength $\delta\dot{m}_\mathrm{c}^+/\dot{m}_\mathrm{s}$. The switching times are larger for low $\dot{m}_\mathrm{s}$ and $\delta\dot{m}_\mathrm{c}^+/\dot{m}_\mathrm{s}$ values.

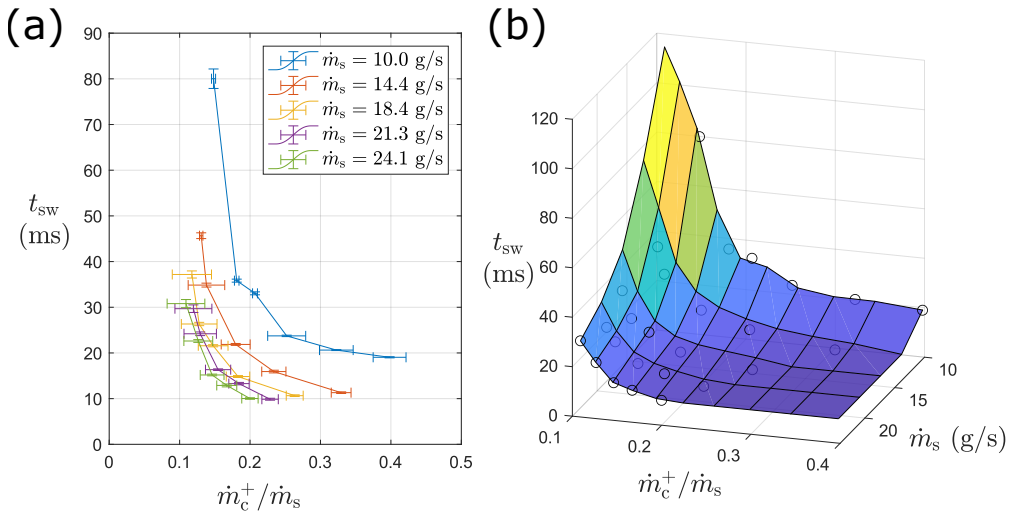

Fig. 4.38 (a) Measured SVV diverter section radial (non-vortex) to tangential (vortex) state switching times (2σ errorbars) and (b) lookup table data constructed from a thin-plate smoothing spline interpolation.

4.3.4 Vortex Chamber Characterisation

The dimensionless vortex chamber characteristics are of the form

$$\frac{\Delta p_\mathrm{vx}}{q_\mathrm{vx}} = \frac{p_\mathrm{out}^+ - p_a}{q_\mathrm{vx}} = F\left(\frac{\dot{m}_\mathrm{c}^+}{\dot{m}_\mathrm{s}}, \frac{\dot{m}_\mathrm{c}^-}{\dot{m}_\mathrm{s}}, Re, \alpha\right) \tag{4.14}$$

In the model, these take the form of two 3-dimensional lookup tables, one for the tangential state ($\alpha = 1$) and the other for the radial state ($\alpha = 0$). The vortex

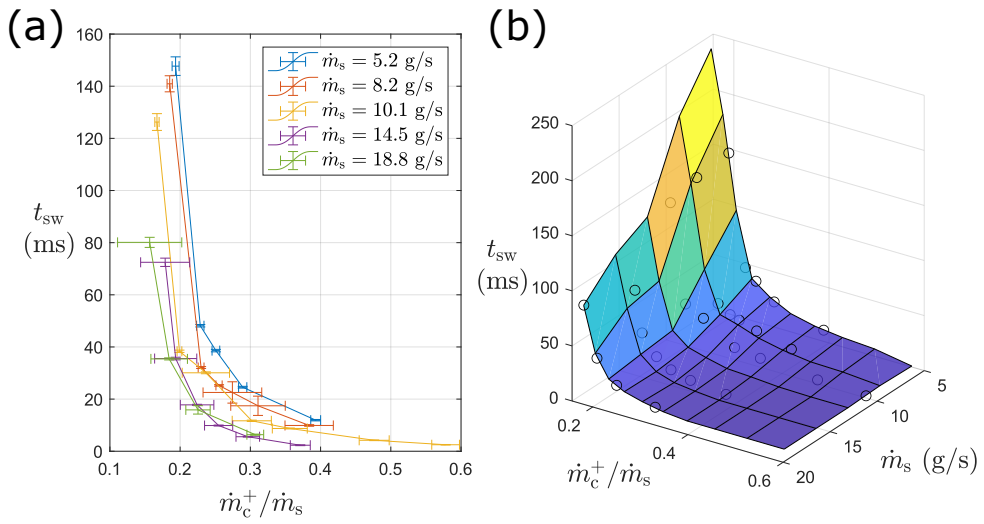

Fig. 4.39 (a) Measured SVV diverter section tangential (vortex) to radial (non-vortex) state switching times (2σ errorbars) and (b) lookup table data constructed from a thin-plate smoothing spline interpolation.

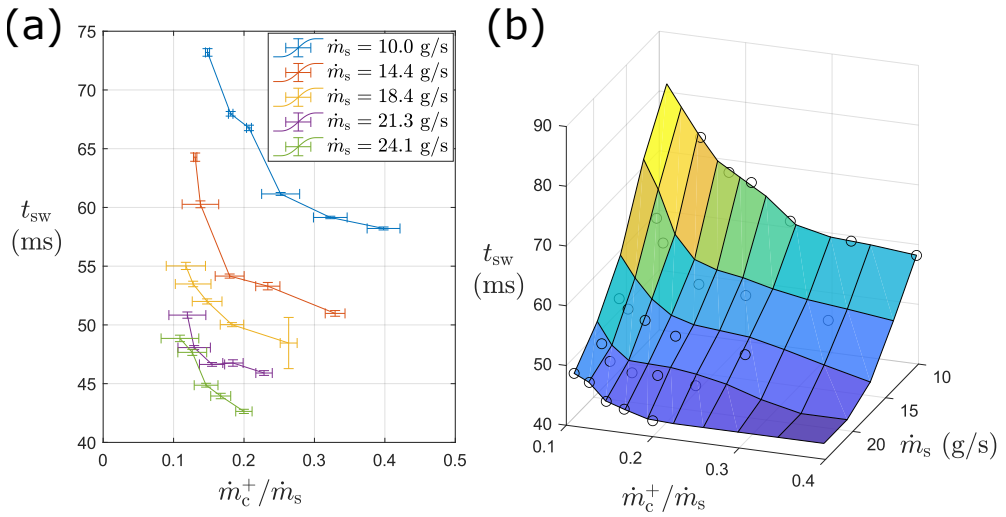

Fig. 4.40 (a) Measured vortex chamber radial (non-vortex) to tangential (vortex) state switching times (2σ errorbars) and (b) lookup table data constructed from a thin-plate smoothing spline interpolation

chamber is integral to the SVV cavity and cannot be tested in isolation. Consequently, the characteristic data presented here (figs.4.42) was measured concurrently with the SVV switch section characteristics.

Note that unlike the diverter section characteristics of both the pilot and the SVV, the Reynolds number parameter significantly impacts the vortex chamber

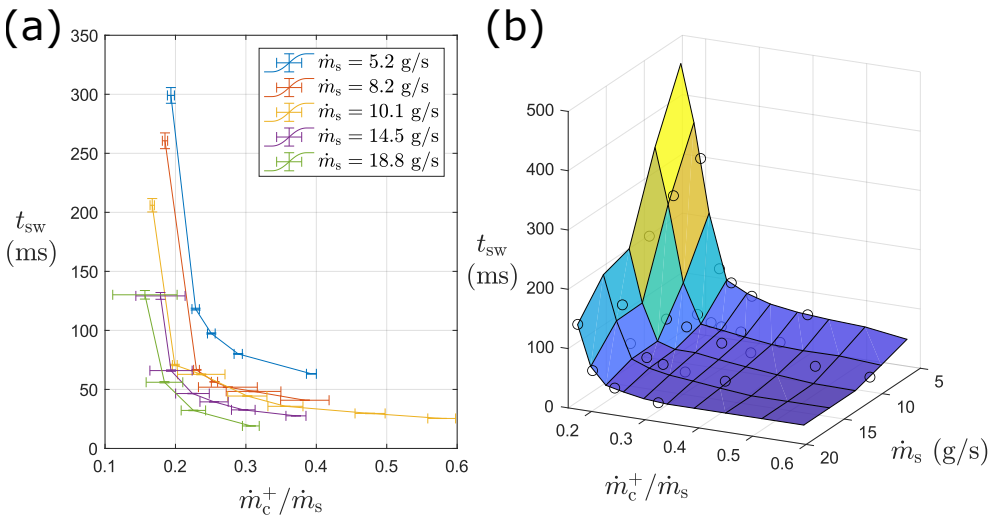

Fig. 4.41 (a) Measured vortex chamber tangential (vortex) to radial (non-vortex) state switching times (2σ errorbars) and (b) lookup table data constructed from a thin-plate smoothing spline interpolation.

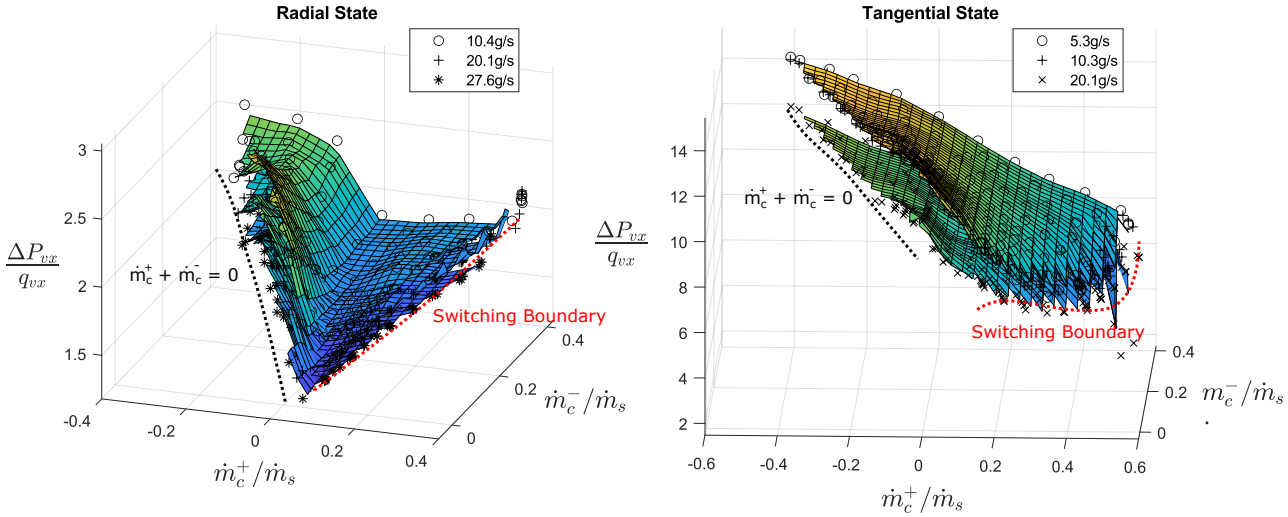

Fig. 4.42 Vortex chamber steady-state characteristics

characteristics. This is observed as an offset between characteristic surfaces when varying the supply flow rate ($\dot{m}_s$). This is not unexpected; as discussed in section 3.5, viscous forces are very influential when describing the steady-state behaviour of the vortex chamber.

Interestingly, increasing the Reynolds number in the tangential state only has a noticeable effect on the vortex chamber characteristic at the higher flow rates. Vastistas [108, 107] developed an analytical model that predicts the viscous vortex

core size and the pressure drop across a vortex chamber in the tangential state. The model predicts that the vortex core size and the dimensionless pressure difference ($\Delta p_{\mathrm{vx}}/q_{\mathrm{vx}}$) are functions of the vortex chamber geometry and are independent of the supply flow rate. Vatistas verifies these predictions with experimental observations in [107]. However, as part of the derivation of the analytical model, it is assumed by Vatistas that flows in the vortex chamber are incompressible. At lower flow rates ($\dot{m}_{\mathrm{s}} = 5.3\,\mathrm{g/s}$ and $10.3\,\mathrm{g/s}$), the tangential state characteristics agree with the constant $\Delta p_{\mathrm{vx}}/q_{\mathrm{vx}}$ prediction made by Vatistas. However, at higher supply flow rates, the vortex chamber transitions into the compressible flow regime, hence the emergence of dependence on $\dot{m}_{\mathrm{s}}$.

In both the radial and the tangential states, $\dot{m}_{\mathrm{c}}^{+}$ has more influence over the jet characteristic shape than $\dot{m}_{\mathrm{c}}^{-}$. This is consistent with the switch-section characteristics, which shows that $\dot{m}_{\mathrm{c}}^{+}$ has more influence over the switch section jet position.

In the radial state, it was expected that the flow field would be sensitive to small changes in the inlet jet position (figure 4.43). Under ideal circumstances (figure 4.43(a)), the inlet jet evenly bisects the vortex chamber, splashes against the vortex chamber wall and forms two counter-rotating vortices of roughly equal size. However, if the jet position is perturbed slightly from this ideal, one vortex will be slightly larger than the other. The larger vortex will exacerbate things by pushing against the jet, moving it further from its ideal position and further strengthening the larger vortex. In this manner, the flow field becomes asymmetrical, with the outlet port being exposed more to the interior portion of the dominant vortex. This reduces the average static pressure at the vortex chamber outlet and increasing Δp_{vx}.

A line of minima close to $\dot{m}_{\mathrm{c}}^{+} = 0$ is evident in the shape of the radial state characteristic. Any substantial $\dot{m}_{\mathrm{c}}^{+}$ control flows (negative or positive) will push the device away from the ideal state, increasing Δp_{vx}, although for $\dot{m}_{\mathrm{c}}^{+} > 0$, the Δp_{vx}

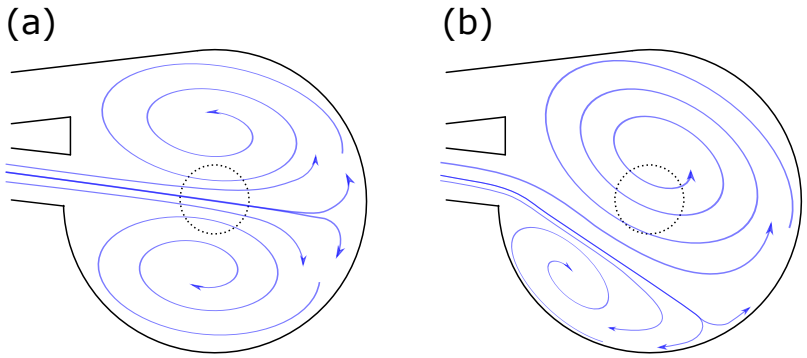

Fig. 4.43 Effect of a small change in inlet jet position for vortex chamber in the radial (non-vortex) state

variations are much smaller, forming a plateau in the characteristic. This plateau arises because the splitter constrains how far the jet can move in response to $\dot{m}_c^+$ (see figure 4.44). By this logic, there should be a similar plateau in the characteristic for $\dot{m}_c^+ << 0$, where the attachment wall starts to constrain the jet from moving in the other direction. A small portion of a second plateau does emerge in the radial characteristic for $\dot{m}_c^-/\dot{m}_s < -0.2$.

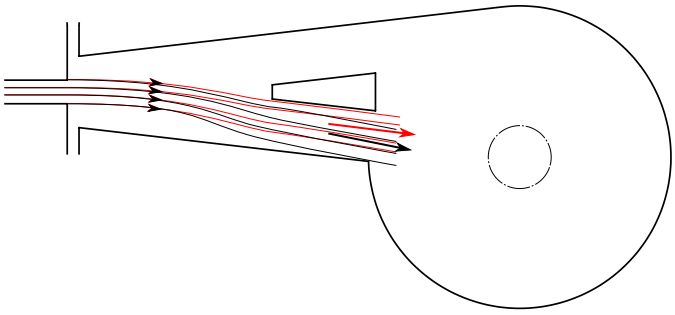

Fig. 4.44 Constraint on radial jet position imposed by the splitter.

The shape of the tangential characteristic is different; the attached side control jet is influencing the vortex chamber performance, but without encountering the constraints observed in the radial state. If the supply jet is not firmly attached to the duct wall upon entering the vortex chamber, the vortex formed will be elliptical rather than circular (see figure 4.45). An elliptical vortex will be weaker and positioned off-centre from the outlet port. $\dot{m}_c^+ > 0$ control flows will weaken attachment,

whilst $\dot{m}_c^+ < 0$ will strengthen attachment. So in general, increasing $\dot{m}_c^+ > 0$ in the tangential state will lower Δp_{vx}.

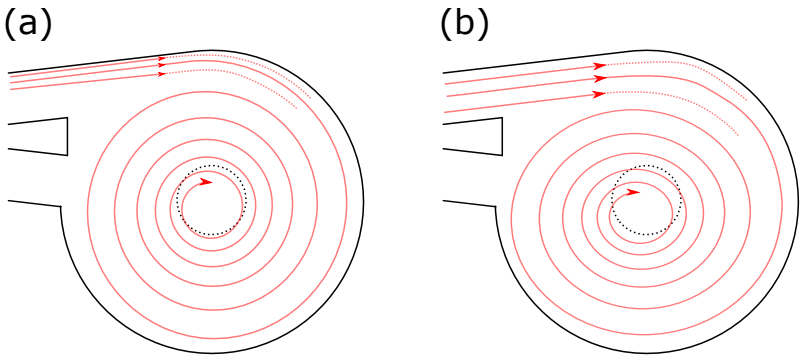

Fig. 4.45 Effect of change to jet profile on vortex chamber flow field in the tangential (vortex) state

4.4 Summary

The experimental data presented here characterises the steady-state and transient behaviour of the pilot and SVV stages in isolation. This data is used to tune the pilot and SVV stages of the model. Both halves of the model are now complete, and in isolation, they reliably replicate the behaviour of the pilot and SVV stages, as prescribed by the characteristics. However, correctly replicating the behaviour of the individual stages in isolation, does not guarantee that the model of the combined system will accurately recreate the inter-stage interactions that govern the steady-state and dynamic behaviours of the staged SVV.

Chapter 5
Numerical and Experimental Results with Mass Flow Injection Control

The previous chapter covered the acquisition of steady-state and transient characteristics for the pilot and SVV stages. This tuning data completes the grey-box model of the staged SVV, the construction of which is discussed in chapter 3.

The model's steady-state and dynamic predictions need to be compared with direct observations to assess the validity of the 2-stage model. The physical 2-stage device (figure 5.1) used for this comparison consists of the same diverter pilot and SVV stages used in chapter 4. The outlet ports of the pilot stage were designed to fit directly onto the control ports of the SVV, with o-ring seals at the pilot-SVV interface.

The experimental setup used to acquire both the steady-state and transient data with the staged SVV is presented in figure 5.2. The control mass flow rate was measured using an Omega FMA-A2323 mass flow meter. Pressures were measured using First Sensor HCX series pressure transducers (table 4.1) at the tappings indicated in figure 5.3. The locations of physical pressure tappings correspond to specific pressure nodes in the model, which allows for direct comparisons with simulated predictions of steady-state and transient behaviours.

Jet engines typically have pressure ratios of 1.1-1.3 for the compressor-to-turbine coolant flow paths. Within this range of applied pressure ratios, the coolant flow ducts are usually suitably sized to avoid significant losses, with flows generally in the incompressible flow regime. It is expected that a staged SVV used to modulate coolant flows would also have to be suitably sized to minimise losses in the radial (high flow) state and avoid entering into the compressible flow regime.

Most of the experiments and numerical simulations presented in this chapter have the staged SVV operating with gauge supply pressures of 30 mbar, 50 mbar or 70 mbar. The staged SVV vents to atmosphere, so these supply pressures can be expressed as applied pressure ratios 1.03, 1.05 and 1.07. The exception to this is the switching dynamics of section 5.3, which has the staged SVV entering into regimes with pressure ratios of 1.17-1.22 for radial-to-tangential switching and 1.018 for tangential-to-radial switching. Within the range of pressure ratios explored in this chapter, the pilot supply flow range is 1.5 - 5.7 g/s and the SVV supply flow range is 6.5 - 24 g/s. At these flow rates, the nozzle hydraulic diameter Reynolds number ranges are 6900-30000 for the pilot stage and 13000-50000 for the SVV stage. The nozzle Mach number ranges are 0.048-0.21 for the pilot stage and 0.046-0.17 for the SVV stage. Consequently, flows are expected to be completely turbulent and in the incompressible flow regime (outside the vortex chamber).

5.1 Steady-State Behaviour

The pilot and SVV stages of the model are tuned using steady-state characteristics gathered from the physical pilot and SVV devices (chapter 4). Consequently, it is expected that the pilot and SVV stages of the model will reliably predict the steady-state behaviours of both stages in isolation. However, it is still necessary to

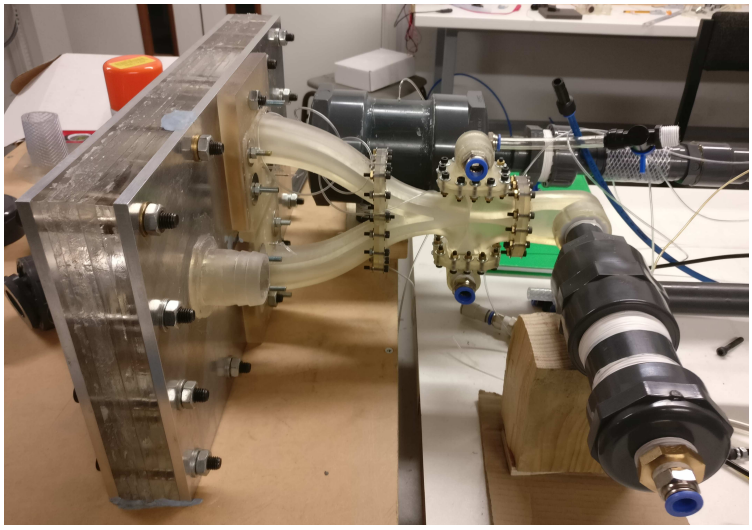

Fig. 5.1 Assembled staged SVV

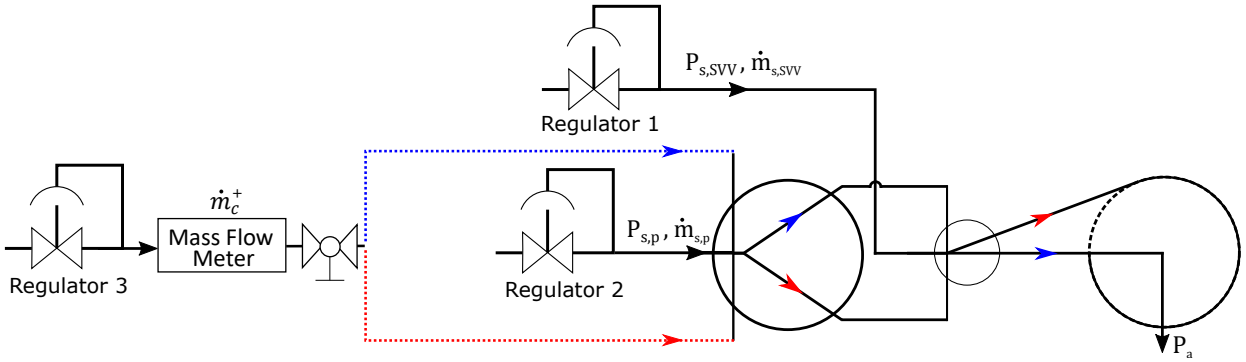

Fig. 5.2 Experimental setup for staged SVV with mass flow injection control. Differences in experimental setup for the radial (non-vortex) and tangential (vortex) states are marked in blue and red, respectively

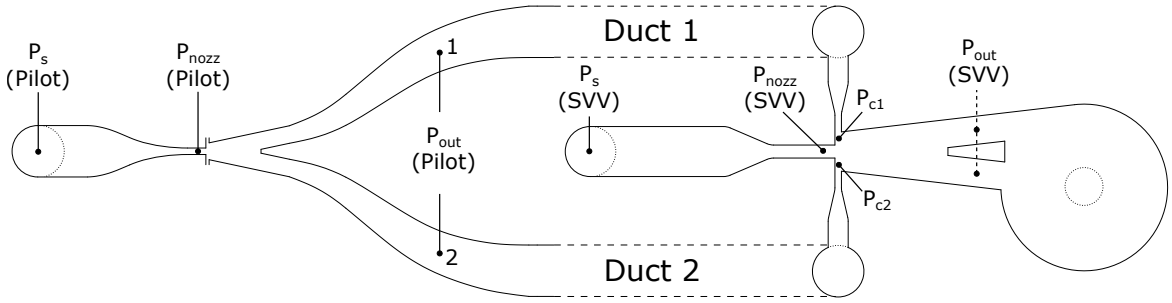

Fig. 5.3 Locations of key pressure taps for 2-stage system

make sure that the model correctly simulates steady-state behaviour for the combined system.

In figure 5.4, key pressures in both the pilot and SVV stages are compared with their simulated counterparts. In this case, both the pilot and the SVV stages have similar total supply pressures of 50 mbar gauge, with the SVV outlet venting to atmospheric pressure, this corresponds to an applied pressure ratio of 1.05. The predicted pressures in both the radial and the tangential states are very close to the measured values. The maximum deviation from measured values is 0.26 mbar (0.6%) in the tangential state and 0.83 mbar (2.0%) in the radial state. However, there are some pressure nodes for which the simulated values lie outside the uncertainty bounds (95% confidence interval) for the measured values. The discrepancies around the p_{out} nodes in the radial state are particularly noticeable.

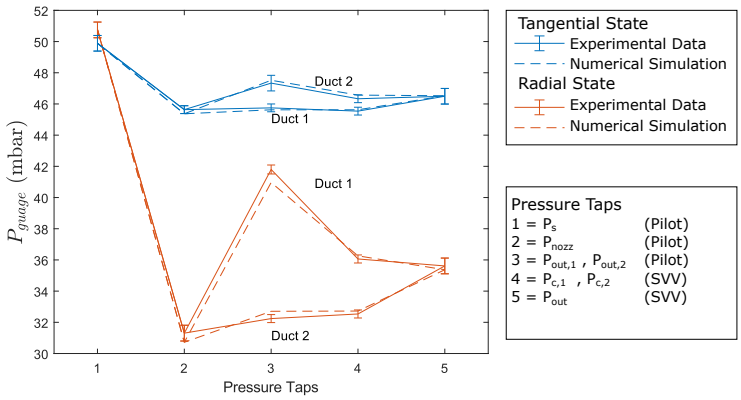

Fig. 5.4 Key pressures in the 2-stage system, when the pilot and SVV stages are supplied by the a 50 mbar source (PR ≈ 1.05).

There are some potential sources of error with regards to steady-state predictions. By characterising the devices in isolation before using those characteristics to construct the 2-stage model, some assumptions had to be made. First, there is the effect of acoustic tones on the steady-state behaviour of the diverter sections. It will be shown in chapter 6 that acoustic actuation at particular frequencies can shift the time-averaged steady-state operating points of the pilot diverter section. In [62, 59, 61, 57] Mair argues that acoustic tones influence diverter behaviours by exciting shear layer instabilities (see section 2.1.2). If this is the case, then acoustic tones could alter

the operating point of the pilot and SVV stages by shifting the operating points of their respective diverter sections. Both stages produce acoustic noise. There is the broadband noise associated with the jet shear layer turbulence. For the SVV, there is also an audible tone produced by the vortex chamber in the tangential state. In the tangential state, the vortex chamber resembles the vortex whistle device described by Vonnegut [111], the frequency of which increases linearly with supply mass flow rate [111, 114]. When incorporated into the staged SVV, the acoustic noise produced by the SVV could be altering the operating point of the pilot stage, whilst acoustic noise produced by the pilot stage could be having a similar effect upon the SVV stage.

5.2 Switching Dynamics

The transient switching process for the staged SVV was recorded using the same experimental setup as used for the steady-state observations (figures 5.2 and 5.3). Pressures were continuously recorded at a sampling rate of 15 kS/s, whilst the staged SVV was switching. The switching process was triggered by mass flow injection at the attached side control port of the pilot diverter section. The control flow rate was controlled by a screw-gate located downstream of the $\dot{m}_c^+$ mass flow meter. To capture a switching event, $\dot{m}_c^+$ was gradually increased until the device just switched.

Kelm KRS600-25-F-3 600 series pressure regulators were used to set the pilot and SVV supply pressures, reducing from a line pressure of 6.9 bar down to 50 mbar gauge. Interestingly, rather than observing constant pressures at the regulator outlets, there were noticeable shifts in the measured pressures when the staged SVV switched. The regulators were designed to operate with outlet pressures between 0 and 10 bar [42]. The observed pressure rise is due to the regulators being insensitive to small outlet pressure variations ~ 0.1 bar. The internal restriction size will remain fixed if the regulator is insensitive to outlet pressure variations. It may also be assumed that flow

at the restriction is choked; this is a reasonable assumption considering the $\sim 6.9\,\text{bar}$ pressure drop across each regulator. In that case, the regulators act as constant mass flow rate sources rather than constant pressure sources. When the staged SVV switches from the radial state to the tangential, the overall flow impedance of the staged SVV increases. For a constant mass flow source and exhaust pressure p_a, the supply pressures will increase. Conversely, for a tangential to radial switching event, the overall flow impedance will decrease, and there will be a supply pressure drop. In effect, the staged SVV is acting as a pressure modulation device rather than a mass flow modulation device due to the behaviour of upstream regulators.

In a jet engine, it is intended that a staged SVV be used to modulate coolant flow rates. If the staged SVV is inserted into the turbine coolant flow path, the supply and exhaust pressures will be set by conditions in the compressor and turbine sections of the jet engine. Given a fixed engine load, the pressure drop across the device will be approximately constant during a switching event. Provided that the staged SVV is suitably sized, the diverter sections will operate in the incompressible flow regime for both the high and low flow states. The experimental setup does not replicate a constant pressure drop. However, this is still a useful validation test of the model's transient response during a switching event , as the staged SVV is still switching between flow states in the incompressible flow regime. To make the comparison with the transient data, the model was simply modified to accept a constant mass flow source rather than a constant pressure source.

The transient pressures of radial-to-tangential and tangential-to-radial switching events are presented in figures 5.5 and 5.6, with experimental traces plotted alongside their simulated counterparts. Note that the maximum mass flow rates are 4.9 g/s for the pilot stage and 17.3 g/s for the SVV stage, which correspond to nozzle Mach

numbers 0.16 and 0.12.

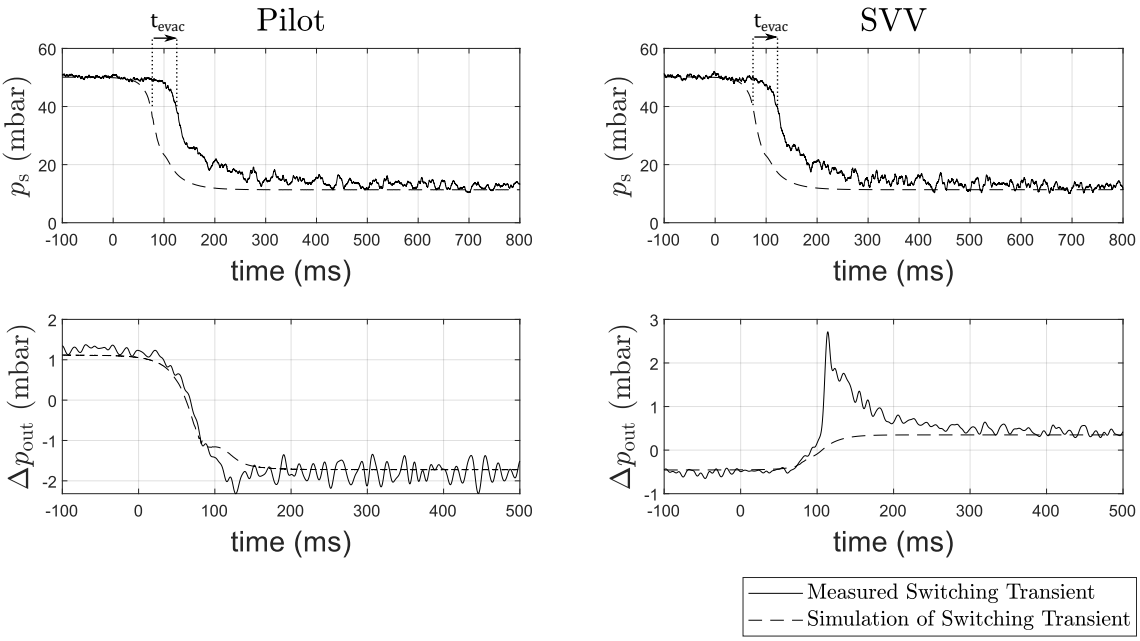

Fig. 5.5 2-stage switching from the tangential (vortex) to the radial (non-vortex) state.

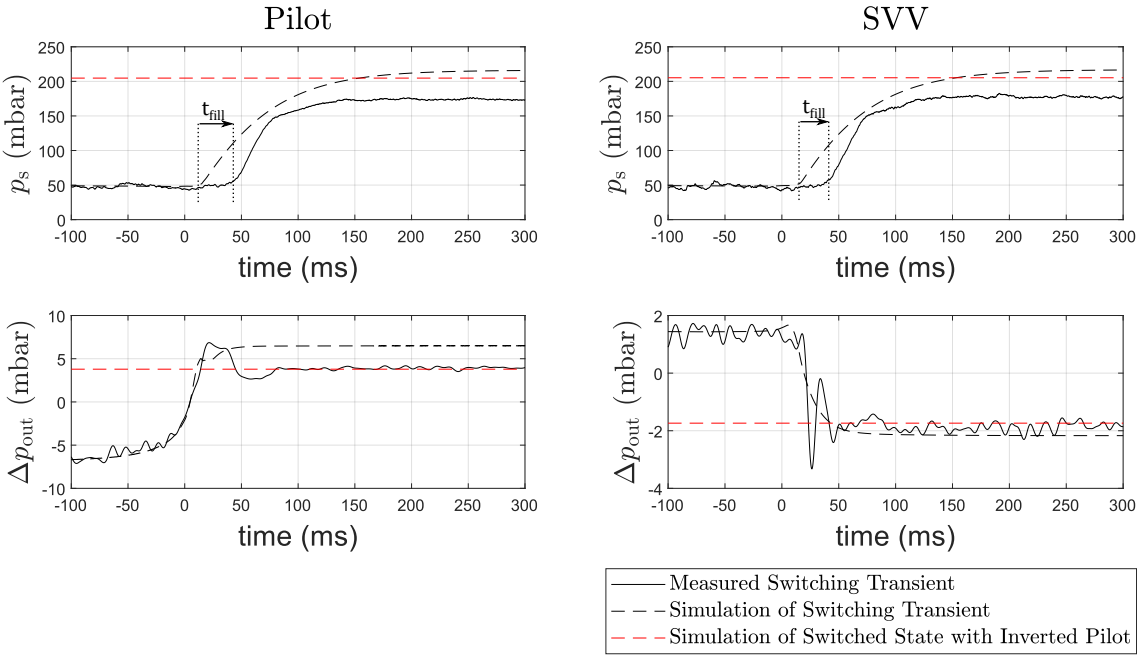

Fig. 5.6 2-stage switching from the radial (non-vortex) to the tangential (vortex) state.

The pressures plotted in figures 5.5 and 5.6 are the gauge supply pressures p_s and the diverter outlet pressure differences $\Delta p_{out} = p_{out,2} - p_{out,1}$ of the pilot and SVV stages. p_s values represent the overall switch state, with p_s rising and falling with the overall flow impedance of the staged SVV. Δp_{out} values represent each diverter section's attachment state. In most cases, the static pressure is higher in the attached outlet leg of a diverter switch. Thus the signs of Δp_{out} change when the diverter sections switch.

These transients highlight both the strengths and weaknesses of the grey-box modelling approach when it comes to predicting the transient behaviour of the staged SVV. The model is able to recreate switching behaviour in response to mass flow injection for both radial-to-tangential and tangential-to-radial switching. For tangential-to-radial switching, the model accurately predicts the steady-state pressures both and after the switching event. The model also gives a reasonable estimate of the rise and fall times of these pressures for tangential-to-radial switching. The rise and fall times of Δp_{out} and p_s are directly linked to the switching times of diverter and SVV sections. However, there are also notable discrepancies between the measured transients and the model's predictions for both tangential-to-radial and radial-to-tangential switching.

Most of these discrepancies arise because the grey-box model in its current form does not accurately simulate the propagation of pressure changes that originate at the vortex chamber as they travel upstream towards the supply regulators. In both the tangetial-to-radial and radial-to-tangential switching processes, the experimental p_s transients lag behind the modelled versions. These lag times are the result of finite fill and evacuation times (t_{fill} and t_{evac}) for the staged SVV cavity. When the outlet impedance of the staged SVV increases as a result of the vortex chamber switching from the non-vortex to the vortex state, it takes a finite amount of time

t_{fill} for the pressure rise at the vortex chamber to propagate upstream to the p_{s} pressure taps at the inlet ports of the pilot and SVV stages. Similarly, when the outlet impedance of the staged SVV decreases because the vortex chamber switches into the non-vortex state, it takes a finite amount of time t_{evac} for the subsequent pressure drop to propagate upstream to the p_{s} taps. In its current form, the model was designed to simulate inter-stage interactions, with the fill and evacuation times of the interstage ducting being recreated by the lumped element models of the ducts. However, the diverter and vortex chamber sections themselves constitute a considerable proportion of the staged SVV's internal volume, and the fill and evacuation times of these volumes are not accounted for in the model's design. Consequently, the model underestimates both t_{fill} and t_{evac} for the staged SVV as a whole.

The longer evacuation time for tangential-to-radial switching explains the appearance of a pressure spike in the SVV diverter sections Δp_{out} transient. When the vortex chamber initially switches from the vortex to the non-vortex state, there is a transient reduction in the outlet back-pressure for the SVV diverter section, and thus a transient increase in the flow velocities for the diverter. This increase in flow rates increases the pressure discrepancy between the attached and unattached sides of the diverter section, which leads to a transient increase in the pressure difference between the diverter section outlet ducts.

A consequence of the longer fill time for radial-to-tangential switching is that both diverter sections are able to almost complete the switching process before the pressure rise propagates through the pilot diverter section. However, as the pressure rise propagates upstream from the vortex chamber, there is a transient decrease in the pressure ratio across the pilot stage, the pilot diverter jet velocity decreases, and the Coandă effect is weakened. Consequently, the adverse outlet back-pressure difference imposed on the pilot diverter section by the nearly fully

switched SVV diverter section destabilises attachment and switches the pilot diverter. This secondary switching event for the pilot diverter section can be seen in the pilot's transient data as a sudden decrease in Δp_{out} at $t \approx 40ms$. Since the pilot stage has switched a second time, but the SVV stage has only switched once the pilot state no longer matches the SVV state, see figure 5.7.

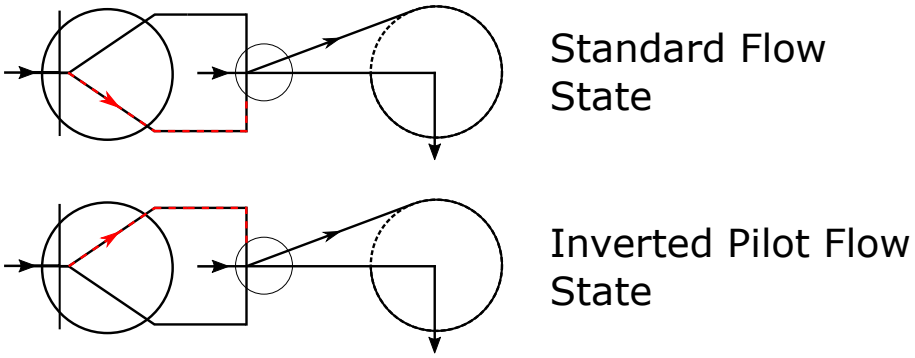

Fig. 5.7 2-stage device in the tangential (vortex) state with the pilot stage in the standard and inverted flow states.

The model does not anticipate a second switching event of the pilot stage for radial-to-tangential switching of the staged SVV. However, the model can be used to simulate steady-state pressures for this inverted pilot state[1]. The simulated steady-state pressures for the inverted pilot state are marked on figure 5.6. The pilot diverter Δp_{out} predicted by the model for the inverted pilot state closely matches the measured steady-state value after switching, partially corroborating the hypothesis that the pilot diverter section switches a second time.

However, despite accurately predicting the pilot diverter Δp_{out} value of the inverted pilot state, the model does not predict that the inverted pilot tangential state will be stable. To get predictions of the steady-state pressures for this state, the model's switching mechanism has to be deactivated. According to the model, $\dot{m}^{+}_{\text{out}}/\dot{m}_{\text{s}} = 0.27$ in this state, which should be too low for the pilot stage to remain

[1]To recreate the inverted state in the model, the switching mechanism is disabled and the switch state flags are set manually.

stable. Furthermore, the model does not accurately predict the final steady-state p_s values for tangential-to-radial switching. Interestingly, for the pilot diverter section to be stable, $\dot{m}^+_{out}/\dot{m}_s$ needs to be higher. Increasing $\dot{m}^+_{out}/\dot{m}_s$ would increase how much of the pilot's supply flow is directed towards the attached side control port of the SVV stage, which would lower the vortex chamber pressure loss coefficient and thereby reduce the p_s values. Consequently, it is theorised that the discrepancies with both the inverted pilot state's stability and the final p_s values have the same route cause. It is unknown what this route cause might be. However, it should be noted that in the tangential (vortex) state, the vortex valve produces a loud acoustic tone. The amplitude and frequency of this tone increase at higher flow rates, and the highest flow rates tested here were for radial-to-tangential switching. Furthermore, it will be shown in chapter 6 that both the outlet mass flow split and the stability of a diverter can be altered by subjecting it to acoustic tones.

5.3 Investigation of Oscillatory Instability

Staged fluidic devices with wall attachment components are susceptible to oscillatory instabilities [47]. These instabilities arise when upstream stages are not provided with high enough supply pressures (section 2.4). This instability has been observed experimentally with the staged SVV, and the investigation of this instability was one of the major motivations behind the development of the present numerical model.

The 2-stage device is stable in both the radial and tangential states provided $p_{s,p} \gtrsim p_{s,SVV}$. However, in the radial state, if the pilot supply pressure is gradually reduced, oscillatory instability will be triggered at a given threshold pressure. Once triggered, the entire system begins to oscillate, with both stages of the device switching back and forth between attachment states. Figure 5.8 presents the measured

transient pressures for the oscillatory instability alongside the simulated recreation. The model successfully recreates this oscillatory instability when the simulated pilot supply pressure is degraded. The experimental and simulated pressure traces capture the first four cycles of the oscillation, with the instability being triggered at $t = 0$. The simulation convincingly emulates the experimental pressure traces. The experimental and simulated Δp_{out} traces show both stages alternate between attachment states at a frequency of approximately 4 Hz, with the SVV stage lagging the pilot stage by approximately 50 ms. A small discrepancy in the frequency of oscillation is observed, with the real physical device oscillating at 4.4Hz but the numerical simulation predicting a frequency of 3.7Hz. Whilst the device is oscillating, there is corresponding a rise and fall in the supply pressures p_{s}, as the SVV stage changes state. When the SVV switches into the vortex state, there is a rise in the flow impedance and subsequently, the pressure drop across the device increases.

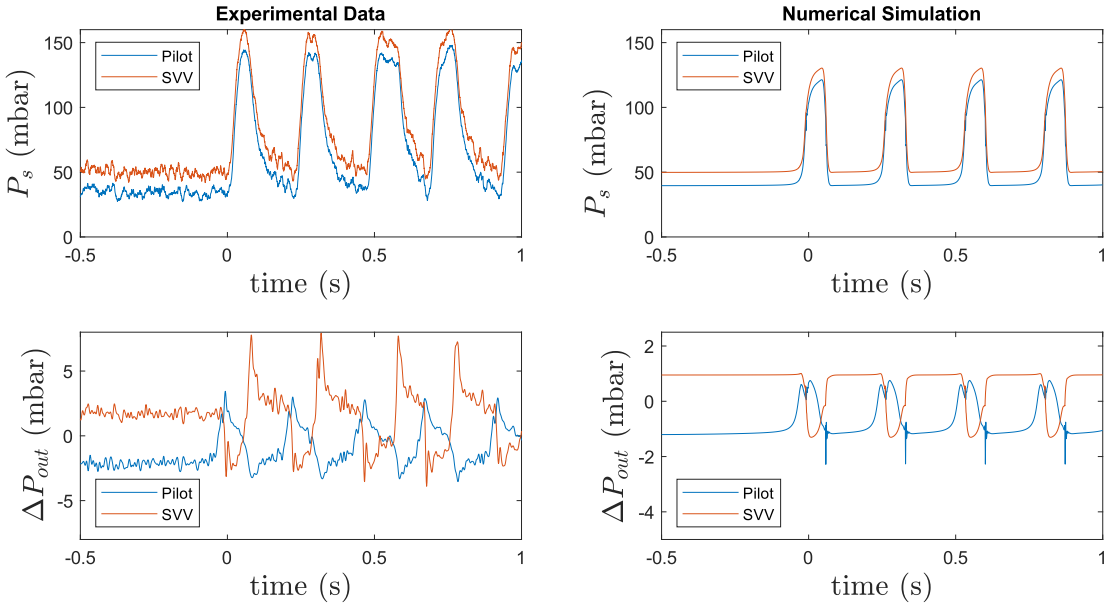

Fig. 5.8 Back-pressure switching oscillation cycle, $p_{\text{s,SVV}} = 50$ mbar

There are some discrepancies between the measured and simulated pressures in this case. The subtle differences in the shape of the pressure traces arise due to the way the switching process is modelled. As discussed in the previous section, switching

is modelled using symmetrical sigmoid functions that do not perfectly emulate the observed switching pressure traces of sections 4.2.4 and 4.3.3. The amplitudes of the p_s pressure spikes and the steady-state Δp_{out} values are slightly smaller for the simulated case. These differences can be attributed to the pilot pressures being slightly different at the instability threshold, $p_{s,p} = 0.68 p_{s,SVV}$ for the experimental data, whilst $p_{s,p} = 0.63 p_{s,SVV}$ for the simulation.

Figure 5.9 presents the supply pressure ratios $p_{s,p}/p_{s,SVV}$ at the instability threshold over a range of $p_{s,SVV}$ values. Over the range of $p_{s,SVV}$ values tested, both the experimental and numerically determined thresholds lie in the range $0.6 < p_{s,p}/p_{s,SVV} < 0.7$. The experimental work and numerical simulations show that the stability threshold's location is largely fixed, with only subtle variations as the SVV supply pressure increases. However, the simulation predicts a gradual lowering of the threshold as $p_{s,SVV}$ increases, whilst experimental observations show the threshold gradually rising. As mentioned in section 5.1, the model does not account for the effects of acoustic noise produced by the SVV stage. The steady-state operating point of the pilot stage will shift when subjected to acoustic tones (section 6.3.3). If the steady-state behaviour is acoustically modified, the stability threshold will shift with it. At higher $p_{s,SVV}$ values, the SVV stage was perceptibly noisier. Therefore, the acoustic modification of steady-state behaviour would be most pronounced at higher $p_{s,SVV}$ values. The largest discrepancies between the experimentally observed switching threshold and numerical predictions occur at higher $p_{s,SVV}$ values.

To understand the mechanism that underlies these oscillations better, figure 5.10 presents a single simulated oscillation cycle with the outlet pressure differences, the pilot stage outlet mass flow rates and the attachment state flags for the two diverter sections.

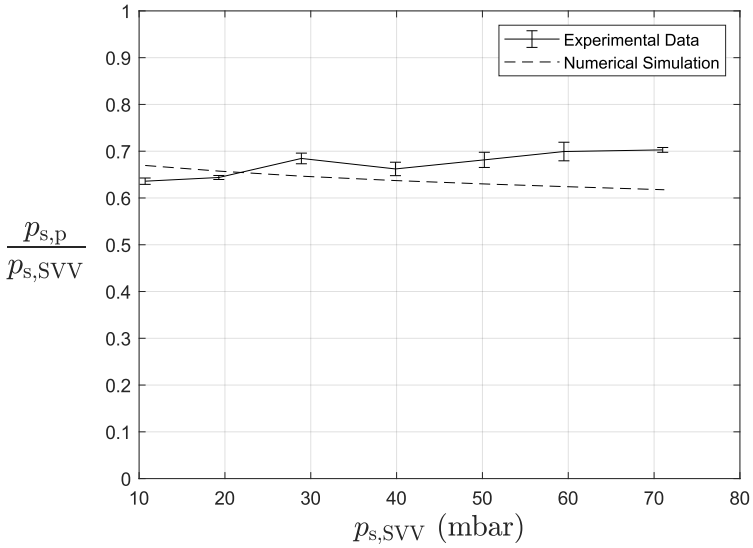

Fig. 5.9 Pilot supply pressures at the onset of oscillation

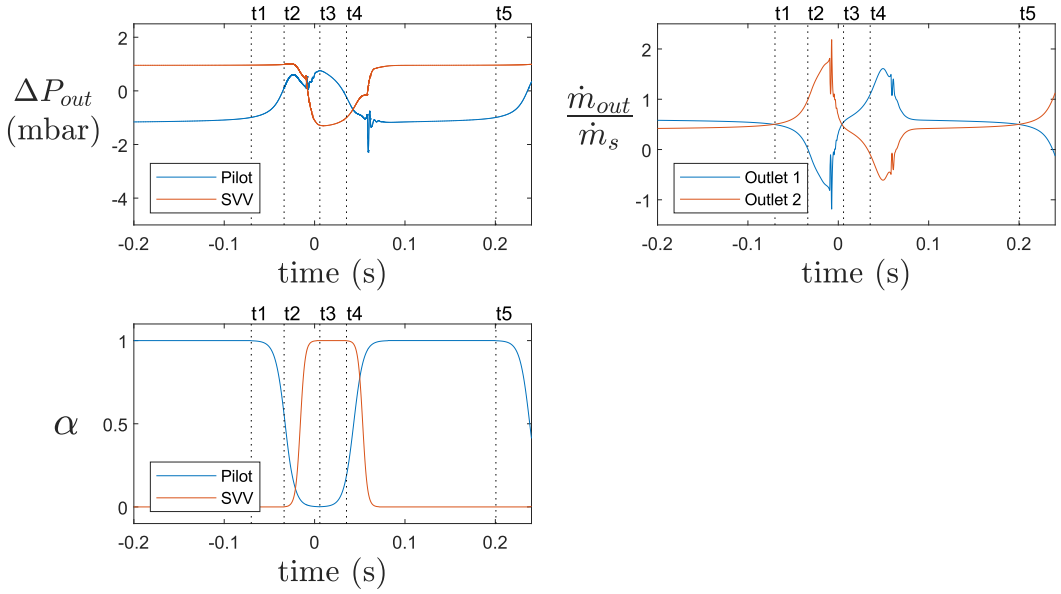

Fig. 5.10 Analysis of simulated oscillation cycle

The state flags can be used to pinpoint the times at which switching is triggered for both the pilot and SVV stages. Highlighted in figure 5.10 are five switching events labelled $t1$-$t5$. There are four switching events in a single oscillation cycle, two for the pilot stage ($t1$ and $t3$), and two for the SVV stage ($t2$ and $t4$). The fifth switching event $t5$ marks the start of the next oscillation cycle.

On the run-up to the first switching event ($t < t1$), the simulation shows a gradual rise in the pilot outlet pressure difference, and there is a corresponding drop in the attached side outlet mass flow split for the pilot ($\dot{m}_{\mathrm{out},1}/\dot{m}_{\mathrm{s}} = \dot{m}^{+}_{\mathrm{out}}/\dot{m}_{\mathrm{s}}$). This is a result of the adverse pressure difference imposed by the SVV stage upon the pilot stage. Under steady-state conditions, the pilot stage's attached outlet duct is connected to the unattached control port of the SVV. The SVV recirculation bubble ensures that $p^{+}_{\mathrm{c,SVV}} < p^{-}_{\mathrm{c,SVV}}$. Therefore, the SVV imposes a back-pressure difference that is in direct opposition to the primary flow path of the pilot. For sufficiently high pilot supply pressures, the Coandă effect for the pilot diverter section is strong enough to overcome this adverse back-pressure difference. However, as the pilot supply pressure is degraded, the diverter jet velocities decrease, weakening wall attachment. For weaker wall attachment, the adverse back-pressure difference has more influence over the outlet mass flow split and thus $\dot{m}^{+}_{\mathrm{out}}/\dot{m}_{\mathrm{s}}$ decreases.

At $t = t1$, the pilot outlet mass flow rate curves cross, as adverse back pressures push the pilot diverter to the point where more flow is spilling over the splitter than is being directed down the attached duct. Experimentally, pilot diverter section switching was observed for $\dot{m}^{+}_{\mathrm{out}}/\dot{m}_{\mathrm{s}} \approx 0.5$, and this switching boundary was incorporated into the model. The oscillations start when the back-pressure difference switches the pilot diverter. Switching initiated by the application of adverse back pressures will from here on be referred to as load-switching.

Once the pilot diverter section switches, the $\dot{m}_{\mathrm{out},2}$ duct becomes the attached outlet duct, the adverse back-pressure difference becomes a sympathetic back-pressure difference, and in response $\dot{m}_{\mathrm{out},2}/\dot{m}_{\mathrm{s}}$ rises rapidly. For $t1 < t < t3$, most of the pilot flow is being directed towards the attached control port of the SVV, and as $\dot{m}_{\mathrm{out},2}$ increases, the SVV attachment state weakens to the point where the SVV starts switching to the tangential state at $t = t2$. It takes a finite amount of time for the

SVV to switch and for the sympathetic pressure difference imposed by the SVV on the pilot to change back to an adverse back-pressure difference. After the SVV starts switching, $\dot{m}_{\mathrm{out},2}/\dot{m}_{\mathrm{s}}$ continues to rise until the back-pressure difference imposed by the SVV starts to counteract it. The attached side mass flow split starts to decrease again until the pilot diverter load switches at $t = t3$. Once again $\dot{m}_{\mathrm{out},1}$ becomes the attached side outlet mass flow rate, the back-pressure difference is sympathetic, and $\dot{m}_{\mathrm{out},1}/\dot{m}_{\mathrm{s}}$ rises until the SVV starts switching back to the radial state at $t = t4$.

5.4 Investigation into the Effect of Inter-Stage Duct Restrictions

One advantage of using a modular modelling approach is that it allows for modifications to the simulated 2-stage geometry. Ducting sections, in particular, can be modified with relative ease, as they do not rely on any empirical characterisation data. This would be particularly useful when designing the device for a real engine. It is expected that wherever the device is fitted, the space available will be restricted. If the staged SVV is to be packaged into a single compact unit, convoluted duct geometries may be required to minimise the volume it occupies. Alternatively, the device may be split up, with the SVV stage still positioned directly in the coolant path but with the pilot stage located at some distance from the main body of the device. This would require long lengths of inter-stage ducting connecting the halves of the device but would allow easy access to the control actuators attached to the pilot stage. In either case, a variety of ducting geometries might need to be investigated to find a design that fits within the physical space available while maintaining reasonable steady-state performance and avoiding oscillatory instabilities.

A simple test case that can be explored using the model is the addition of restrictions to the inter-stage ducting. As part of the characterisation process, it was discovered that vortex chamber performance is influenced by the SVV control flow rates $\dot{m}^{\pm}_{\mathrm{c,SVV}}$. Since $\dot{m}^{\pm}_{\mathrm{c,SVV}} = \dot{m}^{\mp}_{\mathrm{out,p}}$, if the pilot outlet mass flow split $\dot{m}^{+}_{\mathrm{out,p}}/\dot{m}_{\mathrm{s,p}}$ can be shifted by partially blocking one of the inter-stage ducts, then the pressure difference across the vortex chamber should shift, altering the total flow rate of the staged SVV.

The steady-state performance of a flow modulation device can be measured in one of two ways. There is the total mass flow rate in the high flow state, and there is also the turn-down ratio (TDR). As discussed in 2.2 and 2.3, the TDR compares mass flow rates in the high $\dot{m}_{\mathrm{out,R}}$ and low $\dot{m}_{\mathrm{out,T}}$ flow states [2]. For a staged SVV

$$\mathrm{TDR} = \frac{\dot{m}_{\mathrm{out,R}}}{\dot{m}_{\mathrm{out,T}}} \tag{5.1}$$

where the supply and exhaust pressures are fixed. The TDR is the device's negative gain as a turn-down amplifier. It is generally desirable that $\dot{m}_{\mathrm{out,R}}$ and TDR are maximised for a given operating pressure.

The effect of inter-stage duct restrictions on $\dot{m}_{\mathrm{out,R}}$ and the TDR was tested both experimentally and numerically. A schematic of the modifications applied to the experimental setup and the numerical model is presented in fig 5.11. For the experimental setup, the constrictions are 3D-printed inserts introduced at the junction between the pilot and SVV stage. Numerically, a duct constriction is recreated by altering the parameters for the $\dot{m}_2$ node of the lumped element model (section 3.3), namely the cross-sectional area A, the forward flow pressure loss coefficient $K_{\mathrm{L,fwd}}$,

[2] Subscripts R and T are used to indicate parameter values for the SVV in the radial (non-vortex) and tangential (vortex) states.

and the reverse flow pressure loss coefficient $K_{\mathrm{L,fwd}}$.

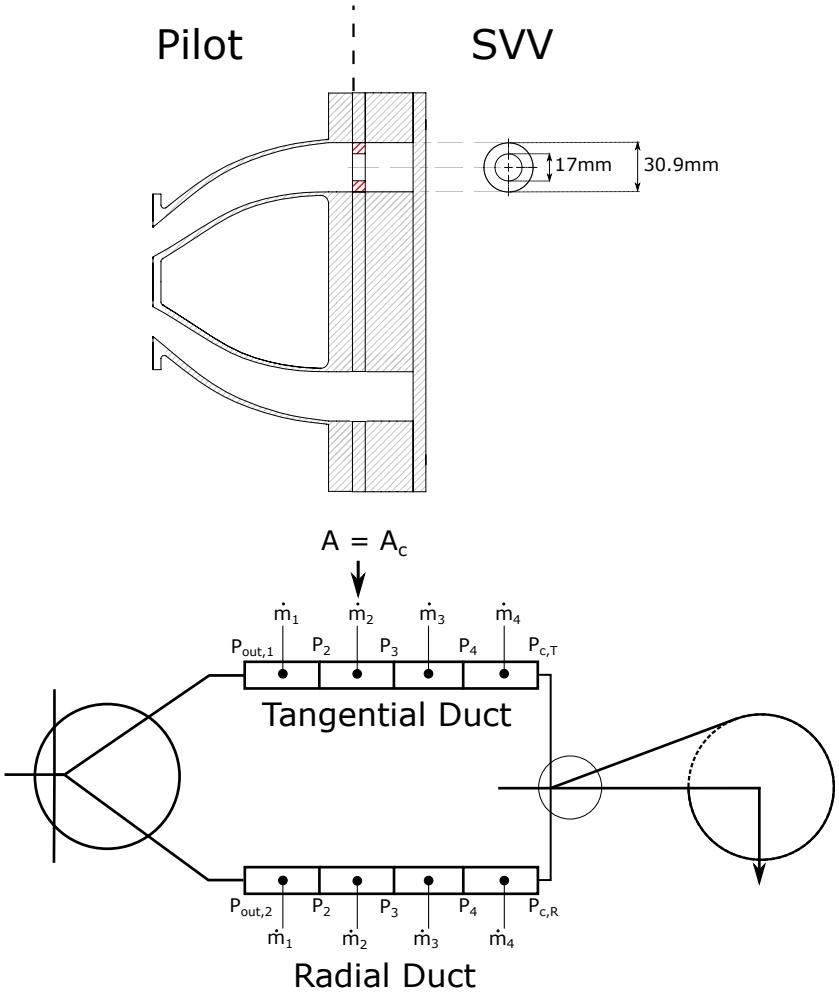

Fig. 5.11 Example of a tangential duct constriction with $d_{\mathrm{c}} = 17\,\mathrm{mm}$, and a marker indicating which node element of the simulated duct is modified.

The cross-sectional area A_2 is changed to the constriction area A_{c}. The forward flow ($\dot{m}_{\mathrm{out}} > 0$) loss coefficient combines loss coefficients for a sudden contraction $K_{\mathrm{L,c}}$, a sudden expansion $K_{\mathrm{L,ex}}$ and an elbow loss coefficient $K_{\mathrm{L,el}}$, such that

$$K_{\mathrm{L,fwd}} = K_{\mathrm{L,c}} + K_{\mathrm{L,ex}} + K_{\mathrm{L,el}} \tag{5.2}$$

The elbow loss is the loss coefficient that exists even in the absence of any restrictions and comes from the right-angle turn the flow is forced to make upon entering the

A_c/A_0	0.1	0.2	0.4	0.6	0.8	0.9
$K_{L,c}$	0.37	0.35	0.27	0.17	0.06	0.02

Table 5.1 Contraction loss coefficients [33]

SVV control duct. The loss coefficient for a typical 90° degree elbow fitting is 0.9, according to Howatson et al. [33]. The cross-sectional area of the flow through the elbow is the same irrespective of whether or not there is a constriction. However, the pressure loss across the mass flow element $\dot{m}_2$ is determined using the dynamic head of the restriction ($\Delta p = K_L.q_c$). To account for this difference in cross-sectional area, a factor $(A_c/A_0)^2$ is introduced, where A_0 is the unconstricted duct cross-sectional area ($d = 30.9\,\text{mm}$), i.e. $K_{L,el} = 0.9(A_c/A_0)^2$. The loss coefficient for the sudden contraction is also taken from Howatson et al. [33], which has a table of $K_{L,c}$ values replicated in table.5.1.

The sudden expansion contribution to the $K_{L,fwd}$ is given by $K_{L,c} = 1 - (A_c/A_0)$; this can be derived using the control volume method [64]. The relation for $K_{L,rev}$ is almost identical; it just lacks the $K_{L,el}$ contribution. As for reverse flow, the elbow loss contribution is still accounted for at the $\dot{m}_2$ node, but $K_{L,rev}$ is applied at the $\dot{m}_3$ node.

The results of numerical simulations and experiments with inter-stage impedances are presented in figures 5.12-5.14. The tangential duct connects the pilot stage to the tangential control port of the SVV, whilst the radial duct connects to the radial control port.

Despite the numerical simulations under-estimating total mass flow rates $\dot{m}_{tot}$, the simulations accurately reproduce the influence duct restrictions have on steady-state performance. The tangential duct restrictions are shown by the simulations to have greater influence over the steady-state behaviour in the radial state (figure 5.12). The simulations predict that $\dot{m}_{tot}$ increases in the radial state as the tangential duct

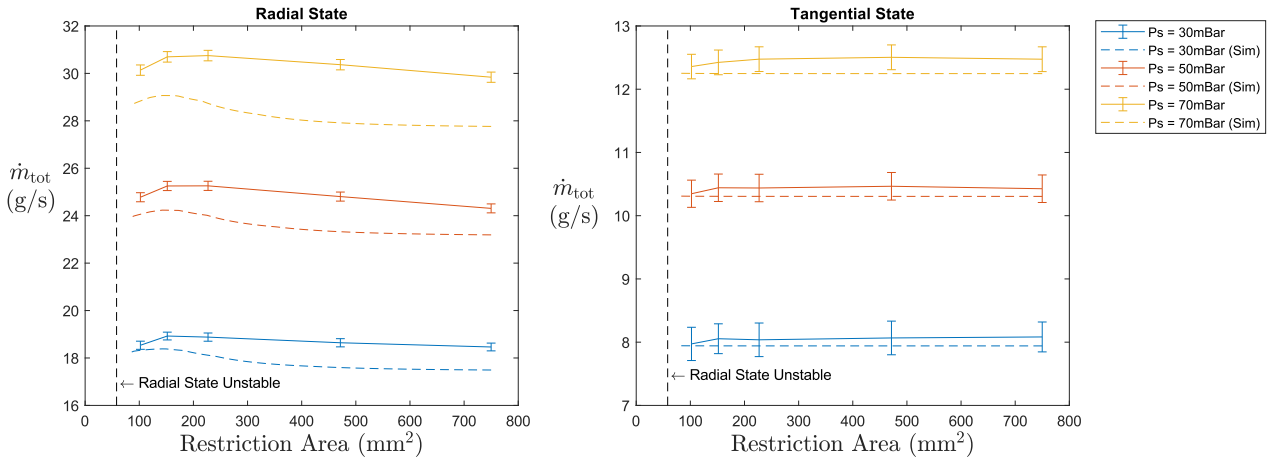

Fig. 5.12 Tangential duct constrictions on total flow rates ($p_{\text{s,p}} = p_{\text{s,SVV}} = p_{\text{s}}$)

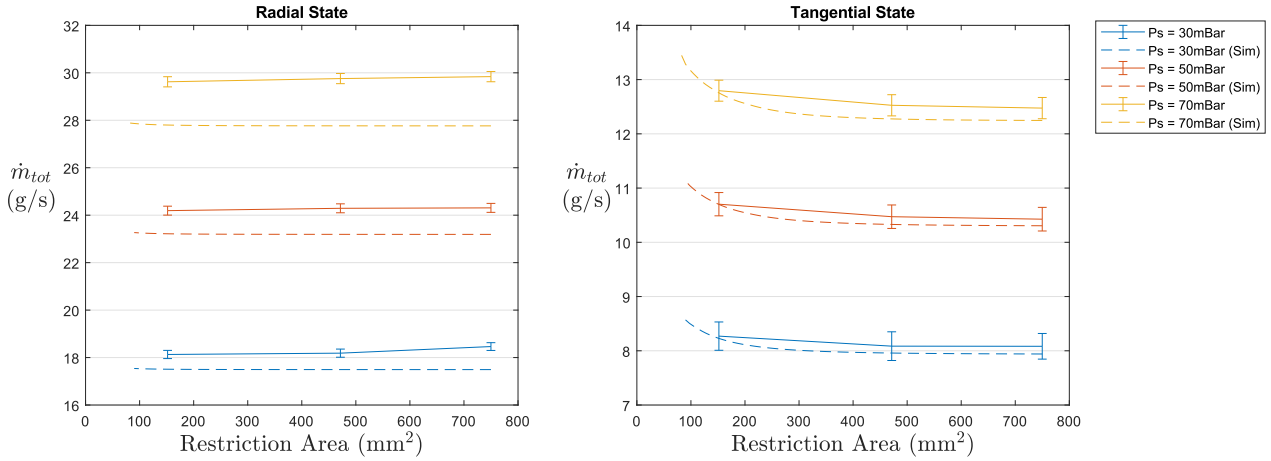

Fig. 5.13 Radial duct constrictions on total flow rates ($p_{\text{s,p}} = p_{\text{s,SVV}} = p_{\text{s}}$)

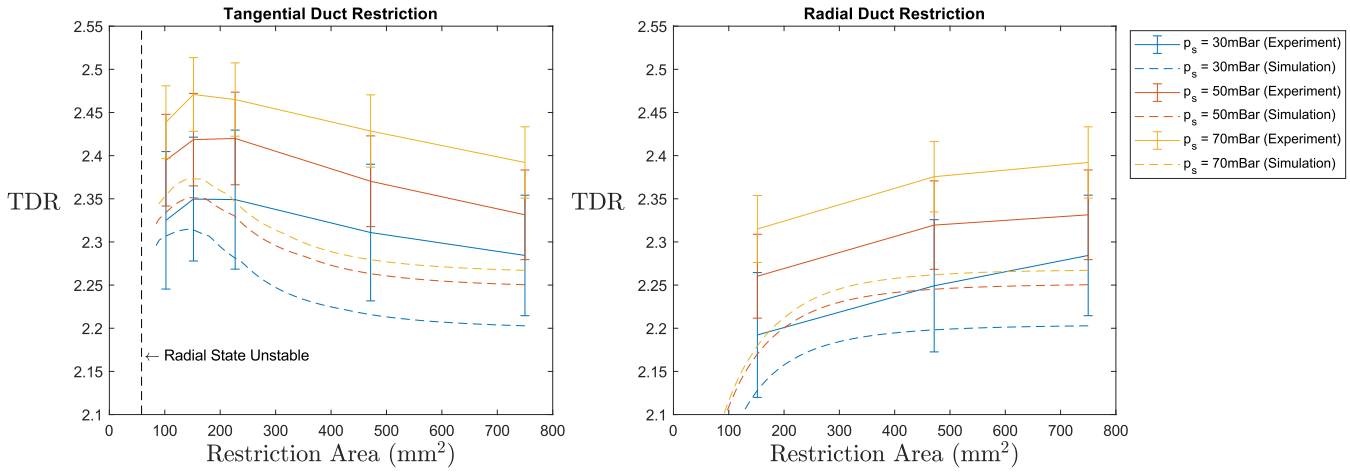

Fig. 5.14 Effect of interstage impedance on TDR of the 2-stage device ($p_{\text{s,p}} = p_{\text{s,SVV}} = p_{\text{s}}$)

restriction area A_c decreases up to an optimum A_c of 154 mm^2 (contraction ratio $A_c/A_0 = 0.205$). Reducing A_c beyond the optimum tangential restriction will reduce $\dot{m}_{tot}$ values in the radial state. If the area of the restriction in the tangential duct Ac is too small, the staged SVV will be unstable in the radial state for $p_{s,p} = p_{s,SVV}$, and will enter into an oscillatory state similar to that described in section 5.3. As represented by the TDR (figure 5.14), the steady-state performance will be improved by higher radial state $\dot{m}_{tot}$ values. These predictions about the effects tangential duct restrictions have on steady-style performance are broadly supported by the experimental observations.

Conversely, the simulations predict that radial duct restrictions have greater influence over the steady-state behaviour in the tangential state (figure 5.13). In general, the simulations predict that reducing A_c for radial duct restrictions will decrease $\dot{m}_{tot}$ in the tangential state. The TDR will decrease as $\dot{m}_{tot}$ decreases in the tangential state. Consequently, simulations show radial duct restrictions having a negative impact upon steady-state performance (figure 5.14). Once again, the predictions of the effects of radial duct restrictions on the steady-state performance of the staged SVV are consistent with experimental observations.

To understand the effects constrictions have on steady-state performance conceptually, it is useful to consider the primary flow paths of the pilot stage. The pilot directs most of its supply flow towards the tangential duct in the radial state. Conversely, most of the supply flow is directed towards the radial duct in the tangential state. The flow rates at the duct constriction and the subsequent pressure drop across the constriction is greater when the constriction lies in the primary flow path of the pilot stage. Consequently, tangential duct restrictions have greater influence over $\dot{m}_{tot}$ in the radial state (figure 5.12), whilst radial duct restrictions primarily

influence $\dot{m}_{\mathrm{tot}}$ in the tangential state (figure 5.12).

The primary flow paths correspond to the attached side outlets of the pilot stage. Restricting the attached outlet ports of the pilot stage reduces $\dot{m}^{+}_{\mathrm{out,p}}$, whilst increasing $\dot{m}^{-}_{\mathrm{out,p}}$. Under steady-state conditions $\dot{m}^{\pm}_{\mathrm{out,p}} = \dot{m}^{\mp}_{\mathrm{c,SVV}}$, so duct restrictions modify the SVV control flow rates. In the radial state, tangential duct restrictions reduce $\dot{m}^{+}_{\mathrm{c,SVV}}$. It was observed during the vortex chamber characterisation process (section 4.3.4) that the non-dimensional pressure difference across the vortex chamber $\Delta p_{\mathrm{vx}}/q_{\mathrm{vx}}$ is sensitive to $\dot{m}^{+}_{\mathrm{c,SVV}}$. In the radial state, for fixed $\dot{m}^{-}_{\mathrm{c,SVV}}$, $\Delta p_{\mathrm{vx}}/q_{\mathrm{vx}}$ decreases as $\dot{m}^{+}_{\mathrm{c,SVV}}$ increases until a minimum is reached ($0 \leq \dot{m}^{+}_{\mathrm{c,SVV}}/\dot{m}^{+}_{\mathrm{s,SVV}} < 0.1$), after which $\Delta p_{\mathrm{vx}}/q_{\mathrm{vx}}$ starts to increase again. For $A_{\mathrm{c}} \leq 154\,\mathrm{mm}^2$, the constrictions increase $\dot{m}^{+}_{\mathrm{c,SVV}}$, $\Delta p_{\mathrm{vx}}/q_{\mathrm{vx}}$ decreases, and $\dot{m}_{\mathrm{tot}}$ rises in response. The $\dot{m}_{\mathrm{tot}}$ maximum at $A_{\mathrm{c}} = 154\,\mathrm{mm}^2$ corresponds to the $\Delta p_{\mathrm{vx}}/q_{\mathrm{vx}}$ minimum of the vortex chamber characteristic surface.

Radial duct restrictions have a generally negative impact on steady-state performance. In a similar fashion to the tangential duct restrictions, radial duct restrictions increase $\dot{m}^{+}_{\mathrm{c,SVV}}$ in the tangential state. However, the vortex chamber characteristics for the tangential state do not have a minimum. Instead, as $\dot{m}^{+}_{\mathrm{c,SVV}}$ increases, $\Delta p_{\mathrm{vx}}/q_{\mathrm{vx}}$ decreases monotonically, and $\dot{m}_{\mathrm{tot}}$ increases in response. Therefore, increasing the tangential state mass flow rate has a negative impact on the steady-state performance as quantified by the TDR.

The numerical model successfully predicted the existence of an optimum constriction size (figure 5.14). The numerical model predicted that this optimum constriction size would be $A_{\mathrm{c}} = 154\,\mathrm{mm}^2$, which corresponds to a constriction area ratio $A_{\mathrm{c}}/A_0 \approx 0.205$. The experimental data also shows that there is an optimum constrictions size, though it appears to occur for a larger constriction area $A_{\mathrm{c}} \approx 190\,\mathrm{mm}^2$ ($A_{\mathrm{c}}/A_0 \approx 0.25$). This discrepancy could be the result of contraction pressure loss

coefficients $K_{\mathrm{L,c}}$ being inaccurate. More reliable $K_{\mathrm{L,c}}$ could be obtained through a characterisation process, this might reduce the observed discrepancy.

For different device geometries or feed conditions, the relative impedance of the inter-stage ducts required for optimum performance would shift. The model could then be used to either size duct restrictions or reprofile and resize the ducts themselves to optimise the overall performance of the multi-stage device. However, high duct pressure losses can make the device more susceptible to the oscillatory instability discussed in section 5.3. The duct pressure drop can increase the adverse back pressure difference experienced by the pilot diverter section, reducing the outlet mass flow split and pushing the diverter closer to the load-switching threshold. Load-switching of the pilot diverter section is the triggering event that initiates the oscillatory instability. Note that for the staged SVV, the optimum radial duct restriction area lies close to the radial state instability limit for $p_{\mathrm{s,p}} = p_{\mathrm{s,SVV}}$. If the inter-stage restriction area is too small, such that it is lower than the instability limit, the device will enter into an oscillatory state. Figure 5.15 shows that as tangential duct restrictions approach the radial state instability limit, the $p_{\mathrm{s,p}}/p_{\mathrm{s,SVV}}$ stability threshold increases. At the optimum restriction size $A_{\mathrm{c}} = 154\,\mathrm{mm}^2$, the stability threshold has increased from 0.68 (without restrictions) to 0.72. This higher stability threshold places tighter limitations on the pilot supply feed design; the supply feed $p_{\mathrm{s,p}}$ cannot degrade as far without triggering an oscillatory instability.

The next chapter will discuss acoustic control and acoustic control schemes that could be used to improve the TDR of the device without having the same deleterious effect on dynamic stability.

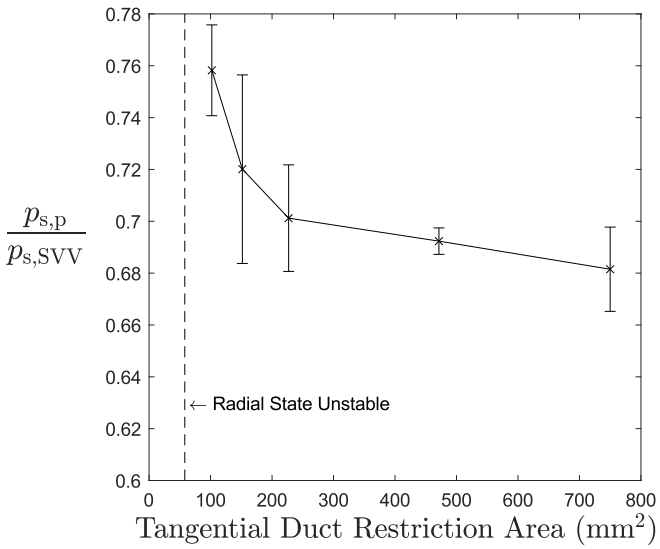

Fig. 5.15 Effect of interstage impedance on back-pressure switching limit of the 2-stage device ($p_{s,SVV} = 50\,\text{mbar}$)

5.5 Summary

This chapter covers the experimental and numerical exploration of the staged SVV with mass flow injection control. It starts with experimental validation of the freshly constructed model, comparing direct observations of steady-state pressures (section 5.1) and the transient pressures of a switching event (section 5.2) with the simulated versions. In both cases, the numerical model convincingly replicates the steady-state and transient behaviour of the staged SVV. Moving forward from here, the numerical model is used in conjunction with experiments to explore oscillatory instabilities in section 5.3. It is shown through an interrogation of internal model flow parameters that observed oscillations involves both stages of the device periodically switching between attachment states. Furthermore, the model also shows that the oscillations are triggered by the SVV load-switching the pilot diverter section. The model is used to investigate the effects of asymmetrical inter-stage constrictions on both steady-state performance and dynamic stability in section 5.4. It is shown both experimentally and numerically that inter-stage constrictions can be used to modify the steady-state performance of the staged SVV. Though the model could not accurately predict the

total flow rates, it successfully predicted the effect duct constrictions would have on steady-state performance. However, it was also shown that these inter-stage constrictions negatively impact the stability of staged SVV, making the device more susceptible to oscillatory instabilities.

Regarding the design of a staged SVV controlled by mass flow injection, some recommendations can be made based on the numerical and experimental observations presented in this chapter.

It has been shown that it is possible to construct a staged SVV with two stable states operation, and it has also been shown that the device can be switched between these states with mass flow injection at the pilot stage. However, some care is needed when designing the supply and interstage ducts. Significant pressure losses for the pilot stage supply duct or the interstage ducts connecting the pilot to the SVV stage will alter the steady-state performance. Furthermore, these pressure losses can make the device more susceptible to entering an unstable oscillatory state. In general, it is recommended that duct losses be minimised as much as possible to avoid destabilising the device. It has been shown that interstage restrictions can be used to passively improve the steady-state performance of a staged SVV. However, this is only possible if, without intervention, the SVV stage operates sub-optimally in the non-vortex state. Ideally, under such circumstances, the SVV geometry would be altered instead to improve steady-state performance, for example, by changing the SVV diverter section wall angle to change the inlet angle of the vortex chamber supply jet. It is theorised that the non-vortex state pressure loss coefficient is minimised when the vortex chamber supply jet is angled such that it near perfectly bisects the vortex chamber.

Chapter 6
Acoustic Actuation of Staged SVV

6.1 Introduction

The device that has been presented so far is switched using mass flow inputs at the pilot stage control ports. These mass flows could be controlled using solenoid valves in a coolant modulation system. However, mechanical valves are susceptible to high levels of wear and tear, particularly when exposed to high temperatures and pressures, and would therefore require regular maintenance. An alternative proposed here is to use acoustic actuation rather than mass flow injection to control the device. It has also already been shown by other studies [62, 57, 60, 59] that diverters can be switched by direct acoustic actuation. However, the acoustic actuation of a multi-stage fluidic device has never been demonstrated.

Piezoelectric actuators provide a robust means of producing control inputs and are well-suited to survival in the harsh environments found in the engine. Furthermore, the signal supplied by acoustic generators is not binary; the magnitude of the control input can be changed by varying the supply voltage. Suppose the acoustic generators can create a large enough flow disturbance to switch the pilot diverter section at lower voltages. In that case, they should be capable of shifting the operating point of the pilot diverter section and, by extension, the pilot stage. Acoustic actuation could then be used to alter the steady-state behaviour of the staged SVV. Furthermore, it will also be shown that sub-switching acoustic signals can be used to suppress the oscillatory instability discussed earlier. Consequently, acoustic actuation can be used

to improve the dynamic stability of the staged SVV.

6.2 Model Modifications

If acoustic generators are used both trigger switching and provide fine-tuned control of the steady-state behaviour, it would be useful to have a reliable numerical model on which to base the control scheme. The model presented in previous chapters has been modified to allow for simulations of the staged SVV with acoustic control inputs.

The acoustic signals are applied to the control ports of the pilot stage. For the model, it is assumed that acoustic signals only affect the pilot diverter section directly. In reality, the acoustic signals could propagate through the inter-stage ducts and influence the SVV diverter section directly, but this is not captured in the architecture of the model. Consequently, only the pilot diverter section of the model is modified for acoustic control. The acoustic signal does affect the behaviour of the SVV stage in the model, but only by changing the operating point of the pilot stage. When the pilot stage's operating point is shifted, it will alter flow conditions at the SVV stage's control ports.

Within the pilot diverter section of the model, references to the control flows $\dot{m}_{\mathrm{c}}^{\pm}$ are replaced by acoustic control parameters. The acoustic control parameters are frequency f, speaker voltage V_{RMS}, and a speaker location parameter $s = 0, 1$ which is a flag indicating to which of the two control ports the control signal is being applied.

With acoustic control, the dimensional steady-state characteristics become semi-dimensional characteristics of the form

$$\frac{\Delta p}{q_{\mathrm{nozz}}} = F\left(\frac{\dot{m}_{\mathrm{out}}^{+}}{\dot{m}_{\mathrm{s}}}, \dot{m}_{\mathrm{s}}, f, V_{\mathrm{RMS}}, s\right) \tag{6.1}$$

Note that a dimensional mass flow parameter $\dot{m}_s$ has been added because the control signal parameter V_{RMS} has not been non-dimensionalised. An attempt was made to non-dimensionalise V_{RMS}, with the assumption that sound pressure produced by the speakers is proportional to V_{RMS} (for a fixed frequency). However, as will be discussed later in section 6.3.3, this method does not work well in all cases.

To model sub-switching behaviour with acoustic steady-state characteristics, the transient equation 3.33 must also be modified, becoming

$$\frac{d}{dt}\left(\frac{\Delta p}{q_{nozz}}\right) = \frac{1}{\tau}\left[-\left(\frac{\Delta p}{q_{nozz}} - F\Big|_{t0}\right) + \sum_i \frac{\partial f}{\partial x_i}\left(x_i - x_i|_{t0}\right)\right] \tag{6.2}$$

where x_i are the parameters of the steady-state characteristic excluding s.

The switching boundaries, response times and switching times must all be modified in a similar manner. These modifications require that all of the pilot diverter section's tuning data be reacquired using an acoustically controlled version of the pilot stage.

In theory, an advantage of the modular model structure is that the entire device does not need to be re-characterised for design modifications that only apply to one component. In this case, the introduction of acoustic actuation for the pilot stage is accounted for by the reacquisition of tuning data for just the pilot diverter section. The SVV stage and ducting sections remain unchanged from the mass flow injection version of the model. However, there are some assumptions inherent to this modular approach.

Firstly, it is assumed that each section of the model is only responsive to bulk conditions at their flow boundaries. Therefore, the model does not account for any change in a section's behaviour that might result from changes in the flow profiles

at flow boundaries. Secondly, it is assumed that neither the jet noise produced by the diverter section nor the acoustic tone produced by the vortex chamber significantly impacts the diverter sections' behaviour. These assumptions are discussed in section 5.1 as potential sources of error for the mass flow injection version of the model.

With the introduction of acoustic actuation, some additional assumptions are made. Firstly, it is assumed that the acoustic tones produced by actuators attached to the pilot stage only directly influence the behaviour of the pilot diverter section. In other words, it is assumed that the amplitude of the acoustic tones have sufficiently diminished by the time they reach the SVV stage that they have minimal effect on the behaviour of the SVV diverter section. Secondly, it is assumed that the pulsating outlet flows produced by the pilot diverter section in response to acoustic actuation (more on this in the next section) do not affect the time-averaged steady-state behaviour of the SVV stage.

6.3 Acoustic Characterisation of the Pilot Stage

6.3.1 Pilot Stage Modifications

The acoustically controlled 2-stage model is based on the same physical device used in previous chapters, with modifications to the pilot stage to allow a pair of FR 58 8 Ohm Visaton loudspeakers to be fitted. Although the speakers are designed to operate between 120-20000 Hz, the frequency response is particularly flat within the reduced range of 180-2500 Hz, with maximum sound pressure deviations of ± 2 dB (1 W/1 m) see figure 6.1. This response spectrum does not account for any non-linear interactions between the loudspeakers and the amplifier/signal generator. The spectrum also does not account for the acoustic resonance properties of the pilot stage

cavity.

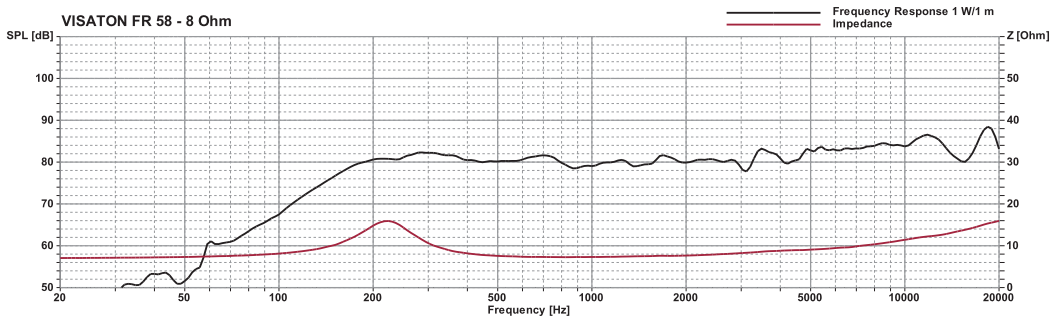

Fig. 6.1 Loudspeaker frequency response graph from the datasheet [110]

The speakers are connected to the diverter section using 3D-printed loudspeaker adapters that replace the mass flow control port adapters (see figures 6.2 and 6.3). Each speaker is housed in an air-tight volume that connects to the main cavity via the 3 mm bleed ducts. These bleeds equalise the pressure across the speaker cone. Differential pressures across the cone can impact the speaker performance. The speakers are driven by a Tektronix signal generator (AFG1022) via a 40 W power amplifier (Kemo Electronic M034N).

6.3.2 Frequency Response of the Pilot Diverter Section

A complete model could have characterisations that cover a wide range of frequencies and voltages. However, in practice, there exist particular frequencies that elicit a much stronger response from the pilot diverter section than others. It therefore makes more sense to narrow the focus of any characterisations to these particular frequencies.

The experimental setup used to measure the acoustic steady-state characteristics and gauge the pilot stage's frequency response is the same, figure 6.4. This setup is similar to the configuration used to measure the mass flow control characteristics. The only significant difference, apart from the addition of loudspeakers, is a 25 m length of flexible tubing (internal diameter= 44.3 mm) inserted between the attached

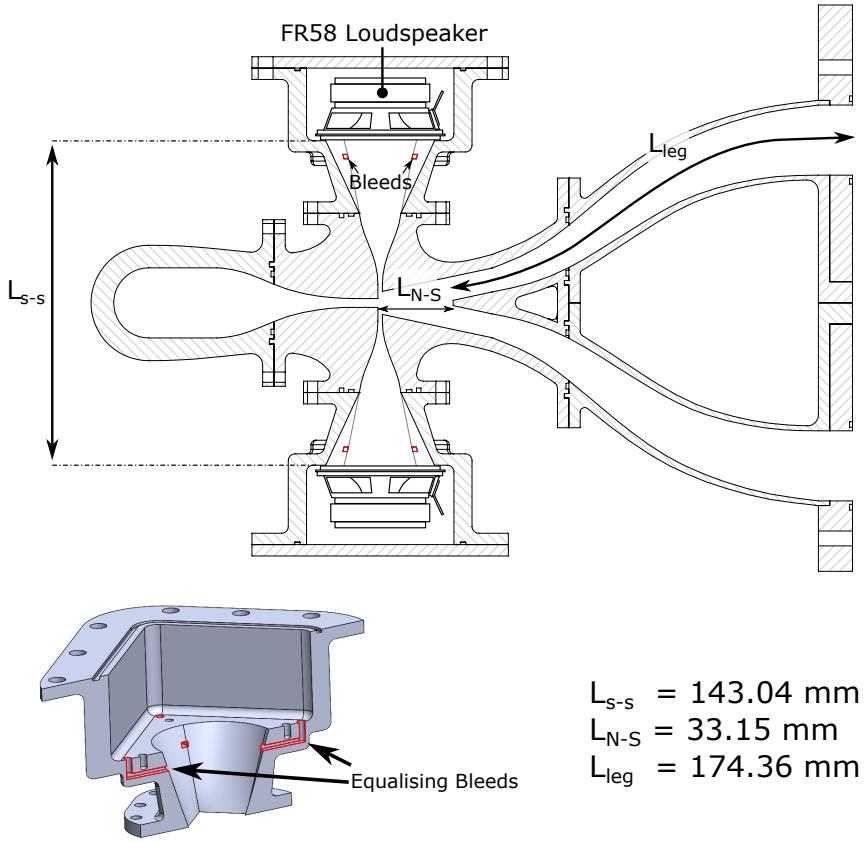

Fig. 6.2 Schematic of modified pilot stage with loudspeakers. Equalising bleeds marked in red

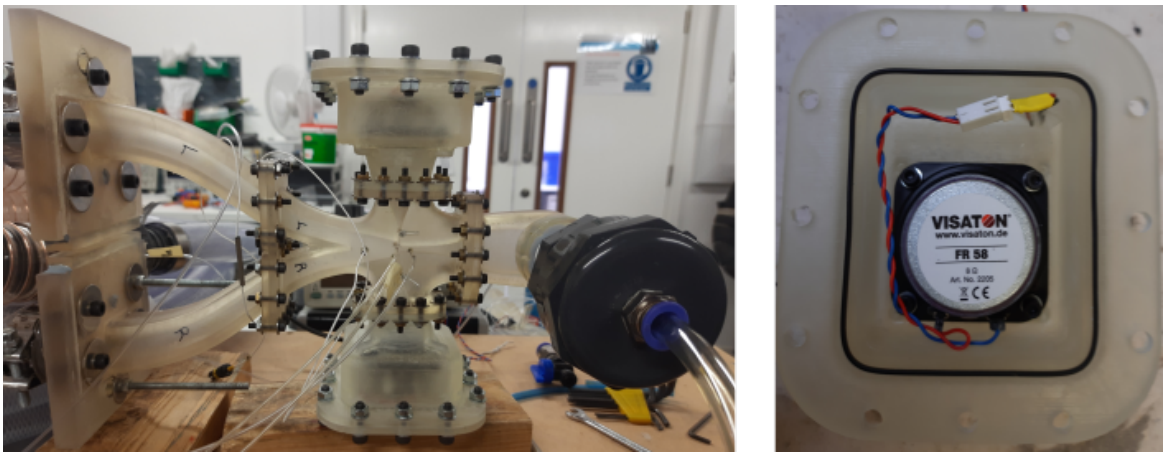

Fig. 6.3 Pilot stage modified for acoustic actuation

outlet port and the orifice meter. When acoustic tones were applied to the pilot stage, there was a noticeable rise in the amplitude of pressure fluctuations observed at the pilot stage pressure tappings. Furthermore, without the coil of tubing, there were also large transient fluctuations in the pressure drop measured across the $\dot{m}^{+}_{\text{out}}$ orifice

meter. The orifice meter pressure drop fluctuations indicated a pulsating outlet flow. As discussed in chapter 2, acoustic tones excite the shear layer instabilities of a diverter supply jet, inducing the early formation of shear layer roll-up vortices. It is believed that the observed increases in pressure and mass flow fluctuations correspond to jet perturbations by strengthened shear layer vortices. Practically speaking, pulsating outlet flows negatively impact $\dot{m}^{+}_{\mathrm{out}}$ measurement accuracy, as the orifice meter is not designed to operate with pulsating flows [3]. This loss of accuracy manifests as an increase in the time-averaged measurements of $\dot{m}^{+}_{\mathrm{out}}$ when acoustic tones are applied, even when $\dot{m}_{\mathrm{s}}$ is held constant and the unattached outlet port of the pilot stage is blocked ($\dot{m}^{-}_{\mathrm{out}} = 0$). Since there is no possible physical source for the additional mass flow, the observed increase in $\dot{m}^{+}_{\mathrm{out}}$ values must be the result of measurement error. The 25 m length of tubing mitigates this issue, as viscous forces attenuate the fluctuations as they propagate downstream. With the additional tubing in place, the outlet orifice plate pressure drop fluctuations were minimised, and the measured mass flow rate discrepancies disappeared even for higher speaker voltages.

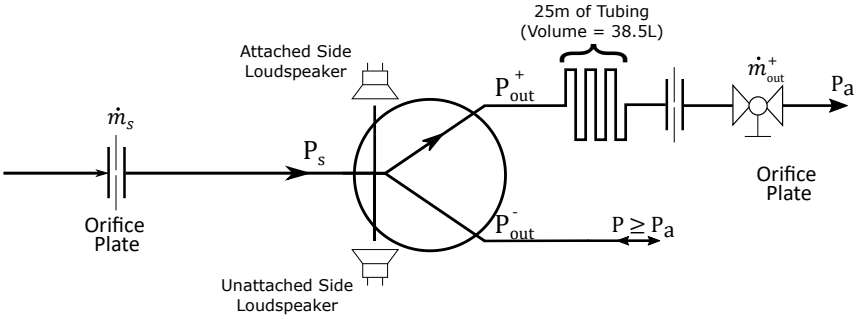

Fig. 6.4 Experimental setup for measurement of pilot stage acoustic characteristics

The frequency response spectra of the pilot stage acquired using this experimental setup are presented in figure 6.5. The outlet mass flow splits $\dot{m}_{\mathrm{out}}/\dot{m}_{\mathrm{s}}$, and outlet pressure differences Δp_{out} were measured whilst sweeping through actuation frequencies. This process was repeated for different supply flow rates and swapping between

the speakers at the attached and unattached sides of the device. The applied voltage in each case was set to the maximum value possible without triggering a switching event; this was done to maximise the pilot stage response and make it easier to pick out the maximum response frequencies accurately.

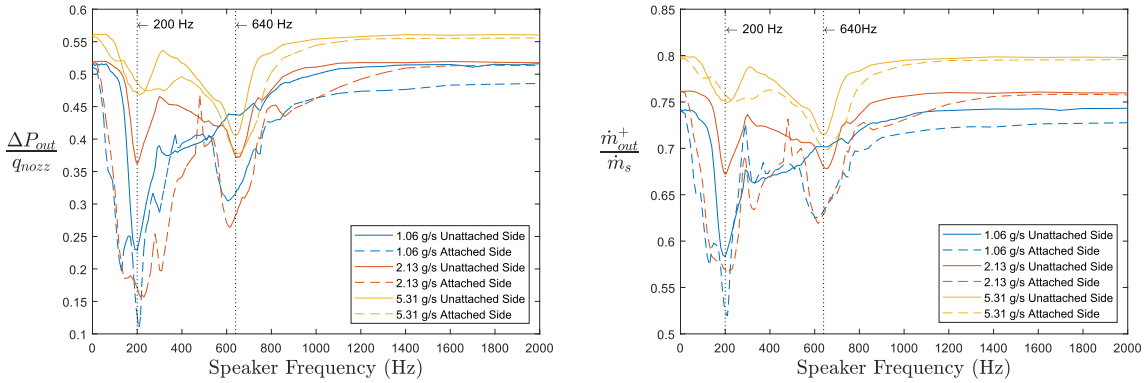

Fig. 6.5 Frequency response of the pilot stage operating point.

Two distinct maximum response frequencies emerge from the spectra, 200 Hz and 640 Hz. Although the attached side maximum response frequencies increase slightly with $\dot{m}_s$, these frequency shifts are reasonably small. According to some sources [62, 59, 57, 69], acoustic tones influence a diverter's behaviour by exciting shear layer instabilities and thus increasing the jet spreading rate. The fundamental vortex frequency for a jet is given by the momentum thickness Strouhal number $St_\theta = 0.012$ [35, 120]. Consequently, a diverter should be more responsive to frequencies close to the Strouhal frequency $St_\theta = 0.012$ [62] or one of its sub-harmonics [59]. If maximum response frequencies 200 Hz or 640 Hz correspond to $St_\theta = 0.012$ or one of its harmonics, then there should be a strong dependence on $\dot{m}_s$ since

$$St = St\frac{f\theta}{\bar{u}} \tag{6.3}$$

However, the maximum response frequencies have been found to respond only weakly to $\dot{m}_s$. It is therefore theorised that the pilot stage is more responsive to $f = 200$ Hz

and 640 Hz because of cavity resonance frequencies.

Length scales within the cavity are too short to justify a 200 Hz standing-wave resonance. The longest continuous length within the cavity is the supply nozzle to outlet distance $L_{\text{N-O}}$.

$$\begin{aligned} L_{\text{N-O}} &\approx L_{\text{N-S}} + L_{\text{leg}} \\ &= 207.5 \text{ mm} \qquad \text{see figure 6.2} \\ &= 0.12\lambda_{200\,\text{Hz}} \end{aligned} \tag{6.4}$$

The combination of the loudspeaker, loudspeaker adapter and control port is similar to the construction of a synthetic jet actuator. Synthetic jets are discussed in greater depth in (chapter 2), but they primarily consist of a flow cavity with a nozzle at one end and an acoustic actuator at the other. Analytical models of these devices are presented in [23, 75], both of which closely emulate experimental observations and suggest the existence of two maximum response frequencies f_1 and f_2. Frequencies f_1 and f_2 are related but not necessarily identical to the cavity Helmholtz frequency f_{H} and the actuator diaphragm frequency f_{D}. These maximum response frequencies arise due to coupling between the cavity and the acoustic actuator resonances and are given by roots of the relation

$$\psi^2 + \left[f_{\text{D}}^2\left(1 - C_{\text{d}}/C_{\text{c}}\right) + f_{\text{H}}\right]\psi + f_{\text{D}}^2 f_{\text{H}}^2 = 0 \tag{6.5}$$

where C_{d} and C_{c} are acoustic compliances of the diaphragm and the cavity. In the limit where the cavity volume is large or the diaphragm is very stiff $C_{\text{d}}/C_{\text{c}} \to 0$, frequencies f_1 and f_2 coincide with f_{D} and f_{H}. Note that if f_1 and f_2 are roots of equation 6.3.2 then

$$f_1 f_2 = f_{\text{D}} f_{\text{H}} \tag{6.6}$$

The resonance frequency of the loud speaker was 190 Hz [110]. If $f_1 = 200\,\text{Hz}$ and $f_D = 190\,\text{Hz}$, then $f_2 = 0.95 f_\text{H}$. The Helmholtz frequency of a cavity is given by

$$f_\text{H} = \frac{c}{2\pi}\sqrt{\frac{A}{V_\text{c} L'}} \quad [8] \tag{6.7}$$

where A is the throat area, V_c is the cavity volume, and L' is the equivalent neck length. The equivalent neck length is given by

$$L' = L + kD_\text{h} \tag{6.8}$$

where L is the actual neck length, $k = 0.3 - 0.85$ is a length correction factor, and D_h is the hydraulic diameter of the neck. The volume of the loudspeaker adapter-control duct cavity is $4.69{\times}10^4\,\text{mm}^3$, the control port cross-sectional area is $39\,\text{mm}^2$, the control port length is 3 mm, and the hydraulic diameter is 3.55 mm. Based on these physical dimensions, the Helmholtz resonator frequency of the loudspeaker adapter-control duct cavity is estimated to be $636 - 774\,\text{Hz}$. Consequently, the synthetic jet resonance frequencies f_1 and f_2 are candidates for the 200 Hz and 640 Hz maximum response frequencies. In other words, applying acoustic excitation at 200Hz and 640Hz may be producing a synthetic jet at the control port outlets.

Alternatively, the 640 Hz maximum response frequency could result from a standing-wave resonance formed between the loudspeaker boundaries. Only one of the two speakers is turned on for the spectra presented in figure 6.5. For a speaker-to-speaker standing wave, the active loudspeaker is a flow displacement node, whilst the inactive speaker acts as a rigid wall making it a flow displacement anti-node. Thus the first resonance frequency should correspond to a 1/4 wavelength. The loudspeaker-to-loudspeaker distance $L_\text{S-S} = 143\,\text{mm} = 0.27\lambda_{640\,\text{Hz}}$.

An omnidirectional condenser microphone (Kingstate MKD-7690) was used to test the hypothesis that 200 Hz and 640 Hz maximum response frequencies correspond to resonance frequencies. A hole was drilled close to the splitter (figure 6.6), and the microphone was inserted into the hole and glued in place. The microphone was not positioned directly next to the control ports because of concerns that even subtle changes to the geometry close to the control ports might affect the device's behaviour. Sound pressure levels measured whilst sweeping through the frequencies are presented in figure 6.7. The combined effects of cavity resonances and speaker output variations should be evident in the spectra measured, figure 6.7.

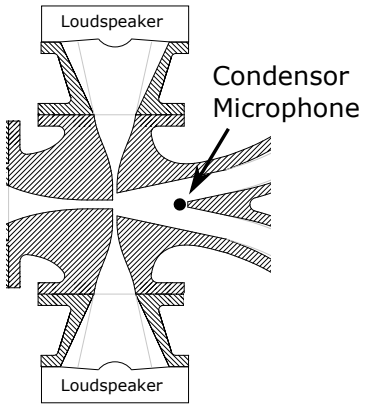

Fig. 6.6 Mounting location of the condensor microphone.

The resonance frequencies of 290 Hz and 580 Hz measured at the splitter are far from the maximum response frequencies of the pilot stage. Unfortunately, the exact mechanisms by which the acoustic signal interacts with the jet to effect a change in state is not yet fully understood. However, since the maximum response frequencies only respond weakly to changes in $\dot{m}_{\mathrm{s}}$, resonance is still the best explanation for these frequencies. The difference between the resonance frequencies measured at the splitter with the pilot stage maximum response frequencies could be attributed

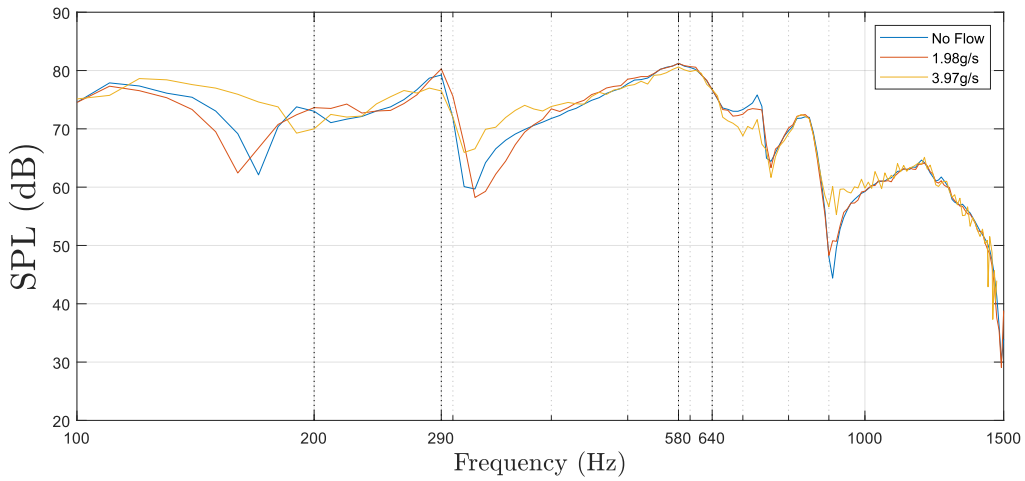

Fig. 6.7 Resonance spectra of the pilot stage cavity measured at the splitter.

to spatial variations in the acoustic response spectra of the cavity. The maximum response frequencies may only be dominant at or close to locations where the diverter section is most responsive to actuation.

This actuation localisation may explain some of the observed speaker location biases. For example, consider the acoustic responses presented in figures 6.8 and 6.9. In each case, the speaker voltage is gradually increased from $0\,\mathrm{V_{RMS}}$ to $10\,\mathrm{V_{RMS}}$ and then lowered back to $0\,\mathrm{V_{RMS}}$. Where there is a sharp change in $\dot{m}^{+}_{\mathrm{out}}$ and an associated hysteresis, the acoustic actuation has switched the diverter section. In general, the device only switched when applying 200 Hz signals to the unattached side or a 640 Hz signal to the attached side. If the physical mechanisms that trigger switching for unattached and attached side actuation differ, the physical location at which the device is most susceptible to acoustic actuation may also differ. If the maximum response frequencies vary spatially, this would explain why different frequencies are required for attached and unattached side switching.

In Mair [57], it is theorised that switching for unattached and attached side acoustic actuation are triggered by different mechanisms. Acoustic actuation increases jet spreading at both the unattached and attached shear layers of the diverter

supply jet. Using PIV experiments, Mair [57] demonstrated that acoustic actuation preferentially excites the shear layer closest to the source. Thus, acoustic actuation from the unattached control port will increase the flow entrainment rate more for the unattached shear layer, resulting in a larger pressure drop on the unattached side of the jet, weakening jet attachment. However, acoustic actuation from the attached control port will have the opposite effect, with higher entrainment rates at the attached side shear layer, strengthening jet attachment. To explain attached side switching, Mair [57] defers to the synthetic jet switching mechanism presented by Martin et al. [63]. Similar to the modified pilot stage geometry used here, Mair's diverter geometries often [62, 59, 57] include control cavity/acoustic actuator combinations that resemble synthetic jet actuators. Synthetic jets are zero net mass flow actuators that impart non-zero momentum to the flow. If the acoustic actuators act, at least partially as synthetic jets, then attached side actuation will impart transverse momentum to the supply jet, deflecting the jet away from the attached side of the diverter section. If the supply jet is deflected far enough by the synthetic jet, then the jet will start impinging on the splitter, and jet-splitter interactions will destabilise attachment, triggering the switching process.

200 Hz could be the preferred frequency for unattached side switching because 200 Hz produces an anti-node close to the unattached side shear layer. Similarly, the preferred frequency for attached side switching, 640 Hz could be a resonance frequency for the loudspeaker adapter-control port cavity.

Irrespective of the acoustic-jet interaction mechanisms involved, it is clear from the sub-switching responses that the pilot stage is more responsive to acoustic tones of 200 Hz and 640 Hz. Furthermore, for sufficiently high speaker voltages, 200 Hz and 640 Hz tones applied to the unattached and attached sides, respectively, will switch the diverter section. Consequently, the acoustic tuning data acquired for the pilot

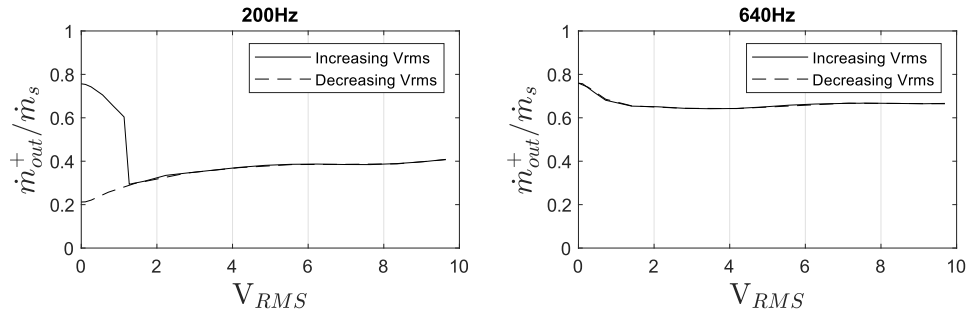

Fig. 6.8 Acoustic actuation from the initially unattached side of the pilot diverter section ($\dot{m}_\mathrm{s} = 1.98\,\mathrm{g/s}$)

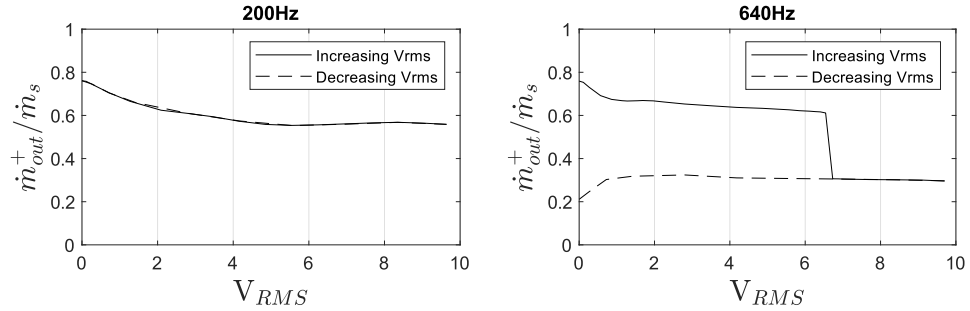

Fig. 6.9 Acoustic actuation from the initially attached side of the pilot diverter section ($\dot{m}_\mathrm{s} = 1.98\,\mathrm{g/s}$)

stage was limited to frequencies of either 200 Hz or 640 Hz.

6.3.3 Steady-State Characteristics

As discussed in section 6.2, the steady-state characteristics used by the model are of the form

$$\frac{\Delta p}{q_\mathrm{nozz}} = F\left(\frac{\dot{m}^+_\mathrm{out}}{\dot{m}_\mathrm{s}}, \dot{m}_\mathrm{s}, f, V_\mathrm{RMS}, s\right) \tag{6.9}$$

where Δp is either Δp^+_c, Δp^-_c, Δp^+_out or Δp^-_out. However, since $s = 0$ or 1 and $f =$ 200 Hz or 640 Hz, the lookup tables used by the model are three dimensional. For each characteristic pressure difference (Δp^+_c, Δp^-_c, Δp^+_our or Δp^-_out), the model has four lookup tables corresponding to the four combinations of s and f. To construct these three dimensional characteristics, pressure differences (Δp^+_c,Δp^-_c,Δp^+_out and Δp^-_out) were recorded at approximately regular intervals within the three dimensional domain

$$0 \leq \frac{\dot{m}^{+}_{\text{out}}}{\dot{m}_{\text{s}}} \lesssim 1.5 \tag{6.10}$$

$$0.99 \leq \quad \dot{m}_{\text{s}} \leq 4.91\,\text{g/s} \tag{6.11}$$

$$0 \leq \text{V}_{\text{RMS}} \leq \quad 10 \tag{6.12}$$

The Matlab function **griddatan** was then used to apply a three dimensional linear interpolation to the three dimensional dataset to create the regular grids of $\Delta p/q$ values required to populate the model's characteristic lookup tables. As discussed in section 4.2.2, diverter section characteristics $\Delta p^{\pm}_{\text{c}}/q$ and $\Delta p^{\pm}_{\text{out}}/q$ can be converted into the more physically meaningful $\Delta p_{\text{c}}/q$ and $\Delta p_{\text{out}}/q$ characteristics. Figures 6.10-6.13 presents the Δp_{c} and Δp_{out} characteristics where the scatter points are experimentally determined values of Δp, and the surfaces are constructed using the **griddatan** interpolation.

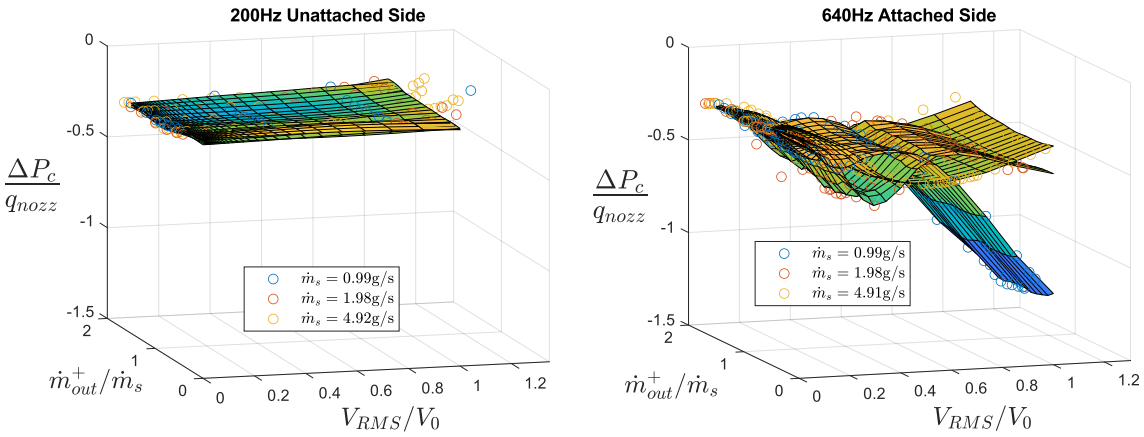

Fig. 6.10 Acoustic Δp_{c} characteristics for cases with switching boundaries, i.e. 200 Hz unattached side and 640 Hz attached side

Note that the characteristics have been split into two groups, those with switching boundaries, figures 6.10, 6.12 (200 Hz unattached, 640 Hz attached), and those without, figures 6.11, 6.13 (200 Hz attached, 640 Hz unattached). In the cases with

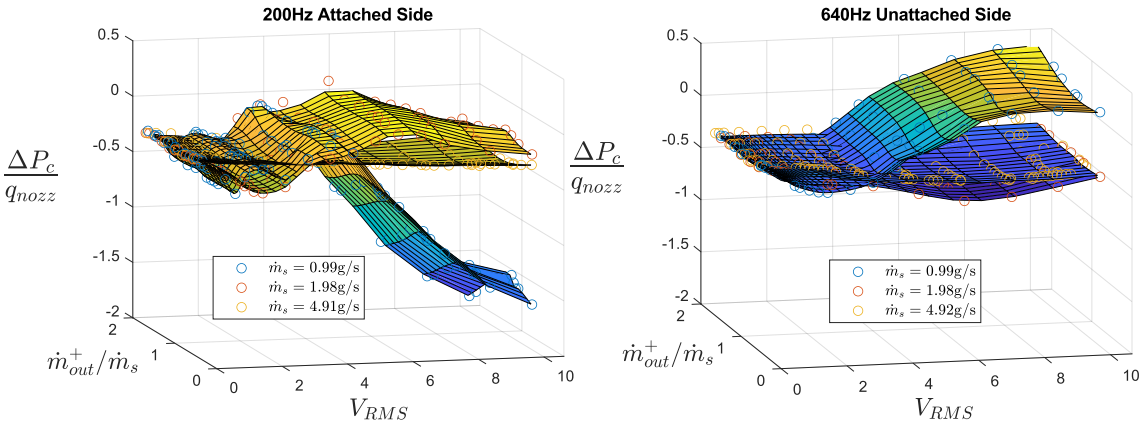

Fig. 6.11 Acoustic Δp_c characteristics for cases without switching boundaries, i.e. 200 Hz attached side and 640 Hz unattached side

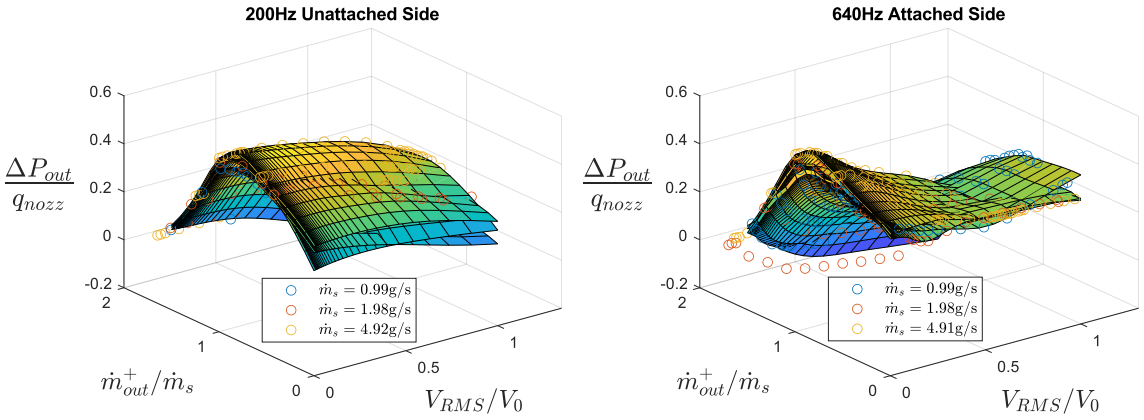

Fig. 6.12 Acoustic Δp_{out} characteristics for cases with switching boundaries, i.e. 200 Hz unattached side and 640 Hz attached side

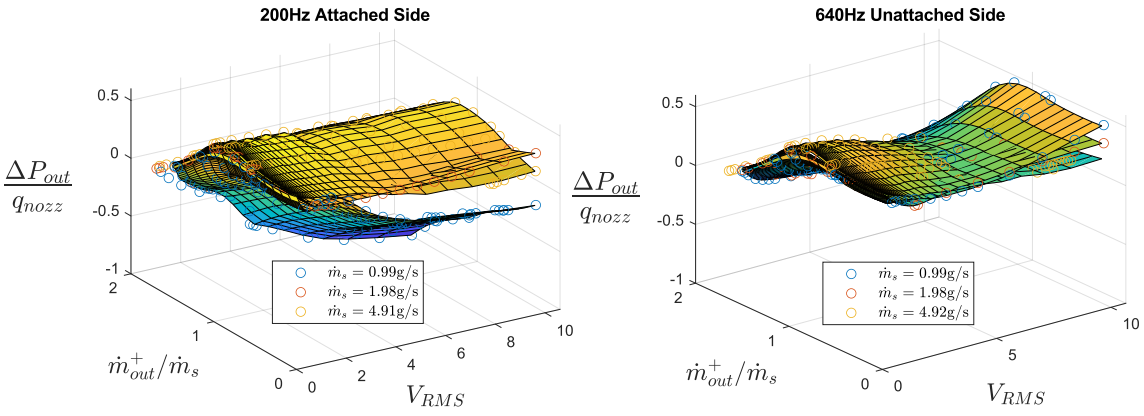

Fig. 6.13 Acoustic Δp_{out} characteristics for cases without switching boundaries, i.e. 200 Hz attached side and 640 Hz unattached side

$\dot{m}_s$ (g/s)	200 Hz Unattached V_0	640 Hz Attached V_0
0.99	0.338	5.7
1.98	1.202	7.1
4.91	6.2	10

Table 6.1 Normalisation voltages for the steady-state characteristics

switching boundaries, the V_{RMS} dimension is normalised by V_0. V_0 values (table.6.1) are average switching voltages for each $\dot{m}_s$ tested.

Focusing upon the Δp_c characteristics first, it is clear that the speaker voltage, and thus acoustic SPL, has more influence over jet position/curvature than conditions at the outlet boundaries do, parameterised by $\dot{m}_{\text{out}}/\dot{m}_s$. To get a clearer impression of the influence acoustic tones have on $\Delta p_c/q_{\text{nozz}}$, figures 6.14 and 6.14 present $\dot{m}_{\text{out}}/\dot{m}_s = 1$ slices of the $\Delta p_c/q_{\text{nozz}}$ characteristic surfaces.

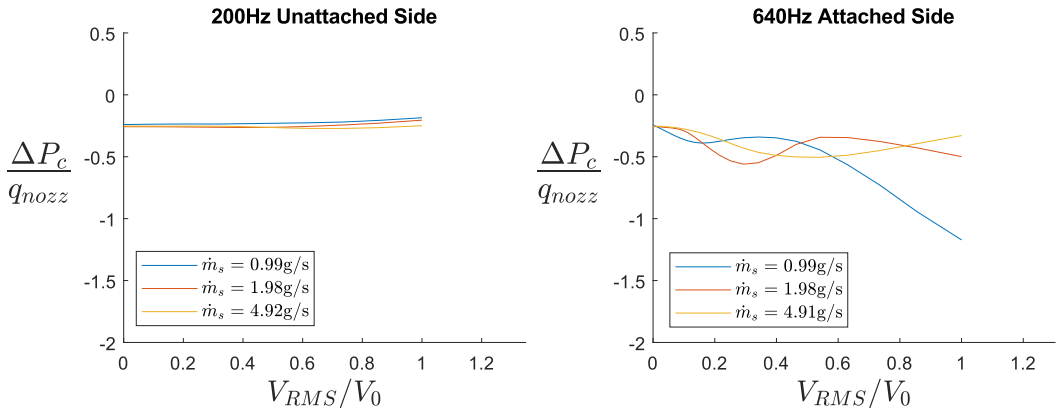

Fig. 6.14 $\dot{m}^+_{\text{out}}/\dot{m}_s = 1$ slice of acoustic Δp_c lookup table, for cases with switching boundaries, i.e. 200 Hz unattached side and 640 Hz attached side

200 Hz unattached side actuation has minimal impact upon the steady-state value of $\Delta p_c/q_{\text{nozz}}$. In this case, comparatively low switching thresholds limit the speaker voltages. Furthermore, since neither the p_c/q_{nozz} nor $p_{\text{out}}/q_{\text{nozz}}$ shift as much before switching occurs, it shows that 200 Hz unattached side switching is not triggered by a significant change in the time-averaged operating point of the diverter section.

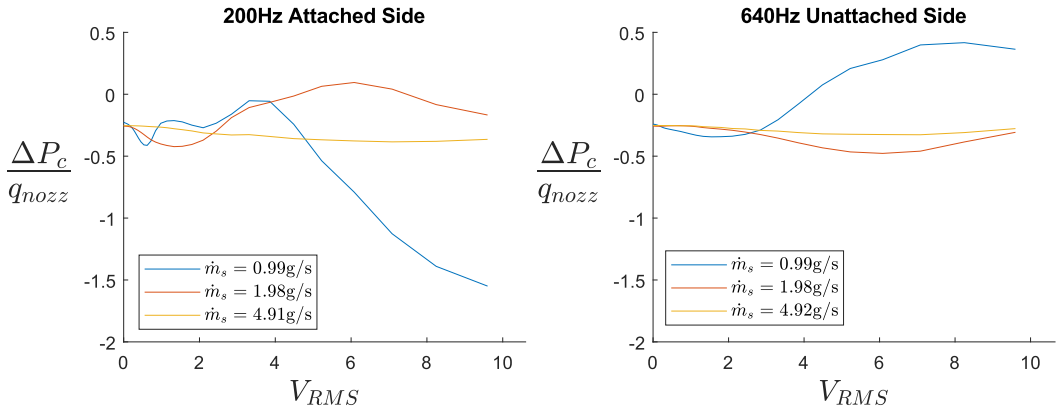

Fig. 6.15 $\dot{m}^{+}_{\mathrm{out}}/\dot{m}_{\mathrm{s}} = 1$ slice of acoustic Δp_{c} lookup table, for cases without switching boundaries, i.e. 200 Hz unattached side and 640 Hz attached side

Instead, the diverter must be switching due to the transient response of the diverter to acoustic actuation.

It has already been established that acoustic excitation increases jet spreading/entrainment rates by strengthening shear-layer roll up vortices [16, 57]. As these strengthened vortices are convected downstream, there are perturbations to both the static pressures and the flow field. When acoustic signals were applied to the pilot stage, strongly pulsating outlet flows were observed (section 6.3.2), and there was also a marked increase in pressure fluctuations measured. These observed phenomena have been attributed to the acoustically excited shear-layer roll up vortices. Even though the time-averaged jet position does not vary much when a 200 Hz attached side signal is applied, the jet will have transient excursions towards the splitter that could trigger a switching.

Excluding 200 Hz unattached side actuation, there seems to be an alternating push-pull effect on the jet, with Δp_{c} going through cycles of increasing/decreasing as the applied speaker voltage increases (figure 6.14, 6.15). This cyclical behaviour is particularly noticeable for the low supply flow rate ($\dot{m}_{\mathrm{s}} = 0.99\,\mathrm{g/s}$) curves, where acoustic tones have greater control authority. Figure 6.16 focuses upon the 200 Hz attached side curves of figure 6.15, breaking them down into the attached side p^{+}_{c}

and unattached side p_c^- contributions. From figure 6.16, it is clear that the cyclical rise and fall of Δp_c can be traced back to both the p_c^+ and p_c^- pressures.

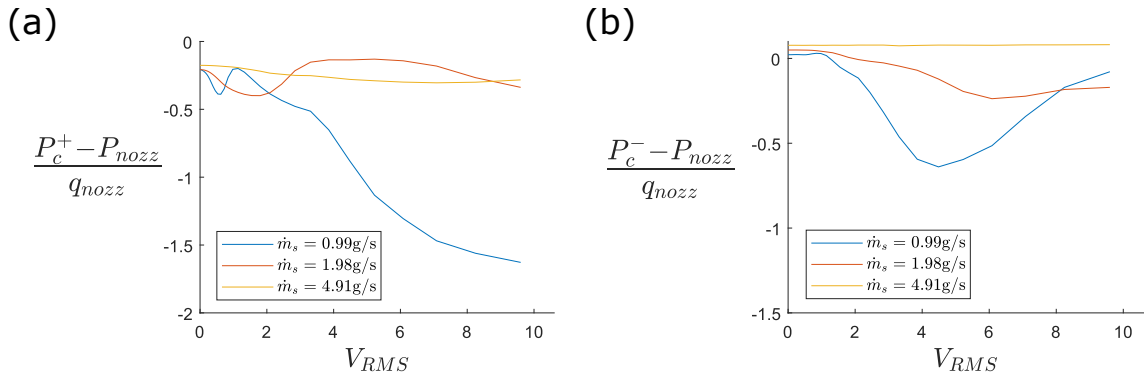

Fig. 6.16 Breakdown of 200 Hz attached side $\dot{m}_{\text{out}}^+/\dot{m}_{\text{s}} = 1$ slices into attached and unattached side contributions

According to Mair [57], acoustic tones excite shear layer instabilities. Consequently, the jet spreading rates and shear-layer entrainment rates increase, and within the confines of the diverter cavity, pressures on both sides of the jet will drop. How much the pressure drops at p_c^+ and p_c^-, depends at least in part on the entrainment rates at the attached and unattached shear layers of the jet. It might be expected that as the speaker voltage increases, the entrainment rates at both shear layers will increase, and there will be a subsequent decrease in pressure at both sides of the jet. However, this expectation conflicts with the observed p_c^+ and p_c^- pressure traces in figure 6.16. The model will still correctly replicate the steady-state behaviour using steady-state characteristics as input data. However, this highlights that the physical mechanisms that underlie the acoustic-diverter interactions are not yet fully understood.

Unlike the Δp_c characteristics, the outlet characteristic surfaces (figures 6.12 and 6.13) are responsive both to the speaker voltage and the outlet conditions. The effect of varying $\dot{m}_{\text{out}}/\dot{m}_{\text{s}}$ is similar for all the Δp_{out} characteristic surfaces. In

general, there is a maximum around $\dot{m}_{\mathrm{out}}/\dot{m}_{\mathrm{s}} \approx 1$, with Δp_{out} decreasing as $\dot{m}_{\mathrm{out}}/\dot{m}_{\mathrm{s}}$ moves away from this maximum. As discussed in section 4.2.2, Δp_{out} reflects the interplay between the outlet conditions and the diverter outlet mass flow split. For $\dot{m}_{\mathrm{out}}/\dot{m}_{\mathrm{s}} \geq 1$, the outlet mass flow split is set by the back-pressure difference Δp_{out}; to achieve higher $\dot{m}_{\mathrm{out}}/\dot{m}_{\mathrm{s}}$ values requires a lower Δp_{out} (more sympathetic) outlet pressure difference. However, for $\dot{m}_{\mathrm{out}}/\dot{m}_{\mathrm{s}} < 1$, as $\dot{m}_{\mathrm{out}}/\dot{m}_{\mathrm{s}}$ decreases, more of the supply flow spills over the splitter, pressure recovery in the attached duct decreases, whilst pressure recovery in the unattached duct increases, and Δp_{out} decreases as a result.

To get a better visualisation of the influence V_{RMS} has over Δp_{out}, figure 6.17 presents $\dot{m}^{+}_{\mathrm{out}}/\dot{m}_{\mathrm{s}} = 1$ slices of the Δp_{out} characteristic surfaces. How much of the supply jet dynamic head is recovered at the $p^{\pm}_{\mathrm{out}}$ tappings is dictated by the mass flow split $\dot{m}^{+}_{\mathrm{out}}/\dot{m}_{\mathrm{s}}$. Fixing $\dot{m}^{+}_{\mathrm{out}}/\dot{m}_{\mathrm{s}}$ for the curves in figure 6.17 ensures that the Δp_{out} variations do not result from varying amounts of pressure recovery.

The curves of figure 6.17 can be interpreted as the back-pressure difference that would need to be imposed by varying outlet restriction sizes to keep $\dot{m}^{+}_{\mathrm{out}}/\dot{m}_{\mathrm{s}} = 1$. If Δp_{out} decreases, this implies that a more sympathetic back-pressure difference needs to be imposed on the diverter section to keep $\dot{m}^{+}_{\mathrm{out}}/\dot{m}_{\mathrm{s}} = 1$. This reduction in Δp_{out} could be achieved by increasing the attached outlet restriction area, reducing the amount of blockage in the primary flow path of the pilot stage. Consequently, if Δp_{out} decreases, this suggests that if the outlet restriction areas had not been adjusted, $\dot{m}^{+}_{\mathrm{out}}/\dot{m}_{\mathrm{s}}$ would have decreased.

In most cases, Δp_{out} decreases as V_{RMS} increases. The Δp_{out} characteristics therefore suggest that acoustic actuation generally pushes the diverter towards a reduced $\dot{m}_{\mathrm{out}}/\dot{m}_{\mathrm{s}}$ state. This observation is in agreement with earlier results presented in

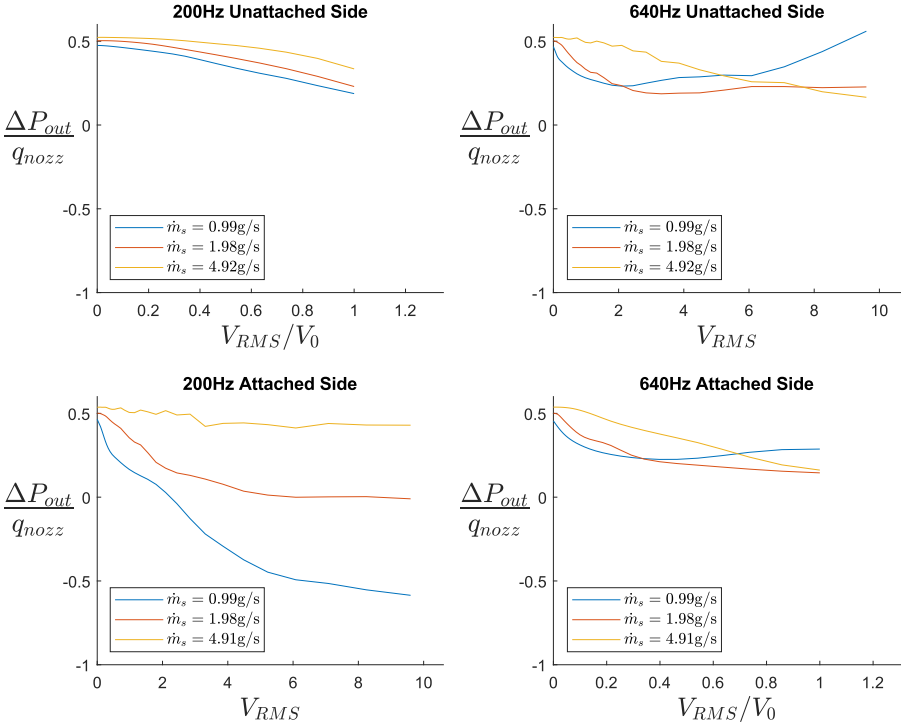

Fig. 6.17 $\dot{m}^+_{\text{out}}/\dot{m}_{\text{s}} = 1$ slice of acoustic Δp_{out} lookup table

figures 6.8 and 6.9.

Interestingly, the Δp_{out} curves are almost entirely decoupled from the Δp_{c} curves presented in figures 6.14 and 6.15. This decoupling is particularly noticeable for 200 Hz attached side actuation; despite Δp_{c} going through increasing and decreasing phases, Δp_{out} exhibits a continuous downward trend. If Δp_{c} is increasing, then the centripetal force that maintains jet curvature is decreasing, so the jet curvature should decrease. However, a decreasing Δp_{out} implies that without intervention, $\dot{m}^+_{\text{out}}/\dot{m}_{\text{s}}$ should decrease. It is possible that even as Δp_{c} decreases, the increase in jet spreading at the unattached shear layer of the jet will alter the jet-splitter interactions, encouraging more of the supply flow to be peeled off by the splitter. However, this is conjecture, and both the Δp_{out} and Δp_{c} characteristics show that the current understanding of acoustic-jet interactions is incomplete and requires further investigation.

6.3.4 Switching Boundaries

The acoustic switching boundaries are recorded as part of the steady-state characteristic measurements. The device is considered to be switched when there is a sharp change in the switch state with an associated hysteresis. Figure 6.18 presents a subset of the operating points observed during the steady-state characterisation process (640 Hz attached side actuation, $\dot{m}_\mathrm{s} = 1.98\,\mathrm{g/s}$). The line between switched and unswitched states are marked as switching boundaries.

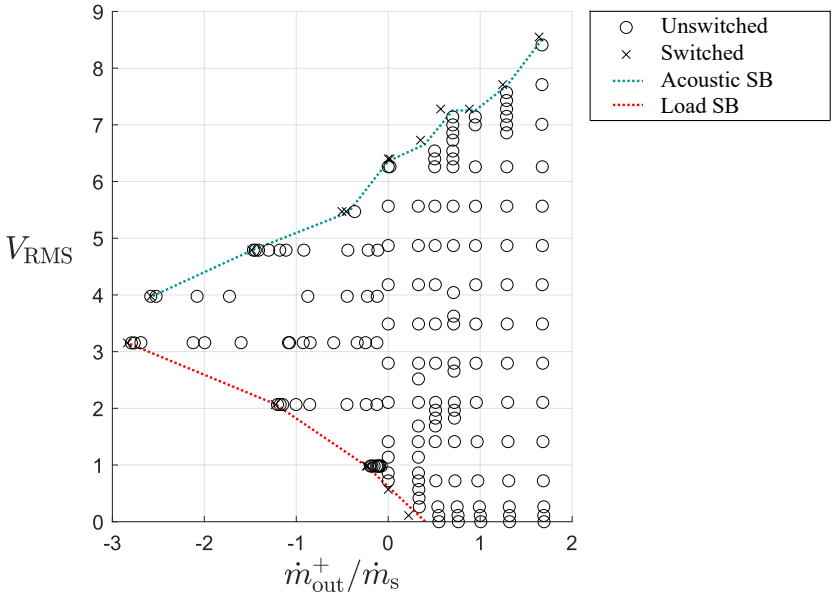

Fig. 6.18 Operating points tested for 640 Hz attached side, $\dot{m}_\mathrm{s} = 1.98\,\mathrm{g/s}$, with the acoustic switching and load-switching boundaries marked out.

Interestingly, two distinct switching boundaries emerged as part of the steady-state characterisation process. These two boundaries are marked on figure 6.18 as an acoustic switching boundary and a load-switching boundary. Switching that occurs at the acoustic boundary is triggered by increasing the speaker voltage. The switching at the other boundary is triggered by tightening the attached side outlet restriction until the adverse back-pressure difference switches the diverter section (load-switching).

Schematics of the diverter section flow fields over a range of outlet mass flow splits ($\dot{m}^+_{\text{out}}/\dot{m}_{\text{s}}$) are presented in figure 6.19. As the attached outlet restriction is tightened, the outlet mass flow split decreases. Without any acoustic actuation, the minimum stable $\dot{m}^+_{\text{out}}/\dot{m}_{\text{s}}$ value is around 0.5. When $\dot{m}^+_{\text{out}}/\dot{m}_{\text{s}} = 0.5$, the supply flow is evenly split between the attached side outlet duct and the unattached outlet duct. However, if a 640 Hz signal is applied to the attached side of the diverter, then the load-switching threshold is reduced. The diverter section will remain unswitched even for $\dot{m}^+_{\text{out}}/\dot{m}_{\text{s}} < 0.5$. In an unswitched $\dot{m}^+_{\text{out}}/\dot{m}_{\text{s}} < 0.5$ state, the jet will remain attached to one side of the diverter section, but most of the diverter supply flow will be directed down the unattached outlet duct. The load-switching threshsold drops rapidly as V_{RMS} increases. For $V_{\text{RMS}} \geq 1$, the attached outlet port restriction can be tightened to the point where $\dot{m}^+_{\text{out}} < 0$ without switching the device. In the unswitched $\dot{m}^+_{\text{out}} \leq 0$ state (figure 6.19(d) and (e)), downstream of the reattachment point, the jet will need to bend away from the attachment wall to divert all the pilot supply flow towards the unattached outlet duct. Furthermore, for the unswitched $\dot{m}^+_{\text{out}} < 0$ state, flow in the attached outlet duct is reversed, with the attached duct outlet supplying mass flow to the unattached duct (figure 6.19(e)).

Figure 6.18 shows that the sub-switching acoustic signals can improve the diverter's resistance to load-switching. This feature of acoustic actuation is potentially very useful. In section 5.3, it was shown that self-excited oscillations of the staged SVV are triggered when the pilot stage's diverter section is load switched. If a sub-switching acoustic signal can be used to improve the pilot diverter's resistance to load-switching, acoustics could be used to improve the dynamic stability of the staged SVV. As mentioned previously, there are design incentives to minimise size and weight whilst maximising the steady-state performance. These design incentives push for a smaller pilot stage with a potentially degraded supply feed. Acoustic actuation could be used to stabilise a staged SVV design that has greater steady-state

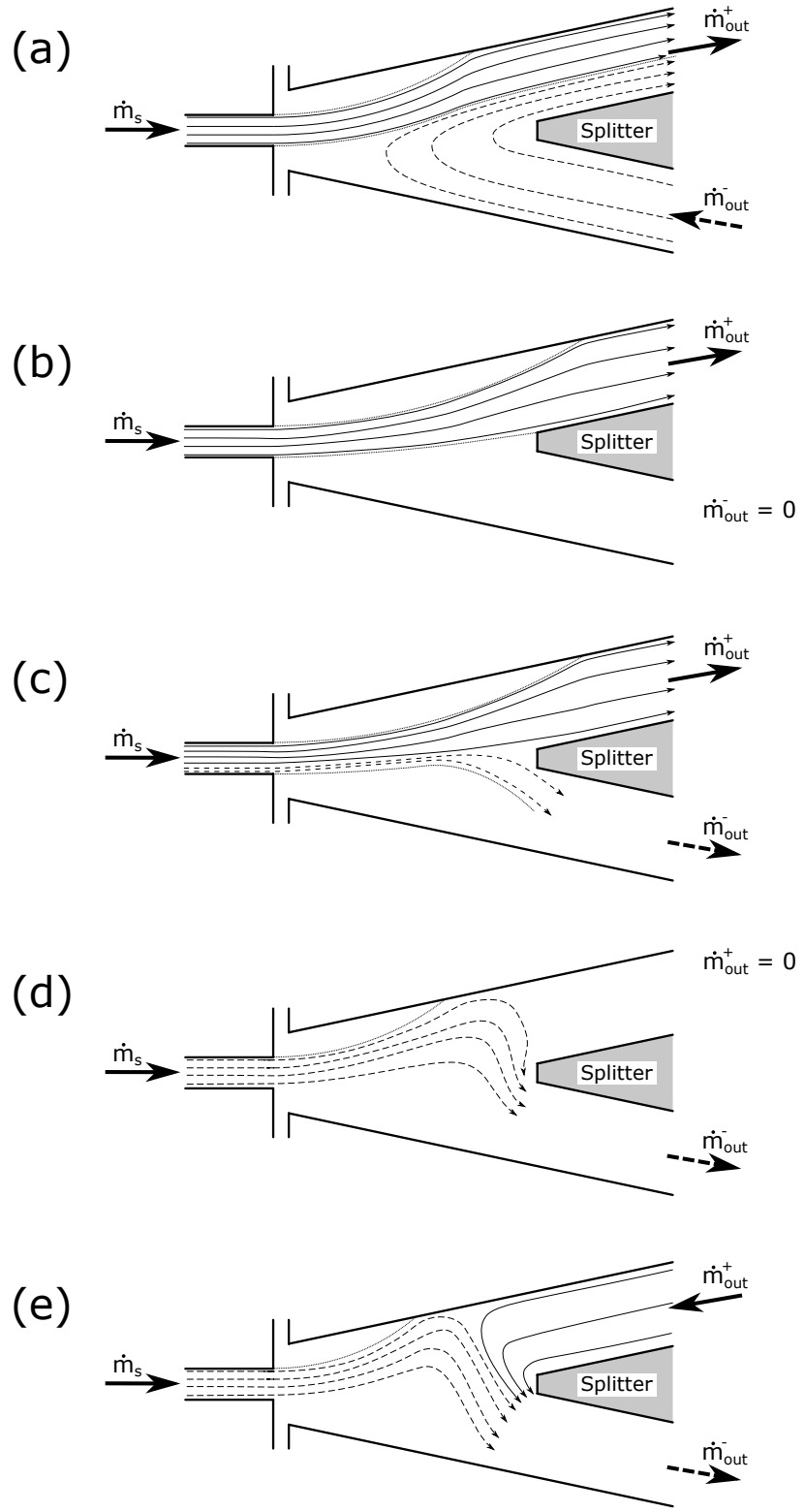

Fig. 6.19 Schematic of diverter section flow fields for differing amounts of outlet mass flow split. (a) $\dot{m}^+_{\mathrm{out}}/\dot{m}_{\mathrm{s}} > 1$, (b) $\dot{m}^+_{\mathrm{out}}/\dot{m}_{\mathrm{s}} = 1$, (c) $0 < \dot{m}^+_{\mathrm{out}}/\dot{m}_{\mathrm{s}} < 1$, (d) $\dot{m}^+_{\mathrm{out}}/\dot{m}_{\mathrm{s}} = 0$, (e) $\dot{m}^+_{\mathrm{out}}/\dot{m}_{\mathrm{s}} < 0$.

performance but is dynamically unstable. Alternatively, even if a staged SVV is designed to be dynamically stable, unforeseen circumstances could force it to operate in off-design conditions that push it towards dynamic instability. Acoustic actuation could be used as an interventive measure when the staged SVV operates in off-design conditions.

This acoustic stabilising effect was observed both at 200 Hz and 640 Hz when applied to either the attached and unattached sides of the pilot diverter section (figure 6.20). This result is seemingly at odds with the Δp_c characteristics presented in section 6.3.3, which exhibit phases of Δp_c increasing and decreasing as V_{RMS} increases. Both Mair [57] and Nicholls [69] tie this pressure difference to attachment strength and, by extension, the switch stability. However, suppose wall attachment strength is going through phases of increasing and decreasing strength. In that case, the respective load-switching boundary should also be rising and falling, but this is not what has been observed. Instead, the load-switching boundary decreases continuously as V_{RMS} increases.

In general, acoustic actuation is expected to excite both shear layers of the supply jet, increasing the entrainment rate at both shear layers. How much the entrainment rates increase at the attached and unattached side shear layers will dictate whether Δp_c rises or falls in response to acoustic actuation. However, even if the magnitude of Δp_c decreases and the jet curvature decreases in response, the increased entrainment rate at the attached shear layer will increase the jet resistance to perturbation. Consider the sequence of events when the attached side back-pressure p^+_{out} is increased by tightening the attached side outlet restriction. A fraction of the p^+_{out} increase is conveyed upstream into the recirculation bubble. The subsequent p^+_c pressure rise reduces the magnitude of Δp_c, and the centripetal force maintaining jet curvature decreases. The entrainment mass flow rate is proportional to both the

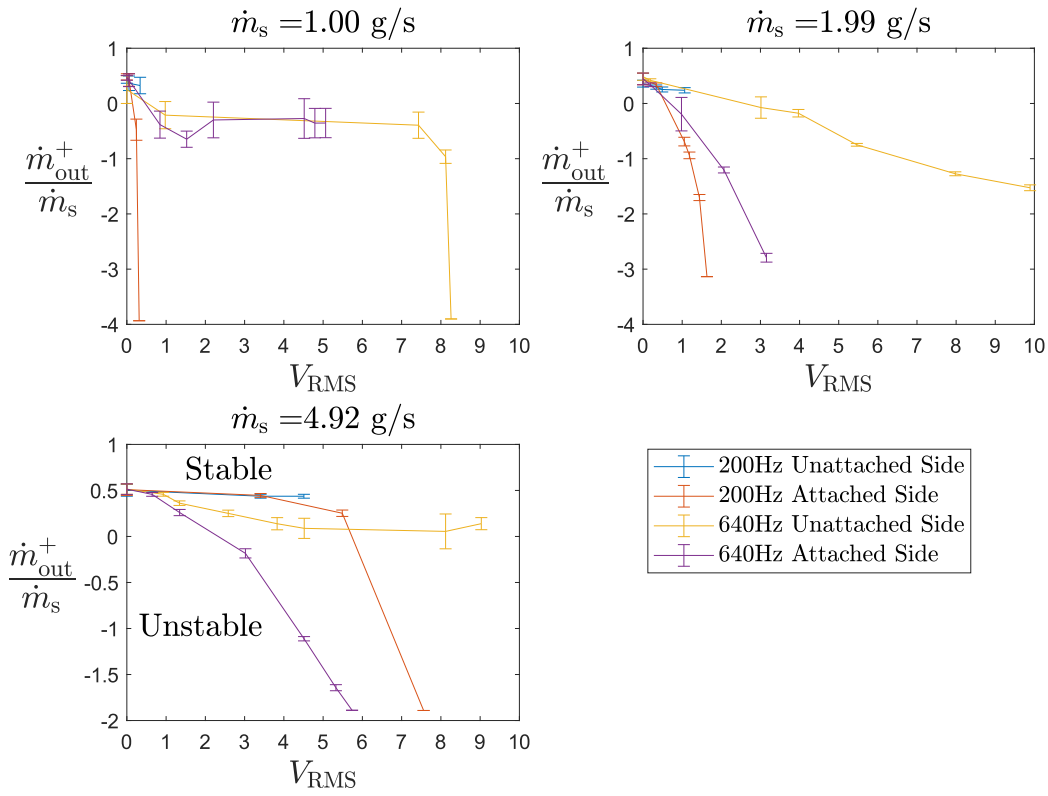

Fig. 6.20 Effect of sub-switching acoustic signals on the pilot diverter section's load-switching boundary. Diverter section switches when $\dot{m}^+_{out}/\dot{m}_s$ drops below the load-switching boundary.

attached side shear layer length and the entrainment rate. As the magnitude of Δp_c decreases, the recirculation bubble will start to grow in size, and the shear layer will lengthen. The resulting increase in the entrainment mass flow rate creates a mass flow imbalance for the recirculation bubble

$$\dot{m}_r - \dot{m}_e < 0 \tag{6.13}$$

where $\dot{m}_e$ is the entrainment mass flow rate, and $\dot{m}_r$ is the recirculating mass flow rate (see section 2.1). The transient reduction in the recirculation bubble fluid mass will result in an entrainment region pressure drop that counteracts the pressure rise due to the applied back-pressure. This negative feedback has a stabilising effect on wall attachment. When acoustic actuation increases the attached side entrainment rate, it strengthens this stabilisation mechanism. Consequently, acoustic actuation

makes wall attachment more resistant to load-switching.

Figure 6.20 presents the load-switching boundary for three supply mass flow rates 1.00 g/s, 1.99 g/s and 4.92 g/s. For each supply mass flow rate, figure 6.20 compares the load-switching boundaries for four types of acoustic actuation signal: 200 Hz attached side (200A), 200 Hz unattached side (200U), 640 Hz attached side (640A), and 640 Hz unattached side (640U). The 200U curves for all three mass flow rates tested and the 640A curve for $\dot{m}_\mathrm{s} = 1.00\,\mathrm{g/s}$ terminate early because in these cases, over the range of operating points tested, the acoustic switching and load-switching boundaries merge, see figure 6.21 for an example of this. The early termination points of these curves correspond to the intersection points of acoustic switching and load-switching boundaries.

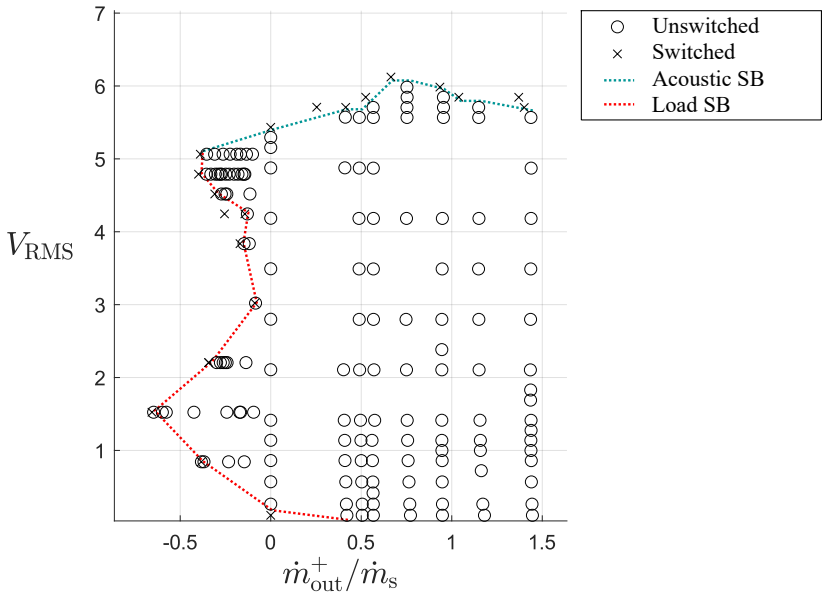

Fig. 6.21 Operating points tested for 640 Hz attached side, $\dot{m}_\mathrm{s} = 1.00\,\mathrm{g/s}$, with the acoustic switching and load-switching boundaries marked out.

Acoustic actuation increases resistance to load-switching by increasing the entrainment rate at the attached side shear layer. Therefore, acoustic actuation signals applied from the attached side of the diverter section are generally more effective

at lowering the $\dot{m}^{+}_{\text{out}}/\dot{m}_{\text{s}}$ load-switching boundary. The load-switching boundary decreases faster when applying a 200A rather than a 200U signal. Similarly, the switching boundary decreases faster when applying a 640A signal rather than a 640U control signal.

Over the range of voltages tested, acoustic switching was only observed for 200U and 640A signals. The acoustic switching boundaries constructed from the steady-state characterisation data are presented in figure 6.22. In general, it is easier to switch from the unattached side (200U). This actuation location preference is consistent with other studies of acoustically switched diverters by Mair [62, 59, 57]. Mair found that acoustically actuated diverters are easier to switch when applying the acoustic signal from the unattached side.

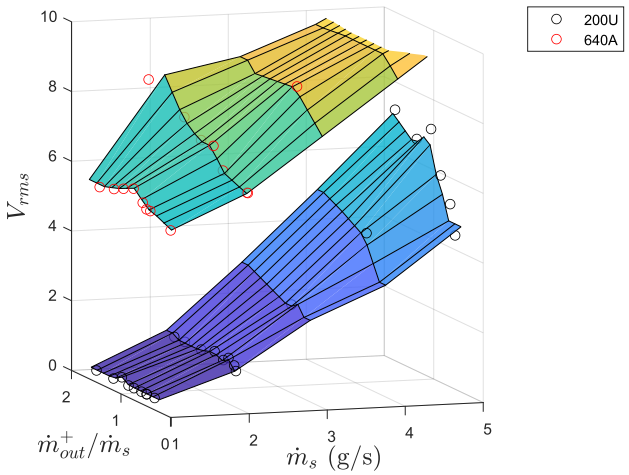

Fig. 6.22 Acoustic actuation upper switching boundaries

In general, the 640A switching boundaries presented in figure 6.22 should be treated with caution as it was often difficult to definitively locate 640A switching boundaries. When applying 200U signals to the pilot stage, there was always a clear distinction between stable and unstable states, with the pilot diverter section consistently switching cleanly into the opposite switch state when crossing the switching boundary. However, this was not always the case for 640A signals. Often there were

noticeable shifts in the apparent location of switching boundaries when repeating observations, or there would be a perceptible time delay between the V_{RMS} increase and the diverter section switching. Consequently, in addition to lower switching boundaries, a 200U signal would be the preferred choice for switching due to its greater reliability.

6.3.5 Switching Section Transients

Figure 6.23 presents the experimental setup used to acquire transient characteristic data for the acoustically actuated pilot stage. The experimental setup is similar to that used to acquire transient data for the mass flow injection controlled pilot stage. The primary difference is the input signal; the step signal is provided by a signal generator when it is turned on at a particular voltage and frequency. The orifice meter and all fittings are removed from the outlet ports of the pilot stage. These outlet obstructions will not exist when the pilot stage is incorporated into the staged SVV. There were concerns that acoustic reflections at the outlet ports might create physically unrepresentative transient responses. Consequently, the only obstruction at the outlet ports is a single pitot probe at the unattached outlet port. The physical size of the pitot probe is small when compared with the 30.9 mm outlet port. The pitot probe provides the output signal used to capture both sub-switching and switching responses to the input signal. Examples of sub-switching and switching responses captured using this setup are presented in figures 6.24 and 6.25. The speaker voltage is used to fix the start time of the transient responses, with the start time being defined as the first time the voltage magnitude reaches 75% the peak value. This start time is used to set t_0 of the following curve

$$A\left[1-\exp\left(\frac{t-t_0}{\tau}\right)\right]$$

that is fitted to the normalised output signals. This curve is the step response expected when a system can be described by a first-order transfer function with response time τ. Consequently, the transient times for each test case is taken to be the fitted τ parameter.

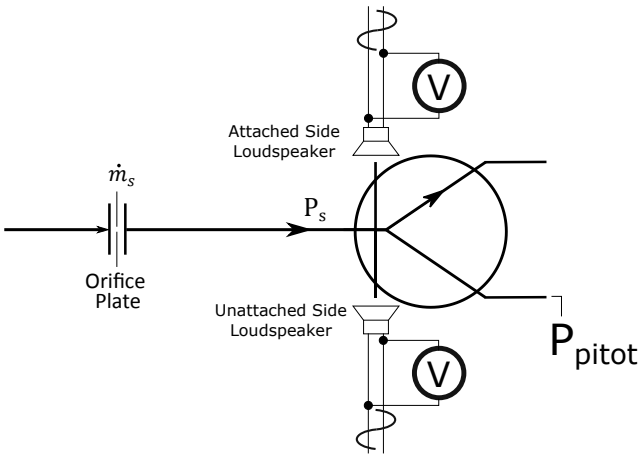

Fig. 6.23 Experimental setup for measurement of pilot diverter section's acoustic transient responses

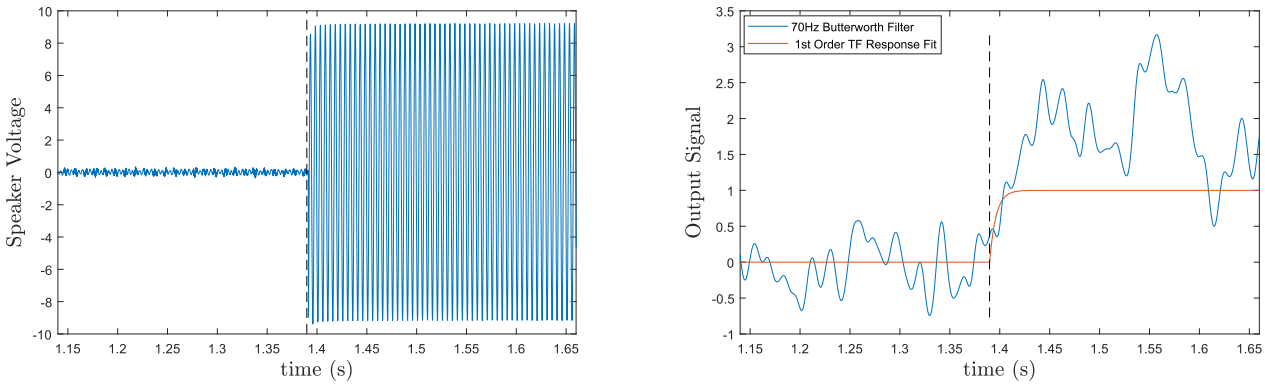

Fig. 6.24 Example of response to sub-switching acoustic signal ($\dot{m}_s = 4.91\,\mathrm{g/s}$, $6.5\,\mathrm{V_{RMS}}$, $f = 200\,\mathrm{Hz}$)

As was the case with mass flow injection, the low-pass filter cannot entirely eliminate the turbulent noise, and in some cases, the signal-to-noise ratio can be quite low. Therefore, the measurement process was repeated 50 times per test case to get a meaningful ensemble average for both response and switching times.

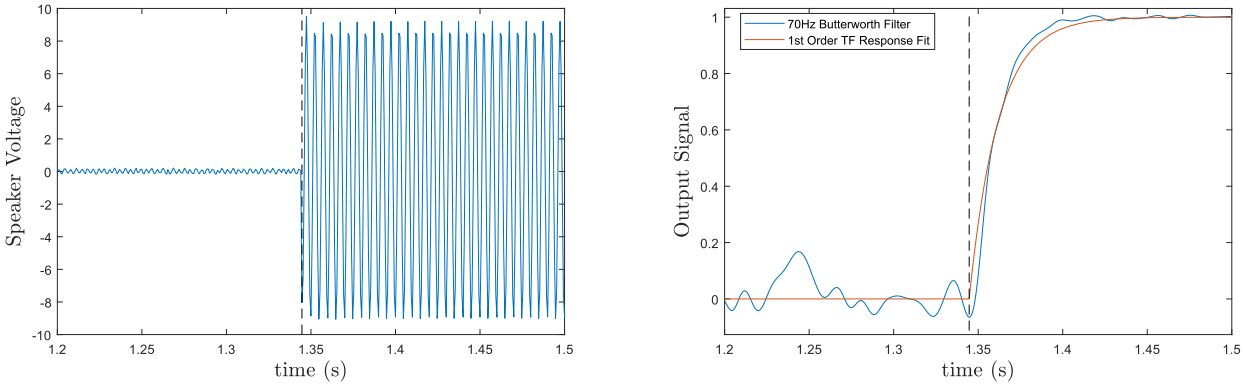

Fig. 6.25 Example of response to switching acoustic signal ($\dot{m}_s = 1.98\,\mathrm{g/s}$, $6.5\,\mathrm{V_{RMS}}$, $f = 200\,\mathrm{Hz}$)

Unlike mass flow injection control, the typical jet noise spectrum of the diverter supply jet changes noticeably when some control signals are applied. In particular, when applying 200 Hz tones to the unattached side of the pilot diverter section, 200 Hz harmonics ($f_i = 200i$) appear in the jet noise spectrum, see figures 6.26 and 6.27. These harmonics appear in the turbulent noise spectrum because acoustic tones excite shear layer instabilities whose frequencies match the excitation frequency [16, 120]. This phenomenon has to be accounted for when choosing the filtering corner frequency f_c of the low-pass Butterworth filter. Figure 6.28 shows the effect f_c has on the ensemble averages of response τ and switching t_{sw} times based on filtered p_{pitot} transients. Note that for a 200U switching signal, there is a noticeable change in the t_{sw} value as f_c drops below 400 Hz and similarly for the 200U sub-switching signal when f_c drops below 200 Hz. A comparatively strict filter with $f_c < 90$ Hz is required to avoid the estimates of response and switching times being biased by noise produced by acoustically excited turbulence. However, if f_c is too low, response/switching times could be overestimated as higher frequency components are removed from the p_{pitot} output signal. The examples presented in figure 6.28 represent test cases that produced the fastest response/switching times. These test cases show that the negative effects of over-filtering are not evident for $f_c > 50$ Hz. For acoustic response and switching times presented in this section, a

low-pass filter with $f_c = 70$ Hz has been applied to the transient output signals.

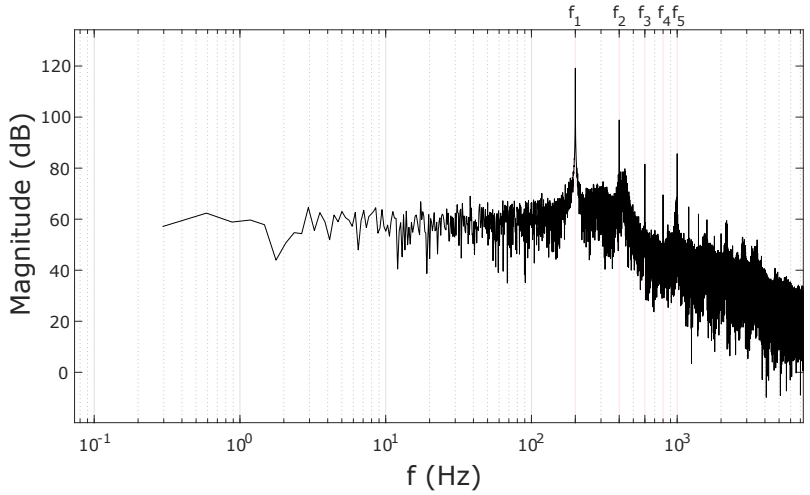

Fig. 6.26 Jet noise spectrum when applying a sub-switching 200 Hz acoustic tone to the unattached side of the pilot diverter section. The supply flow rate for this signal is 4.9 g/s and the speaker voltage is 5.0 V_{VRMS}. The noise spectrum is acquired by applying Matlab's **FFT** function to the p_{pitot} recording.

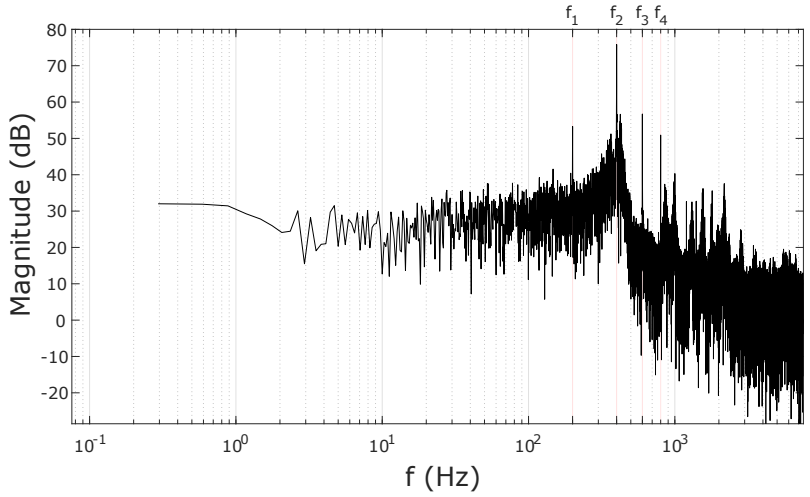

Fig. 6.27 Jet noise spectrum when applying a switching 200 Hz acoustic tone to the unattached side of the pilot diverter section. The supply flow rate for this signal is 3.0 g/s and the speaker voltage is 7.9 V_{VRMS}. The noise spectrum is acquired by applying Matlab's **FFT** function to the p_{pitot} recording.

Measured response times are presented in figures 6.29 - 6.32, whilst switching times for 200 Hz unattached side signals are presented in figure 6.33. The range

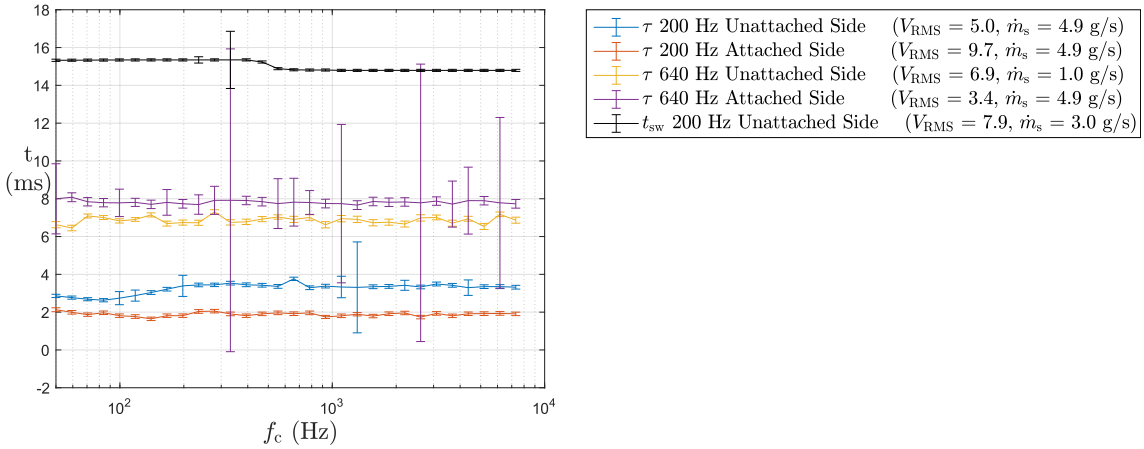

Fig. 6.28 Effect of f_c on the estimated values of t_{sw} and τ.

of response times that could practically be measured for a given flow rate $\dot{m}_s$ was limited. If the speaker V_{RMS} is too low, the subsequent pilot diverter response signal is too small to discern from the jet noise. On the other hand, if the V_{RMS} is too high, then the applied acoustic tone will switch the pilot diverter section. These limits are particularly stark for the 200 Hz unattached side actuation response times (figure 6.29), where the limits compress the response time surface down to a single curve, with $t_R = t_R(\dot{m}_s)$. In practical terms, it is unimportant for the model if the t_R values are incorrect for input signals that are too weak to have a discernable impact on the diverter operating point, or are so strong that they trigger switching.

In a similar fashion to mass flow injection, the response and the switching times generally decrease as both $\dot{m}_s$ and the magnitude of the control inputs increase. An exception to this is noticeable for $\dot{m}_s = 0.98$ g/s and 1.98 g/s. It seems that if V_{RMS} is allowed to go high enough, the switching times start increasing rather than continuing to decrease. It has been assumed up to this point that the entrainment rates on the attached and unattached sides of the jet are asymmetrical. This asymmetry leads to a reduction in the pressure difference across the jet, weakening the wall attachment effect to the point where the pilot diverter section switches. However, there may be a physical limit to how much acoustic actuation can increase entrainment rates. If

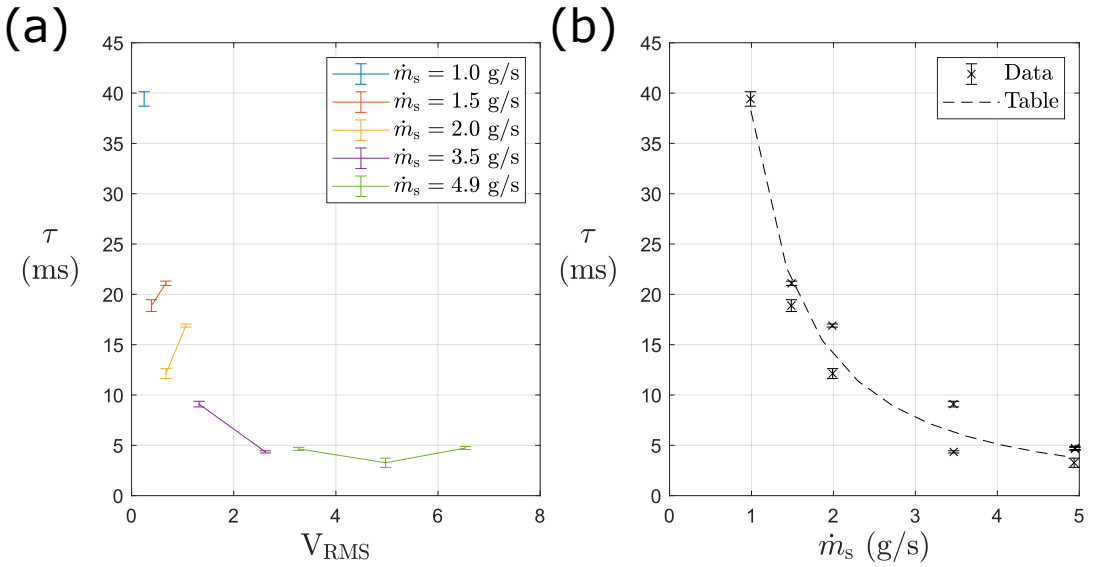

Fig. 6.29 Response times of the pilot diverter section when subjected to a 200Hz unattached side control signal.

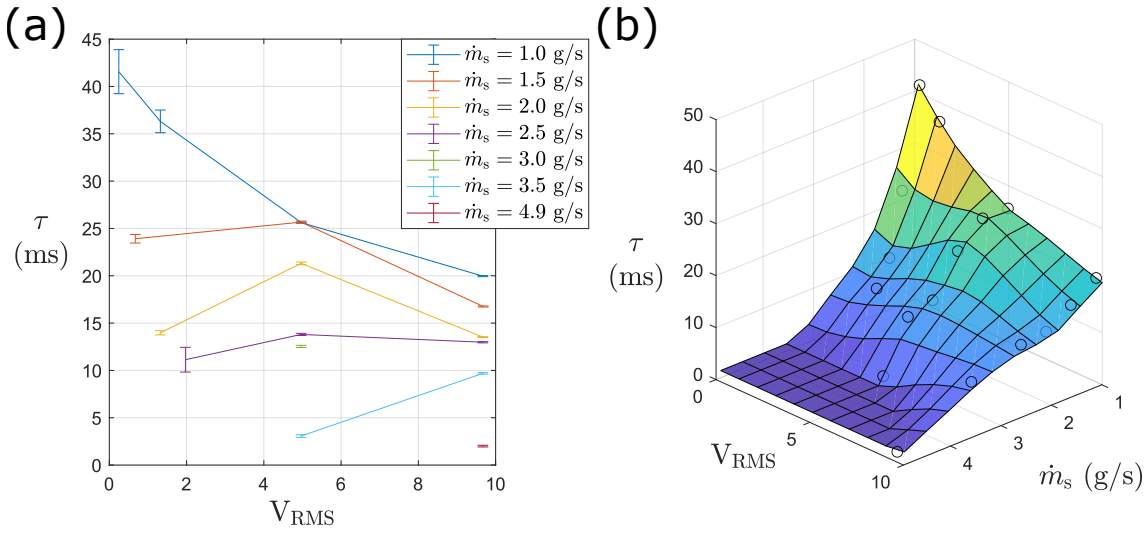

Fig. 6.30 Response times of the pilot diverter section when subjected to a 200Hz attached side control signal.

this is presumed to be the case, then if SPL levels get high enough, the entrainment rates at the shear layer closest to the acoustic source will saturate first. Continuing to increase the SPL will only increase entrainment rates at the shear layer furthest from the acoustic source, leading to a reduction in the effectiveness of the acoustic tone to switch the jet.

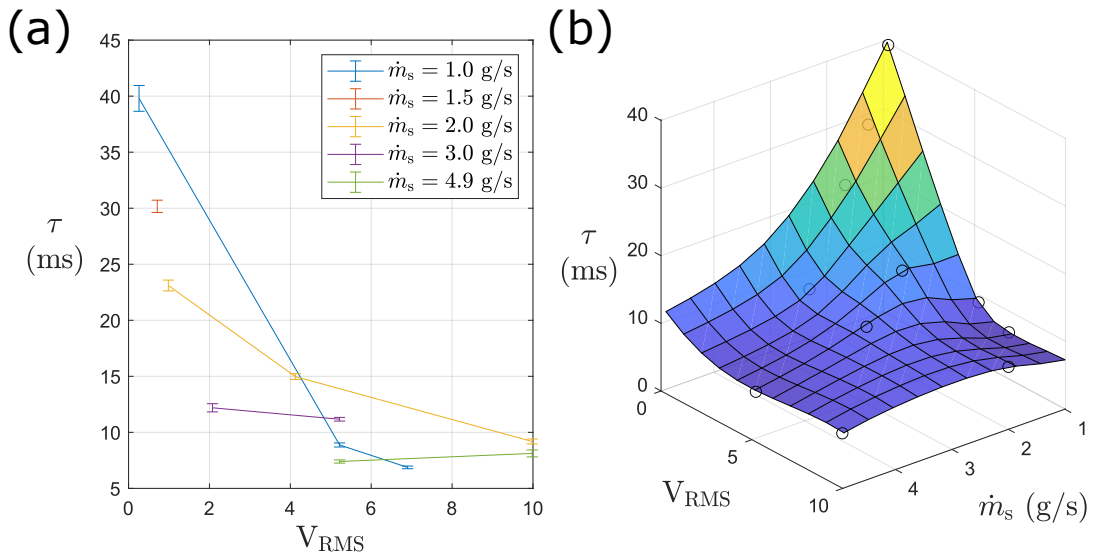

Fig. 6.31 Response times of the pilot diverter section when subjected to a 640Hz unattached side control signal.

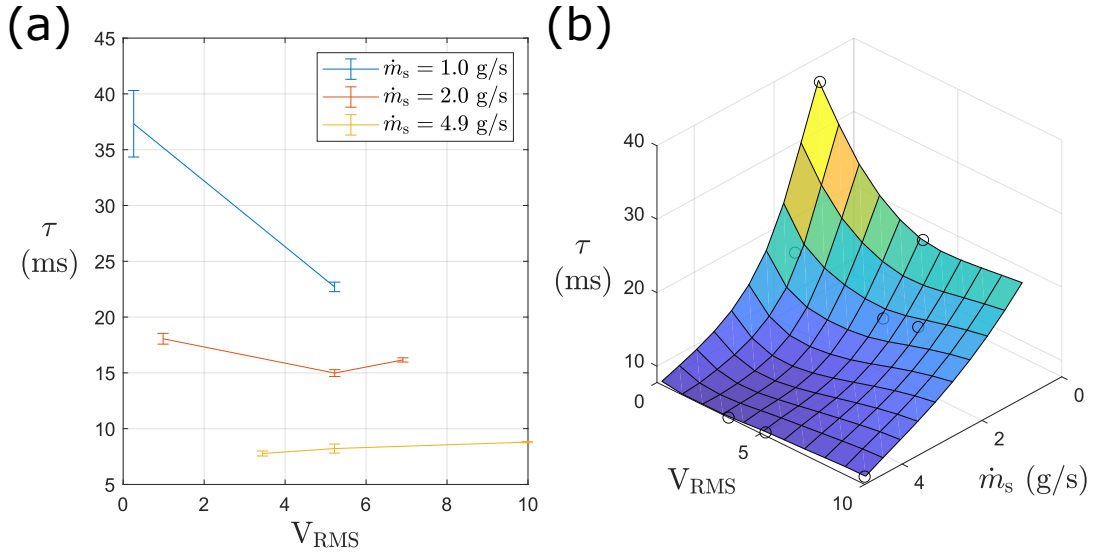

Fig. 6.32 Response times of the pilot diverter section when subjected to a 640Hz attached side control signal.

6.4 Numerical and Experimental Results with Acoustic Control

As with mass flow injection, the acoustically switched pilot stage can be combined with the SVV to form the acoustically controlled staged SVV. The combined experimental device is presented in figure 6.34. Experimental data acquired from this

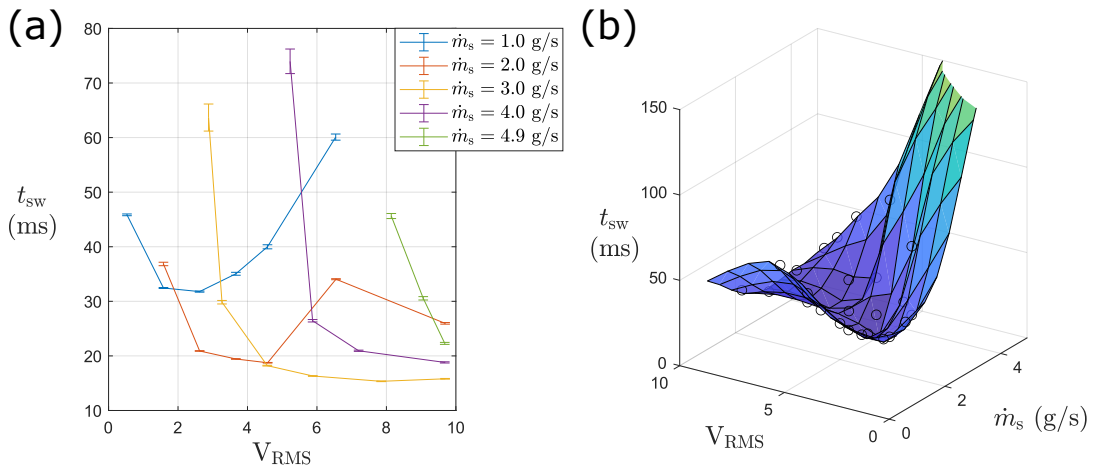

Fig. 6.33 Switching times for the pilot diverter section when switching is triggered by 200 Hz unattached side signal.

device are used both to validate the numerical model and explore alongside the model the effects of acoustic actuation upon steady-state performance and stability. The experimental setup used is presented in figure 6.35. Here the 12.8 mm orifice meters are used to measure the supply mass flow rates for both the pilot and SVV stages.

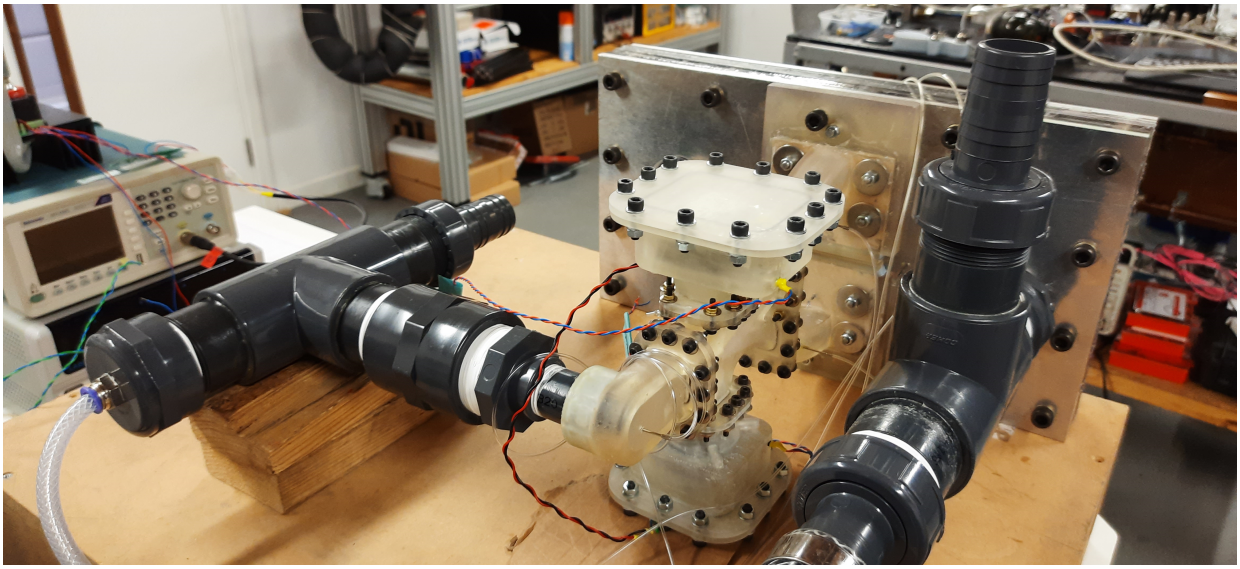

Fig. 6.34 Experimental Staged SVV device with loudspeaker actuators

In a similar fashion to chapter 5, the pilot stage and SVV stage supply pressures for experiments and numerical simulations are restricted to the 30-70 mbar range. As discussed at the start of chapter 5, within this range of supply pressures, the expected

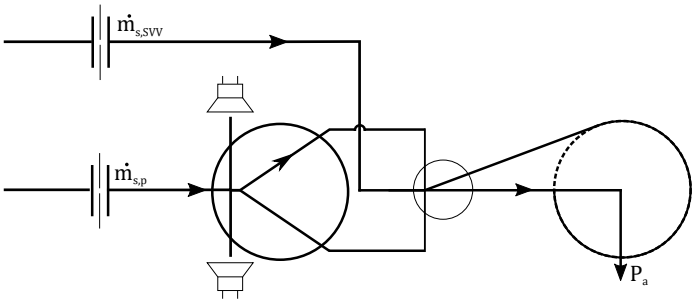

Fig. 6.35 Experimental setup for acoustically controlled staged SVV

range of nozzle hydraulic diameter Reynolds numbers is 6900-30000 for the pilot stage and 13000-50000 for the SVV stage. Similarly, the nozzle Mach number ranges are 0.048-0.21 for the pilot stage and 0.046-0.17 for the SVV stage. Consequently, the chosen range of supply pressures ensures that flows are completely turbulent whilst remaining in the incompressible flow regime outside the vortex chamber.

6.4.1 Acoustic Switching Threshold and Steady-State Performance Under Continuous Excitation

A major motivation of this project was to investigate whether or not it is possible to acoustically switch a multi-stage fluidic device. However, in the process of investigating the response of the pilot diverter section's response to sub-switching acoustic signals (section 6.3.3), it was discovered that acoustic actuation can be used to alter the steady-state behaviour of the pilot diverter section and increase its resistance to load-switching. Consequently, there is the possibility that non-switching acoustic actuation signals can be used to improve the steady-state performance of the staged SVV. The vortex chamber performance can be manipulated by acoustically altering the pilot stage outlet mass flow split. Furthermore, there exist control schemes that can influence the pilot diverter state without the risk of triggering a switching event. Both 200 Hz attached side and 640 Hz unattached side signals can alter steady-state

behaviour, but switching of the pilot diverter section has not been observed in either case over the range of speaker voltages tested.

Ideally, acoustic actuation would enable TDR optimisation. The acoustic signals would push the vortex chamber towards its optimum states, maximising flow impedance in the radial state and minimising it in the tangential state.

The same numerical simulations and experiments are used to confirm that the Staged SVV can be switched acoustically and to examine the effects sub-switching acoustic signals have on steady-state performance. These experiments and numerical simulations involved fixing the supply pressures for the pilot and SVV stages, selecting a speaker location and frequency and then incrementally increasing the speaker V_{RMS} until $V_{\mathrm{RMS}} = 10$ $\mathrm{V_{RMS}}$ or the staged SVV switches.

To start with, the case where the pilot and SVV stages have the same supply pressure of 50 mbar is used as a baseline. Figures 6.36-6.41 show the effects of acoustic actuation on the supply mass flow rates in both the radial and tangential states and highlight switching thresholds for a selection of inlet conditions.

For each of the selected cases, both numerical and experimental observations show that it is possible to switch between the radial (non-vortex) and tangential (vortex) states with an appropriate choice of acoustic control signal. There are examples of staged SVV switching achieved using both 200 Hz unattached side (200U) and 640 Hz attached side (640A) signals. However, in all of these cases, it is considerably easier to switch with 200U signals, with the 200U switching V_{RMS} always being substantially lower than the 640A switching V_{RMS}. These observations are consistent with the behaviour of the pilot stage in isolation (section 6.3.4).

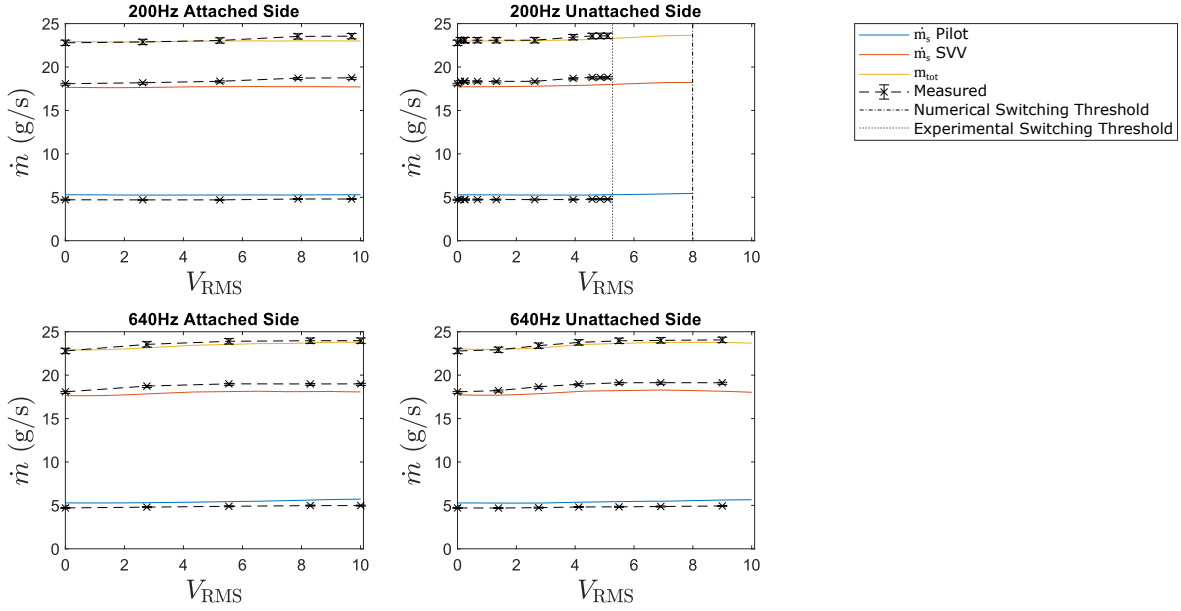

Fig. 6.36 Staged SVV mass flow rates (radial state, $p_{\mathrm{s,p}} = p_{\mathrm{s,SVV}} = 50\,\mathrm{mbar}$)

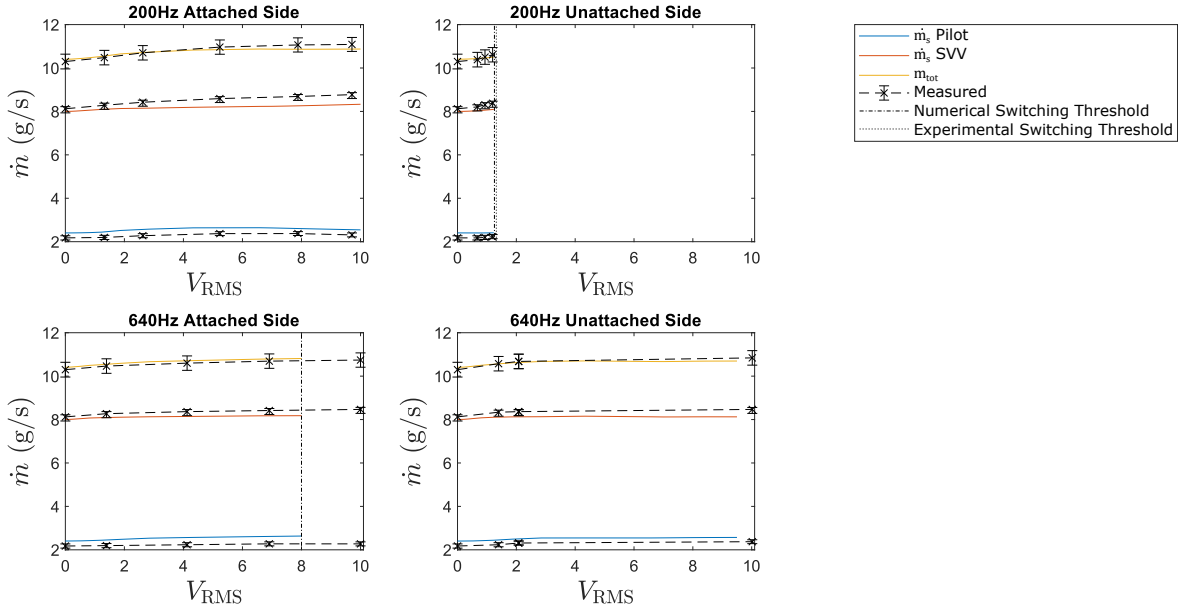

Fig. 6.37 Staged SVV mass flow rates (tangential state, $p_{\mathrm{s,p}} = p_{\mathrm{s,SVV}} = 50\,\mathrm{mbar}$)

In many cases, there are noticeable discrepancies between numerical and experimental observations when it comes to predicting the exact V_{RMS} values required to switch the staged SVV.

The numerical model consistently overestimates the stability of the staged SVV when applying 200U signals in the radial state. This discrepancy can be attributed

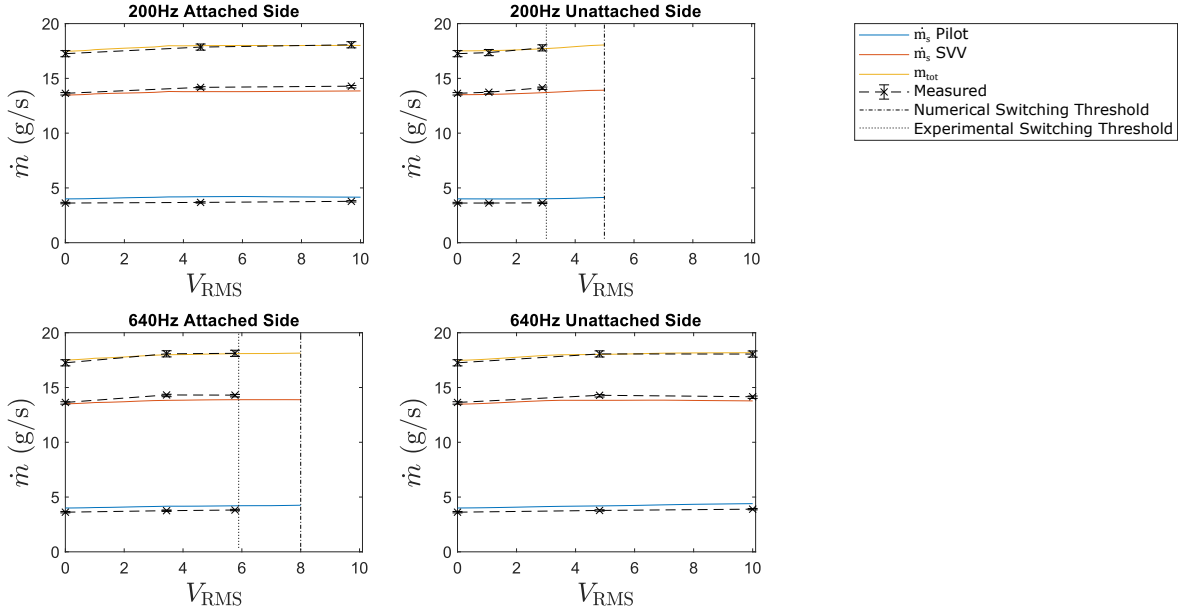

Fig. 6.38 Staged SVV mass flow rates with reduced supply pressures (radial state, $p_{\mathrm{s,p}} = p_{\mathrm{s,SVV}} = 30\,\mathrm{mbar}$)

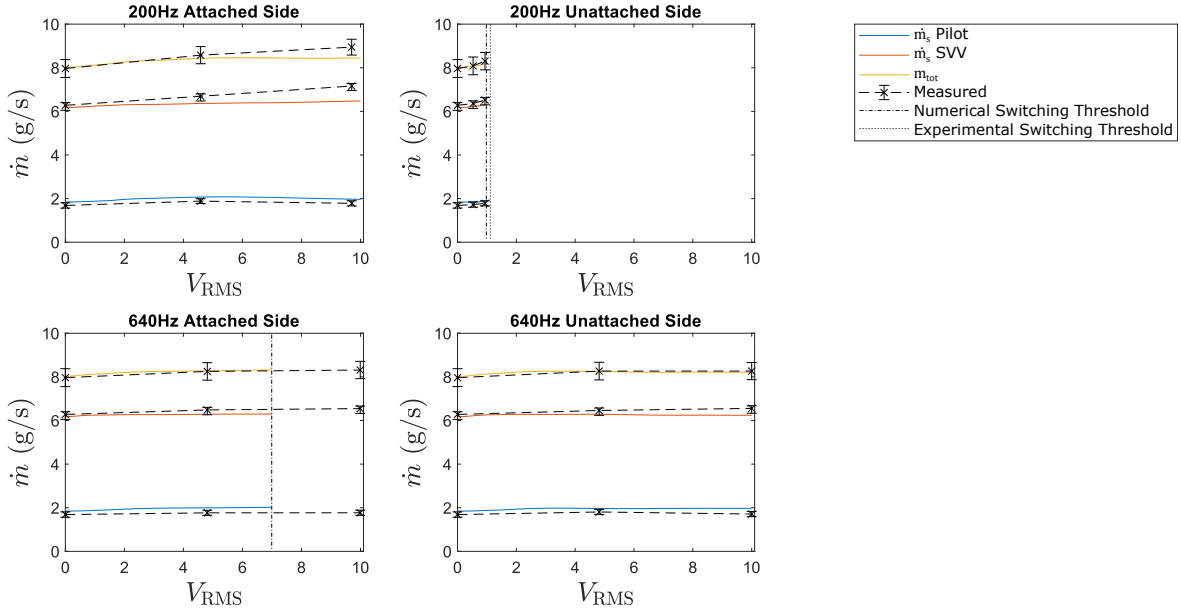

Fig. 6.39 Staged SVV mass flow rates with reduced supply pressures (tangential state, $p_{\mathrm{s,p}} = p_{\mathrm{s,SVV}} = 30\,\mathrm{mbar}$)

to unsteady boundary conditions imposed by the SVV on the pilot stage. It has been observed by Turner et al. [104] that the weaker vortices formed in the radial state vortex chamber precess, generating pressure fluctuations within the SVV. Consequently, the back pressures imposed upon the pilot stage by the SVV will transiently

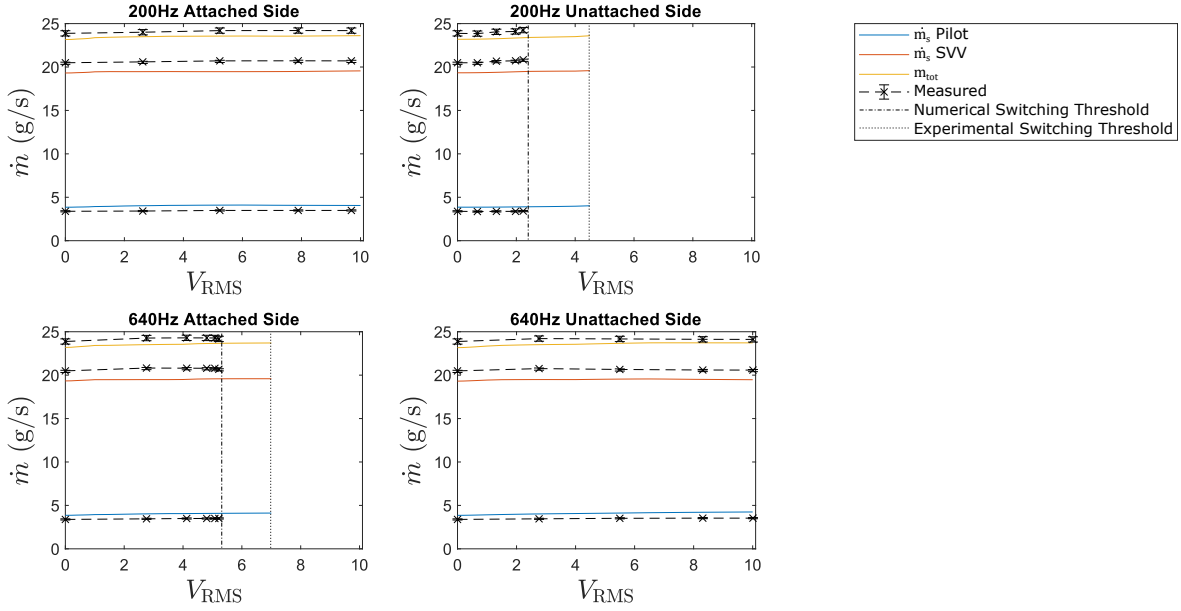

Fig. 6.40 Staged SVV mass flow rates where pilot supply pressure has been degraded (radial state, $p_{\mathrm{s,p}} = 40\,\mathrm{mbar}$, $p_{\mathrm{s,SVV}} = 50\,\mathrm{mbar}$)

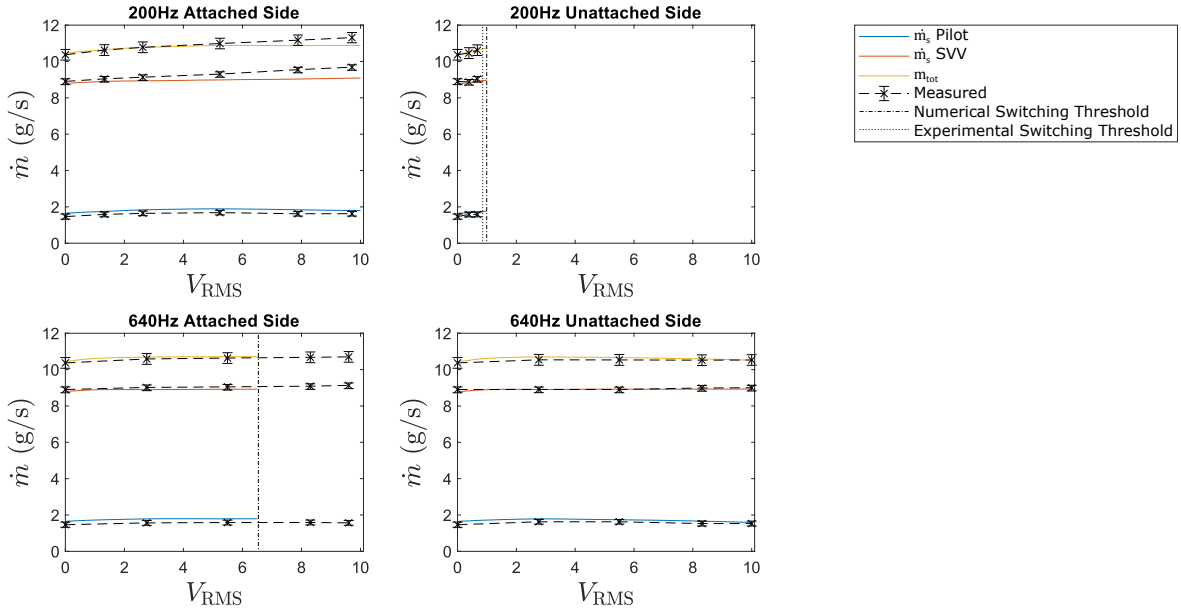

Fig. 6.41 Staged SVV mass flow rates where pilot supply pressure has been degraded (tangential state, $p_{\mathrm{s,p}} = 47.7\,\mathrm{mbar}$, $p_{\mathrm{s,SVV}} = 50\,\mathrm{mbar}$)

fluctuate. The numerical model does not simulate these pressure fluctuations as the model uses time-averaged steady-state characteristics. The pilot diverter section will start switching when it transiently enters an unstable state as a result of transient fluctuations in the outlet boundary pressures. Therefore, the staged SVV in the

radial state will switch at lower V_{RMS} than that predicted by the model.

There are also noticeable discrepancies for all switching boundaries for 640A signals, irrespective of the staged SVV switch state. In this case, this is attributed to difficulties encountered when attempting to definitively locate 640A switching boundaries for the pilot diverter section, as discussed in section 6.3.4.

Regarding sub-switching behaviour, figures 6.36-6.41 show good agreement between the numerical model and the experimental observations. In general, acoustic actuation would appear to increase the total flow rate irrespective of the vortex state. To better understand the mechanism that underlies this result, figures 6.42 and 6.43 presents some of the simulated flow parameters for the 2-stage device. As discussed in section 6.3.3 though the mechanisms by which unattached and attached side tones interact with the pilot diverter section jet may be different, both reduce the diverter outlet mass flow fraction $\dot{m}_{\mathrm{out}}/\dot{m}_{\mathrm{s}}$. The consequence of this, for the 2-stage device, is that acoustic tones increase $\dot{m}^{+}_{\mathrm{c,SVV}}$; this weakens the SVV wall attachment, $\Delta p_{\mathrm{c,SVV}}$ increases, and the SVV supply jet curvature decreases. The shift in the SVV jet position influences the flow field of the vortex chamber. The vortex chamber steady-state characteristics of section 4.3.4 have the dimensionless pressure difference across the vortex chamber ($\Delta p_{\mathrm{vx}}/q_{\mathrm{vx}}$) decreasing as $\dot{m}^{+}_{\mathrm{c}}$ increases.[1] As $\Delta p_{\mathrm{vx}}/q_{\mathrm{vx}}$ decreases, the overall flow impedance of the 2-stage device decreases and $\dot{m}_{\mathrm{tot}}$ increases.

For this device, it would appear that acoustic actuation can lower the overall flow impedance, not increase it. This means acoustic actuation cannot be used to lower the total flow rate in the tangential state, and the TDR can only be improved

[1] In the radial state $\Delta p_{\mathrm{vx}}/q_{\mathrm{nozz}}$ there is actually a minimum around $\dot{m}^{+}_{\mathrm{c}}$ = 0-7% of $\dot{m}_{\mathrm{s,SVV}}$. This minimum is visible in figure 6.42(c) around $V_{\mathrm{RMS}} = 0.8$ for the 640 Hz signal applied to the unattached side of the pilot diverter section.

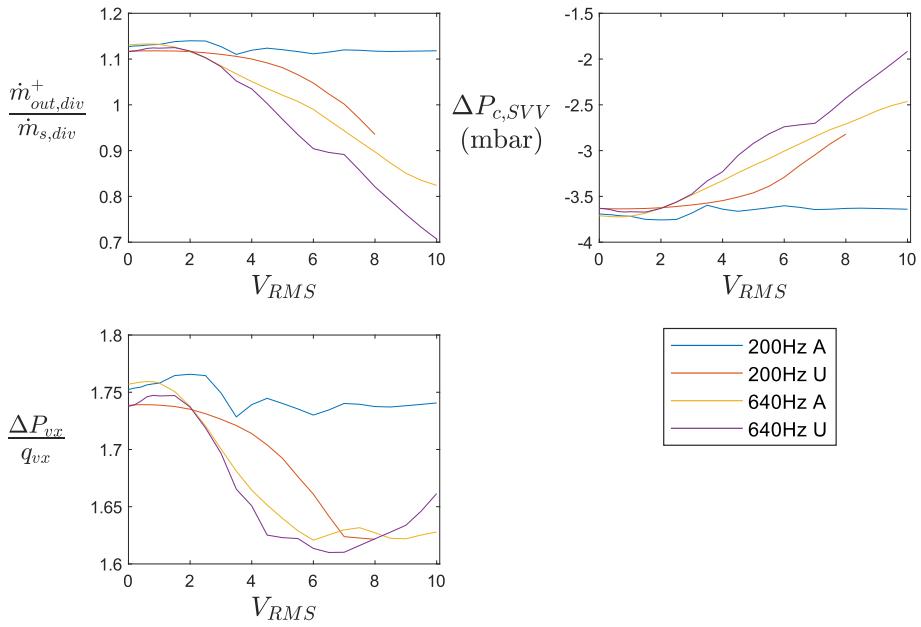

Fig. 6.42 Simulated effect of acoustic actuation on internal flow parameters (radial state, $p_{\mathrm{s,p}} = p_{\mathrm{s,SVV}} = 50\,\mathrm{mbar}$)

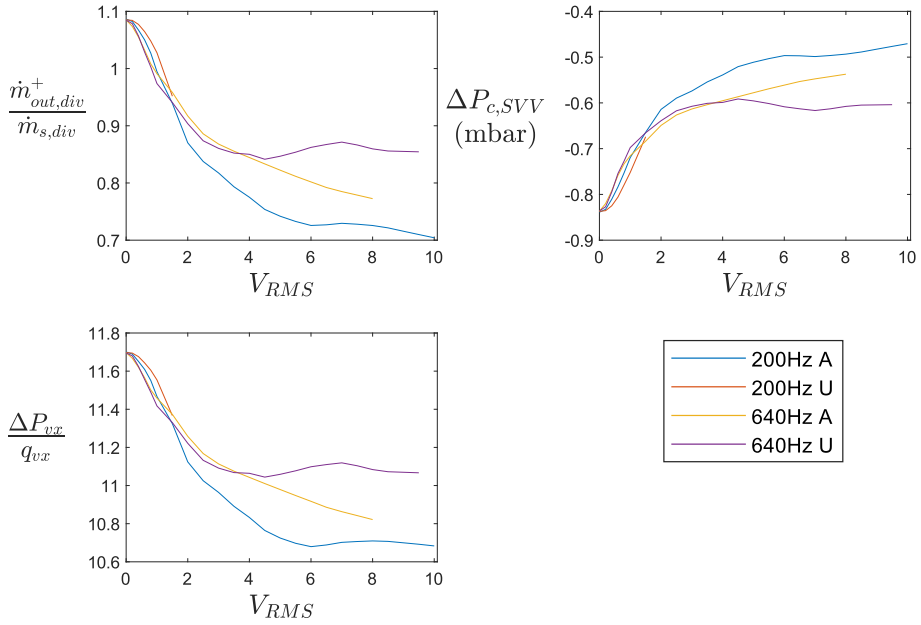

Fig. 6.43 Simulated effect of acoustic actuation on internal flow parameters (tangential state, $p_{\mathrm{s,p}} = p_{\mathrm{s,SVV}} = 50\,\mathrm{mbar}$)

by increasing the total flow rate in the radial state. Considering the baseline case (figures 6.36 and 6.37), the largest shift in radial state flow rates was observed with a 640 Hz unattached side signal with $\dot{m}_{\mathrm{tot}} = 22.8\,\mathrm{g/s} \rightarrow 24.1\,\mathrm{g/s}$ or a 5.6% increase, which translates to a 5.6% TDR increase (assuming no acoustic actuation in the

tangential state). Note that this is comparable to the performance improvement achieved using inter-stage restrictions, where the maximum TDR increase observed was 3.8% ($p_{s,p} = p_{s,SVV} = 30\,\text{mbar}$, tangential duct restriction area= $154\,\text{mm}^2$).

Whilst there seems to be reasonable agreement between simulation and observation with regards to $\dot{m}_{tot}$, discrepancies start to become evident when breaking this down into the pilot-SVV mass flow split. In general, the simulation underestimates $\dot{m}_{s,p}$, whilst overestimating $\dot{m}_{s,SVV}$. This will have a knock-on effect upon the simulation's predictions of the oscillatory instability thresholds (section 6.4.2). Oscillations start when the pilot supply pressure/flow rate is degraded to the extent that it cannot overcome the adverse pressure difference imposed by the SVV. Any error associated with the $\dot{m}_{s,p}/\dot{m}_{s,SVV}$ ratio will naturally impact predictions of the $p_{s,p}/p_{s,SVV}$ ratio at which the device starts to oscillate.

To diagnose the source of this error it is useful to examine the key pressures in staged SVV, figure 6.44. The total flow rate $\dot{m}_{tot}$ is largely dictated by the pressure difference coefficient of the vortex chamber. In figure 6.44, the simulated vortex inlet pressures $p^+_{out,SVV}$ are quite close to the measured values. However, the mass flow split is dictated by pilot-SVV interactions. The largest difference between simulated and observed pressures seems to occur consistently at the $p^+_{out,p}$ pressure tapping. This $p^+_{out,p}$ error could be due to an error in the Δp^+_{out} characteristic. However, the $p^+_{out,p}$ error could also be due to an inaccurate calculation of the interstage duct pressure losses. The largest source of pressure loss for the inter-stage duct portion of the model occurs at the nozzle-recirculation bubble interface. The pressure loss coefficients at this interface was an estimate based fluid dynamic arguments (section 3.3). Improved values of pressure loss coefficients could be obtained through a characterisation process, and that this might reduce the observed discrepancy.

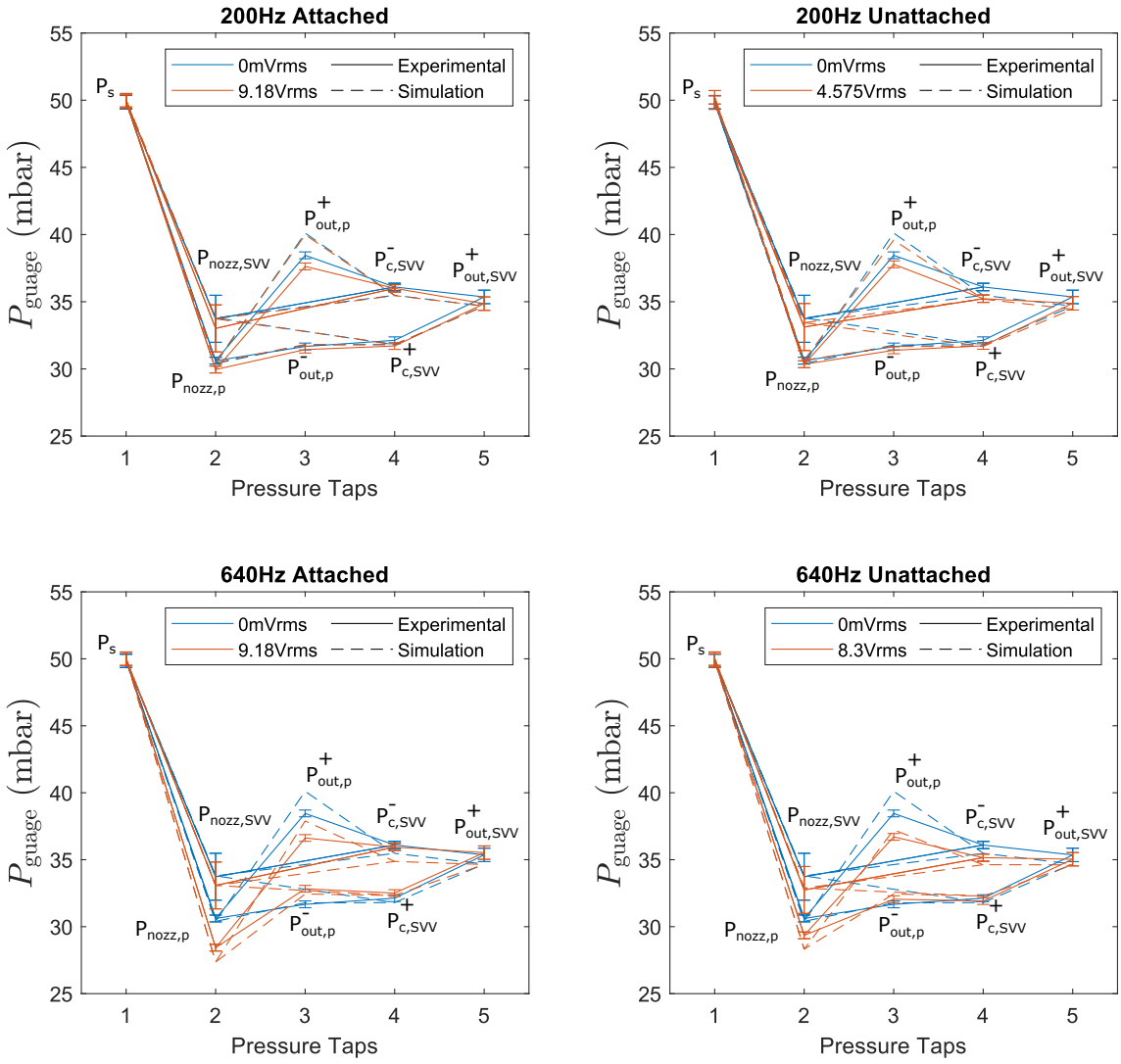

Fig. 6.44 Key pressures of Staged SVV (radial state, $p_{s,p} = p_{s,SVV} = 50\,\text{mbar}$)

6.4.2 Load Switching Oscillations

The oscillatory instability that occurs when degrading the pilot stage supply pressure has been observed both experimentally and numerically (section 5.3). Through the use of numerical simulations, it has been established that, without acoustic actuation, oscillations are triggered when the back-pressure difference imposed by the SVV on the pilot load-switches the pilot diverter section. It has been shown experimentally that for the pilot stage in isolation (section 6.3.4), pilot diverter load-switching can be suppressed by acoustic tones. If pilot diverter load-switching can be acoustically suppressed, then it seems reasonable to expect that acoustic tones could be used to

suppress oscillatory instabilities for the staged SVV.

Figures 6.45-6.48 presents both simulated and experimental oscillatory stability thresholds observed with acoustic actuation from the attached side. As the threshold ratio of gauge supply pressures $p_{s,p}/p_{s,SVV}$ decreases, the staged SVV is more stable, as this represents how far the pilot stage supply can be degraded without triggering the oscillatory instabilities. It is not expected that the simulation will replicate the experimental switching threshold perfectly, as it has already been established that the simulation does not accurately capture the pilot-SVV mass flow split (section 6.4.1). Furthermore, there are the measurement uncertainties associated with the switching thresholds for the pilot and SVV stages. In spite of these issues, for the radial state, the simulated stability threshold trend shapes do agree with experimental observations, even if the absolute values for $p_{s,p}/p_{s,SVV}$ do not align.

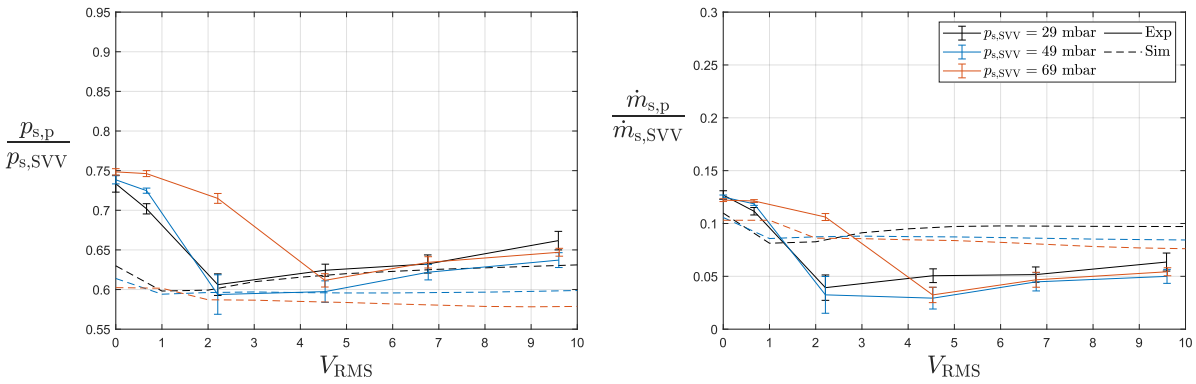

Fig. 6.45 Effect of 200 Hz attached side acoustic signal on oscillatory instability threshold when in the radial (non-vortex) state

Both simulations and experimental observations show that in the radial state, acoustic tones can be used to improve the stability of the staged SVV, but the associated reduction in $p_{s,p}/p_{s,SVV}$ is smaller than expected. The model can be used to find the underlying reason for the limited efficacy of acoustic actuation in the radial state. To find the stability threshold for a given speaker voltage, the pilot supply pressure $p_{s,p}$ is gradually reduced until the simulation detects that one of the

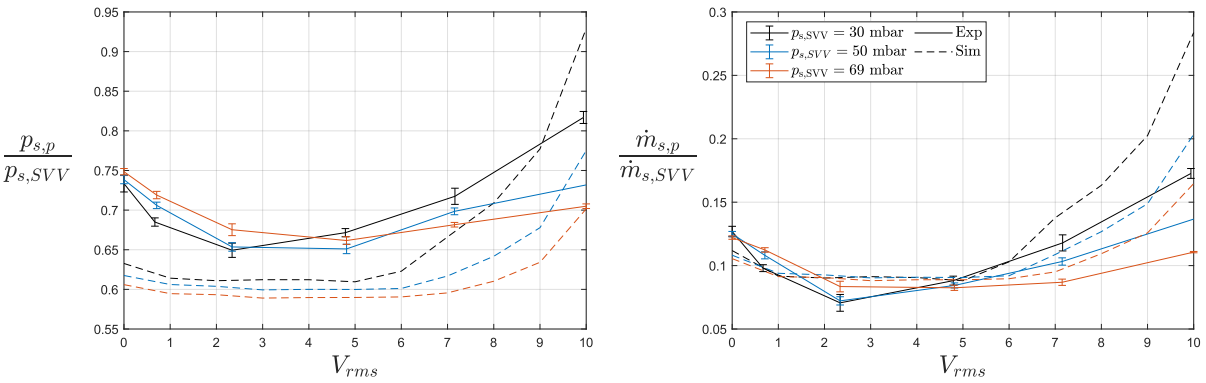

Fig. 6.46 Effect of 640 Hz attached side acoustic signal on oscillatory instability threshold when in the radial (non-vortex) state

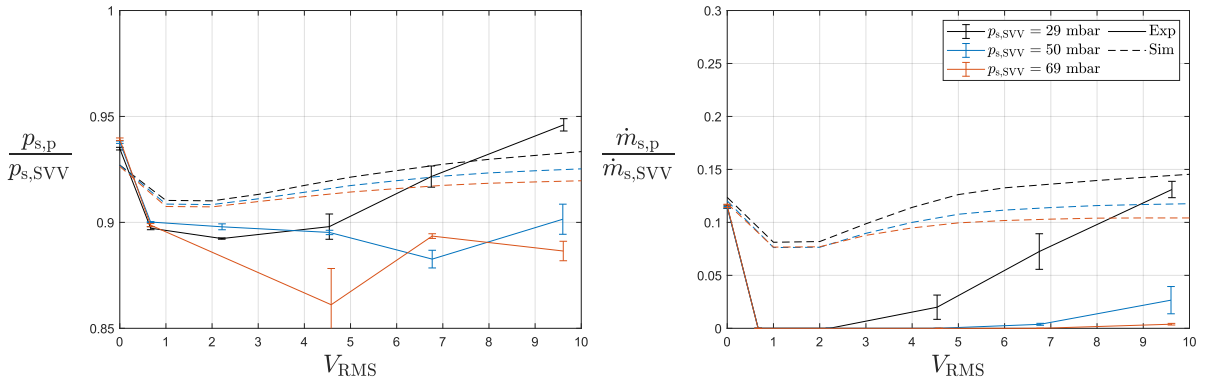

Fig. 6.47 Effect of 200 Hz attached side acoustic signal on oscillatory instability threshold when in the tangential (vortex) state

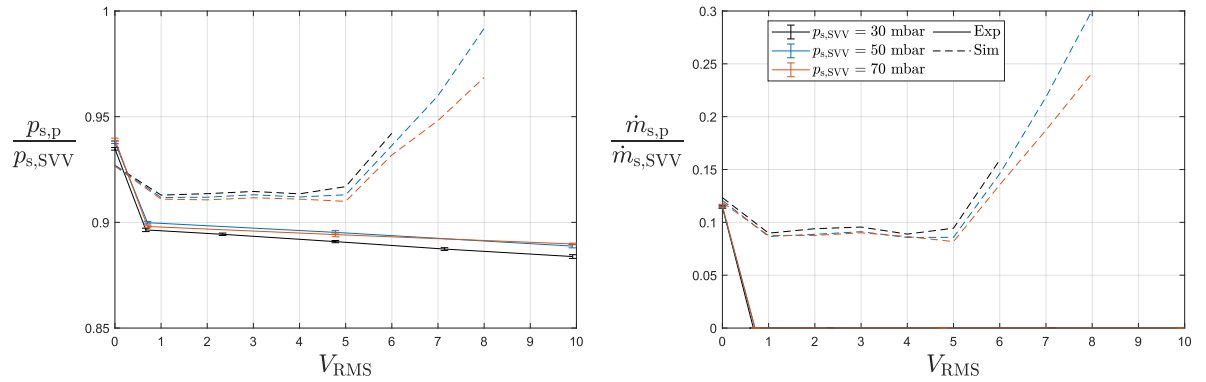

Fig. 6.48 Effect of 640 Hz attached side acoustic signal on oscillatory instability threshold when in the tangential (vortex) state

two diverter sections (pilot or SVV) has started to switch. Figures 6.49 and 6.50 present internal flow parameters for the simulation at the point of switching. As $p_{s,p}$ decreases, wall attachment weakens, and the imposed outlet pressure difference $\Delta p_{c,SVV}$ (figures 6.49(b) and 6.50(b)) has more influence over the outlet mass flow

split $\dot{m}_{\mathrm{out,p}}/\dot{m}_{\mathrm{out,SVV}}$ (figures 6.49(a) and 6.50(a)). Without acoustic actuation ($V_{\mathrm{RMS}} = 0$), oscillations begin when $\dot{m}_{\mathrm{out,p}}/\dot{m}_{\mathrm{out,SVV}}$ crosses the load-switching boundary at 0.45. However, with the introduction of acoustic actuation, the load-switching boundary drops (acoustic stabilisation), and thus $p_{\mathrm{s,p}}$ needs to be reduced further before $\dot{m}_{\mathrm{out,p}}/\dot{m}_{\mathrm{out,SVV}}$ crosses the switching threshold. Although there is an initial sharp drop in the $\dot{m}_{\mathrm{out,p}}/\dot{m}_{\mathrm{out,SVV}}$ curves of figures 6.49 and 6.50 that corresponds to the stability improvement presented in fig 6.45 and 6.46, it rapidly plateaus around 1-2 $\mathrm{V_{RMS}}$. This plateau corresponds with a change in the switching behaviour of the oscillations; instead of the oscillations being triggered when the pilot diverter section is load-switched, it actually starts with the SVV stage switching instead. As $\dot{m}_{\mathrm{out,p}}/\dot{m}_{\mathrm{out,SVV}}$ decreases, more flow is directed towards the attached control port of the SVV until $\dot{m}_{\mathrm{c,SVV}}$ exceeds the switching threshold of the SVV ($\dot{m}_{\mathrm{c,SVV}} \approx 0.1 \times \dot{m}_{\mathrm{s,SVV}}$). At low $p_{\mathrm{s,p}}$, the SVV is effectively switching itself with $\Delta p_{\mathrm{c,SVV}}$ driving flows from the unattached control port to the attached control port. The pilot diverter supply jet does not have enough momentum to counteract this irrespective of its switch state. An example of the simulated oscillations that arise when acoustic tones are suppressing pilot diverter load-switching is presented in figure 6.51. These oscillations closely resemble the oscillatory instability explored in section 5.3; there are regular increases in supply pressure as the SVV switches into the high impedance tangential state, and there are also oscillating output pressures for both diverter sections (pilot and SVV). However, the pilot diverter section's attachment state remains fixed, which means there is no load-switching of the pilot diverter section. Consequently, acoustic tones cannot suppress this instability by stabilising the pilot diverter section. At higher speaker voltages ($V_{\mathrm{RMS}} > 6\,\mathrm{V}$), 640 Hz attached side actuation can have a negative impact upon stability. The acoustic switching threshold voltage decreases as the pilot supply flow rate decreases (section 6.3.4). As $p_{\mathrm{s,p}}$ is reduced, for fixed V_{RMS}, the switching threshold decreases until it drops below the applied speaker voltage, at which point the pilot diverter section

switches triggering an oscillatory instability.

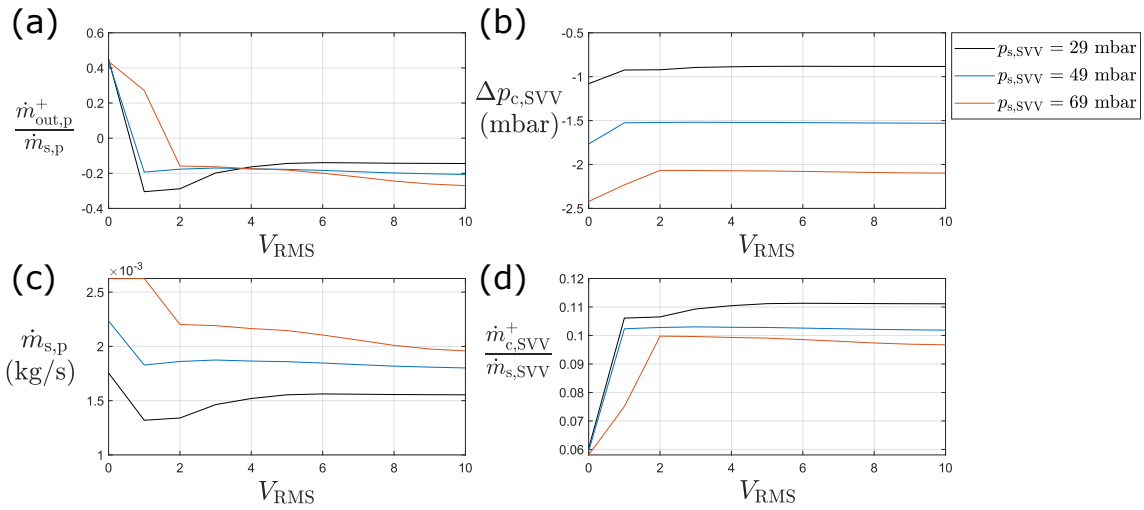

Fig. 6.49 Simulated device parameters at the oscillatory instability threshold, for 200 Hz attached side actuation in the radial (non-vortex) state

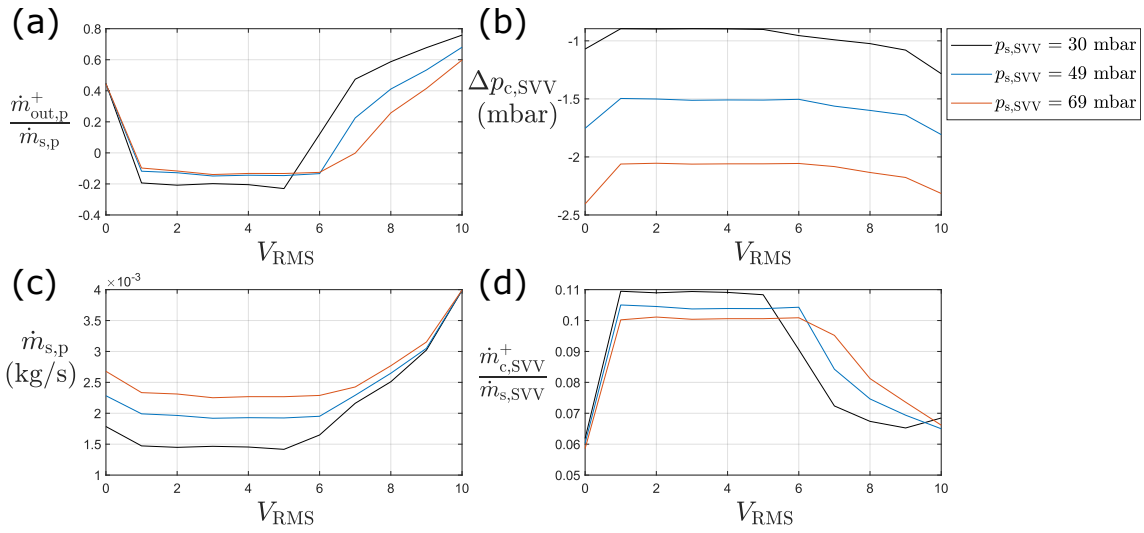

Fig. 6.50 Simulated device parameters at the oscillatory instability threshold, for 640 Hz attached side actuation in the radial (non-vortex) state

The model is less reliable at predicting the device stability in the tangential state, figures 6.47 and 6.48. In particular, it has been observed experimentally that 200 Hz tones with a speaker voltage of 4.5 V_{RMS} can drastically improve the staged SVV stability in the tangential state; at higher $p_{\text{s,SVV}}$ the pilot supply can be degraded almost to the point that $\dot{m}_{\text{s,p}} = 0$. However, this is not predicted by the model. The

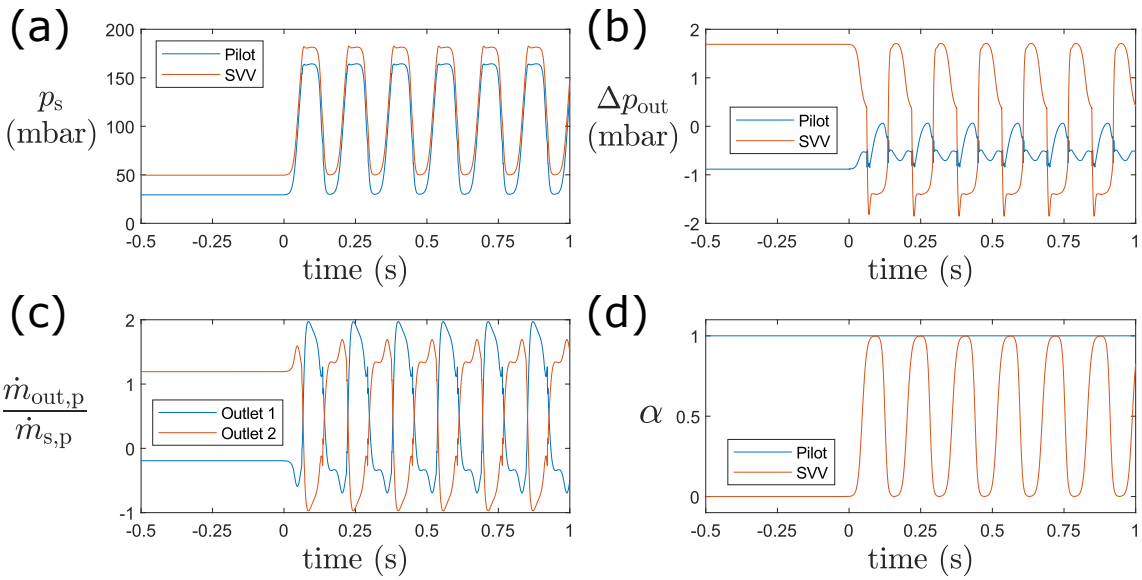

Fig. 6.51 Simulated transition to oscillatory instabilitity, with $p_{s,SVV} = 49\,\text{mbar}$ and $1\,V_{RMS}$, 200 Hz actuation from the attached side

model produces stability threshold curves that resemble the radial state stability threshold curves. With such a large discrepancy between the simulated stability threshold and experimental observations, it seems unlikely that it can be merely the fault of measurement uncertainties or interpolation errors for the steady-state characteristics used to tune the model. Note that there is good agreement between the model and observations for $V_{RMS} = 0$. It is only with the introduction of acoustic actuation that the model and the observations start to diverge. If it is assumed that the load-switching of the pilot diverter section is eliminated with the introduction of acoustic actuation, then the stability threshold is dictated by the SVV switching threshold. It is possible that acoustic actuation, either directly or indirectly, is influencing the stability of the SVV stage. The direct mechanism would involve jet-acoustic interactions for the SVV. It has already been established that acoustic signals can improve the diverter's resistance to load-switching, potentially by increasing the attached side entrainment rate and thus strengthening the Coandă effect. It is conceivable that despite the loudspeakers being located considerably further from the SVV than the pilot stage, acoustic tones are propagating through the interstage ducts

and interacting with the SVV diverter section jet directly, influencing the SVV's susceptibility to switching. Alternatively, acoustic actuation could be influencing the SVV stability indirectly. It has been observed, that with the introduction of acoustic tones that there is a dramatic increase in the amplitude of low frequency pressure fluctuations propagating downstream from the pilot diverter section, section 6.3.2. The frequency of these fluctuations is considerably lower than the actuation frequency, whilst the pressure amplitude is considerably larger. It is theorised that this is the result of acoustic tones exciting shear layer roll-up vortices and thus increasing supply jet flutter. The practical upshot of this is that acoustic actuation will likely result in pulsating control flows for the SVV stage. The model does not simulate this flow unsteadiness, and it is possible that the time-averaged response of the SVV to pulsating control flows may differ from its response to steady control flows with the same average mass flow rate.

6.5 Summary

This chapter introduces acoustic actuation for both the model and the physical device it is based on. Modifications to the staged SVV model accommodating acoustic actuation were presented in section 6.2. These modifications primarily consist of substituting the control mass flow rate parameters of the pilot stage diverter section with the acoustic actuation parameters, namely frequency, speaker voltage and speaker location. This modification of the model, necessitates the re-acquisition of pilot diverter section characterisation data with acoustic actuation. The fresh characterisation data is acquired using a modified version of the pilot stage used in previous chapters, with the control ports altered to accommodate loudspeakers that can be used to acoustically actuate the pilot diverter. The characterisation data is presented in section 6.3 and consists of steady-state characteristics, switching boundaries, and transient response and switching times. With the implementation

of the acoustic characterisation data, the acoustically actuated version of the staged SVV model is complete. After establishing that both the numerical and physical versions of the acoustically actuated staged SVV can be reliably switched between the high and low flow states using 200 Hz tones applied to the unattached side of the pilot stage, section 6.4 uses the model in conjunction with the physical device to explore the effects of non-switching acoustic tones on steady-state performance and dynamic stability.

It was shown by the model that by shifting the operating point of the pilot diverter section, non-switching acoustic tones indirectly shift the operating point of the vortex chamber, modifying the vortex chamber flow field and subsequently the pressure difference across it. Thus with an appropriate choice of frequency and speaker voltage, acoustic actuation can be used to improve the steady-state performance of the staged SVV, primarily by increasing the total flow in the radial state. It was observed that in the radial state, with gauge pilot and SVV supply pressures of 50 mbar gauge, a 640 Hz unattached side tone can be used to increase the total flow rate by 5.6%.

It was also discovered that low voltage acoustic tones could be used to improve the dynamic stability of the staged SVV, delaying the onset of oscillatory instabilities as the pilot supply pressure is degraded. Both the model and experimental observations show that there is a small yet significant improvement in the staged SVV stability when applying low SPL acoustic tones in the radial state. Interrogation of model parameters indicates that the initial improvement to stability can be attributed to acoustic suppression of pilot diverter load-switching. However, the model also shows that this improvement in stability is limited. Decreasing the pilot supply pressure reduces the momentum of the pilot diverter supply jet, reducing its influence over the inter-stage duct flows. At a given point, as the pilot supply pressure is reduced, the

inter-stage duct flows transition from being directed by the pilot diverter supply jet to being driven by the pressure difference between the SVV control ports. The SVV starts switching itself, the diverter section of the SVV starts to oscillate. A more significant improvement in the stage SVV stability is observed in the tangential state, although the exact mechanism that underlies this is not yet understood as the model does not replicate this behaviour. However, it is theorised that this improvement in stability could arise from direct or indirect interactions between the acoustic tones and the SVV stage stability.

Based on the results of these experiments, it is clear that acoustics can be used not only to switch a staged SVV but also to stabilise it and increase its steady-state performance. For real engine applications, the choice of control scheme will depend upon the exact geometry of the staged SVV, the inlet/outlet conditions and the desired flow rates for the high and low flow states. The geometry will not only affect the steady-state performance and stability of the staged SVV without acoustic intervention, it will also affect how the device responds to acoustic signals. In particular, the maximum response frequencies are likely to be highly sensitive to even subtle changes in the pilot stage as these are believed to correspond to resonance properties of the acoustically actuated pilot stage. The inlet and outlet conditions will be set by conditions in the compressor and turbine sections of the jet engine, and thus the pressure ratio across the staged SVV will depend upon engine loads. The range of expected pressure ratios will need to be taken into account when designing the control scheme, as the staged SVV will become less responsive to acoustic actuation at higher flow rates. Finally, the desired flow rates will depend on how much coolant is actually required by the turbine section. Since sub-switching acoustic actuation can alter the flow rates in the high and low flow states, coolant flow rates could be subtly altered to more closely match how much coolant is actually required, given

the engine load.

Hypothetically, given the setup presented in this study, with an applied PR of 1.05, the device can be switched between high and low flow states at will using a 200Hz unattached side signal with $V_{\mathrm{RMS}} > 5.1$. If fitted to an engine, this signal would be used to switch between high and low flow rates for higher and lower engine loads. Provided that the pilot and SVV stages have similar supply pressures, the staged SVV is generally stable. Thus the control scheme for non-switching conditions can be used primarily for modifying steady-state performance. With 640 Hz unattached side signals with speaker voltages between 0 and 10 $\mathrm{V_{RMS}}$, it is possible to alter the total flow rate by 5.6% in the radial (high flow) and by 5.3% in the tangential (low flow state). If the goal is to maximise the TDR, then this can be achieved by applying a 10 $\mathrm{V_{RMS}}$ signal in the radial state and no acoustic tones in the tangential state. This control scheme would maximise flow rates in the high flow state whilst minimising flow rates in the low flow state to achieve a TDR of 2.34 (TDR without actuation is 2.21). Suppose the pilot stage supply pressure is degraded due to pressure losses in a supply manifold. In that case, acoustic actuation can be used to improve the stability of staged SVV and make it less likely to enter an oscillatory state. In this case, the device was found to be most stable when applying 200 Hz or 640 Hz attached side signals with speaker voltages between 2 and 5 $\mathrm{V_{RMS}}$.

The functionality of any control scheme could be greatly improved with the introduction of strategically placed pressure taps to keep track of the staged SVV flow state and enable active control. The speaker voltage would be continuously modified to achieve the desired flow rate that matches the engine load or to provide an interventive signal to stabilise the device as it approaches an unstable flow regime.

Chapter 7
Conclusions

7.1 Summary of Work

This thesis presents a novel fluidic valve, an acoustically switched staged SVV, alongside a grey-box numerical model of this valve. The staged SVV is a two-stage fluidic device consisting of a diverter pilot stage and a Switched Vortex Valve (SVV) power stage. This study presents the first successful implementation of an acoustically actuated, multi-stage fluidic device.

The grey-box numerical model was built to model inter-stage interactions of the staged SVV. Of particular interest were the oscillatory instabilities that are known to occur when supply pressures are too low for the upstream stages of a multi-stage fluidic device. Oscillatory instabilities arise for the staged SVV when the supply pressure for the pilot stage is significantly lower than that of the power stage. Design pressures imposed upon the staged SVV push for a smaller upstream pilot stage with a degraded supply feed. Consequently, these design pressures encourage staged SVV designs that are susceptible to oscillatory instabilities. It was intended that the model be used to identify the underlying mechanism behind the oscillatory instability and provide enough insight to be informed as to what design changes should be made to maximise both stability and steady-state performance.

The model was initially constructed to model the staged SVV with mass flow injection control. The model conceptually subdivides the staged SVV into smaller subsections: supply and inter-stage ducting, diverter switch sections, and vortex

chamber. The ducting is modelled using a lumped parameter model. The duct is subdivided into an alternating series of mass flow, and pressure nodes, which are modelled using 1-D discretised versions of the Navier-Stokes and continuity equations. By contrast, the switch sections and vortex chamber are treated as black-box objects governed by steady-state and transient characteristics obtained from experimental data.

The characteristic data were acquired from the pilot and SVV stages in isolation. Consequently, to validate the model, steady-state pressures and transient responses of the combined system were compared with the predictions of the completed two-stage model. The model convincingly replicates the staged SVV's steady-state pressures and transient switching behaviour. Furthermore, the model also recreates the oscillatory instability that was the primary motivation behind the model's development. The model shows both stages switching between attachment states during the oscillation cycle. The model confirms the assertion made by Tippets & Royle [103] that oscillations are triggered when the upstream stage is load-switched by the downstream stage. As the pilot stage's supply pressure is reduced, wall attachment strength in the pilot diverter section diminishes to the point that it is overcome by the adverse back-pressure gradient imposed by the SVV. As a result, the staged SVV enters a cycle of self-excited switching where the pilot switches the SVV, which then load-switches the pilot.

As part of the characterisation process, it was observed that the steady-state performance of the SVV is sensitive to the SVV control mass flow rates. Altering the SVV control flow rates changes the SVV supply jet position, which affects the vortex chamber flow field. This determines the non-dimensional pressure difference across the vortex chamber, which sets the SVV through-flow rate given constant

supply and exhaust pressures.

As part of the staged SVV, the SVV control flow rates are determined by the pilot outlet mass flow split. Introducing inter-stage constrictions is one method to alter the mass flow split passively. The effect of inter-stage constrictions was explored both experimentally and numerically. It was found that a TDR improvement of 3.8% could be achieved by introducing a localised constriction with constriction ratio $A_c/A_0 = 0.25$ into the inter-stage duct attached to the tangential control port of the SVV. However, this performance improvement comes at a cost. The inter-stage constrictions introduce duct pressure losses that can exacerbate the adverse back-pressure gradient imposed upon the pilot diverter section. Therefore, inter-stage constrictions can make it easier to push the staged SVV into an oscillatory state. The staged SVV is less stable if the minimum supply pressure to the pilot $p_{s,p}$ required for overall system to be stable is increased. For example, in the radial state, the $A_c/A_0 = 0.25$ tangential duct constriction raises the $p_{s,p}$ stability threshold from 68% to 72% of the SVV supply pressure $p_{s,SVV}$.

The next steps involved adapting both the physical device and the numerical model for acoustic control. The physical device was modified by attaching loudspeakers to the control ports of the pilot stage, whilst for the model the pilot diverter section characterisation process had to be repeated, but with control flow dimensions replaced by acoustic control variables, namely frequency, speaker voltage and speaker location (attached or unattached control ports of the pilot diverter section). It was found that the pilot diverter section was most responsive to applied tones around 200 Hz and 640 Hz, so the characterisations focused upon these frequencies.

The pilot diverter section would only switch in response to 200 Hz tones applied from the unattached side or 640 Hz tones applied from the attached side. Unattached side switching was consistently easier to achieve than attached side switching. The

speaker voltages required for switching were anywhere from 3.5 to 16 times greater when applied from the attached side. Both the difference in preferred frequencies and the ease with which the device can be switched from the unattached side are consistent with observations made by Mair et al. [62] for an acoustically switched diverter.

The acoustically actuated pilot stage was characterised in isolation. The acoustically actuated version of the model validated in a similar manner to the mass flow injection version. Model predictions for the combined system are compared with experimental observations of the two-stage device.

The model predicts that it is possible to switch the staged SVV with acoustic tones and experimental observations confirmed this. The 2-stage device can be switched between the radial and tangential states using similar acoustic signals to those that could switch the pilot stage in isolation. This switching is most easily achieved with 200 Hz tones applied to the unattached side of the pilot diverter section. Specifically, the staged SVV operating at a pressure ratio of 1.05 can make a radial-to-tangential switch with a speaker voltage $> 5.1\,\mathrm{V_{RMS}}$ and a tangential-to-radial switch with a speaker voltage $> 1.2\,\mathrm{V_{RMS}}$.

The model's predictions of steady-state pressures and mass flow rates closely replicate the experimental observations. What is revealed by both predictions and experimental observations is that sub-switching acoustic tones reduce the overall flow impedance of the device, irrespective of the attachment state of the SVV (tangential or radial). Given constant supply and exhaust pressures, the radial state total flow rate can be increased by 5.6%. This steady-state performance improvement is made possible by the sensitivity of the vortex chamber to the SVV supply jet position. Acoustic actuation, whether applied from the attached or unattached side of the pilot diverter section, will reduce the pilot outlet mass flow split, which will increase

the SVV attached side control flow rate moving the SVV supply jet.

As well as improving steady-state performance, it was also discovered that acoustic actuation could be used to stabilise the staged SVV, suppressing the self-excited oscillatory instability observed when degrading the pilot supply pressure. Generally speaking, the oscillatory instability is triggered when the SVV load-switches the pilot diverter section. Acoustic actuation increases the pilot diverter section's resistance to load-switching by increasing the stability of wall attachment. In fact, the model shows that at relatively low speaker voltages ($\gtrsim 2\,\mathrm{V_{RMS}}$), the SVV does not load-switch the pilot diverter section. However, self-excited oscillatory instabilities still occur for the acoustically actuated device. If the pilot supply pressure is low enough, the pressure difference between the SVV control ports can still drive a switching control flow rate, irrespective of the pilot diverter attachment state.

7.2 Conclusions and Research Outcomes

It has been successfully demonstrated through a proof concept device (the staged SVV) that it is possible to reliably switch a bistable multi-stage fluidic device with both mass flow injection and, with minimal modifications, acoustic tones. Switching is made considerably easier by diverter sections in a fluidic circuit that act as control signal amplifiers. Consequently, a staged architecture allows large fluidic valves to be switched using comparatively small, low power acoustic actuators. Acoustic actuators are generally lightweight, cost-effective, and less susceptible to wear and tear than the mechanical valves required to switch a fluidic device by mass flow injection.

As a part of this investigation, it has been shown that it is possible to construct a grey-box model of a staged fluidic device. The complex flow interactions of fluidic sections are encapsulated by black-box objects tuned by steady-state and transient

characterisation data, which are connected by lumped element duct sections. Despite its apparent simplicity, this model architecture has been shown to convincingly replicate both steady-state and transient behaviour of the staged SVV, demonstrating that this modelling strategy is a valid technique for simulating the behaviour of staged fluidic devices.

This empirical modelling technique has some distinct advantages over conventional numerical modelling techniques. The inherent simplicity means that models of this type will have short run times. Since all the complex fluid interactions are encapsulated inside black-box sections, unphysical behaviours cannot arise within these sections. If a fluidic component is altered, the entire model does not need to be rebuilt from scratch. Instead, that component just needs to be returned with fresh characterisation data. This model architecture can be quite flexible when it comes to the positioning of fluidic components and the geometry of the interconnecting ducts. The duct geometries can be altered without acquiring fresh characterisation data; thus, a range of staged configurations can be tested. This feature could be particularly useful when a device needs to be fitted into a compact space where there might be packaging issues. Finally, it has been shown that this type of model can predict the steady-state performance (mass flow rates), switching thresholds, and conditions that trigger oscillatory instabilities. All three of these properties are important criteria when considering the design of multi-stage fluidic devices. Therefore, grey box modelling of the architecture described could prove to be a useful design tool for future projects.

In the process of investigating the staged SVV, it was discovered that the stability and performance of a multi-stage device are sensitive to the relative flow impedances of the inter-connecting ducts. By altering the duct impedances, it is possible to alter the relative mass flow split between inter- stage ducts and shift the operating point of a staged fluidic device. If the device is naturally operating in a sub-optimal

state, an appropriate modification of the duct impedances can be used to improve the steady-state performance. However, it has also been shown that modifying these inter-stage impedances can also influence a device's stability. For instance, if the inter-stage impedances are increased, the subsequent rise of inter-stage pressure losses can make the device more susceptible to undesirable oscillatory instabilities. Consequently, inter-stage ducts cannot be designed to maximise steady-state performance without some consideration of the effects that this would have on stability. A grey box model of the type presented could prove useful in this scenario. The duct geometries are one of the easiest aspects to modify, so a grey-box model can be used to find the optimal duct geometry that balances performance against stability.

An important discovery that was made by this investigation was that sub-switching control signals could have a significant effect on both the performance and stability of staged fluidic devices. Both mass flow and acoustic control signals have been shown to influence the stability of diverter switch sections. In the case of mass flow injection, it was found that even a relatively low unattached side control flow rate would stabilise a diverter and make it less susceptible to conventional switching. As for acoustic actuation, any acoustic tone that does not trigger switching was observed to make a diverter switch considerably less susceptible to load-switching. Therefore, sub-switching control signals can be used to suppress self-excited oscillations for staged devices. Currently, stability is one of the most important considerations when it comes to designing and operating multi-stage fluidic devices. Consequently, other desirable properties such as steady-state performance and compactness may have to be compromised to ensure device stability. If self-excited oscillations can be actively suppressed, this design limitation can be removed. Furthermore, this solution comes at zero cost for acoustically actuated devices, as all the equipment required to suppress these oscillations are already built into the device.

Similarly, it has also been shown that sub-switching acoustic control signals can alter the operating point of staged devices. Therefore, sub-switching control signals can be used to improve the performance of staged devices operating in sub-optimal flow states. Once again, this can remove design constraints for staged devices. For instance, a device could be designed for compactness first and performance second, knowing that a sub-switching control signal will be used to compensate for the device naturally operating in a sub-optimal flow state. Alternatively, a device could find itself operating in off-design conditions, and an active control system could intervene here and compensate for the resulting performance penalty. Therefore, an active control system can use sub-switching control signals to make a device more flexible and robust to changes in the operating conditions.

7.3 Suggested Future Work

The major achievements of this study were developing a grey-box model for a staged SVV and showing that acoustic actuation is a practical method for providing active control over multi-stage fluidic devices. However, some improvements can be made to the model to improve both its accuracy and practical utility. Furthermore, there are multiple examples in chapter 6, where the acoustic response of the pilot diverter section acts contrary to expectations. These unexpected diverter responses highlight that diverter-acoustic interactions are not yet fully understood and represent further avenues for investigation.

The current model can reliably predict steady-state and dynamic behaviour for the staged device. Furthermore, it has been shown that the model can be used for both the mass flow injection and acoustically controlled versions of the staged SVV. However, discrepancies between model predictions and experimental observations exist, and some potential sources of error have been identified. First, there are fitting

errors associated with the generation of characteristic lookup tables. This issue can be minimised by gathering more characteristic data and increasing the resolution of the characteristic data sets. Second, the pressure loss coefficient that marks the SVV control port nozzle boundary is thought to be unreliable; this parameter should be experimentally characterised. Third, circumstantial evidence suggests that both the pilot and SVV stages are responsive to acoustics. It has been established both in this study and others [63, 62, 59, 61, 57, 70, 69] that acoustic tones influence the behaviour of wall attachment devices. The model predicts the effects of direct acoustic actuation on the pilot diverter section but neglects to account for the impact actuation tones may have on the SVV diverter section. This issue may be exacerbated by acoustic noise produced by both the pilot and SVV stages. Future studies should quantify how much influence various acoustic sources have over all the diverter sections. Depending on the results, the model may need to incorporate acoustic response characteristics for all diverter sections of the device. Finally, it has been noted that pulsating flows are produced in the pilot stage outlet ducts when the pilot diverter section is subjected to acoustic tones. Future studies should investigate sonic wave effects, e.g. the pulsating flows produced by an acoustically manipulated pilot and how these interact with downstream stages such as an SVV. If necessary, the model could be modified to incorporate a mechanism for generating pulsating duct flows in response to acoustic actuation.

This study focused on the staged SVV, where flows outside the vortex chamber operate in the incompressible flow regime. To minimise the pressure loss coefficient of the staged SVV in the high flow state, it might seem reasonable to have suitably large duct cross-sections to avoid having compressible flows in the high flow state. However, design constraints will place a practical size limit on any flow modulation device. Consequently, in some cases, a staged SVV may have to operate in the compressible flow regime. Therefore, future work may need to explore the behaviour

of a staged SVV operating in the compressible flow regime. The model in its current form cannot be used to model the behaviour of the staged SVV in the compressible flow regime. Both the duct sections and switch sections of the model would need to be modified to incorporate the effects of compressible flows, including the effects of choking if Mach numbers exceed 0.6.

This study has used the model to explore the effect of altering stage supply conditions, modifying inter-stage duct geometries, and introducing sub-switching acoustic control signals. However, one crucial feature of multi-stage fluidic devices remains unexplored, the relative scale of fluidic stages. The same design pressures that push for degraded pilot supply also push for an undersized pilot stage. It would be helpful to have a model that can be used to explore the effects of varying the size of the pilot stage. At present, the mass flow injection characteristics for the pilot's diverter section are non-dimensionalised. These non-dimensionalised characteristics may be length scale invariant for sufficiently high Reynolds numbers. However, this assertion has yet to be tested experimentally. Assuming that the characteristics are length scale invariant, then it would be a simple matter to scale the pilot stage in the model. The model could then be used to find the optimum pilot stage size that maximises steady-state performance whilst avoiding dynamic instabilities.

Furthermore, if the pilot's diverter section steady-state characteristics are length scale invariant, it would also be relatively easy to modify the model to include more diverter stages. With the current physical setup, it has been shown that acoustic control signals can switch the two-stage device between the radial and tangential states. However, the experimental flow rates were $\sim 10\,\mathrm{g/s}$, whilst engine coolant pipe flow rates are considerably higher $\sim 100\,\mathrm{g/s}$. More diverter stages may be needed to allow the acoustic actuators to have enough control authority to switch an SVV at engine

flow rates. Therefore, it would useful to extend the model by adding more stages, and verifying whether or not the model still works properly with this increased complexity.

The one thing that is clear from the acoustic characterisation process is that the maximum response frequencies 200 Hz and 640 Hz do not correspond to jet or shear-layer instability frequencies, nor do they correspond to any universal resonance frequencies of the cavity. It was theorised but not confirmed that the difference between the resonance frequencies identified by a single microphone and the observed maximum response frequencies could be due to spatial variations in the frequency response of the cavity. Further investigations should be conducted to ascertain the mechanisms by which the acoustic input interact with the switch, and hence why the device responds most strongly to the particular frequencies (in the case of the present device, 200Hz and 640Hz).

According to Mair [57], acoustic actuation can have more influence on an attached jet when the excitation frequency corresponds to the jet preferred mode frequency f_{p}. For a rectangular jet f_{p} is believed to be linked to the jet dynamic head Strouhal number $St_{\mathrm{Dh}} = 0.45$. Using the pilot stage nozzle hydraulic diameter $D_{\mathrm{h}} = 6.5$ mm over the range of mass flow rates tested (0.99-4.92 g/s) produces f_{p} values between 0.89 and 4.44 kHz. This frequency ranges does overlap with the range of frequencies tested 0-2 kHz in this study. However, it would be useful to confirm that jet/shear-layer instability frequencies do not appear in the maximum response spectra at higher flow rates.

References

[1] Aviation: Benefits Beyond Borders. Technical report, Air Transport Action Group, 2020.

[2] Robert B Adams and Coleman B Moore. Flow control apparatus, apr 1963.

[3] AFNOR Association Française de Normalisation. NF EN ISO 5167-2, 2003.

[4] Jin Woo Bae, Kenneth S Breuer, and Choon S Tan. Active Control of Tip Clearance Flow in Axial Compressors. *Journal of Turbomachinery*, 127(2):352–362, 2005.

[5] C. Bourque and B. G. Newman. Reattachment of a Two-Dimensional, Incompressible Jet to an Adjacent Flat Plate. *The Aeronautical Quarterly*, 11(3):201–232, 1960.

[6] Ronald E Bowles and Billy M Horton. Fluid Amplifier US Patent 3276259A. 1960.

[7] K D Brundish, C W Wilson, S Nash, J. Tippetts, and R. Woolhouse. The Initial Design of a Fluidically Controlled Variable Geometry Fuel Injector for Gas Turbine Combustion Systems. In *34th AIAA/ASME/SAE/ASEE Joint Propulsion Conference and Exhibit*, pages 1–8, Cleveland, Ohio, jul 1998. American Institute of Aeronautics and Astronautics.

[8] Michel Bruneau. *Fundamentals of Acoustics*. ISTE Ltd, 1st edition, 2010.

[9] E Buckingham. On Physically Similar Systems: Illustrations of the Use of Dimensional Equations. *Physical Review*, 4(4):345–376, 1914.

[10] Louis N. Cattafesta III and Mark Sheplak. Actuators for Active Flow Control. *Annual Review of Fluid Mechanics*, 43:247–272, jan 2011.

[11] Y Y Chan. Spatial waves in turbulent jets. *Physics of Fluids*, 17(1):46–53, 1974.

[12] Hyo Whan Chang. *Dynamic Analysis of a Monostable Fluid Amplifier*. PhD thesis, Oklahoma State University, Oklahoma, 1978.

[13] Li-Wei Chen, James Turner, Marko Bacic, and Peter Ireland. Plasma-fluidic no moving parts valve: Experiments and Numerical studies. In *8th AIAA Flow Control Conference*, Reston, Virginia, jun 2016. American Institute of Aeronautics and Astronautics.

[14] C F Colebrook and C M White. Experiments with Fluid Friction in Roughened Pipes. *Proceedings of the Royal Society of London. Series A, Mathematical and Physical Sciences*, 161(906):367–381, 1937.

[15] Thomas C Corke, Martiqua L Post, and Dmitriy M Orlov. Single dielectric barrier discharge plasma enhanced aerodynamics: physics, modeling and applications. *Experiments in Fluids*, 46:1–26, 2009.

[16] S. C. Crow and F. H. Champagne. Orderly structure in jet turbulence. *Journal of Fluid Mechanics*, 48(3):547–591, 1971.

[17] Dennis Culley, Sanjay Garg, S J Hiller, Wolfgang Horn, Aditya Kumar, H Kirk Mathews, Hany Moustapha, Hugo Pfoertner, Taylor Rosenfeld, Pavol Rybarik, Klaus Schadow, Ion Stiharu, Daniel E Viassolo, and John Webster. More Intelligent Gas Turbine Engines (Des turbomoteurs plus intelligents). Technical report, The Research and Technology Organisation (RTO) of NATO RTO, 2009.

[18] Dennis E. Culley. Variable Frequency Diverter Actuation for Flow Control. In *3rd AIAA Flow Control Conference*, San Francisco, California, 2006.

[19] Miles O Dustin and Robert E Wallhagen. Design and performance of two integrated circuits for fluidic-controlled pneumatic stepping-motor system, 1969.

[20] M Epstein. Theoretical Investigation of the Switching Mechanism in a Wall Attachment Fluid Amplifier. *Journal of Fluids Engineering*, 93(1):55–62, 1971.

[21] Douglas Feikema and Dennis Culley. Computational Fluid Dynamic Modeling of a Fluidic Actuator for Flow Control. In *46th AIAA Aerospace Sciences Meeting and Exhibit*, Reston, Virigina, jan 2008. American Institute of Aeronautics and Astronautics.

[22] Gene F Franklin, J David Powell, and Michael Workman. *Digital Control of Dynamic Systems*. Addison Wesley Longman, Inc, 3 edition, 1998.

[23] Quentin Gallas, Ryan Holman, Toshikazu Nishida, Bruce Carroll, Mark Sheplak, and Louis Cattafesta. Lumped Element Modeling of Piezoelectric-Driven Synthetic Jet Actuators. *AIAA Journal*, 41(2):240–247, 2003.

[24] R S Gluskin, M Jacoby, and T D Reader. Flodac-A pure fluid digital computer. In *AFIPS Conference Proceedings - 1964 Fall Joint Computer Conference*, pages 631–641, 1964.

[25] Suleyman Gokoglu, Maria Kuczmarski, Dennis Culley, and Surya Raghu. Numerical Studies of a Fluidic Diverter for Flow Control. In *39th AIAA Fluid Dynamics Conference*, Reston, Virigina, jun 2009. American Institute of Aeronautics and Astronautics.

[26] John M Goto and Tadeusz M Drzewiecki. An analytical model for the response of flueric wall attachment amplifiers. Technical report, Harry Diamond Laboratories, Washington, D.C., 1972.

[27] James W Gregory, Ebenezer P Gnanamanickam, John P Sullivan, and Surya Raghu. Variable-Frequency Fluidic Oscillator Driven by Piezoelectric Devices. In *43rd AIAA Aerospace Sciences Meeting & Exhibit*, pages 1–12, 2005.

[28] James W. Gregory, Ebenezer P. Gnanamanickam, John P. Sullivan, and Surya Raghu. Variable-Frequency Fluidic Oscillator Driven by a Piezoelectric Bender. *AIAA Journal*, 47(11):2717–2725, nov 2009.

[29] James W Gregory, Joseph C Ruotolo, Aaron R Byerley, and Thomas E Mclaughlin. Switching Behavior of a Plasma-Fluidic Actuator. *AIAA Journal*, 2007.

[30] Maxime Guillaume. Propulseur par réaction sur l'air, 1922.

[31] Chih-Ming Ho and Lein-Saing Huang. Subharmonics and vortex merging in mixing layers. *J . Fluid Mech*, 119:443–473, 1982.

[32] J H Horlock, D T Watson, and T V Jones. Limitations on Gas Turbine Performance Imposed by Large Turbine Cooling Flows. In *ASME Turbo Expo*, Munich, Germany, may 2000.

[33] A. M Howatson, P. G Lund, and J. D Todd. *Engineering tables and data*. University of Oxford, Department of Engineering Science, Oxford, 3 edition, 2009.

[34] Junhui Huang, Thomas C Corke, and Flint O Thomas. Plasma Actuators for Separation Control of Low-Pressure Turbine Blades. *AIAA Journal*, 44(1), 2006.

[35] Z D Husain and A K M F Hussaint. Natural Instability of Free Shear Layers. *AIAA JOURNAL*, 21(11):1512–1517, 1983.

[36] A K M F Hussain and K B M Q Zaman. Controlled Perturbation of Circular Jets. In *Structure and Mechanisms of Turbulence I*, pages 31–42. 1978.

[37] A K M F Hussain and K B M Q Zaman. The free shear layer tone phenomenon and probe interference. *Journal of Fluid Mechanics*, 87(2):349–383, 1978.

[38] A K M Fazle Hussain. Coherent structures and turbulence. *Journal of Fluid Mechanics*, 173:303–356, 1986.

[39] ISO 527-2. International Standard International Standard. *61010-1 © Iec:2001*, 2003:13, 2003.

[40] P Jiang, Y C Guo, C K Chan, and W Y Lin. Frequency characteristics of coherent structures and their excitations in small aspect-ratio rectangular jets using large eddy simulation. *Computers and Fluids*, 36(3):611–621, 2007.

[41] James W Joyce and Richard N Gottron. Fluidics: Basic Components and Applications. Technical report, Harry Diamond Laboratories, Adelphi, MD, 1979.

[42] Kelm UK. Technical Data Air Preparation (KRS600).

[43] J H Kim, J Kastner, and M Samimy. Active control of a high reynolds number Mach 0.9 axisymmetric Jet. *AIAA Journal*, 47(1):116–128, 2009.

[44] T. S. Kim and S. T. Ro. The effect of gas turbine coolant modulation on the part load performance of combined cycle plants. Part 1: gas turbines. *Proceedings of the Institution of Mechanical Engineers, Part A: Journal of Power and Energy*, 211(6):453–459, 1997.

[45] C F King. Vortex amplifier internal geometry and its effect on performance. *International Journal of Heat and Fluid Flow*, 6(3):160–170, 1985.

[46] Joseph M Kirshner. *Fluid Amplifiers*. McGraw-Hill Inc, Washington, D.C., 1 edition, 1966.

[47] Joseph M Kirshner and Silas Katz. *Design Thoery of Fluidic Components*. Academic Press, Inc., New York, 1 edition, 1975.

[48] N W M Ko and P O A L Davies. The near field within the potential cone of subsonic cold jets. *Journal of Fluid Mechanics*, 50(1):49–78, 1971.

[49] Bharat Koli, John W Chew, Nick J Hills, and Timothy Scanlon. CFD Investigation of a Fluidic Device for Modulation of Aero-Engine Cooling Air. In *Proceedings of ASME Turbo Expo 2014: Turbine Technical Conference and Exposition*, pages 1–12, Düsseldorf, Germany, 2014. The American Society of Mechanical Engineers.

[50] Bharat Ramesh Koli. *CFD investigation of a switched vortex valve for cooling air flow modulation in aeroengine*. PhD thesis, University of Surrey, 2015.

[51] Amol A. Kulkarni, Vivek V. Ranade, R. Rajeev, and S. B. Koganti. Pressure drop across vortex diodes: Experiments and design guidelines. *Chemical Engineering Science*, 64(6):1285–1292, 2009.

[52] Pijush K Kundu and Ira M Cohen. *Fluid Mechanics*. Elsevier Science, 2 edition, 2002.

[53] Sheldon G Levin and Francis M Manion. Jet Attachment Distance as a Function of Adjacent Wall Offset and Angle. Technical report, Harry Diamond Laboratories, Washington, D.C., 1962.

[54] P A Lush. Investigation of the switching mechanism in a large scale model of a turbulent reattachment amplifier. In *Second Cranfield Fluidic Conference*, pages 1–17, Cambridge, England, 1967.

[55] P A Lush. A theoretical and experimental investigation of the switching mechanism in a wall attachment fluid amplifier. In *IFAC Symposium on Fluidics*, 1968.

[56] M Mair, M Bacic, K Chakravarthy, and B Williams. Jet preferred mode vs shear layer mode. *Physics of Fluids*, 32(6), 2020.

[57] Michael Mair. *On Dynamics of Fluidic Jet Switching and More*. PhD thesis, University of Oxford, 2019.

[58] Michael Mair and Marko Bacic. Active Fluidic Switching at High Mach Numbers. In *AIAA Aviation 2019 Forum*, pages 1–11, 2019.

[59] Michael Mair, Marko Bacic, and Peter Ireland. Switching Dynamics of a Fluid Diverter Valve Using Ultrasonic Excitation for Active Flow Control. In *47th AIAA Fluid Dynamics Conference*, pages 1–14, 2017.

[60] Michael Mair, Marko Bacic, and Peter Ireland. Switching Dynamics of a Fluid Diverter Valve Using Ultrasonic Excitation for Active Flow Control. In *2017 AIAA AVIATION Forum*, Denver, 2017.

[61] Michael Mair, Marko Bacic, and Peter Ireland. On Dynamics of Acoustically Driven Bistable Fluidic Valves. *Journal of Fluids Engineering*, 141(061202):1–10, 2019.

[62] Michael Mair, Li-Wei Chen, James Turner, Marko Bacic, and Peter Ireland. Experimental and Numerical Study of a Piezo Driven Fluid Diverter for Active Flow Control. In *52nd AIAA/SAE/ASEE Joint Propulsion Conference*, pages 1–16, Salt Lake City, UT, jul 2016. American Institute of Aeronautics and Astronautics.

[63] Nicholas D. Martin, Michael Bottomley, and Alan Packwood. Switching of a Bistable Diverter Valve with Synthetic Jet Actuators. *AIAA Journal*, 52(7):1563–1568, jul 2014.

[64] P D Mcfadden and R O Cleveland. Engineering Science Prelims: Fluid Mechanics, 2017.

[65] A Michalke. On the inviscid instability of the hyperbolic-tangent velocity profile. *Journal of Fluid Mechanics*, 19(4):543–556, 1964.

[66] A Michalke. On spatially growing disturbances in an inviscid shear layer. *Journal of Fluid Mechanics*, 23:521–544, 1965.

[67] H R Muller. A Study of the Dynamic Features of a Wall-Reattachment Fluid Amplifier. *Journal of Basic Engineering*, 86(4):819–826, dec 1964.

[68] H. R. Muller. Wall Reattachment Device with Pulsed Control Flow. In *Fluid Amplification Symposium: Volume I*, pages 179–215, Washington, D.C., 1964.

[69] Chris Nicholls. *The analysis, modelling and acoustic control of fluidic devices*. PhD thesis, University of Oxford, 2021.

[70] Chris Nicholls and Marko Bacic. Closed-loop control of a piezo-fluidic amplifier. *AIAA Journal*, 58(6):2414–2427, 2020.

[71] P O'Neill, J Soria, and D Honnery. The stability of low Reynolds number round jets. *Experiments in Fluids*, 36(3):473–483, 2004.

[72] D Oster and I Wygnanski. The forced mixing layer between parallel streams. *Journal of Fluid Mechanics*, 123:91–130, 1982.

[73] D Parker, M J Birch, and J Francis. Computational Fluid Dynamic Studies of Vortex Amplifier Design for the Nuclear Industry—I. Steady-State Conditions. *Journal of Fluids Engineering, Transactions of the ASME*, 133(4):1–16, 2011.

[74] S. V. Patankar. *Numerical heat transfer and fluid flow.* Taylor & Francis, 1st edition, 1980.

[75] Tim Persoons. General Reduced-Order Model to Design and Operate Synthetic Jet Actuators. *AIAA Journal*, 50(4):916–927, 2012.

[76] Kay Olaf Ploetner, Rothfeld Raoul, Marcia Urban, Mirko Hornung, Gilbert Tay, and Oluwaferanmi Oguntona. Technological and Operational Scenarios on Aircraft Fleet-Level towards ATAG and IATA 2050 Emission Targets. *17th AIAA Aviation Technology, Integration, and Operations Conference*, pages 1–13, 2017.

[77] Mark L Potter. *Non-Return Valve Instabilities*. Dphil, University of Oxford, 2008.

[78] Geoffrey H Priestman, Timothy J Scanlon, John R Tippets, and Paul Wilson. Flow Control Arrangement, 2011.

[79] Paul R Prokopius. A Fluidic Device for Measuring Constituent Masses of a Flowing Binary Gas Mixture. Technical report, Lewis Research Center, NASA, Cleveland, 1973.

[80] G Raman and A B Cain. Innovative actuators for active flow and noise control. *Proceedings of the Institution of Mechanical Engineers, Part G: Journal of Aerospace Engineering*, 216:303–324, 2002.

[81] Ganesh Raman and Surya Raghu. Cavity Resonance Suppression Using Miniature Fluidic Oscillators. *AIAA Journal*, 42(12):2608–2611, 2004.

[82] Ganesh Raman, Edward J. Rice, and David M. Cornelius. Evaluation of Flip-Flop Jet Nozzles for Use as Practical Excitation Devices. *Journal of Fluids Engineering, Transactions of the ASME*, 116(3):508–515, 1994.

[83] Roger C Reed. *The Superalloys*. Cambridge University Press, 1 edition, 2006.

[84] James P Ries. Dynamic Modelling of the Bistable Fluid Amplifier. Technical report, Department of Mechanical Engineering and Mechanics, Lehigh University, Bethlehem, Pennsylvania, 1972.

[85] R P Roger and S C Chan. Numerical Study of Fluidic Bistable Amplifiers. In *33rd AIAA Fluid Dynamics Conference and Exhibit*, pages 1–10, 2003.

[86] Nicolas Romero Gonzalez. *Design and Optimisation of Power Fluidic Components for Compressible Flow Control*. University of Sheffield, 2014.

[87] M. Samimy, J.-H. Kim, J. Kastner, I. Adamovich, and Y. Utkin. Active control of high-speed and high-Reynolds-number jets using plasma actuators. *J. Fluid Mech*, 578:305–330, 2007.

[88] M Samimy, J H Kim, M Kearney-Fischer, and A Sinha. Acoustic and flow fields of an excited high Reynolds number axisymmetric supersonic jet. *Journal of Fluid Mechanics*, 656:507–529, 2010.

[89] Mo Samimy, Nathan Webb, and Michael Crawley. Excitation of Free Shear-Layer Instabilities for High-Speed Flow Control. *AIAA Journal*, 56(5):1770–1791, 2018.

[90] R A Sawyer. The flow due to a two-dimensional jet issuing parallel to a flat plate. *Journal of Fluid Mechanics*, 9(4):543–559, 1960.

[91] R. A. Sawyer. Two-dimensional reattaching jet flows including the effects of curvature on entrainment. *Journal of Fluid Mechanics*, 17(4):481–498, 1963.

[92] T Scanlon, P Wilson, G Priestman, and J Tippetts. Development of a Novel Flow Control Device for Limiting the Efflux of Air through a Failed Pipe. In *Proceedings of the Asme Turbo Expo 2009*, pages 1–11, 2009.

[93] Sensortechnics. HCX Series Fully signal conditioned pressure transducer, 2007.

[94] Rachelle Speth and Datta V Gaitonde. Parametric study of a Mach 1.3 cold jet excited by the flapping mode using plasma actuators. *Computers and Fluids*, 84:16–34, 2013.

[95] C E Spyropoulos. A Sonic Oscillator. In *Fluid Amplification Symposium: Volume III*, Washington, D.C., 1964.

[96] Brian M T Tang, Marko Bacic, and Peter T Ireland. Effect of active modulation of through-casing coolant injection on turbine efficiency. In *Proceedings of the ASME Turbo Expo: Turbomachinery Technical Conference and Exposition*, volume 2A, pages 1–9, 2017.

[97] V. Tesař. Pump for extremely dangerous liquids. *Chemical Engineering Research and Design*, 89(7):940–956, 2011.

[98] V Tesař. Fluidics: The answer to problems of handling hazardous fluids-a survey. *International Journal of Safety and Security Engineering*, 2(2):167–183, 2012.

[99] Václav Tesař. No-moving-part valve for automatic flow switching. *Chemical Engineering Journal*, 162:278–295, 2010.

[100] D Thoma. Fluid Lines US1839616A, 1929.

[101] J R Tippetts. Finding the operating point of Eulerian flow machines. *International Journal of Heat and Fluid Flow*, 5(1):3–12, 1984.

[102] J R Tippetts, H K Ng, J K Royle, and H Weed. A Fluidic Flowmeter. *Automatica (Journal of IFAC)*, 9:35–45, 1973.

[103] J R Tippetts and J K Royle. Design of Flow Control Circuits Involving Unvented Bistable Amplifiers. *Fluidics Quaterly*, 3(4):1–15, 1971.

[104] James Turner, Marko Bacic, Li-Wei Chen, Michael Mair, and Peter Ireland. Chraracterization of a Plasma-Actuated Fluidic Valve. In *8th AIAA Flow Control Conference*, pages 1–31, 2016.

[105] Y. Utkin, S. Keshav, J.-H. Kim, J. Kastner, I. Adamovich, and M. Samimy. Development and use of localized arc filament plasma actuators for high-speed flow control. *Journal of Physics. D: Applied Physics*, 40(3):685–694, 2007.

[106] Daniel K Van Ness II, Thomas C Corke, and Scott C Morris. Turbine Tip Clearance Flow Control using Plasma Actuators. In *44th AIAA Aerospace Sciences Meeting and Exhibit*, 2006.

[107] G. H. Vatistas, C. Lam, and S. Lin. A Similarity Relationship for the Pressure Drop in Vortex Chambers. *The Canadian Journal of Chemical Engineering*, 67(4):540–544, 1989.

[108] G. H. Vatistas, S. Lin, and C. K. Kwok. Theoretical and Experimental Studies on Vortex Chamber Flows. *AIAA Journal*, 24(4):635–642, 1986.

[109] Hermann Viets. Flip-flop jet nozzle. *AIAA Journal*, 13(10):1375–1379, 1975.

[110] Visaton. FR 58 - 8Ohm Datasheet.

[111] Bernard Vonnegut. A Vortex Whistle. *The Journal of the Acoustical Society of America*, 26(1):18–20, 1954.

[112] Rolf E Wagner. Fluidics-a new control tool. *IEEE Spectrum*, 6(11):58–68, 1969.

[113] H Wang, S B M Beck, G H Priestman, and R F Boucher. Fluidic Pressure Pulse Transmitting Flowmeter. *Chemical Engineering Research and Design*, 75(4):381–391, 1997.

[114] Kajiro Watanabe and Hiroshi Sato. Vortex Whistle as a Flow Meter. In *Conference Proceedings. 10th Anniversary. IMTC/94. Advanced Technologies in I & M. 1994 IEEE Instrumentation and Measurement Technolgy Conference*, volume 3, pages 1225–1228, 1994.

[115] Frank Whittle. Improvements relating to the Propulsion of Aircraft and other Vehicles, 1931.

[116] R J Woolhouse, J R Tippetts, and S B M Beck. A comparison of the experimental and computational modelling of the fluidic turn-up vortex amplifier at full and zero swirl conditions. *Proceedings of the Institution of Mechanical Engineers, Part C: Journal of Mechanical Engineering Science*, 215(8):893–903, aug 2001.

[117] I Wygnanski and H Fiedler. Some measurements in the self-preserving jet. *Journal of Fluid Mechanics*, 38(3):577–612, 1969.

[118] G Xu and R A Antonia. Effect of different initial conditions on a turbulent round free jet. *Experiments in Fluids*, 33(5):677–683, 2002.

[119] K B M Q Zaman and Hussain A K M F. Turbulence suppression in free shear flows by controlled excitation. *Journal of Fluid Mechanics*, 103:133–159, 1981.

[120] K B M Q Zaman and A K M F Hussain. Vortex pairing in a circular jet under controlled excitation. Part 1. General jet response. *Journal of Fluid Mechanics*, 101(part 3):449–491, 1980.

Appendix A
Derivation of Mass Flow and Pressure Relations for Duct Model

A.1 Discretisation of the Navier-Stokes Equation

Consider a single mass flow lump figure A.1

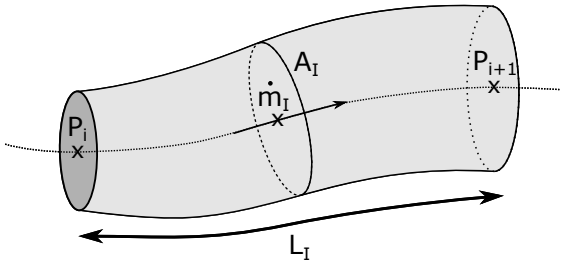

Fig. A.1 Mass flow lump

The lump is modelled as if the streamlines are all parallel to the duct walls. A cylindrical polar coordinate system is projected onto the lump such that the z-axis aligns with the streamlines. The z-component of the Reynolds averaged Navier-Stokes momentum equation is as follows

$$\rho\left(\frac{\partial u_z}{\partial t}+u_z\frac{\partial u_z}{\partial z}\right)=-\frac{\partial p}{\partial z}+\mu\nabla^2 u_z \tag{A.1}$$

the u_r and u_ϕ components of the convection term have been eliminated as $u_r, u_\phi = 0$. Applying a control volume integral and implementing divergence theorem for the diffusion term

$$\int_{CV}\rho\frac{\partial u_z}{\partial t}dV+\int_{CV}\rho u_z\frac{\partial u_z}{\partial z}dV=-\int_{CV}\frac{\partial p}{\partial z}dV+\mu\int_S\nabla u_z.dA \tag{A.2}$$

Dealing with each of these 4 terms sequentially

1.

$$\begin{aligned}\int_{CV}\rho\frac{\partial u_z}{\partial t}dV &\approx \rho\frac{\partial}{\partial t}\int_{CV}u_z dV \quad \text{incompressible approximation}\\ &\approx \rho A_I L_I\frac{d\langle u_z\rangle_I}{dt} \quad \text{constant } A \text{ approximation}\\ &= L_I\frac{d\dot{m}_i}{dt}\end{aligned} \tag{A.3}$$

2.

$$\begin{aligned}\int_{CV}\rho u_z\frac{\partial u_z}{\partial z}dV &\approx \rho\iiint\frac{\partial}{\partial z}\left(\frac{1}{2}u_z\right)rdrd\phi dz \quad \text{incompressible approximation}\\ &= \frac{1}{2}\rho\iint\left[u_z^2\right]_i^{i+1}rdrd\phi\\ &\approx \frac{1}{2}\rho A_I\left[\langle u_z^2\rangle_{i+1}-\langle u_z^2\rangle_i\right] \quad \text{constant } A \text{ approximation}\\ &= A_I\left[q_{i+1}-q_i\right]\end{aligned} \tag{A.4}$$

3.

$$-\int_{CV}\frac{\partial p}{\partial z}dV \approx A_I\left[p_i-p_{i+1}\right] \quad \text{constant } A \text{ approximation} \tag{A.5}$$

4.

$$\begin{aligned}\mu\int_S\nabla u_z.dA &= \mu\int\frac{\partial u_z}{\partial z}dA_{i+1}-\mu\int\frac{\partial u_z}{\partial z}dA_i+\mu\int\frac{\partial u_z}{\partial r}dA_w\\ &= \mu\left[A_{i+1}\frac{\partial\langle u_z\rangle_{i+1}}{\partial z}-A_i\frac{\partial\langle u_z\rangle_i}{\partial z}\right]+\mu A_w\frac{\partial\langle u_z\rangle_w}{\partial r}\end{aligned} \tag{A.6}$$

where A_w is the duct wetted area for this mass flow lump. The wall shear stress term (friction losses) can be estimated using the Darcy-Weisbach equation i.e.

$$\mu A_w\frac{\partial\langle u_z\rangle_w}{\partial r} \approx \left[\frac{A}{L}\frac{1}{2}\rho\frac{\langle u_z\rangle^2}{D_h}f_D\right]_I \tag{A.7}$$

where D_h is the hydraulic diameter.

Pulling all this together the ordinary differential equation for a mass flow lump $\dot{m}_I$ is

$$\frac{d\dot{m}_I}{dt} = \frac{A_I}{L_I}\left[(p+q)_i - (p+q)_{i+1}\right] - R_{fI}\,\dot{m}_I^2 \tag{A.8}$$

where

$$R_{fI} = \left[\frac{1}{2.\rho.A.D_h f_D}\right]_I \tag{A.9}$$

Note that the $\mu A \partial_z \langle u_z \rangle$ diffusion terms are missing. Typically, in CFD models the discretised diffusion terms are combined with the convection terms. Here, with the exception of the wall shear stress term, it is assumed that the contribution of convection is much greater than diffusion and thus these additional diffusion terms are ignored.

A.2 Discretisation of the Continuity Equation

Consider a single pressure lump p_i encapsulated by mass flow nodes $\dot{m}_{I-1}$ and $\dot{m}_I$,

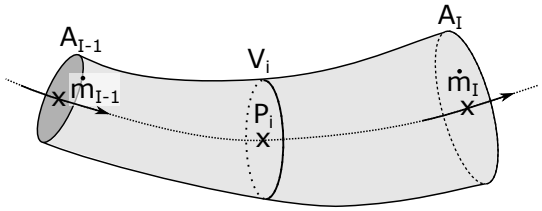

Fig. A.2 Pressure lump

The lumped pressure is modelled using a 1D discretisation of the continuity equation. The adiabatic continuity equation is as follows

$$\frac{1}{c^2}\frac{\partial p}{\partial t} = -\nabla.\left(\rho \mathbf{u}\right) \tag{A.10}$$

A control volume integral is applied to the p_i volume, so

$$\int_{CV} \frac{1}{c^2}\frac{\partial p}{\partial t} dV = -\int_{CV} \nabla.\left(\rho \mathbf{u}\right) dV \tag{A.11}$$

Starting with the left hand side

$$\begin{aligned}\int_{CV} \frac{1}{c^2}\frac{\partial p}{\partial t} dV &\approx \frac{1}{c^2}\int_{CV} \frac{\partial P}{\partial t} dV \quad \text{(assume that temperature variations are small)} \\ &= \frac{1}{c^2}\frac{\partial}{\partial t}\int_{CV} p dV \\ &= \frac{1}{c^2}\frac{dp_i}{dt} V_i \end{aligned} \tag{A.12}$$

where p_i is chosen to be the volume averaged pressure and V_i is the volume of the pressure lump. The right hand side integral is resolved as follows

$$\begin{aligned} -\int_{CV} \nabla.\left(\rho \mathbf{u}\right) dV &= -\int_S \rho \mathbf{u}.\mathbf{dA} \\ &= -\left[-\langle \rho u_\perp \rangle_{I-1} A_{I-1} + \langle \rho u_\perp \rangle_I A_I\right] \\ &= \left[\dot{m}_{I-1} - \dot{m}_I\right] \end{aligned} \tag{A.13}$$

So the relationship used for pressure nodes p_i is

$$\frac{dp_i}{dt} = \frac{c^2}{V_i}\left[\dot{m}_{I-1} - \dot{m}_I\right] \tag{A.14}$$